EPFL

Thèse n° 9837

The effects of kinematics, flexibility, and planform on the vortex formation and aerodynamic performance of flapping wing flight

Présentée le 13 janvier 2023

Faculté des sciences et techniques de l'ingénieur
Laboratoire de diagnostic des écoulements instationnaires
Programme doctoral en mécanique

pour l'obtention du grade de Docteur ès Sciences

par

Alexander GEHRKE

Acceptée sur proposition du jury

Prof. D. Floreano, président du jury
Prof. K. A. J. Mulleners, directrice de thèse
Prof. S. Sponberg, rapporteur
Prof. L. David, rapporteur
Prof. F. Gallaire, rapporteur

École polytechnique fédérale de Lausanne

2023

Wings are a constraint that makes
it possible to fly.
— Robert Bringhurst

Acknowledgements

This thesis has been the result of four very intense, but also fun years. I want to take a moment to thank the people who supported me in these years academically and personally.

I thank my supervisor Prof Karen Mulleners who invited me first for my master's and then for my PhD project to study and work at EPFL and the UNFoLD laboratory. I grew a lot professionally under the guidance during this time, and I am grateful to have had the opportunity to do my studies abroad.

My thanks also go to Prof Simon Sponberg and his research group who helped greatly to extend my project in the biological domain. The collaboration added a lot value to my work and my curiosity by working with insect wing samples and direct applications.

I thank this thesis' jury for taking the time to read and evaluate my work in-depth. The following discussion was very insightful, and I hope to incorporate the ideas and suggestions in my future work.

I would like to thank all my family and friends for supporting me throughout these years. Some of them I met every day, some were there in the time of need, and some were there to enjoy the good times together that followed. We went to coffee breaks, bars, hikes, barbecues, swims, lunches, dinners, play darts, parties, holidays, festivals, and so much more. I am glad to have shared all these great memories.

Many of these memories were shared with the UNFoLD lab. It changed a lot during these years, but it was always full of great people. This made my everyday work siu much more enjoyable, and I could not have asked for better office and lab mates. It will be truly missed.

I am also thankful to my family for being there in tough times, but also for being there to celebrate with me. The holiday seasons were always a very welcomed break and a time to relax and reset for the next years. Even though the ride was long, it felt like home was always within reach. Finally, I am very grateful to my wife Gabriela, who came with me on this journey to Switzerland for my PhD and shared all the great but also difficult times with me. I am glad to have found a companion to explore the world with and to have a hot cocoa when settled. 🐈🐈

Lausanne, December 30, 2022 A. G.

Abstract

Flapping wing flight used predominately in nature by flying insects, birds, and mammals generally has a higher aerodynamic performance than rotary or fixed wing micro air vehicles at low Reynolds numbers. However, due to its complexity the bio-inspired flight system is not as widely used as their rotary wing counter-parts. In this thesis, the aerodynamic challenges in flapping wing flight are addressed. In particular, the effects of different wing kinematics, flexibilities, and planforms on the the leading edge vortex development and aerodynamic performance are investigated.

In a first part, we experimentally optimise the kinematics of a flapping wing system in hover with the objective to maximise the lift production and hovering efficiency. Additional flow field measurements are performed to link the vortical flow structures to the aerodynamic performance for the optimal kinematics. We obtain kinematics which promote the formation of a strong leading edge vortex and yield high lift coefficients, and kinematics which promote leading edge vortex attachment and are more power efficient. We identify the shear layer velocity as a scaling parameter for the growth of the vortex and its impact on the aerodynamic forces. The experimental data agree well with the shear layer velocity prediction, making it a promising metric to quantify and predict the aerodynamic performance of the flapping wing hovering motion for the design and control of micro air vehicles.

In a second part, a novel bio-inspired membrane wing design is introduced, and used to study the fluid-structure interactions of flapping membrane wings. We find optimal combinations of the membrane properties and flapping kinematics that out-perform their rigid counterparts both in terms of increased stroke-average lift and efficiency, and characterise them with an aeroelastic number. Flow field measurements around the membrane wings reveal that the leading edge vortex formation is suppressed at lift and efficiency optimal aeroelastic conditions. These results demonstrate that a leading edge vortex is not always required to generate high lift in flapping wing flight. If the membrane wings become too flexible, the flow separates over the high curvature of the wing, and the wing experiences great losses in lift and hovering efficiency. These findings explain the flight behaviour of bats which adapt either their wing's angle of attack, stiffness, or flight velocity. We suggest using active flow control for artificial membrane wing vehicles, and the leading and trailing edge angles as indicators for the flow state to maintain optimal aeroelastic conditions in flight.

In a third and final part, hawk moth wing shapes are collected and their aerodynamic performance, and leading edge vortex formation compared to flat and rectangular wings. Three-component flow field measurements over the full span and aerodynamic force recordings

are conducted for scaled wing models on a robotic flapping wing system. We investigate if the morphology of hawk moth wings could have evolved to accommodate the formation of a strong and coherent leading edge vortex for aerodynamic benefits. While all wings have the same surface area and aspect ratio, the rectangular wing produces only half the lift and drag coefficients compared to the hawk moth wings. The difference in force production is also reflected in the leading edge vortex formation on the wings. At mid-span the vortex lifts off of the wing on the rectangular planform, and a strong tip vortex impedes on the leading edge vortex formation and span-wise vorticity transport. On the hawk moth wing planform, the local chord length reduces greatly towards the tip and allows the leading edge vortex to expand over the full wing span. In consequence, the hawk moth wings generate double the wing loading compared to the rectangular wings. Higher wing loading improves the flight control and escape capabilities of flapping wing fliers, and allows the smaller, high aspect ratio wings of the hawk moth to produce sufficient lift to stay in hover.

Zusammenfassung

Der Flügelschlag wird in der Natur von fliegenden Insekten, Vögeln und Säugetieren genutzt und kann bei niedrigen Reynolds-Zahlen eine höhere Effizienz als Starrflügel oder Rotoren haben. Aufgrund seiner Komplexität wird das biologisch inspirierte Flugsystem bisher jedoch weniger eingesetzt als Propeller betriebene Drohnen. In dieser Doktorarbeit werden die aerodynamischen Zusammenhänge beim Schlagflügelflug untersucht. Insbesondere werden die Auswirkungen von Flügelbewegung, -flexibilität und -form auf die Entwicklung des Vorderkantenwirbels und die aerodynamischen Kräfte untersucht.

Im ersten Teil optimieren wir experimentell die Bewegung eines Schlagflügelsystems, mit dem Ziel, den Auftrieb und die Effizienz im Schwebeflug zu maximieren. Zusätzlich wird das Strömungsfeld um den Flügel aufgezeichnet, um den Zusammenhang zwischen den Wirbelstrukturen und den aerodynamischen Kräften für den optimalen Flügelschlag herzustellen. Wir finden Flügelkinematiken, die die Bildung eines starken Wirbels an der Vorderkante begünstigen und hohe Auftriebskoeffizienten erzugen, sowie Kinematiken, bei denen der Wirbel nah am Flügel bleibt und die energieeffizienter sind. Wir identifizieren die Geschwindigkeit der Scherschicht an der Vorderkante als geeigneten Parameter, um das Wachstum des Wirbels und seinen Einfluss auf die aerodynamischen Kräfte zu berechnen. Die experimentellen Daten stimmen mit der Vorhersage der Scherschichtgeschwindigkeit gut überein, was sie zu einer vielversprechenden Kennzahl für die Quantifizierung und Vorhersage der aerodynamischen Leistung des Schwebeflugs für die Konstruktion und Steuerung von Schlagflügel Drohnen macht.

In dem zweiten Teil wird ein neuer biologisch inspirierter Membranflügel vorgestellt und zur Untersuchung der Fluid-Struktur-Wechselwirkung von Schlagflügeln verwendet. Wir finden optimale Kombinationen von Materialeigenschaften und Schlagflügelbewegungen, die relativ zu den unflexiblen Flügeln einen erhöhten Auftrieb haben und gleichzeitig die Energieeffizienz des Systems steigern. Diese Fluid-Struktur-Wechselwirkung charakterisieren wir mit der aeroelastischen Zahl. Weitere Strömungsfeldmessungen um die Membranflügel zeigen, dass die Wirbelbildung an der Vorderkante bei optimalen aeroelastischen Auftriebs- und Wirkungsgradbedingungen unterdrückt wird. Diese Ergebnisse suggerieren, dass ein Vorderkantenwirbel nicht immer erforderlich ist, um einen hohen Auftrieb beim Schlagflügelflug zu erzeugen. Wenn die Membranflügel zu flexibel werden, löst sich die Strömung über der starken Krümmung des Flügels ab, und starke Verluste an Auftrieb und Energieeffizienz treten auf. Diese Erkenntnisse erklären zum Teil das Flugverhalten von Fledermäusen, die den Anstellwinkel, die Steifigkeit oder die Fluggeschwindigkeit ihres Flügels anpassen können um eine

zu starke Verformung des Flügels zu verhindern. Diese Art der aktiven Strömungssteuerung könnte auch für künstliche Membranflügel verwendet werden. Die Winkel der Vorder- und Hinterkanten können dabei als Indikatoren für den Strömungszustand verwendet werden, um optimale aeroelastische Bedingungen im Flug aufrechtzuerhalten.
In dem dritten und letzten Teil werden die Flügelformen von Schwärmern untersucht und ihre aerodynamische Leistung sowie die Wirbelbildung an der Vorderkante mit flachen und rechteckigen Flügeln verglichen. Drei-Komponenten-Strömungsfeldmessungen über die gesamte Spannweite und Aufzeichnungen der aerodynamischen Kräfte werden für skalierte Flügelmodelle an einem Roboter-Schlagflügelsystem durchgeführt. Wir untersuchen, ob sich die Morphologie von Falkenmottenflügeln so entwickelt haben könnte, dass sie die Bildung eines starken und kohärenten Wirbels an der Vorderkante ermöglicht, um aerodynamische Vorteile zu erzielen. Obwohl alle Flügel die gleiche Oberfläche und das gleiche Streckungsverhältnis haben, erzeugt der rechteckige Flügel nur die Hälfte der Auftriebs- und Widerstandskoeffizienten im Vergleich zu den Falkenmottenflügeln. Der Unterschied in der Krafterzeugung spiegelt sich auch in der Wirbelbildung an der Vorderkante des Flügels wider. In der Mitte der Spannweite löst sich der Wirbel beim rechteckigen Flügel ab, und ein starker Flügelrandwirbel behindert die Entwicklung und den Wirbelstärketransport des Vorderkantenwirbels. Beim Falkenmottenflügel nimmt die lokale Sehnenlänge zur Spitze hin stark ab, so dass sich der Vorderkantenwirbel über die gesamte Spannweite ausbreiten kann. Dabei erzeugen die Falkenmottenflügel die doppelte Flächenbelastung im Vergleich zu rechteckigen Flügeln. Eine höhere Flächenbelastung verbessert die Flugkontrolle und die Fluchtmöglichkeiten der Schwärmer und ermöglicht es mit kleineren, hochgestreckten Flügeln genügend Auftrieb zu erzeugen, um im Schwebeflug zu bleiben.

Contents

List of Figures

List of Tables

Introduction

After the Wright brothers took the first controlled, powered flight in 1903 [1], high lift production has always been sought after in the research and development of aerodynamics and aeronautics. Higher lift coefficients allow to carry a bigger payload, to reduce the wing size for higher manoeuvrability, and flight at varying speeds. Figure 1 gives an overview of the different flow regimes relevant to natural and engineered flight characterized by the Reynolds number. Fixed wing aircrafts, typically used in flight at higher Reynolds numbers ($Re > 10^6$), reach lift coefficients up to $C_L = 2$ by keeping the flow attached to the airfoil and create large leading edge pressure gradients [2]. At transitional flow velocities ($Re = 10^4$ to 10^6) the maximum lift of a rigid, smooth airfoil is greatly reduced due to boundary layer separation. Turbulators help to keep the flow attached at transitional flight velocities and allow to reach high maximum lift coefficients again. Even at lower Reynolds numbers ($Re < 10^4$, fig. 1), the boundary layer over the airfoil stays laminar and separates easily when subjected to adverse pressure gradients [2]. Conventional airfoils stall even at low angles of attack and yield low lift coefficients, insufficient for sustained flight [4]. Yet, it is in this flow regime where most insects fly successfully.

Most engineered flying vehicles use fixed or rotating wings Flying insects, birds, and mammals can flap their wings to generate lift. Flapping wing fliers generally have a higher aerodynamic performance than revolving wing aircraft at low Reynolds numbers ($Re < 5000$), and their lift-to-power ratio can be improved by up to 200% compared to fixed or revolving wings at $Re < 100$ [9, 10]. Natural fliers move their wings at a high wingbeat frequency relative to their flight speed and create an unsteady flow field around their wings. At the high angles of attack commonly seen by flapping wing fliers, the flow separates over the wing and rolls up into a coherent flow structure - the leading edge vortex (fig. 2c,d). The formation of the leading edge vortex under unsteady flow conditions produces transient high lift coefficients sufficient for sustained flapping wing flight at low Reynolds numbers [11–15]. But the leading edge vortex does not stay on the wing for long. The typical life cycle of a leading edge vortex last between 3 and 6 convective times as presented for an impulsively started flat plate in fig. 3 [2]. At the beginning, a leading and a trailing edge vortex form on the wing. The leading edge vortex is formed due to accumulation of shear-layer vorticity from the leading edge and grows consistently. The starting trailing edge vortex sheds into the wake shortly after. The leading edge vortex gains strength and size until it covers the entire chord length of the wing. Then, the vortex loses coherence and eventually lifts off of the wing. Finally, the vortex sheds when it

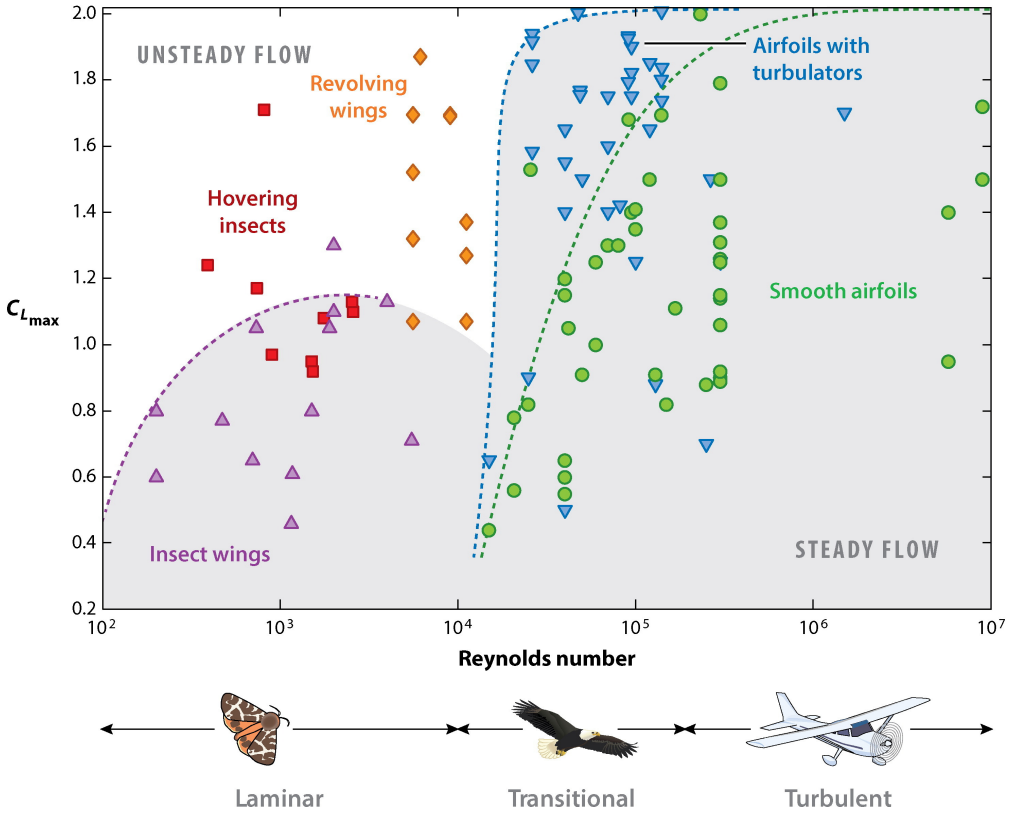

Figure 1 – The maximum lift coefficient $C_{\mathrm{L,max}}$ as function of Reynolds number for different lift generators in steady and unsteady flow. Figure from [2, 3]

no longer accepts additional vorticity from the shear-layer (not shown in fig. 3).

During the vortex' growth cycle flapping wings undergo large variations in force. Figure 4 shows the temporal evolution of the lift and drag coefficient variations over one stroke-cycle for a robotic flapping wing in hover at an angle of attack $\alpha = 40°$ [16]. Here, the dashed lines represent the sinusoidal stroke-velocity profile used by most natural fliers and engineered flapping wing vehicles. During the beginning and end of every stroke cycle (1), the wing rotates to position its leading edge in front of the wing indicated by the grey shaded areas. When the leading edge vortex first emerges, it coincides with a large increase in lift but also drag force coefficient (fig. 4). During the vortex growth (2) the forces on the wing are greatly increased until they reach a peak at mid-stroke, where the wing is at its highest rotational velocity and the vortex has grown in strength and size to cover the full chord. The forces decrease sharply when the wing slows down in the second part of the cycle (3) and the vortex lifts off of the wing. At the end of the stroke cycle (4), the wing rotates to reverse its leading edge for the next cycle. The leading edge vortex sheds into the wake and breaks down. In this last stage of the leading edge vortex growth cycle, the aerodynamic forces on the wing reduce to zero. A new stroke cycle follows and the next leading edge vortex gives rise to high lift forces. The unsteady nature of successive vortex formation and shedding provides the necessary lift in

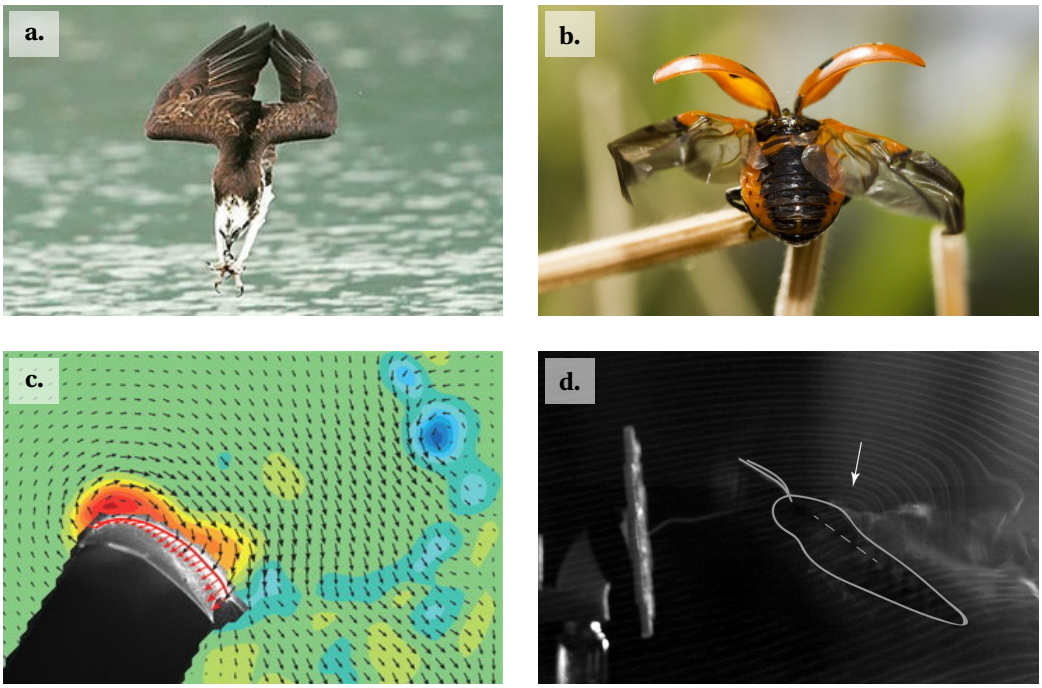

Figure 2 – a. An osprey diving to catch its prey (adopted from [5]). b. A ladybug unfolding its wings (adopted from [6]). c. Flow field around a bat in slow forward flight (adopted from [7]). d. Smoke wire flow visualisation of a hawk moth in hovering flight feeding on an artificial flower (adopted from [8]).

forward or hovering flapping wing flight at Reynolds numbers below $Re < 10$ [17, 18], currently unmatched by human-made flying devices.

The flight at low Reynolds numbers opens up many applications in urban environments, like parcel delivery, communications relay, and environmental monitoring [19, 20]. Especially at the insect scale, autonomous micro air vehicles can provide invaluable assistance during natural disasters like earthquakes in confined spaces or could be employed in environment preservation on a small scale but large areas [21]. Low Reynolds number flight also has the potential to open up aerial exploration on other planets with less dense atmospheres [22], motivated by the recent success of *Ingenuity*, the first autonomous controlled flight of an aircraft in the Mars environment [23].

The reason flapping wing micro air vehicles are not as widely used as their rotary wing counterparts, is due to the great complexity the bio-inspired flight system presents. Successful flapping wing flight in nature is the result of a successful interplay between wing and body morphology [24–27], muscle actuation [28, 29], and sensory control [30, 31]. All of these are controlled by an intricate nervous system, and an underlying flight strategy and navigation [32–34]. Natural fliers present a vast diversity within each of the elements. To generate lift and manoeuvrer insects control the wing motion with great precision [35–37], and can even adapt their kinematics to compensate for wing damage [38, 39], or when they are moving on the surface

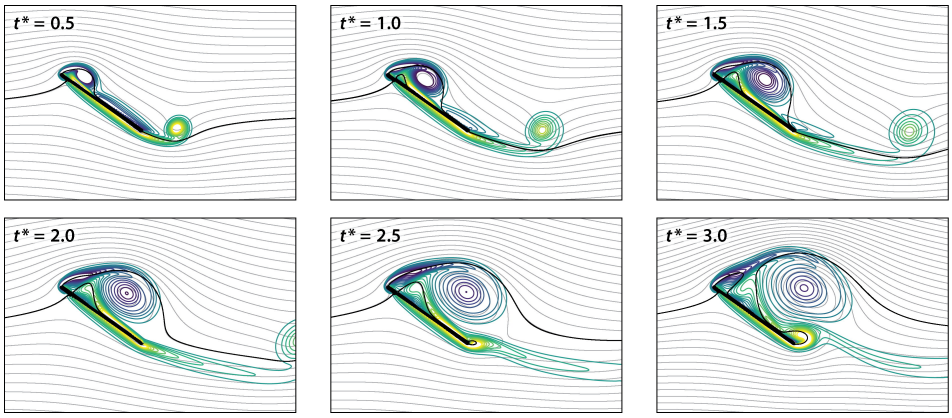

Figure 3 – Leading edge vortex life cycle for an impulsively started, two-dimensional plate in translation at an angle of attack $\alpha = 35°$. The lines represent vorticity field contours (colour), streamlines (grey), and stagnation streamlines (black). Here, $t* = tU/c$ is the convective time based on the wing velocity U and the chord length c. Figure from [2]

of water [40, 41]. Insects and bats adjust the stiffness of their wings to limit the deformation and control the flow separation over their wings [42, 43]. The body and its centre of mass can also play a crucial role. Butterflies undergo large angle rotations with their body which helps to direct the trajectories of their shed vortices and reduce drag [44, 45]. Despite all the challenges associated with flapping wing flight, recent advances in wing actuators and electronic miniaturization paved the way for the successful flight of human-made flapping wing vehicles [46–52].

In this thesis, the aerodynamic challenges in flapping wing flight are addressed. In particular, the effects of different wing kinematics, flexibility, and planforms on the leading edge vortex development and aerodynamic performance are investigated experimentally on a robotic flapping wing platform. The objective of the thesis is to gain an understanding of the underlying fluid dynamic phenomena in flapping wing flight, and to explore different methods for improving the aerodynamic performance in terms of lift production and energy efficiency. The thesis aims to explain morphological and behavioural traits in natural fliers, and to provide guidelines for the design and control of engineered flapping wing vehicles.

Thesis outline

The thesis consists of three parts dedicated to the effects of wing kinematics (part I), wing flexibility (part II), and wing planform (part III) on the vortex formation and aerodynamic performance of flapping wing flight.

In part I, we experimentally optimise the kinematics of a flapping wing system in hover to maximise the average lift production and hovering efficiency with the help of an evolutionary algorithm. In chapter 1, three different approaches to parametrise the motion kinematics for

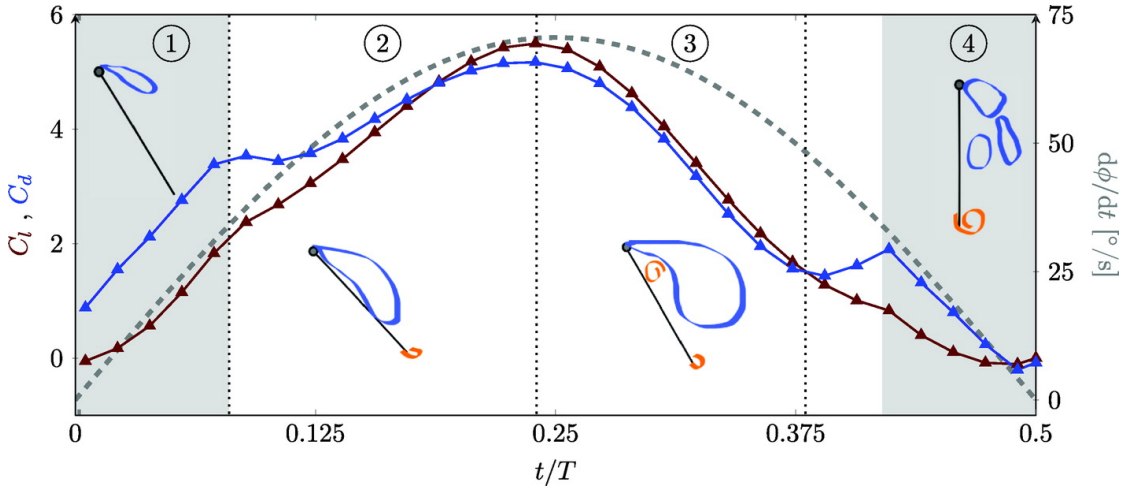

Figure 4 – The lift and drag force coefficients as function of time over one half-cycle for a flapping wing system in hover. The drawings depict the leading edge vortex life cycle. The dashed line represents the stroke velocity $\mathrm{d}\phi/\mathrm{d}t$ The grey shaded areas indicate the wing rotation at the beginning and end of every cycle. Figure from [16]

the experimental optimisation are presented. A set of control points that are connected by a spline interpolation, a finite Fourier series, and a reduced-order modal reconstruction based on a proper orthogonal decomposition of a set of random walk trajectories. We compare the results and performance of the different parametrisations with regard to the diversity of the randomly created initial populations, and the convergence behaviour of the optimisation. Dedicated applications for each parametrisation approach are suggested.

The fluid dynamic analysis and discussion of the flapping wing optimisation is presented in chapter 2. Additional flow field measurements are conducted to link the vortical flow structures to the aerodynamic performance for the Pareto-optimal kinematics. In all cases, a leading edge vortex is fed by vorticity through the leading edge shear layer which makes the shear layer velocity a good indicator for the growth of the vortex and its impact on the aerodynamic forces. We estimate the shear layer velocity at the leading edge solely from the input kinematics and use it to scale and predict the average and the time-resolved evolution of the circulation and the aerodynamic forces.

In part II, chapter 3, we introduce a novel bio-inspired membrane wing design and systematically investigate the fluid-structure interactions of flapping membrane wings. We find optimal combinations of the membrane properties and flapping kinematics that out-perform their rigid counterparts both in terms of increased stroke-average lift and efficiency. The lift and efficiency optima occur at different angles of attack and effective membrane stiffnesses which we characterise with an aeroelastic coefficient. Additional deformation measurements are conducted to link the membrane dynamics to the aerodynamic force production. We identify membrane geometry parameters and thresholds for the control of the optimal membrane shape.

In chapter 4, the impact of the membrane deformation on the leading edge vortex formation at different aeroelastic conditions is investigated. The observations on the flapping membrane wing platform from chapter 3 are expanded with flow field measurements and additional deformation measurements. The goal is to relate the fluid-structure interaction of the passively deforming membrane with the force production on the wing. The findings should explain certain behaviours in bat flight and provide means of flow control applications for flapping membrane wing.

In part III, chapter 5, the effects of different wing planforms and wing shapes on the leading edge vortex formation and aerodynamic performance are explored. The aerodynamic performance and three-dimensional flow fields around scaled hawk moth wing models and basic reference wing shapes are investigated. The objective is to identify key morphological traits which govern the leading edge vortex formation on hawk moth wings and explain the diversification of different wing planforms found in nature. The findings in this chapter, provide guidelines for the design of different wing planforms for flapping wing vehicles.

Finally, the conclusions of this thesis and an outlook are provided in chapter 6.

Part I
Effects of Wing Kinematics

1 On the parametrisation of motion kinematics for experimental aerodynamic optimisation

In this chapter, three different approaches to parametrise the motion kinematics for experimental optimisations are presented. The objective is to evaluate the performance of the different approaches during the experimental optimisation of a flapping wing system in hover. Dedicated applications for each parametrisation approach are suggested. The fluid dynamic analysis and discussion of the optimisation results follows in chapter 2.

The work presented in this chapter has been published in *Experiments in Fluids* [53].

1.1 Introduction

Unsteady locomotion of flying animals such as birds and insects have inspired the development of micro air vehicles, which are less than 15 cm in size and operate in a Reynolds number range from 10 to 10 000 [27, 54, 55]. Their field of application includes information gathering in confined spaces, areal mapping, or the transport of small goods [21, 56]. Flapping wing configurations are a suitable manner of propulsion for micro air vehicles, since they offer better efficiency at low Reynolds number ($Re < 100$) and an improved manoeuvrability in comparison to fixed and rotating wing configurations [57, 58]. The development of complex flapping wing kinematics for various flight scenarios poses a challenge in this field. A similar challenge is the selection of optimal motion kinematics of other bio-inspired propulsion systems such as underwater vehicles mimicking fish propulsion. A standardised optimisation procedure facilitates the identification of motions with desired characteristics. The motion kinematics have to be parametrised by a finite number of variable parameters prior to optimisation to reduce the dimensionality of the solution space and allow for optimal solutions to be found in an affordable way within a reasonable timeframe. The optimisation solution landscape can dependent strongly on the parametrisation and possible optima might be missed [59]. The ideal parametrisation has as little variable parameters as necessary to reduce the computational complexity of the optimisation problem without restricting the

solution space or creating a bias in a certain direction. Yet, any parametrisation will exclude possible solutions due to discretisation in comparison to a continuous solution in an infinite-dimensional solution space and it is vital to carefully select the most suitable approach for each optimisation problem at hand.

Past efforts to optimise bio-inspired motion kinematics initially focussed on simple linear and harmonic motions. [60] numerically optimised a flapping airfoil for combined maximum thrust and efficiency. They parametrised the sinusoidal plunge and pitching motions with a variable amplitude and phase shift for a fixed frequency. [61] implemented a quasi-steady model of insects with a hybrid optimisation algorithm. Their kinematic function enables a continuous transition of the pitching angle evolution β with the parameter C between sinusoidal and trapezoidal motions according to

$$\beta(t) = \frac{\beta_\mathrm{m}}{\tanh(C)} \tanh\big(C \sin(2\pi f t + \Phi)\big) + \beta_0 \tag{1.1}$$

with f being the flapping frequency, Φ the phase shift between the stroke and pitching motions, β_0 the offset angle and a scaling factor β_m for further modulations. The temporal evolutions of the stroke and elevation angles were defined similarly, yielding a total of twelve variable parameters. Solutions for these twelve parameters were determined that maximised the aerodynamic efficiency while providing enough lift to support the body weight of different insects. The aerodynamic performance can be further increased by more complex, non-harmonic, and asymmetric kinematics, which have to be defined using more parameters or different base functions. The pitching kinematics of insects in nature are often asymmetric which could be an evolutionary adaption to improve the performance [62]. Martin and Gharib [63] were among the first to implement a kinematic motion function with the possibility to represent asymmetric motions. Liu and Aono [62] performed an optimisation of the motion of a pectoral fish fin which was defined as a complex combination of trigonometric expressions for all three spatial angles. The motion kinematics were successfully optimised for a combined objective of minimal side-thrust and maximal efficiency. They noticed an increasing difficulty in finding the global optimum with increasing number of parameters describing the kinematics. Mandre et al. [59] investigated the influence of the parametrisation with a finite Fourier series on a heaving and pitching hydrofoil. Small modifications of the parametrisation can lead to a significantly altered solution landscape with a bias towards small but pronounced local optima. The examples highlight the potential of asymmetric and more complex kinematics to push the performance envelope of bio-inspired micro aerial vehicles.

In this chapter, we will present three different approaches to define and parametrise kinematics for optimisation studies. The different approaches will be presented, compared, and evaluated for the example of the experimental optimisation of the pitching kinematics of a flapping wing. An optimisation is performed for each kinematic function with 6, 12 and 18 parameters, leading to more than 30 000 individual experiments in total. The different approaches to parametrise motion kinematics for optimisation selected here are control points connected by a spline interpolation, a finite Fourier series, and a linear combination of modes

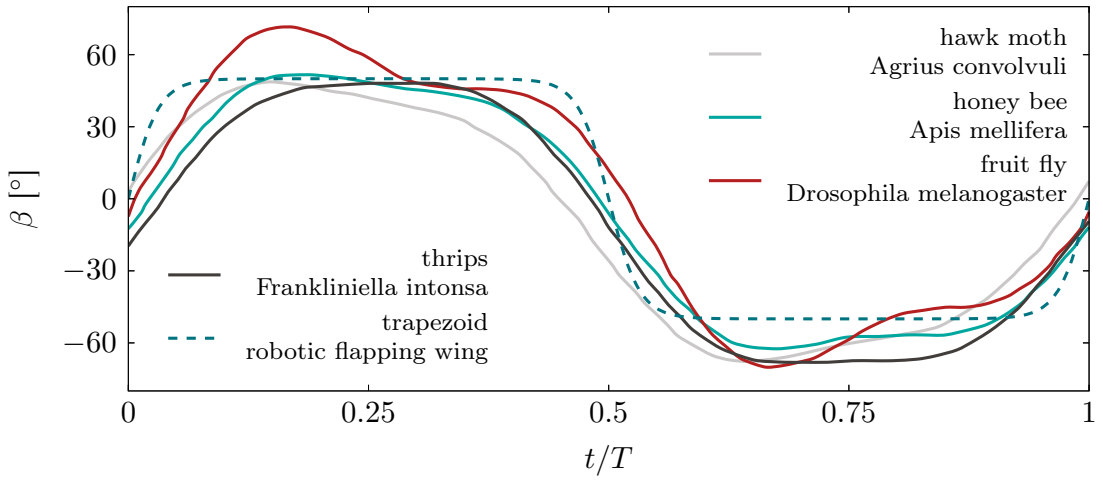

Figure 1.1 – Pitch angle β kinematics of various natural fliers, adopted from [62] and trapezoidal pitch angle kinematics from a robotic flapper [64].

determined by a modal decomposition of kinematics created by a random walk. Dedicated applications for each approach are suggested. The details about the experimental setup and the fluid dynamic interpretation of the results will follow in chapter 2.

1.2 Methods

1.2.1 Kinematic functions

Three different approaches to parametrise motion kinematics are selected here:

- control points connected by a spline interpolation,
- a finite Fourier series, and
- a linear combination of modes determined by a modal decomposition of kinematics created by a random walk.

The different parametrisation were selected by their ability to mimic trapezoidal and sinusoidal pitch angle profiles commonly seen on robotic flapping wing devices as well as more complex pitch angle kinematics observed on nature's fliers (fig. 1.1). We created kinematic functions using the three approaches with three different parameter counts ($p = 6, 12, 18$). The first $(p-1)$ parameters are used to modify the pitching angle evolution and the phase shift is controlled with the last parameter Δt_0 for all kinematic functions. The motions are described by the pitching angle β (fig. 1.1). The sinusoidal stroke angle ϕ remains unchanged throughout the optimisations and the elevation angle is kept at zero due to its negligible influence on the lift production [62].

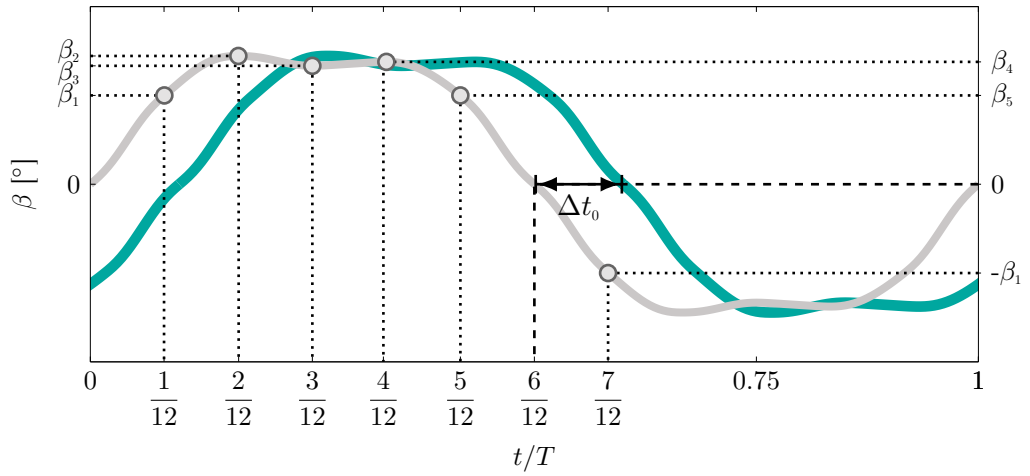

Figure 1.2 – Example of the parametrisation of the pitch angle kinematics using control points connected by a spline interpolation with $p = 6$ parameters. Five parameters describe the pitch angles $(\beta_1, ..., \beta_5)$ of the five control points that are equidistantly distributed within a half stroke. A fifth degree spline connects the five control points and the half half stroke profile is point mirrored to create the full symmetric pitch angle profile in grey. The sixth parameter Δt_0 introduced a phase shift leading to the final pitching profile in colour.

Control points connected by splines

As a first intuitive approach, we select a limited number of control points that will be connected using spline interpolation. To start, we create a symmetric pitch profile by distributing $(p-1)$ control points equidistantly throughout a half-stroke which represents the most efficient use of the available parameters. Freely spaced control points could lead to large gradients for higher parameter counts which can not be executed by our experimental set-up. In a way, the temporal spacing of the control points acts as a build-in low-pass filter for the pitch angle gradients. If the phase of the control points is not fixed, the phase bounds of the individual points depend on each other which makes the selection of the kinematics slightly more complicated. Depending on the specific problem at hand, it is possible to place more control points in certain parts of the motion where larger variations are required to optimise and reduce the parameter count. The beginning and end of the half-stroke are fixed at $\beta = 0°$ and the control points are solely specified by their pitch angle β_n, with $1 \leq n \leq (p-1)$ as indicated in fig. 1.2. Next, the control points are connected by a fifth degree spline interpolation to minimise the local acceleration $\ddot{\beta}$. By point-mirroring the first half-stroke around $(t/T, \beta) = (0.5, 0)$, we obtain a symmetric pitching profile for the back and forth stroke, represented by the grey curve in fig. 1.2. Finally, we added a phase-shifted Δt_0 to allow for advanced and delayed wing rotation with respect to the stroke reversal, leading to the coloured curve in fig. 1.2. This procedure allows us to created complex non-linear and non-harmonic motions with high curvatures. The main advantage of the control point parametrisation, is its intuitive and direct local control of the pitching profiles. Local adjustments can be made by moving individual control points and the values of the control points are directly linked to the pitch angle values,

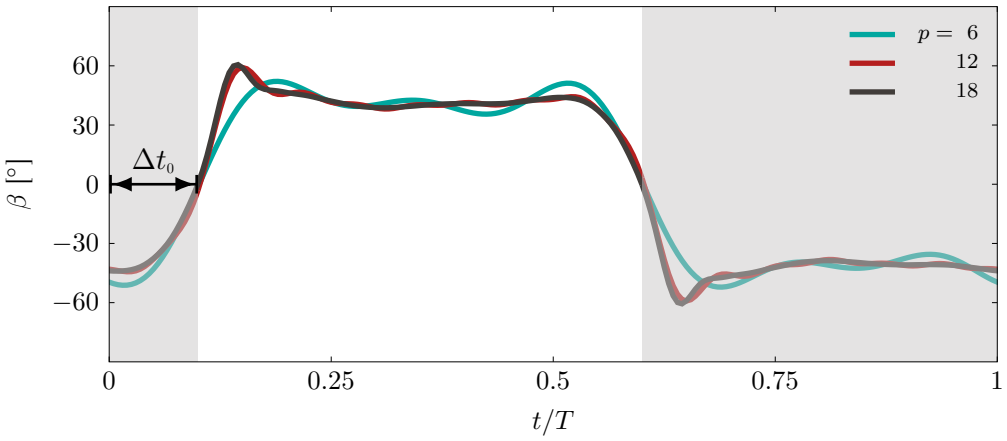

Figure 1.3 – Example of the parametrisation of the pitch angle kinematics using a finite Fouries series $p = 6$, 12, and 18 parameters. The last parameter Δt_0 introduced the phase shift.

which facilitates the formulation of pitch angle constraints due to mechanical and motor limitations. The distribution of the control points along the time axis can be easily varied to adapt the approach to specific restrictions or requirements for a broad range of applications. On the downside, we noticed that the creation of a random set of control point splines is computationally demanding and required 22.8 s on average for motions with 12 parameters on a typical desktop computer. The computational time increases exponentially with the parameter count and takes a couple of minutes for the tests with 18 parameters.

Fourier-series kinematics

In the second approach, we use a finite Fourier sine-cosine series to define our pitching kinematics:

$$\beta(t) = \sum_{k=1,3,5,\ldots}^{N} \left(a_\mathrm{k} \cos\left(2\pi k f_0 t\right) + b_\mathrm{k} \sin\left(2\pi k f_0 t\right) \right) \tag{1.2}$$

with a_k the cosine coefficients, b_k the sine coefficients, and f_0 the flapping frequency. For the current application, we use only the odd coefficients. The first odd sine-coefficients b_k are responsible for the base oscillation whereas the odd cosine-coefficients a_k are used for smaller modulations. The ability to represent higher curvatures, as they appear in trapezoidal motions, mainly depends on the number of Fourier terms included. A finite Fourier series is not ideal to describe sudden jumps or discontinuities and tends to display an overshoot followed by decaying oscillations near sharp gradients. This behaviour is known as the Gibbs phenomenon and can be reduced by adding a Lanczos-σ-factor [65]. The Lanczos-σ-factor is defined as:

$$\sigma\left(\frac{k}{m}\right) = \frac{\sin\left(\frac{k}{m}\pi\right)}{\frac{k}{m}\pi} \tag{1.3}$$

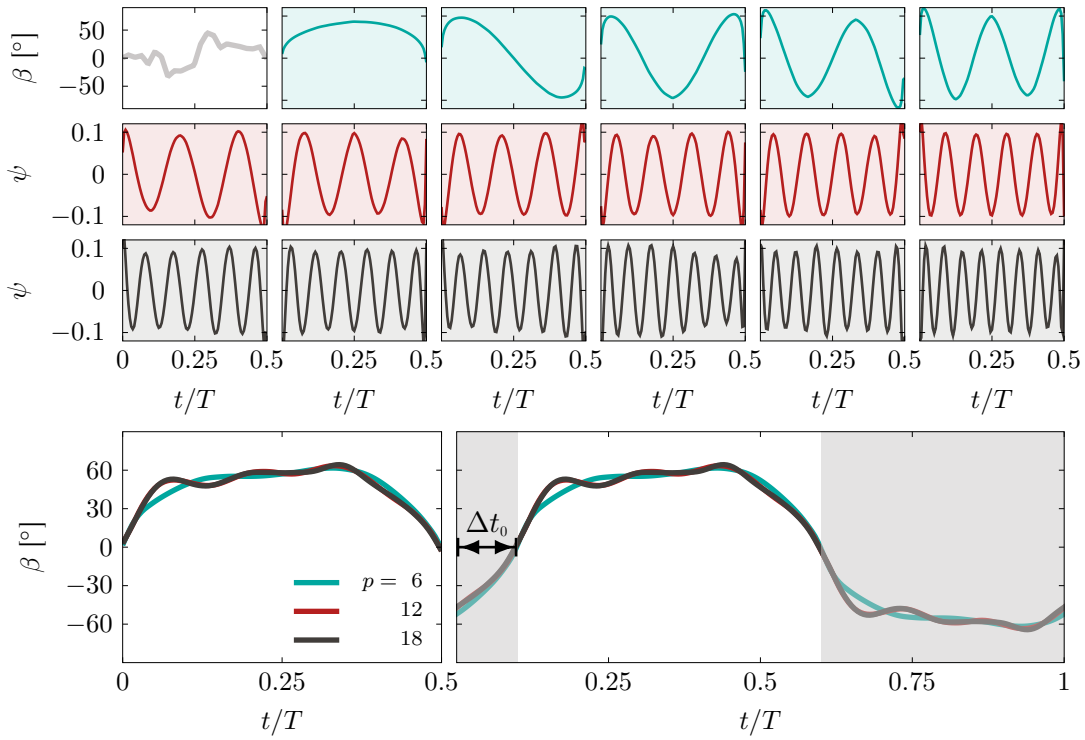

Figure 1.4 – Example of an individual random walk-based motion (top left) and the first 17 eigenmodes of the proper orthogonal decomposition of a family of 2×10^5 random walk-based motions. The first 5 modes are presented with a green background, modes 6 to 11 with a red background, and modes 12 to 17 with a grey background. Examples of new motions created as a linear combination of the first 5, 11, and 17 modes are presented in the bottom left. The half stroke motions are point-mirrored around $(T/2, 0)$ to obtain a full stroke and the phase shift is applied to create the final motions in the bottom right.

with m as the last plus one summing index of a finite Fourier series. The Fourier series based pitching kinematics used in this paper are described by a finite Fourier series with Lanczos-σ correction factor:

$$\beta(t) = \sum_{k=1,3,5,\ldots}^{(p-1)/2} \sigma\left(\frac{2k}{p+1}\right)\left(a_k \cos\left(2\pi k f_0 t\right) + b_k \sin\left(2\pi k f_0 t\right)\right) \tag{1.4}$$

with $(p-1)$ parameters, $(p-1)/2$ cosines and $(p-1)/2$ sine coefficients. The obtained motion kinematics are periodic, continuous in all derivatives and can easily be expressed in a closed form. The half strokes can be asymmetric around the quarter stroke. The phase-shift parameter Δt_0 is again applied at the end to create advanced or delayed wing rotations with respect to the stroke reversal. Exemplary motions created using 6, 12, and 18 parameters are presented in fig. 1.3.

Modal reconstruction

In the third approach, we use a low-order eigenmode reconstruction. The eigenmodes are obtained by a modal decomposition of a family of available arbitrary kinematics. This parametrisation approach is particularly elegant if a family of kinematics is known. For example, if a database of kinematics is available from direct observations of insects or fish motions, we can first reduce the dimensionality of the available kinematics using modal decomposition. Measured and new kinematics can then be created by low-order reconstruction of the most dominant kinematic modes. Here, we do not have a database of measured kinematics at our disposal. To demonstrate the concept of eigenmode reconstruction as a parametrisation approach, we have artificially generated a family of randomised kinematics based on a biased random walk algorithm. The random walk motion generator is not an essential part of the approach it merely serves as bypass to obtain a generalised motion database. The random walk algorithm takes randomly sized steps in a discretised half-stroke. The random expectation value distribution for the individual step sizes is defined such that their sum equals zero over one half-stroke. Each step is defined as the expectation value plus a random fluctuation. The motions starts at $\beta = 0°$ and is set again to zero at the end of the half-stroke. This creates a wider spread of values and higher gradients at the end of the half-stroke in comparison to the start of the half-stroke. This bias is resolved by line-mirroring motions at mid-half-stroke ($T/4$). An example of a random walk-based motion is presented in the top left panel of fig. 1.4. A large amount of motions ($\mathcal{O}(10^5)$) is created within a few minutes with this method.

The family of random walk-based motions are then decomposed using proper orthogonal modal decomposition (POD). All modes start and end with a zero passage and are nearly symmetric (fig. 1.4). The symmetry is expected to improve with a larger data basis of random kinematics whereas the computational complexity of the POD is the limiting factor for the number of input motions. The modes exhibit high similarity with Legendre polynomials starting from the second polynomial. The POD ensures the optimality of the projection space for a given set of training motions and the optimal use of parameters. A large variety of complex, asymmetric motions and oscillations can be defined by a linear combination of the first $(p-1)$ eigenmodes:

$$\beta(t) = \sum_{n=1}^{p-1} a_\mathrm{n} \sqrt{2\lambda_\mathrm{n}}\, \psi_\mathrm{n}(t) \tag{1.5}$$

with ψ_n the POD eigenmodes, λ_n the corresponding eigenvalues, and a_n the parametrisation coefficients. The first 17 eigenmodes, ψ_1-ψ_{17}, are presented in fig. 1.4 for the proper orthogonal decomposition of the family of random walk based motions used in this paper. The coefficients a_n are considered normalised and have values confined between –1 and –1. The motions are point-mirrored around $(T/2, 0)$ to obtain a full stroke and the phase shift is applied to create the final motion as depicted in the bottom row of fig. 1.4. Discontinuities in the gradient between the end and beginning of each half-stroke cannot be executed by the motors and are mitigated by a robust local regression smoothing, which is tuned to mainly affect the sections around stroke reversal. Discontinuities in the velocity $\dot{\beta}$ appear for randomly created

kinematics in the early populations and diminish when the convergence progresses.

1.2.2 Genetic algorithm optimisation

The pitching kinematics of our robotic flapping wing device have been optimised using the multi-objective genetic algorithm optimisation algorithm (`gamultiobj`) from the global optimisation toolbox of Matlab® [66]. More details about the experimental procedure of the optimisation will be provided in chapter 2. A genetic algorithm is a meta-heuristic optimisation method, suited to find the global optimum in a non-linear solution space with a large number of degrees of freedom. It mimics the process of natural selection known from evolution by recombination and mutation. An initial population of 200 individuals, with a uniform distribution of the parameters within their bounds is created to start the optimisation. Each individual corresponds to one periodic flapping motion. The fitness values for two optimisation objectives are directly measured during experiments for each motion. The optimisation objectives are the maximum stroke average lift $\overline{C}_\mathrm{L}$ and the maximum stroke average efficiency $\overline{\eta}$. The stroke average efficiency $\overline{\eta}$ is defined here as:

$$\overline{\eta} = \frac{\overline{C}_\mathrm{L}}{\overline{C}_\mathrm{P}}. \tag{1.6}$$

The overline indicates stroke average quantities. The lift and power coefficients,C_L and C_P, are defined as

$$C_\mathrm{L} = \frac{L}{\frac{1}{2}\rho R c \overline{U}^2} \tag{1.7}$$

$$C_\mathrm{P} = \frac{P}{\frac{1}{2}\rho R c \overline{U}^3}. \tag{1.8}$$

The dimensional lift L and power P are normalised with the density ρ, the wing span R, the chord length c and the stroke average velocity $\overline{U}$. Each motion is executed over eight cycles. The evaluations of the individual experiments take 39 s each, including a settling time for the water in the tank. The fittest individuals produce offspring by recombination and mutation. Recombined individuals account for 60 % of the following population with the parameters calculated by a randomised linear combination $child = parent\ 1 + R(parent\ 2 - parent\ 1)$, with R a randomly picked number from a uniform distribution covering the interval $[0,1]$ [66]. The remaining 40 % of the new population are created by random mutation of the individuals' parameters. No clones from the elite are transferred into the next generation. The fitness values of the new individuals are determined and the procedure is repeated until convergence is detected, after which the optimisation is stopped. The final output of the genetic algorithm optimisation is a global Pareto front, which consists of all non-inferior solutions in the $\overline{C}_\mathrm{L}$ versus $\overline{\eta}$ space. The solutions on the Pareto front are called non-inferior solutions if the value for each objective can only be improved by decreasing the value of another one. The results of 9 optimisations will be presented and compared here. We have considered each of the

parametrisation approaches with $p = 6$, 12, and 18 parameters.

The experimental set-up is subjected to mechanical and safety constraints to protect the equipment. The will constrain the boundaries of the optimisation. The maximum pitching angle is limited by the range of free movement in the experimental set up such that $|\beta_{\max}| \leq 90°$. The minimum angle of $\beta_{\min} = 0°$ is imposed for the parametrisation of the initial half stroke before applying the phase-shift Δt_0 to avoid ambiguous solutions where advance or delayed rotation is not governed entirely by the phase-shift. The phase shift is bound by $[-\pi/2, \pi/2]$. The minimum and maximum pitch angle bounds are easy to define for the control point approach by directly limiting the values of β of the control points. This does not apply for the Fourier series and modal reconstruction based parametrisations. Here, the extreme angles are the result of a combination of different parameters. We opted here to keep the allowed parameter ranges as wide as possible and to reject proposed kinematics that are not safe or not feasible for the experimental mechanism before execution.

The most important constraint for our robotic flapper is the pitch angle acceleration. High accelerations put stress on the load cell due to the inertial forces on the wing and have to be limited to avoid damage. The maximally allowed pitch angle accelerations are $|\ddot{\beta}_{\max}| \leq 1800\,°/s^2$. The majority of randomly created individuals for the control point and modal reconstruction approach exceed the acceleration constraint. This leads to a validity rate of $\leq 10\,\%$ in combination with the constraint $|\beta_{\max}| \leq 90°$. The parameter bounds are tightened for the Fourier series approach to keep the share of invalid motions within a range of 10 % to 15 %. A simple restriction of the parameter space does not have the same effect for the splines connecting control points and the modal reconstruction. Here, a pre-selection of kinematics is necessary to obtain a full initial population of 200 individuals. The average and peak acceleration values of the randomly created motions increase with the parameter count and so does the share of randomly generated motions that cannot be executed. The pre-selection process takes a couple minutes for the modal reconstruction with 6 parameters and up to 4 h for the control points connected by splines with 12 parameters on a standard desktop computer. The control point approach with 18 parameters has very tightly spaced control points, which lead to high local accelerations above the limit value but they only appear for a very short time such that their risk of damaging the set-up is deemed low. The constraint of a minimum angle $\beta_{\min} \geq 0°$ in combination with the acceleration and velocity constraints is too strict for the modal reconstruction approach to create an initial population in a reasonable amount of time. By loosening the lower angular constraint $\beta_{\min}$, and allowing $\beta_{\min} < 0$, we obtain more kinematics that have a maximum acceleration below the mechanically allowed limit. All parametrisation approaches required a customised implementation of the constraints and adapted selection of the parameter bounds. The implementation of the experimental constraints was most straight forward for the control point based approach due to the more direct local access to the kinematics.

1.2.3 Convergence criterion

To monitor the progress of the optimisations and to decide when to consider the result to be converged, we have implemented a generational distance measure. The generational distance allows for a quantitative comparison between the optimisations of the different kinematic functions possible. It is a common measure to determine optimisation progress in genetic algorithms if no optimal Pareto front as reference is known [67]. The generational distance (GD) is defined by [68] as:

$$\mathrm{GD}(S,P) = \frac{1}{|S|}\left(\sum_{s\in S}\min_{r\in P} \parallel F(s) - F(r) \parallel^{p}\right)^{\frac{1}{p}}, \tag{1.9}$$

with S the set of Pareto front members of the current generation, P the Pareto set members of the previous generation, F the objective function, and p the selected distance norm. The generational distance describes the average distance the Pareto front members are shifted between successive generations and represents the optimisation progress. The individual distances are measured between the point of the current front and the closest point from the previous front. All distance measures for the efficiency $\overline{\eta}$ and stroke over lift coefficient $\overline{C}_{\mathrm{L}}$ are normalised by the average range of values for the first ten generations (or all generations if less that ten generations have been tested). The convergence speed is defined as the gradient of the generational distance.

An optimisation is considered converged if the convergence speed $\leq 5\times10^{-4}$ for two consecutive generations and if the generational distance $\leq 5\times10^{-3}$. The changes of the Pareto front are assumed to be minor after the convergence criterion is fulfilled.

1.3 Results and discussion

Here, we will analyse and compare the performance of the three selected parametrisation approaches for optimisation applications by the example of a multi-objective optimisation of the pitching kinematics of a flapping wing. The pitching kinematics are parametrised by

- control points connected by a spline interpolation,
- a finite Fourier series, and
- a modal reconstruction of POD eigenmodes.

Each of the approaches has been tested with 6, 12, and 18 parameters. This lead to more than 30 000 experimental iterations that have been executed over a period of several weeks. We will first compare how well the different approaches cover the motion space, discuss the optimisation process and convergence. The Pareto front solutions and the optimised kinematics will be discussed in chapter 2.

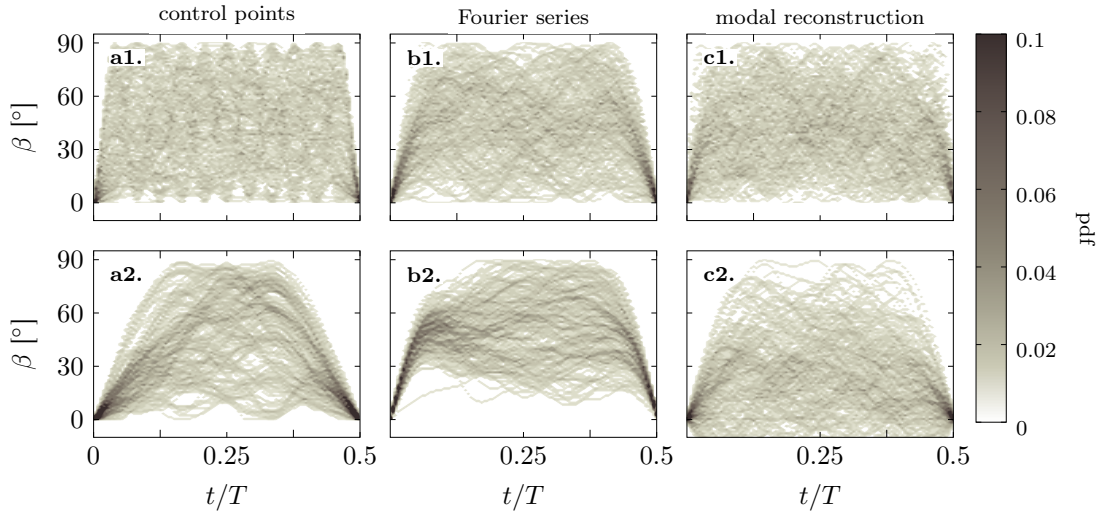

Figure 1.5 – Probability density map of a randomly selected initial population consisting of 200 individuals for the different parametrisations with 12 parameters without applying a phase-shift. The pitching angle is bound by $\beta_{\min} = 0°$ and $\beta_{\max} = 90°$. First row shows the coverage of the solutions space for the different parametrisation methods: a) control points connected by a spline interpolation, b) finite Fourier series, c) modal reconstruction, without taking into account an acceleration constraint. The second row shows the coverages when the acceleration constraint ($\ddot{\beta}_{\max} \leq 1800\,°/s^2$) is applied. The lower angular bound was lifted for the modal reconstruction when applying the acceleration constraint to allow for a set of 200 executable individuals to be found in a reasonable amount of time.

1.3.1 Coverage of the kinematic solution space

Suitable parametrisation approaches for optimisation studies should be able to represent a high variety of qualitative shapes and achieve good initial coverage of the solution space to not a priori exclude potential optimal solutions. To quantify and compare the ability of the different approaches to cover the solution space, we randomly created an initial population consisting of 200 individuals for the different parametrisations with 12 parameters without any acceleration constraint and without applying the phase-shift. The probability density maps for these initial populations of pitching kinematics are presented in the top row of fig. 1.5 to give a visual impression of the coverage of the solution space. The density maps for $p = 18$ do not show significant differences and lead to the same conclusions as for $p = 12$. The splines connecting control points and the modal reconstruction functions cover almost all achievable angles in the first half-stroke (fig. 1.5a1,c1). The Fourier-series have a slightly narrower band of admissible motions around stroke reversal with lower diversity (fig. 1.5b1). The fixed phase-locations of the control points lead to the occurrence of regions in the density map with higher local probabilities indicating an inhomogeneous coverage and slight bias towards low angles at the control points.

A quantitative comparison is presented in fig. 1.6, where the brighter bars indicate the values

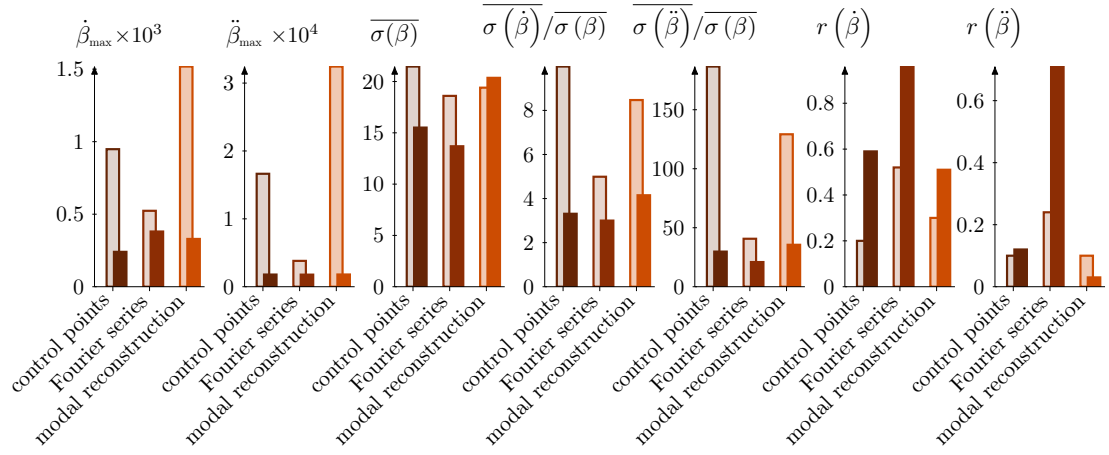

Figure 1.6 – Quantitative comparison of the characteristic properties of the initial population consisting of 200 individuals for the different parametrised of the kinematics for 12 parameters. The brighter bars indicate values obtained without taking into account the acceleration constraint. The darker bars include the influence of the acceleration constraint. The diversity of the population is characterised by the maximum pitch rate $\dot{\beta}_{\max}$, maximum pitching acceleration $\ddot{\beta}_{\max}$, the half-stroke-averaged standard deviation of the pitching angle $\overline{\sigma(\beta)}$, the half-stroke-averaged normalised standard deviation of the pitch rate $\overline{\sigma(\dot{\beta})}/\overline{\sigma(\beta)}$ and the pitching acceleration $\overline{\sigma(\ddot{\beta})}/\overline{\sigma(\beta)}$, and the correlation-coefficients for the pitch rate $r(\dot{\beta})$ and pitching acceleration $r(\ddot{\beta})$.

without the application of the acceleration constraint. The parameters we calculated to characterise the coverage of the solutions space and diversity of the parametrised motions kinematics include the maximum pitch rate $\dot{\beta}_{\max}$ and pitch acceleration $\ddot{\beta}_{\max}$, the half-stroke-averaged standard deviation of the pitching angle $\overline{\sigma(\beta)}$, the half-stroke-averaged normalised standard deviation of the pitch rate $\overline{\sigma(\dot{\beta})}/\overline{\sigma(\beta)}$ and the pitch acceleration $\overline{\sigma(\ddot{\beta})}/\overline{\sigma(\beta)}$. The Fourier series-based kinematics have the lowest maximum pitch rate and pitch accelerations and a lower diversity based as indicated by lower values of the standard deviations of the pitch angle, rate, and acceleration compared to the control point approach and the modal reconstruction. The highest gradients are measured among the modal reconstruction solutions if the acceleration constraint is not applied. The control point kinematics exhibit the highest diversity closely followed by the modal reconstruction method if we do not apply the acceleration constraint.

If we apply the acceleration constraint to omit solutions that cannot or should not be executed by our experimental device, we obtain the probability density plots presented in the bottom row of fig. 1.5. The quantitative measures after application of the acceleration constraint are depicted in fig. 1.6 by the darker bars. Here, the acceleration is limited to $\ddot{\beta} \leq 1800\,°/s^2$.

The coverage achieved by the initial populations is now reduced for all approaches especially near the stroke reversal. Motions with larger angles around stroke reversal are omitted due to the acceleration limit. This affects the control point approach the most. The splines connecting

the control points tend to develop characteristic spikes when the distance between control points decreases which leads to accelerations above the allowed limit. The initial population for Fourier series kinematics exhibits a small band of angles with very low diversity around stroke reversal and a poor coverage for smaller β. This is caused by the different restriction of the parameter space for the Fourier series. The best coverage is achieved for all kinematic functions at moderate angles between $t/T = 0.125 - 0.375$. The modal reconstruction has the highest density at lower angles compared to the others (fig. 1.5c1). Unfortunately, this increases the chance that a randomly selected individual does not meet the acceleration constraint and needs to be omitted and replaced when building he initial population. To obtain a set of 200 executable individuals for the initial population within a reasonable amount of time, the lower angular constraint $\beta_{\min}$ is loosened. This explains the non-zero probability for $\beta_{\min} < 0$ in fig. 1.5c2.

All kinematic functions show a significant loss in diversity following the application of the acceleration constraint. The modal reconstruction now outperforms the control point approach and the Fourier series in all measures. Most of the diversity of the initial control point approach without constraint is created over the tightly spaced control points with a large spectrum of admissible angles. This allows for a large variety of angles, velocities, and accelerations, but it also leads to higher number of omitted kinematics. This could potentially be reduced by distributing the control points differently or by also considering their time coordinates as variable parameters.

Alternative measures for the diversity of the randomly selected individuals in an initial population are obtained by determining the correlation-coefficients for the pitch rate $r(\dot{\beta})$ and the pitch acceleration $r(\ddot{\beta})$. They are calculated as the ensemble average correlation-coefficient r for each individual with the rest of the population. A higher diversity within a population now leads to a lower correlation coefficient r. Overall, the diversity decreases upon application of the acceleration constraint as the correlation values increase. The control point approach and the modal reconstruction show again a higher diversity than the population of Fourier series.

To more quantitatively compare the similarity between different randomly generated kinematic, we borrow ideas here from a network topology approach proposed by [69] and more recently used e.g. by [70] for comparing the similarity between trajectories. The similarity between kinematics can be quantified using the maximum cross-correlation coefficient $R_{\mathrm{i,j}}$ for each pair of kinematics β_{i} and β_{j}. The maximum cross-correlation coefficient is defined as:

$$R_{\mathrm{i,j}} = \max_{\tau=0\ldots T} \frac{cov\left(\beta_{\mathrm{i}}(0:T), \beta_{\mathrm{j}}(\tau:(T+\tau))\right)}{\sqrt{var\left(\beta_{\mathrm{i}}(0:T)\right) var\left(\beta_{\mathrm{j}}(\tau:(T+\tau))\right)}} \tag{1.10}$$

with T the period, $cov(.)$ the covariance, and $var(.)$ the variance operators. By taking the maximum over all possible phase shifts τ, the resulting value only evaluates the shape similarity and is not influence by a phase shift, e.g. introduced by Δt_0 here. Another metric proposed

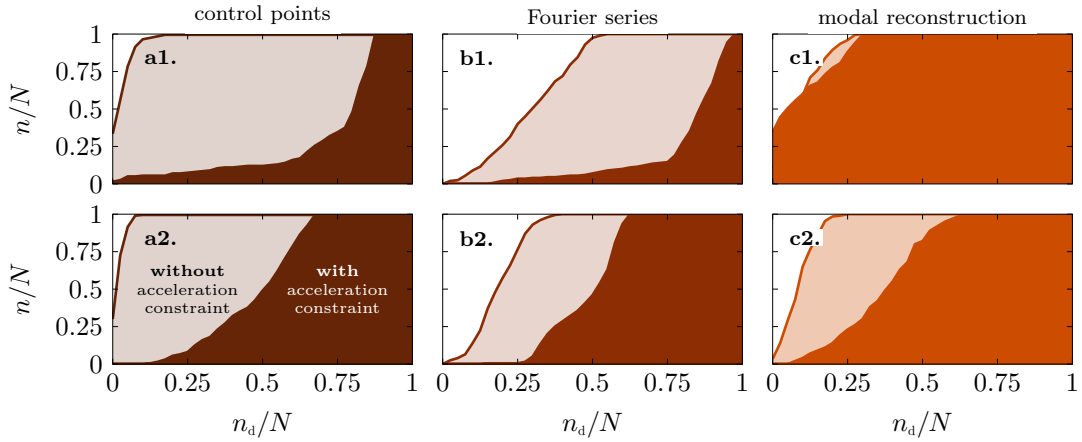

Figure 1.7 – Cumulative distribution of the relative node degree n_d/N in the similarly networks describing the initial population of $N = 200$ individuals for the three parametrisation approaches. Distributions corresponding to the networks based on $R_{i,i}$ are in the top row, those based on $D_{i,i}$ are in the bottom row. The light and dark shading correspond respectively to randomly selected populations without and with the application of the acceleration constraint.

by [69] is the mean absolute error $D_{i,j}$ between two curves, which is defined here as:

$$D_{i,j} = \min_{\tau=0\ldots T} \frac{1}{T} \sum_{t=0}^{T} \left| \beta_i(t) - \beta_j(t+\tau) \right| \quad . \tag{1.11}$$

We normalised $D_{i,j}$ by the period T and expressed the result in degree such that $D_{i,j}$ can be interpreted as an average pitch angle amplitude difference between two kinematics. Two identical curves have a maximum cross-correlation coefficient $R_{i,j} = 1$ and a minimal mean absolute error $D_{i,j} = 0$. Both quantities evaluate different aspects, $R_{i,j}$ provides a measure for the shape similarity between curves and $D_{i,j}$ provides a measure for the amplitude variations between curves. We use both here to evaluate the degree of similarity within a randomly generated population.

After calculating $R_{i,j}$ and $D_{i,j}$ between all curves with the initial population, we construct two similarity networks. Each kinematic motion is represented by a node in the network. Different nodes are connected to each other if the shape similarity measure $R_{i,j}$ is higher than a predefined threshold R_{th} or if the amplitude dissimilarity measure $D_{i,j}$ is lower than a predefined threshold D_{th}. We then determine the node degree for each node, which corresponds to the number of nodes it is connected to. Kinematics with a low node degree show similarity only to a low number of other kinematics in the population. The cumulative distributions of the node degrees (n_d) among the initial population for the three different parametrisation approaches with $p = 12$ are presented in fig. 1.7. The light and dark shading correspond respectively to randomly selected populations without and with the application of the acceleration constraint. The more diverse a population of kinematics the more kinematics we expect with a low degree

of connectivity and the larger the coloured area in fig. 1.7. The distributions in the top row have been obtained for the networks based on the shape similarity measure $R_{i,j}$ and indicate how diverse the population is in terms of the shape of the kinematics. The distributions in the bottom row have been obtained for the networks based on the amplitude difference measure $D_{i,j}$ and indicate how diverse the population is in terms of the amplitudes of the kinematics.

The unconstraint populations for the control point and the modal reconstruction have a high degree of diversity as the majority of the kinematics have a low node degree and show similarities to only a few other kinematics in the population. The Fourier series performs slightly lower than the two others. By construction, the Fourier series have an inherent similarity in shape and it is not entirely unexpected to find more nodes with a higher node degree for this approach. Almost all cumulative distributions in fig. 1.7 shift to higher node degrees when the acceleration constraint is applied, indicating that the constraint decreases the diversity both in terms of shapes and in terms of amplitudes. The only exception is the shape diversity for the modal reconstruction which remains nearly unaffected by the constraint. The spline population is the most diverse for the unconstrained case and the modal population exhibits the highest diversity for the constrained case.

We have also used these metrics to analyse the ability of the different approaches to create the insect-like kinematics and trapezoidal motions presented in fig. 1.1. All approaches except the modal reconstruction are capable to mimic the presented kinematics with a minimum correlation coefficient $R \geq 0.993$ and a maximum mean absolute error $D \leq 1°$. The modal reconstruction does equally well for most of the motions except for the trapezoid with steep edges which is approximated with a larger mean absolute error of $D = 2.3°$.

Based on all visual and quantitative comparison presented here, the control point method yields the best coverage of the solution space and the largest diversity within an initial population if no acceleration constraint is applied. The modal reconstruction method performs better than the control point method when the constraint is applied. The Fourier series populations are least diverse and have the lowest coverage, but still perform sufficiently well for our optimisation application.

1.3.2 Optimisation progress and convergence

Due the specific implementation of the genetic algorithm for our flapping wing optimisation, we can not replace individual kinematics that are omitted based on the acceleration constraint. This is not a general limitation of the approach and can be overcome for future applications. However, in the current study, the total number of the executable individuals in first generations is significantly lower than the nominal 200 individuals due to the implementation (fig. 1.8). This is in particular the case for the control point and modal reconstruction methods with 12 or 18 parameters. The Fourier series method is less affected and also the optimisation with a lower number of control points has populations with consistently close to 85 % of executable individuals. The number of executable individuals per generation increases for

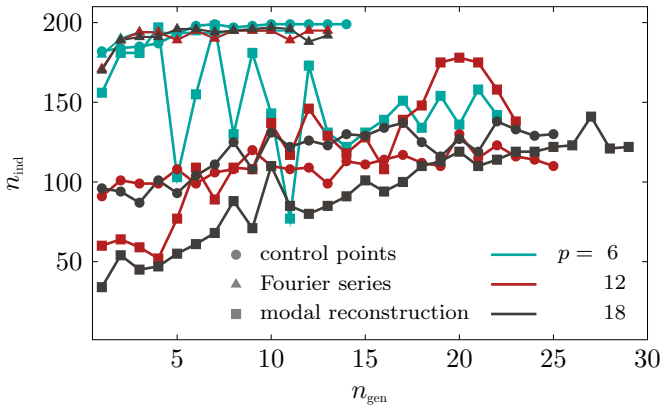

Figure 1.8 – Number of executable motions or individuals per generation for all optimisations with 6, 12, and 18 parameters and the three parametrisation approaches.

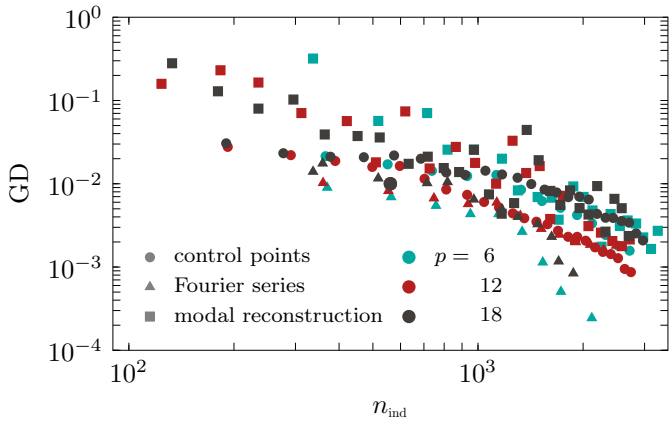

Figure 1.9 – Moving average over 10 iterations for the generational distance (GD) versus the number of iterations. Each iteration corresponds to the evaluation of one flapping motion.

most of the optimisations but never reaches full population size with exception of the control point approach with 6 parameters. The control point approach with 12 parameters and the modal reconstruction approach have particularly low numbers of executable individuals in the early generations, but the situation improves in the course of the optimisation. The lower number of executable individuals in the populations decrease the diversity which hampers the search for the optimum solutions and delays convergence.

The convergence of the different approaches is analysed based on the generational distance introduced in equation 1.9. The variation of the generational distance with the number of executed motions is presented in fig. 1.9. Surprisingly, the parameter count is not the most important factor that influences the convergence behaviour. The largest influence on the convergence is the parametrisation approach. The optimisations using the same parametrisation form groups with similar convergence speed according to the generational distance metric.

Table 1.1 – Number of iterations and generations required until convergence for the different parametrisation approaches. Convergence is reached if the convergence speed $\leq 5 \times 10^{-4}$ and generational distance $\leq 5 \times 10^{-3}$ for two consecutive generations.

parametrisation	p	iterations	generations
control points	6	2718	14
	12	2742*	25*
	18	2968	25
Fourier series	6	2118	11
	12	2486	13
	18	2491	13
modal reconstruction	6	2683	18
	12	2721	23
	18	2702	29

* The convergence for this case is determined manually by observing the evolution of the Pareto kinematics.

The modal reconstructions exhibit the highest relative generational distance and convergence speed at the very beginning. The modal reconstruction with 18 parameters has the highest initial generational distance of 0.346 but also the modal approach with 12 (GD=0.129) and 6 parameters (GD=0.125) have initial values that are one magnitude larger than the values obtained for the other conditions. The higher initial generational distance can be explained by a larger diversity of the initial population. The convergence speed behaves proportionally to the generational distance such that all optimisations converge in comparable time. The smallest relative generational distance and convergence speed is observed for the Fourier series. The motions of the initial Fourier population are less diverse and closer to the final solution due to the different constriction of the parameter bounds. The optimisation progress is slower because the differences between the motions are less pronounced and consequently harder to determine. On the other side, higher diversity for the initial populations leads to higher convergence speed.

The total convergence time differs by 40 % between the slowest (control point approach with $p = 12$) and fastest (Fourier series approach with $p = 6$) optimisation and the majority takes between 2486 (Fourier series approach with $p = 12$) and 2742 (control point approach with $p = 12$) iterations (table 1.1). The optimisations are not deterministic and uncertainties are introduced due to random initialisation, recombination and mutation. The differences in convergence time are small when considering that the computational complexity of the optimisations increases exponentially with the parameter count. The Fourier series optimisations tend to reach convergence slightly faster than the modal and control point approaches.

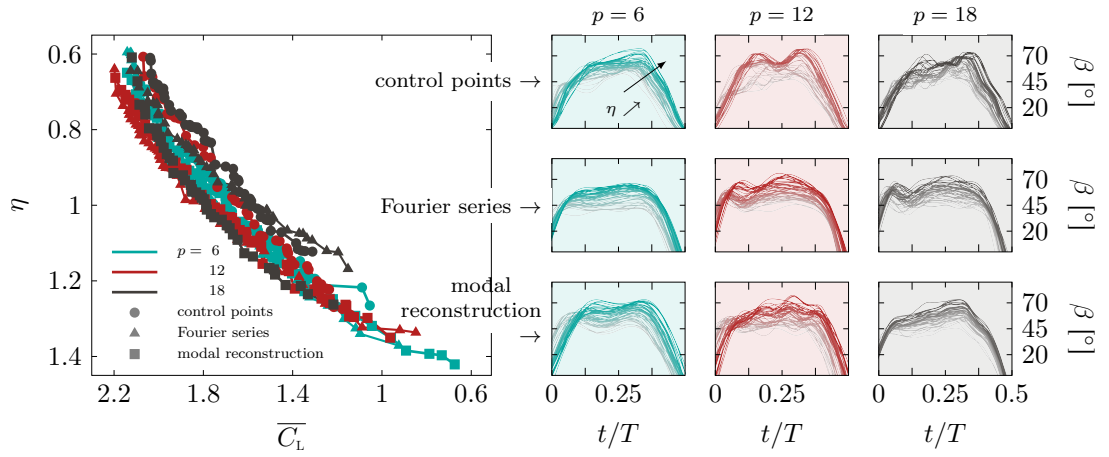

Figure 1.10 – Global Pareto front for all kinematic function optimisations for the last generation. Kinematics corresponding to the final global Pareto front solutions for the different kinematic functions.

1.3.3 Pareto fronts and optimal kinematics

The resulting Pareto fronts for all 9 optimisations are presented in fig. 1.10. The colours indicate the number of optimisation parameters and the symbols indicate the parametrisation approach. The different Pareto fronts have the same shape but there is a shift between them and they reach slightly different extreme values. The modal reconstruction approach with $p = 6$ finds the most efficient solutions (up to $\eta \approx 1.4$) and the Fourier series approach with $p = 12$ finds the solutions that generate the highest stroke average lift (up to $\overline{C}_L \approx 2.2$). Overall, the optimisations with the highest number of parameters are most limited in finding highly efficient solutions. The higher number of parameters might lead to more complex kinematics that require more power to achieve the same performance in lift. For our current example, $p = 12$ seems to provide the best balance across the different parametrisation approaches. The additional complexity provided by 12 optimisation parameters compared to the $p = 6$ optimisations is beneficial in improving the aerodynamic performance without increasing the power requirements and penalising the efficiency. Increasing the parameter count leads to slower convergence and kinematics with higher harmonics variations. To aid the genetic algorithm to fine tune the parameters, we have conducted an additional optimisation where we have taken the results for $p = 6$ as a start point for a $p = 12$ optimisation using the Fourier series parametrisation approach. The results did not lead to significant differences with respect to the regular $p = 12$ optimisation and are not presented here. Overall, the differences between Pareto fronts are of the same order of magnitude as the inherent experimental variations. The influence of the number of parameters seems to have a stronger influence than the parametrisation approach.

In general, the performance of the three parametrisations is comparable and we can not identify a clear preference of any one of them. The optimal kinematics that make up the Pareto

front are included in fig. 1.10. The columns with the same background colour correspond to optimisations with the same number of parameters. The rows correspond to different parametrisation approaches. The colour of the $\beta(t/T)$ curves for one half stroke varies from grey to green, red, or black with increasing efficiency. All Pareto kinematics show a continuous transition from high lift motions to more efficient ones, which indicates that the solutions are converged and we obtained a well developed Pareto front. For the same number of parameters, the Pareto kinematics show similar characteristic features for the three parametrisation approaches but also display some subtle differences that cause the shifts in the Pareto front.

The main differences between the Pareto optimal kinematics of the different cases are the number of local maxima and their timing. The control point and modal reconstruction approaches with $p = 6$ show two local maxima around $t/T = 0.125$ and $t/T = 0.375$ (fig. 1.10). These two maxima are less pronounced or even absent in the Fourier series kinematics which look more like a smooth trapezoidal profile. The two local maxima become more pronounced for the control point approach with $p = 12$ and only the second one around $t/T = 0.375$ remains present when p is increased to 18 for this approach. The modal reconstructions for $p = 18$ are also characterised by a single peak that is located around $t/T = 0.32$. The Fourier series with $p = 12$ and $p = 18$ have a distinct bump at the beginning of the stroke, around $t/T = 0.1$. Overall, the complexity of the motions increases with the parameter count and different shapes and kinematics can lead to similar Pareto fronts depending on the choice of the parametrisation and the parameter count. This is due to the complex relationship between the flow development and the growth of the leading edge vortex for flapping wings motions [64, 71] and are further discussed in chapter 2.

1.4 Conclusion

In this study, we presented three different approaches to parametrise motion kinematics, demonstrated their application, and evaluated their performance by the example of an experimental optimisation of the pitching kinematics of a robotic flapping wing in hover. The pitch angle kinematics in our application are described by

- control points that are connected by a fifth-order spline interpolation,
- a finite Fourier series, and
- a linear combination of modes determined by a modal decomposition of kinematics created by a random walk.

Each of the parametrisation approaches is implemented with three different parameter counts: 6, 12 and 18, which leads to a total of nine optimisations and more than 30 000 experimental iterations conducted over a period of several weeks. The performance of the different approaches has been analysed by comparing the diversity of the solutions and coverage of the motion space, the optimisation process and convergence.

The coverage of the solution space was qualitatively evaluated based on a probability density map of the random initial population of 200 individuals. For a more quantitative comparison of the coverage and the diversity of the solutions, we introduced a number of diversity measures including the maximum pitch angle, rate, and acceleration, their standard deviations, and correlation coefficients for the pitch and acceleration. To further quantify the diversity between the kinematics within the initial populations, we calculated similarity networks based on a mutual shape similarity measure and an amplitude error. The cumulative distribution of the node degree in a population is an intuitive quantitative measure to compare the diversity of the kinematics based on their shape and amplitude. Based on all qualitative and quantitative measures, the control point kinematics exhibit the highest diversity closely followed by the modal reconstruction method if no experimental constraints are in place. The Fourier series-based kinematics have the lowest maximum pitch rate, pitch acceleration, and a lower diversity compared to the control point and the modal reconstruction approach.

In most experimental applications, the theoretical parameter space cannot be fully explored due to mechanical, electrical, or other constraints for example related to the measurement equipment. In our case, the main limitation is imposed by the sensitivity and measurement range of the load cell and the performance envelope of the motor that controls the pitching motion. These limitations lead to a pitch acceleration constraint that significantly reduces the coverage and the solution diversity for all three parametrisation approaches. The practical implementation of an acceleration constraint is easier for the Fourier series approach than for the two other approaches. The modal reconstruction parametrisation performs best in the various diversity measures, followed by the control point and the Fourier series approaches when the acceleration constraint is in place.

The generational distance criterion is implemented to monitor the progress of the optimisation and as a convergence measure to end the optimisation. All optimisations converged in comparable time which did not depend on the parameter count. In the presented optimisation study, it is desirable to have fewer parameters as more parameters increase complexity without a clear aerodynamic benefit. The subtle changes in the kinematics lead to variations in the loads that are of the same order as the inherent experimental fluctuation of the system. This can slow down the convergence of the genetic algorithm especially in later stages when only minor aerodynamic improvements are achieved.

The resulting Pareto fronts for the different optimisations are similar in shape and in the range of values of the two objective functions they cover. The parameter count has a stronger influence on the final results than the parametrisation approach. This is encouraging for the robustness of the three parametrisation approaches presented here. The optimal kinematics corresponding to the Pareto fronts have slightly different shapes depending on the parameter count and the parametrisation approach selected but they yield comparable fitness values. The main differences between the optimal kinematics of the different cases are the number of local maxima and their timing.

The goal of this paper was to present three different methods to parametrise complex motion kinematics for optimisation studies and to compare their performance on an experimental flapping wing system. Each optimisation application has different objective functions, constraints, and specific challenges. There is no one solution that fits all and the different approaches to parametrise the solutions have their specific advantages and disadvantages outlined in table 1.2. The Fourier series approach is the easiest method to implement but the introduction of parameter constraints and the parameter bounds cannot be as directly contained as for the control point approach. Nevertheless, the Fourier series has an analytical definition and continuous high-order derivatives which make it a promising parametrisation for structurally sensitive applications like vertical-axis wind turbines or flapping-foil energy harvesters. By definition, the control points are more intuitive to constrain and their parameter values can be interpreted directly in terms of their influence on the temporal evolution and amplitude of the kinematics. With the ability to create sharp and zero gradient curves, the control point method is most suitable for intermittent kinematics like burst and coast swimming of fish- and squid-like devices, and flapping wing flight. The modal reconstruction is extremely versatile and adaptable. The initial family of solutions can be generated by a random walk method as presented here, but can also be a family of kinematics measured in nature or in the lab. Building a parametrisation upon an existing library of kinematics can be an extremely powerful tool. Complex animal-like locomotions can be described by only a few modes which would require many parameters being constructed by analytical kinematic definitions.

Depending on the individual complexity of the mode shapes, it is difficult to restrict parameters bounds to meet experimental constraints. Instead, motions have to be omitted after generation if they do not meet constrains such as start and end position and acceleration. This can severely hamper the creation of initial populations for a genetic algorithm optimisation, for example. In the presented application of an experimental optimisation of a robotic flapping wing mechanism, all three approaches yielded similar results in a comparable amount of time. Other applications might have different challenges, but we expect that the main characteristics of the presented approaches are valid for different systems and that the choice of the most suitable parametrisation approach can be guided by the properties listed in table 1.2.

Table 1.2 – Overview of the key characteristics for the different parametrisations.

	Complexity	Handling of constraints	Interpretability of parameters	Applications
control points	-	+	+	intermittent kinematics, e.g. burst and coast swimming
Fourier series	+	∘	-	vertical axis wind turbines, flapping foil energy harvester
modal reconstruction	∘	-	∘	complex animal-like locomotion

2 Phenomenology and scaling of optimal flapping wing kinematics

In this chapter, a kinematic optimisation for highest aerodynamic performance on a robotic flapping wing system is performed. Additional flow field measurements are conducted to link the vortical flow structures to the aerodynamic performance for the Pareto-optimal kinematics. The objective is to identify vortex characteristics and scaling parameters for optimal flapping wing kinematics. The extend of this work, provides guidelines for the aerodynamic design of human-engineered devices that automatically adapt their motion kinematics to optimally fit varying flight conditions.

The work presented in this chapter has been published in *Bioinspiration & Biomimetics* [71].

2.1 Introduction

Bio-inspired mechanical flapping wing systems have been increasingly used in the past decades to study and understand the behaviour of natural fliers and serve as inspiration for the design of flapping wing micro air vehicles (MAV) [11, 72–74]. Recently, MAV with similar sizes and weights as natural fliers have found their applications [46–49]. With the development of novel wing actuators [52] and the miniaturisation of flight control systems and improvements in energy storage, MAV are employed to accomplish complex autonomous missions in urban environments [20]. With the decrease in size, the Reynolds number reduces and unsteady effects have more influence on the aerodynamic performance of the fliers. At lower Reynolds numbers ($Re < 5000$), flapping wing vehicles generally perform better than revolving wing aircraft and at $Re < 100$ the lift-to-power ratio is about twice as high for flapping wings in comparison to their revolving counterparts [9, 10].

Natural flapping wing fliers are extremely versatile. They seamlessly change between hovering and forward flight, use their wings to generate both lift and thrust, and can even glide to conserve energy. Flapping wings operate at high angles of attack above the static stall angle of the wing. These high angles cause a shear layer to separate at the leading edge which rolls up and forms a large scale coherent structure, the leading edge vortex. The stall of the wing is

delayed through the rotational acceleration of the flapping wing which stabilises the leading edge vortex during the majority of the stroke cycle [75]. A bound leading edge vortex creates a low pressure region on the suction side of the wing which generates high aerodynamic forces and torques required for the fast maneuverings of flapping wing fliers [76, 77]. The unsteady aerodynamic effects of the leading edge vortex give rise to exceptional lift and thrust yields well beyond the aerodynamic performance of fixed wings under steady-state conditions [3, 78]. At the end of the flapping half-cycle, the wing rotates to keep the leading edge in front of the trailing edge along the stroke direction. During the end-of-stroke rotation, the vortex separates from the shear layer and sheds into the wake and a new stroke begins.

Nature's flapping wing fliers do not cease to amaze us with their incredible flight performance and efficiency, but many bio-inspired human-engineered devices do not yet manage to compete with their natural inspirers [79]. One reason for this is that the functional morphology of insect wings is not yet fully understood and can not directly be incorporated in robotic flapping wing vehicles. During the natural evolution of birds and insects, the wing shape and their kinematics advanced simultaneously and different wing shapes favour specific kinematics for hovering flight [74]. Complex flapping wing motions are observed in nature [80, 81] and especially the pitch angle profile is highly depended on the wing geometry and elasticity but also varies with the flight conditions or flow characteristics expressed by the Reynolds number and reduced frequency [8, 62]. Recent improvements in miniature wing actuators motivate the exploration of the influence of more complex wing kinematics on the flapping wing performance [52].

Wing kinematics measured on birds and insects provide a starting point to design effective flapping wing motions but they are specific to each wing's properties and actuation system. Various parameter studies have been carried out in the past to characterise the performance of flapping wing kinematics for different wing planforms [17, 64, 72, 82]. On a dynamically scaled mechanical model of a fruit fly Sane and Dickinson [72] varied the stroke amplitude, angle of attack, flip timing, flip duration and the shape and magnitude of stroke deviation in an extensive parameter study. Among other findings, they concluded that the mean drag increases monotonically with increasing angle of attack and a short flip duration advanced of the stroke reversal is beneficial for lift production. The influence of different stroke- and pitch angle waveforms at a fixed flapping frequency and amplitude was investigated recently by Bhat et al. [64] for a fruit fly wing planform. The stroke angle evolution was modulated between a sinusoidal and a triangular profile and the pitch angle evolution between a sinusoidal and a trapezoidal profile. The stroke angle evolution has a main influence on the magnitude of the lift coefficient C_{L} maxima whereas the pitch angle evolution mostly impacts the instantaneous C_{L} at stroke reversal.

The vast parameter space of possible complicated flapping wing kinematics makes it challenging to derive general relationships between motion parameters and optimal aerodynamic performance. Experimental and numerical optimisations can aid to find optimal kinematics within the vast parameter space of the flapping wing actuation. Optimisations have been

applied primarily to numerical models which are only limited by the computational cost and the validation of the numerical method [61, 83, 84]. A hybrid optimisation approach which combines aspects of a genetic algorithm and a gradient-based optimiser was applied by Berman and Wang [61]. They parameterised the stroke, pitch, and elevation angle profiles to minimise the power usage on three differently weighted insect models in hovering flight. The aerodynamic forces are computed using a quasi-steady model and assuming a thin flat plate wing. The optimal kinematics found in their study exhibit a sinusoidal stroke evolution where the pitch angle is kept constant throughout the cycle. The kinematic functions found take advantage of passive wing rotation by using the aerodynamic moments to reverse the wing pitch. By treating the flapping wing kinematics optimisation as a calculus-of-variation problem along with quasi-steady aerodynamics, Taha et al. [83] find that a triangular waveform for the stroke angle and a constant pitching angle throughout the half-stroke yield the best performance index in terms of $C_{\mathrm{D}}^2/C_{\mathrm{L}}^3$ with C_{D} the drag coefficient. A stroke profile with a harmonic waveform requires 20 % more aerodynamic power compared to the triangular waveform for the same performance evaluation. More recently, Lee and Lua [84] used a two-stage optimisation algorithm to investigate the effects of more complex, insect-like pitch angle kinematics on the hovering flight of a hawkmoth. They initiate the optimisation with a semi-empirical quasi-steady model to narrow down the parameter space and then use a computational fluid dynamics simplex optimisation method to refine the optimal pitch angle kinematics found.

Quasi-steady or low-order unsteady aerodynamic models have good computational performance, however they are often restricted to wing kinematics within their local validated trajectory space. Computational fluid dynamics simulations at low Re can accurately calculate the aerodynamic loads generated by a flapping wing, but are too computationally expensive to use in large scale optimisations.

Experimental optimisations with dynamically scaled wings and force measurements combine accurate measurements with comparatively low experimental times [63, 85, 86]. Automated data transfer and processing between the experimental system and the optimisation framework is required and the mechanism needs to have a robust control scheme and mechanical design to conduct a large number of iterations without human supervision. The early work of Milano and Gharib [85] on experimental flapping wing optimisations applies a genetic algorithm to a two-axis system of a translating and rotating wing. The solution that yields the most lift in hovering flight was related to the strongest leading edge vortex growth. Martin and Gharib [63] employed a covariance matrix adaptive evolutionary strategy to find effective kinematics for a bio-inspired flapping fin which can be used as a side or a rear propulsor for underwater vehicles.

In this study, we propose a unique robust optimisation scheme to obtain optimal pitch angle kinematics for a given wing geometry and Reynolds number on an experimental flapping wing platform. We employ a multi-objective evolutionary algorithm to find complex flapping wing motions which yield highest stroke-average lift and highest efficiency during hovering.

The trade-off between lift and efficiency of the optimal solutions is represented by a Pareto front. Complementary velocity flow field measurements are conducted for the Pareto optimal kinematics to determine the leading edge vortex circulation and its position throughout the flapping wing cycle. The results consist of two parts. In a first part, we focus on explaining the interaction between the complex motion kinematics and the resulting aerodynamic performance using flow field data and qualitative information on the state of the leading edge vortex development. In the second part, we quantitatively describe and propose a novel approach to scale the temporal evolution of the vortex development and the aerodynamic forces and efficiency for all solutions along the Pareto front.

2.2 Materials and Methods

2.2.1 Wing Model and Kinematics

The flapping wing kinematics can be described by three angles and their temporal evolution, the stroke angle ϕ, the pitch or rotation angle β, and the flap or elevation angle ψ. The stroke angle θ describes the position of the wing in the horizontal stroke plane (fig. 2.1b). In hovering flight, the stroke follows a sinusoidal profile for most insect species. The pitch angle β in fig. 2.1b describes the rotational position of the wing and determines the geometric angle of attack. The pitching motion is the most complex motion function in the hovering flight kinematics and its shape varies strongly between different species [87]. The pitch actuation is the main focus of this study. The elevation angle ψ is measured relative to the vector normal to the stroke plane (not shown in fig. 2.1). It plays a minor role in the hovering of insects with similar Reynolds number and wing aspect ratio [62]. In this study, the flap angle is kept constant at $\psi = 0°$ and the stroke angle varies sinusoidally with a fixed amplitude and frequency.

2.2.2 Dynamic scaling

The two non-dimensional parameters that characterise the aerodynamic properties of the flapping wing in hover are the reduced frequency k and the Reynolds number Re. The reduced frequency k measures the degree of unsteadiness of the flow by relating the spatial wavelength of the flow disturbance to the chord length c and can be calculated as:

$$k = \frac{\pi c}{2\phi R_2} \quad , \tag{2.1}$$

where 2ϕ is the peak-to-peak stroke amplitude and $R_2 = \sqrt{\int_0^R (R_0 + r)^2 dr / R}$ is the radius to the second moment of area. For a rectangular wing, which is used in this study, R_2 is also the span-wise position where the force applies [88]. The root cutout R_0 of the wing is indicated in fig. 2.1c and is the distance between the stroke axis and the wing root.

The Reynolds number Re describes the ratio between the inertial and viscous forces and is

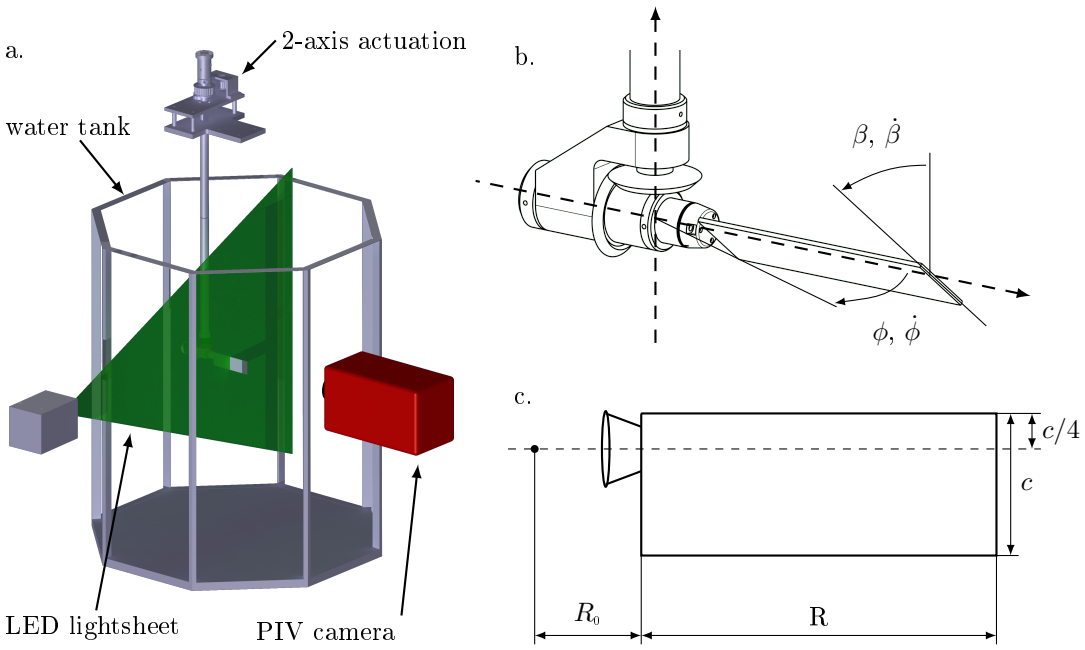

Figure 2.1 – a. Schematic of the experimental configuration with the flapping wing mechanism submerged in an octagonal water tank. A light-sheet and camera are positioned to record the velocity field normal to the axis of rotation of the wing. b. Definition of stroke ϕ and pitch angles β characterising the flapping wing kinematics, and c. wing dimensions.

determined for the hovering flight by

$$Re = \frac{\overline{U}c}{\nu} = \frac{2\phi f c R_2}{\nu} \quad , \tag{2.2}$$

where ν is the kinematic viscosity of the fluid and the characteristic velocity $\overline{U} = 2\phi f R$ is defined as the stroke average wing velocity at the second moment of area R_2 [72, 88].

The experimental parameters for the model wing are summarised in table 2.1. They are selected to match the characteristics of larger insects, such as hawk moths, or the hummingbird in hovering flight [27, 86].

The model wing used in this study has a rectangular planform (fig. 2.1c). Even though insect or bird wing in nature are typically not rectangular, the rectangular planform is commonly used to study the aerodynamic of revolving and flapping wings [16, 27, 89]. The performance of flapping wings is influenced by the wing shape and geometry and the wing planform can be optimised for specific flight modes and mission profiles of the aerial vehicle [90]. Results of systematic investigations of the influence of the wing geometry by Ansari et al. [91] revealed that planforms with straight leading edges are desirable for increased performance. Therefore, we believe that the flat plate is a valid simplification of an insect wing. Our numerical results will still be specific to the selected wing planform but the main procedure and underlying flow

physics are expected to be generalisable for different more insect-inspired wing planforms.

2.2.3 Experimental Setup

A schematic representation of the experimental setup is depicted in fig. 2.1a. The flapping wing mechanism is submerged in an octagonal tank with an outer diameter of 0.75 m filled with water. For a tip-to-tip amplitude of 0.47 m this leads to a 6.91c minimum tip clearance which has been shown to be sufficient to avoid wall effects in flapping wing experiments [16, 92]. The stroke and pitch motion are driven by two servo motors (Maxon motors, type RE35, 90 W, 100 N mm torque, Switzerland) reduced by 35 : 1 with a planetary gear-head for the stroke and 19 : 1 for the pitch actuation. This experimental flapping wing mechanism is a unique set-up in terms of its robustness, repeatability, and the variety of kinematic motions that can be executed. Initial tests on the highest lift kinematics showed an error of $< 0.1°$ between the motor input signal and the motor response measured by the encoder throughout the entire cycle. A motion controller (DMC-4040, Galil Motion Control, USA) is used to control the motors. The aerodynamic loads are recorded with a six-axis IP68 force-torque transducer (Nano17, ATI Industrial Automation, USA) with a resolution of 3.13 mN for force and 0.0156 N mm for torque measurements positioned at the wing root. The forces are recorded via a data acquisition card (National Instruments, USA) with sampling frequency of 1000 Hz. The force data was filtered with a zero phase delay low-pass 5th order digital Butterworth filter. The cut-off frequency was chosen to be 12 times higher than the flapping frequency f.

A high-power light-emitting diode (LED) (LED Pulsed System, ILA_5150 GmbH, Germany) and a cylindrical lens are used to produce a 4 mm-thick light-sheet. The illuminated plane of interest is recorded by a sCMOS camera (ILA_5150 GmbH / PCO AG, Germany) with a 2560 px × 2160 px resolution covering a 119 mm × 101 mm field of view. Phase-locked particle image velocimetry (PIV) is conducted by triggering the LED and camera simultaneously to record a single image pair for a specific phase angle ϕ. To record the different phase positions throughout the stroke cycle the initial stroke angle is shifted relative to the LED-plane similar to the procedure used by Krishna et al. [16]. A total of 39 different stroke angle positions are recorded and averaged over 64 flapping cycles. A multi-grid algorithm with a resulting

Table 2.1 – Summary of the experimental parameters of the dynamically scaled wing used throughout this study. The working fluid in the experiments is water with $\nu_{20\,°C} = 1.00 \times 10^{-6}\,\mathrm{m}^2/\mathrm{s}$.

Parameters		model wing
Wing stroke frequency	f	0.25 Hz
Wing chord	c	34 mm
Wing span	R	107 mm
Stroke amplitude	ϕ	180°
Reduced frequency	k	0.19
Reynolds number	Re	4895

interrogation window size of 48 px × 48 px and an overlap of 50 % is used to correlate the raw images and reconstruct the velocity flow field with a physical resolution of 1.1 mm or 0.034 c. The flow field measurements were conducted on the plane normal to the span-wise direction at the R_2 location or $0.56R$ measured from the wing root (fig. 2.1a). To quantify the flow properties for the converged optimisation kinematics, PIV experiments are carried out for 19 out of the 35 Pareto front individuals.

2.2.4 Optimisation

Genetic algorithms and other evolutionary optimisation strategies employ a survival of the fittest strategy. Multiple sets of parameters are tested each generation and the best performing individuals are advanced to improve further generations. Genetic algorithms have proven to be effective and robust for experimental data which is prone to more noise in the data. Due to their stochastic nature, evolutionary algorithms are strong in evading local optima which is especially important for unsteady aerodynamics where some changes in the actuation can cause a cascade of events and a drastic change in the performance. The objective scores of the evolutionary algorithm do not need to be weighted to be used in a multi-objective optimisation. This gives the genetic algorithm the natural ability to determine the trade-off between objectives in the Pareto front.

The two optimisation targets in this study are the stroke average lift coefficient $\overline{C}_\mathrm{L}$ and the hovering efficiency η. The force and power coefficients of the system can be calculated from the force and torque measurements by the load transducer positioned at the root of the wing (fig. 2.1a) according to:

$$C_\mathrm{L} = \frac{L}{\frac{1}{2}\rho R c \overline{U}^2}, \quad C_\mathrm{P} = \frac{P}{\frac{1}{2}\rho R c \overline{U}^3}, \tag{2.3}$$

where L is the instantaneous lift, D the drag, and P the aerodynamic power of the system. For the two-axis motion, the power P is calculated as the sum of pitching power P_p and the stroke power P_s. The pitching power is the power required to rotate the wing around its pitching axis and is given by $P_\mathrm{p} = T_\mathrm{p}\dot{\beta}$, with T_p the measured pitch torque and $\dot{\beta}$ the angular velocity of the pitching motion. The stroke power is given by $P_\mathrm{s} = T_\mathrm{s}\dot{\phi}$ with T_s the stroke torque and $\dot{\phi}$ the stroke velocity. The stroke torque cannot be measured directly and is calculated from the drag force D along the span $T_\mathrm{s} = \int_R D(r) r \, dr$ [72]. For a uniform drag coefficient distribution along the span, the torque can be computed as $T_\mathrm{s} = DR_\mathrm{d}$, where D is the drag measured at the wing root and acting on the radial position $R_\mathrm{d} = \frac{3}{4}\frac{(R_0+R)^4 - R_0^4}{(R_0+R)^3 - R_0^3}$.

The hovering efficiency of the flapping wing system is computed as the ratio between the stroke average lift coefficient $\overline{C}_\mathrm{L}$ and stroke average power coefficient $\overline{C}_\mathrm{P}$:

$$\eta = \frac{\overline{C}_\mathrm{L}}{\overline{C}_\mathrm{P}} \quad . \tag{2.4}$$

This basic definition of efficiency expresses how much energy is invested to generate a certain

amount of lift. Other definitions of the hovering efficiency quantify the dimensionless aerodynamic power to keep a unit weight in hover [93] which involves specifying the weight of the hovering insect or aerial vehicle.

The optimisation scheme is implemented with a genetic algorithm from the MATLAB Global optimisation Toolbox (The MathWorks Inc., USA) [66]. Genetic algorithms explore the solution space of a process or function by using artificial evolution, a strategy also known as the survival of the fittest. Analogous to natural evolution, the fittest individuals of a population reproduce to ensure advancement of succeeding generations. In this study, seven parameters characterising the pitch angle motion β are the genes or chromosomes in the genetic algorithm population. The total population consists of 100 individuals where the 35 highest performing genes make up the Pareto front individuals. The pitch angle function $\beta(t)$ displayed in fig. 2.2 is defined by four parameters for the pitch angle extrema and three parameters for their respective timings. The parameters can vary between certain bounds listed in table 2.2 to cover a wide range of possible kinematics similar to those observed in nature [62]. The objective or fitness function converts the parameters into the specific kinematics and evaluates their performance experimentally on the flapping wing system. Each kinematic is executed over eight consecutive flapping cycles and its fitness, the stroke average lift coefficient, and hovering efficiency, are calculated from the load cell data of the last four cycles to ensure a steady-state is reached and the influence of transient effects is limited. Under certain flight conditions like forward flight or hovering with an inclined stroke planes, asymmetric stroke and pitch profiles are used [94, 95]. In this study, the stroke and pitch angle kinematics are symmetric and the front- and backstroke are identical which is the normal hovering flight as observed by the majority of insects [27]. Due to the symmetry of the prescribed motion and thanks to the high precision of our flapping wing device we obtain symmetric force and torque responses. The differences between the forces measurements during the front- and the backstroke are less than 5 % of the maximum values. Only the results for one half cycle are presented to give a more compact presentation of the kinematics and the aerodynamic performance.

The initial population is randomly drawn from a uniform distribution bounded by the constraints in table 2.2. After all kinematics of the population have been evaluated, the individuals are ranked based on their fitness and obtain a score relative to the inverse square root of their rank. Several individuals of the population are then selected and their chromosomes are either used directly (cloned), randomly modified (mutated), or combined with other genes (crossover) to create the individuals for the next generation. The genes used for this process are chosen stochastically based on their previous performance, where a higher score leads to a higher probability to be selected. For the presented optimisation, 5 % of the previous generation's elite are clones, 60 % are created as crossover, and 35 % as mutation offsprings. The genes generated by the crossover function combine the parameters of two parents according to the following rule: child = parent_A + rand × (parent_B - parent_A), where rand is a random number between 0 and 1 drawn from a uniform distribution. After the new generation of offsprings is created, its fitness is evaluated by the objective function and the process continues until a

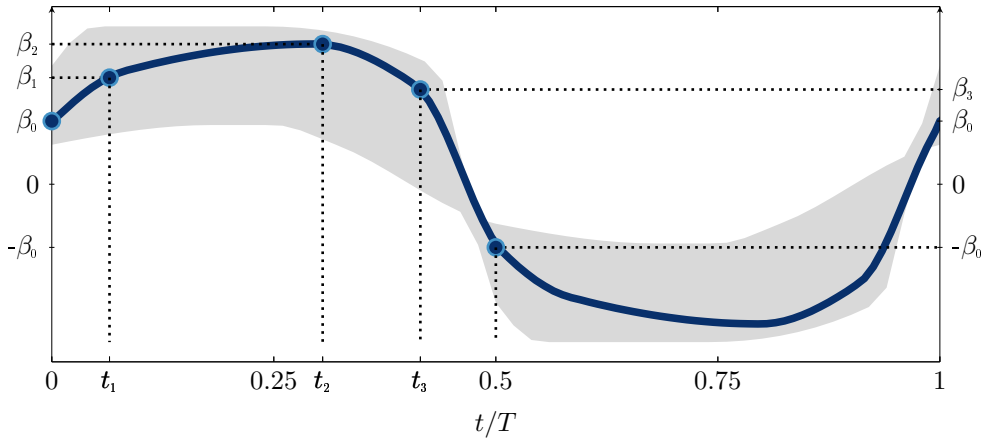

Figure 2.2 – Pitch angle β optimisation function used throughout the experiments. The four angles $\beta_0, \beta_1, \beta_2, \beta_3$ and the three phase times t_1, t_2, t_3 are optimised by the evolutionary algorithm to improve the objective function.

Table 2.2 – Parameter bounds for the pitching motion optimisation

	β_0	β_1	β_2	β_3	t_1	t_2	t_3
minimum	30°	30°	30°	20°	$0.05T$	$t_1 + 0.2(t_3 - t_1)$	$0.33T$
maximum	60°	75°	75°	60°	$0.18T$	$t_3 - 0.2(t_3 - t_1)$	$0.43T$

predefined termination condition is reached. The optimisation for this study converged after 40 generations conducting 4000 experiments on the flapping wing apparatus over the course of three consecutive days. The evolution of the pitch angle kinematics β progressed quickly for the first ten generations, then the solutions vary only slightly within a small margin for the remainder of the optimisation where only minor improvements are made. The genetic algorithm optimisation was halted after the average fitness of the Pareto front individuals did not advance within the last ten generations.

2.3 Results

2.3.1 Phenomenological Overview

The two optimisation objectives in this study are the stroke average lift coefficient $\overline{C}_L$ and the stroke average hovering efficiency η. The final shape of the Pareto front in fig. 2.3a represents the trade-off between those two optimisation targets. The coloured markers represent the individuals of the final generation on the Pareto front whose specific kinematics and associated aerodynamic loads will be analysed in more detail here. The x and y-axis in fig. 2.3a have been inverted following standard conventions. The stroke-average lift $\overline{C}_L$ produced by the optimised kinematics ranges from 1.20 to 2.09 and the aerodynamic performance η varies from 0.60 to 1.17. By trading off up to 43 % of its maximum lift capacity, the flapping wing system's efficiency can be increased by 93 % by merely adjusting the pitch angle kinematics.

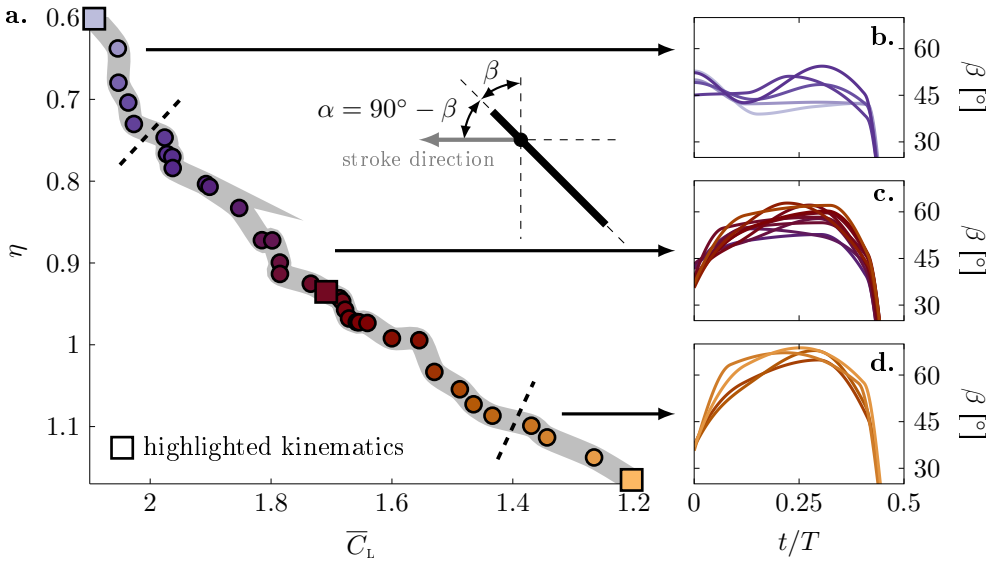

Figure 2.3 – a. Final Pareto front for the optimisation objectives hovering efficiency η vs stroke average lift coefficient $\overline{C}_L$. Solutions marked with a square marker are examined in more detail in Section 2.3.1. b.-d. Temporal evolution of the pitch angle β for a single stroke for different sections of the Pareto front.

The Pareto front can be divided in three sections based on the local change in the gradient $d\eta/d\overline{C}_L$ along the front. Along the large central part of the Pareto front, the lift increases approximately linearly with decreasing efficiency. In this bulk part of the Pareto front, an increase of $\Delta\overline{C}_L = 0.1$ costs $\Delta\eta = 0.058$ or an increase of $\Delta\eta = 0.1$ costs $\Delta\overline{C}_L = 0.167$. Near the tails of the Pareto front, there is a larger trade off between lift and efficiency. For the highest lift cases, we can squeeze out an increase of $\Delta\overline{C}_L = 0.1$ at the expense of losing $\Delta\eta = 0.138$. For the highest efficiency cases, we can squeeze out an increase of $\Delta\eta = 0.1$ at the expense of losing $\Delta\overline{C}_L = 0.257$.

The pitch angle kinematics β have a distinctly different evolution for the three different regions of the Pareto front. The evolutions of β are presented in fig. 2.3b-d for half of the flapping cycle. The motion is perfectly symmetric and the front- and backstroke are identical. The selected axes limits highlight the variations of β during the main portion of the stroke prior to the rapid end of stroke rotation where β drops to zero for all kinematics. All kinematics on the Pareto front have an advanced rotation, which means that the majority of the end of stroke rotation occurs before the end of the stroke. The pitch angle is the function optimised by the genetic algorithm. The aerodynamic angle of attack α during this stroke is related to the pitch angle as $\alpha = 90° - \beta$.

The kinematics in the high lift tail of the Pareto front (fig. 2.3b) have an almost trapezoidal pitch angle profile. The pitch angle is more or less constant around $\beta = 45°$ for $0 < t/T < 0.4$ and there is an abrupt end of stroke rotation. The kinematics in the high efficiency tail of the Pareto front (fig. 2.3d) have a more rounded, sinusoidal profile with a maximum pitch angle

$\beta > 60°$ around mid-stroke. The high pitch angle leads to a substantially lower angle of attack in the high efficiency tail compared to the high lift tail. The transition into the end of stroke rotation is smooth. The kinematics in the bulk of the Pareto front (fig. 2.3c) gradually evolve from the more trapezoidal high lift kinematics towards the almost sinusoidal high efficient kinematics.

The intermediate and most efficient pitch angle kinematics obtained in the optimisation resemble pitch angle evolutions observed in a dynamically scaled crane fly model in hover [96]. The stroke actuation of this crane fly model was fixed while the wing was allowed to passively pitch in response to the aerodynamic forces. Similar pitch angle profiles were also found as efficient hovering motions of a hawkmoth obtained by a numerical-based optimisation [84]. The high lift kinematics along the Pareto front share the same features that can be observed in the free-hovering flight wing kinematics of a horned beetle [97]. The wings of the horned beetle are flexible and significant contributions of the wing inertia and elastic storage from the wing deformation lower the total power requirements for the hovering motion. Yet, the pitch kinematics found for these natural flexible wings with different planform shapes match the solutions obtained by our optimisation. This confirms that we are able to optimise the underlying aerodynamic effects that govern effective flapping wing flight with the use of a rectangular rigid plate.

To understand and characterise the variations between the different kinematic solutions and their force and flow responses, we have selected three solutions along the Pareto front to guide the description. The selected solutions are the highest lift generating, the most efficient, and an intermediate solution. They are indicated by the square markers in fig. 2.3a.

The pitching kinematics of the selected cases and their flow and forces responses are presented first for the intermediate solution (fig. 2.4), then for the highest lift generating (fig. 2.6), and finally for the most efficient solution (fig. 2.8). The pitching kinematics are expressed now in terms of the aerodynamic angle of attack α. Only one half cycle is shown in the figures for a more concise representation of the results. Both the kinematics and the corresponding force responses are symmetric between front- and backstroke. The differences between the forces measurements during the front- and the backstroke are less than 5 % of the maximum values which is of the same order of magnitude as the differences between cycles. The flow and force responses are summarised by selected snapshot of the velocity and vorticity field and the temporal evolutions of the lift and power coefficient and the leading edge vortex circulation. The leading edge vortex circulation was computed inside the Γ_2-contour with $\Gamma_2 = 0.5$ and a radius of 5 pixels over one half-cycle [98].

The summary of the input kinematics and their response for the intermediate solution along the Pareto front corresponding to $\overline{C}_L = 1.71$ and $\eta = 0.94$ is presented in fig. 2.4. The angle of attack of the intermediate kinematics in fig. 2.4a is already reduced to 51° at the start of the stroke due to the advanced end-of-stroke rotation. Initially, the angle of attack continues to decrease rapidly while the stroke velocity increases. When the angle of attack has reached a

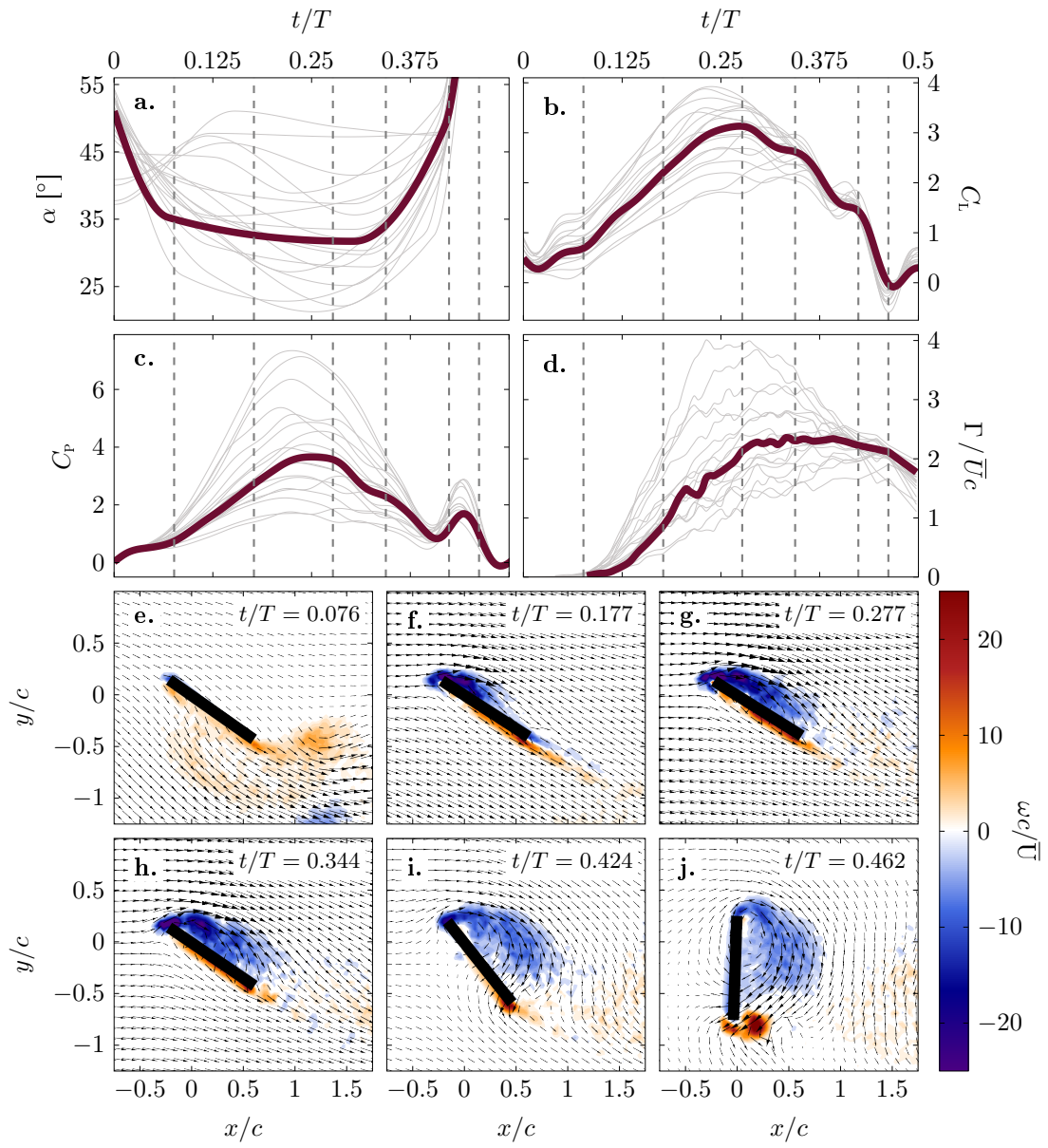

Figure 2.4 – Overview of the intermediate Pareto front kinematics and their aerodynamic performance ($\overline{C}_L = 1.71, \eta = 0.94$). a. Temporal evolution of the angle of attack α, b. lift coefficient $\overline{C}_L$, c. power coefficient C_P, and d. leading edge vortex circulation Γ. e.-j. Selected velocity and vorticity fields within a single stroke. The grey lines in a.-d. represent all Pareto optimal solutions for reference. The bold lines represent the results for the intermediate Pareto front kinematics.

value of 35° around $t/T = 0.06$, a leading edge vortex starts to form (fig. 2.4e). The wing in the flow field snapshots accelerates from right to left. While the leading edge vortex grows in chord-wise direction, the angle of attack continues to decrease but at a lower rate than before. Despite the gradual decrease of the angle of attack, the lift and power coefficients

increase in the first half of the stroke. The increase is due to the growing leading edge vortex (fig. 2.4e-g) and the influence of the sinusoidal stroke motion. The power coefficient reaches a maximum value around the mid-stroke at $t/T = 0.25$. The lift coefficient reaches a maximum value shortly thereafter around $t/T = 0.28$ when the leading edge vortex circulation levels off. At this point, leading edge vorticity covers the entire chord length and continues to spread in the chord-normal direction (fig. 2.4g-h). This stage in the vortex development is know as vortex lift-off [16]. Once the vortex lifts off of the wing, its circulation no longer increases and the lift decreases. Around $t/T = 0.33$, the wing starts its end-of-stroke rotation and the angle of attack increases rapidly when the wing rotates back to its vertical orientation. The axes limits in fig. 2.4a highlight the variations in the angle of attack during the main portion of the stroke and cut off the fast rotation at the end of the stroke. The fast end-of-stroke pitch rotation pushes the leading edge vortex away and prompts the formation of a trailing edge vortex (fig. 2.4i-j), which yields a secondary peak in the power coefficient (fig. 2.4c).

The different phases of the leading edge vortex development are more clearly visualised in fig. 2.5 by the space-time representation of the surface velocity, snapshots of the finite time Lyapunov exponent (FTLE) ridges, and the position of the leading edge vortex with respect to the wing. The leading edge vortex position is determined as the vorticity density centre within the $\Gamma_2 = 0.5$-contour. Figure 2.5a shows the spatiotemporal evolution of the velocity component u_{surf} parallel to the wing's surface, close to the surface. Positive values of u_{surf} indicate a surface flow towards the trailing edge indicative of attached surface parallel flow. Negative values of u_{surf} indicate a surface flow towards the leading edge induced by a leading edge vortex. From $t/T = 0.13$ to 0.21, the leading edge vortex emerges at the leading edge and gradually spreads in the chord-wise direction but never fully covers the wing chord. This is clearly visualised by the region of negative surface velocity which gradually grows towards the trailing but only covers about 75 % of the chord at $t/T \approx 0.33$ when the end of stroke motions sets in. The limited chordwise growth of the leading edge vortex is also evidenced by the expansion of the positive-time FTLE ridges that indicate the outer boundary of the vortex. The FTLE fields are calculated from the phases averaged velocity fields following the same procedure as described by Krishna et al. [16, 99]. The scalar FTLE field is a measure of local Lagrangian stretching of nearby trajectories as the flow evolves in space and time. The stretching of particle trajectories can can be calculated forward and backward in time to yield positive and negative-time FTLE fields (pFTLE and nFTLE). The maximising ridges of the FTLE fields are effective at identifying coherent structure boundaries and aid to analyse the dynamics in vortex-dominated flows [100, 101]. The ridges in the nFTLE fields indicate candidate attracting material lines along which particle trajectories will locally contract. The ridges in the pFTLE fields indicate candidate repelling material lines along which particle trajectories will diverge. The points along the chord where pFTLE ridges seem to meet the wing surface downstream of the leading edge vortex mark the location of surface half saddle points. The location of a half saddle point indicates the extend of the vortex. This surface half saddle moves downstream in time while the region of negative surface vorticity grow until reaching mid-chord at $t/T \approx 0.2$. Hereafter, the surface half saddle does not move further

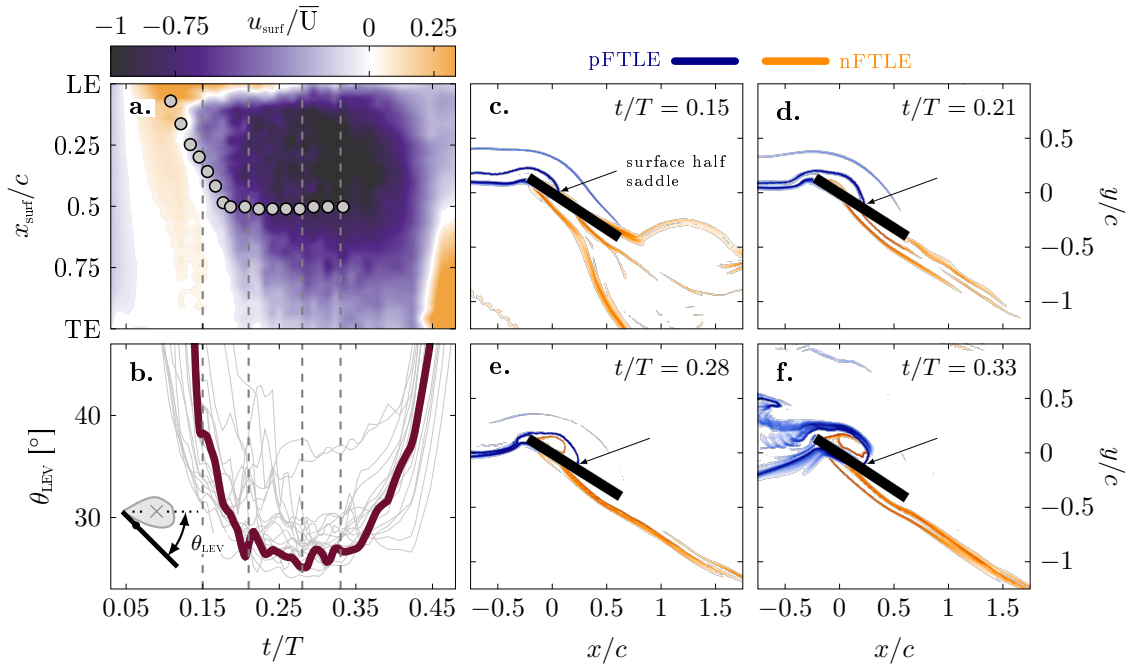

Figure 2.5 – a. Space-time representation of the surface velocity. The grey dots indicate the trajectory of the surface half saddle. b. evolution of the angular location of the leading edge vortex with respect to the wing and the leading edge. The grey lines in b represent all Pareto optimal solutions as reference. The bold line represents the intermediate Pareto front kinematics ($\overline{C}_L = 1.71, \eta = 0.94$). c.-f. Snapshots of the FTLE ridges for selected time instants indicated by the vertical dashed lines in a and b.

downstream and the leading edge vortex grows in chord-normal direction. The downstream trajectory of the surface half saddle is added on top of the surface velocity in fig. 2.5a. The end of the chord-wise growth coincides with the saturation of the leading edge vortex circulation. The end of the chord-wise vortex growth can also be observed by analysing the evolution of the angular position of the leading edge vortex with respect to the wing's surface in fig. 2.5b. The angle θ_{LEV} is defined as the angle between the wing's surface and the line connection the leading edge and the vorticity density centre marking the position of the leading edge vortex as indicate in the sketch in fig. 2.5b. This angle can also be interpreted as the angle of the shear layer that feeds the leading edge vortex. When the vortex grows in chord-wise direction, θ_{LEV} decreases rapidly until reaching a local minimum values of about 25° at $t/T \approx 0.20$. Hereafter, the angle remains approximately constant and increases again once the end-of-stroke rotation has set in. The apparent stagnation of the surface half saddle and the angle θ_{LEV} between $t/T = 0.2$ and $t/T = 0.33$ indicates that the leading edge vortex remains stable without growing in size and circulation but not not shedding into the wake either.

The flow and force response for the highest lift generating kinematics along the Pareto front are presented in fig. 2.6. The angle of attack for the intermediate kinematics started around 51° and decreased to $\alpha = 35°$ where it remained for the majority of the stroke. The evolution of

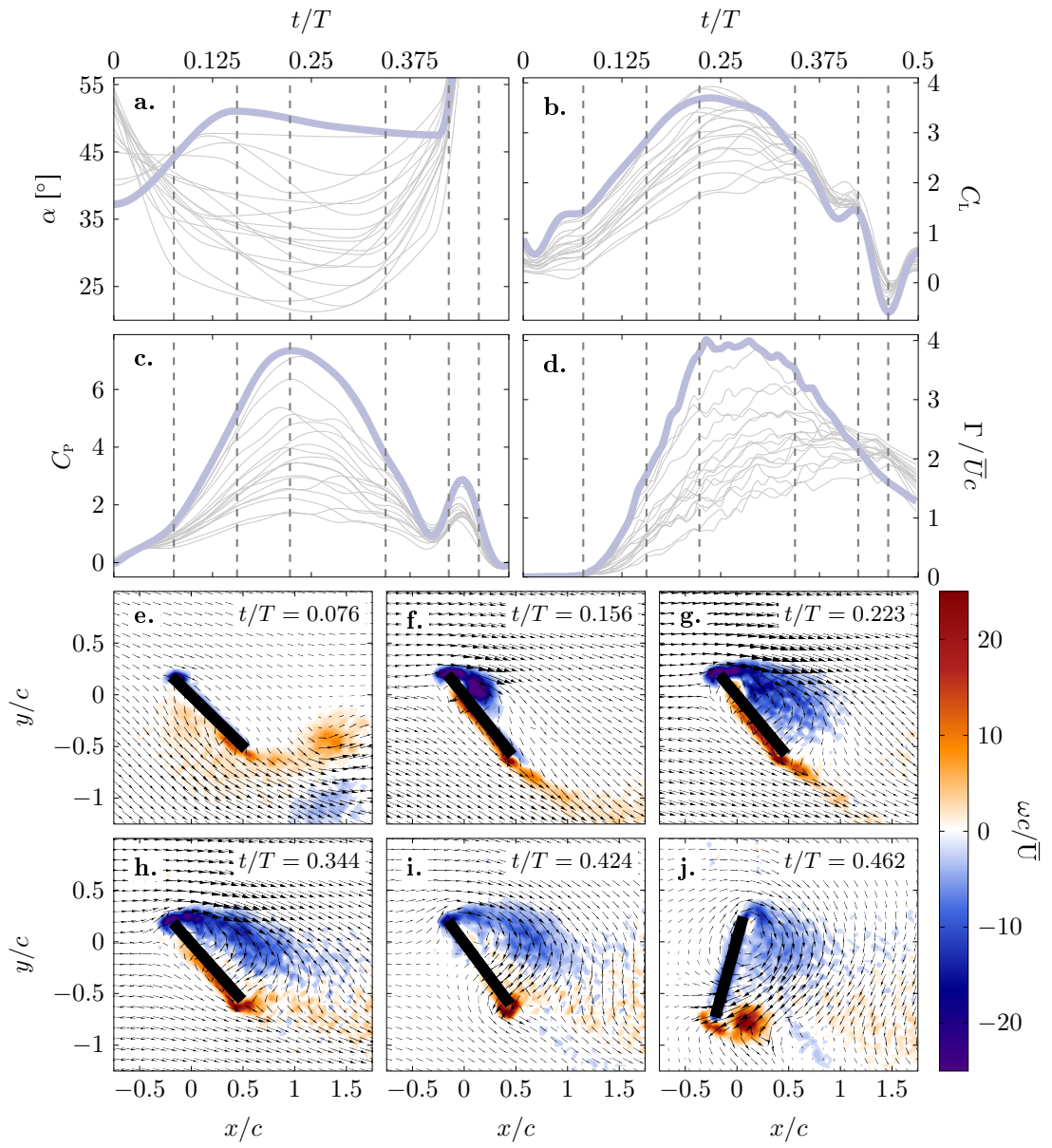

Figure 2.6 – Overview of the highest lift generating Pareto front kinematics and their aerodynamic performance ($\overline{C}_L = 2.09, \eta = 0.60$). a. Temporal evolution of the angle of attack α, b. lift coefficient $\overline{C}_L$, c. power coefficient C_P, and d. leading edge vortex circulation Γ. e.-j. Selected velocity and vorticity fields within a single stroke. The grey lines in a.-d. represent all Pareto optimal solutions for reference. The bold lines represent the results for the highest lift generating Pareto front kinematics.

the angle of attack for the highest lift generating cases is the other way around. The angle is slightly above 35° at the start of the cycle and increases to values around $\alpha = 50°$ until a very abrupt end of stroke motion sets in. The overall higher angles of attack lead to higher values of lift, power, and leading edge vortex circulation during the entire cycle. The leading edge

vortex development (fig. 2.6e-j) is similar to the intermediate case, but the vortex evolves faster due to the higher angle of attack and associated higher circulation rate. This also results in earlier achievement of the maximum lift, power, and circulation. The higher lift generating kinematics thus prefer a higher overall angle of attack yielding a stronger leading edge vortex that reaches its maximum capacity earlier.

The space-time representation of the surface velocity in fig. 2.7a confirms the faster evolution of the leading edge vortex. The negative surface velocity starts to spread earlier and reaches all the way through the trailing edge by $t/T \approx 0.20$. For the intermediate case, this did not occur prior to the end-of-stroke rotation. This moment coincides with the moment the surface half saddle point extracted from the pFTLE ridges reaches the trailing edge (fig. 2.7c-e). When the surface half saddle reaches the trailing edge, it merges with the half saddle at the trailing edge stagnation point into a full saddle that will move away from the wing marking the separation or the lift off of the vortex [16, 100, 102]. The time at which the vortex can no longer grow in the chordwise direction again coincides with the moment the angle θ_{LEV} reaches a minimum value (fig. 2.7b). The local minimum in θ_{LEV} and the surface half saddle and negative surface velocity reaching the trailing edge all indicate the end of the growth of the leading edge vortex. The end of the vortex growth is followed by vortex lift off. The vortex lift off is significantly faster and more pronounced than for the intermediate case and all other cases which are shown by the thin grey lines (fig. 2.7b). The minimum value of the angle θ_{LEV} is higher which indicates that the vortex is less shielded by the wing, which explains the higher drag and higher power coefficient that in required to execute these kinematics. The earlier vortex lift-off gives also more opportunity for a trailing edge vortex to roll up around the trailing edge. This leads to a higher secondary peak in the power coefficient (fig. 2.6i-j).

The flow and force response for the most efficient kinematics along the Pareto front are presented in fig. 2.8. The evolution of the angle of attack (fig. 2.8a) varies more gradually than all other kinematics and reaches values as low as 21° around mid-stroke. At these low angles of attack, the leading edge vorticity remains close to the wing's surface and the circulation continues to grow during the entire stroke until the end-of-stroke motion sets in. The low angles of attack and compact distribution of the vorticity close to the wing lead to low values of the power coefficient during the entire stroke. The largest power values are now observed during the end-of-stroke rotation. The overall lift coefficient is also reduced as a result of the low angles and the lower vortex circulation, but it continues to increase during most of the stroke.

The high lift generating kinematics aimed to accelerate the leading edge vortex development to create a larger and stronger vortex around mid-stroke. The most efficient kinematics seem to be doing the opposite and slowing down the vortex growth to delay vortex lift-off and reduce the power by keeping the vortex bound to the wing. This is confirmed by the surface velocity, FTLE saddle points, and the evolution of θ_{LEV} in fig. 2.9. The negative surface velocity spreads slower than in the previous cases and does not cover the entire surface before the end-of-stroke rotation sets in (fig. 2.9a). The surface half saddles also do not reach the trailing

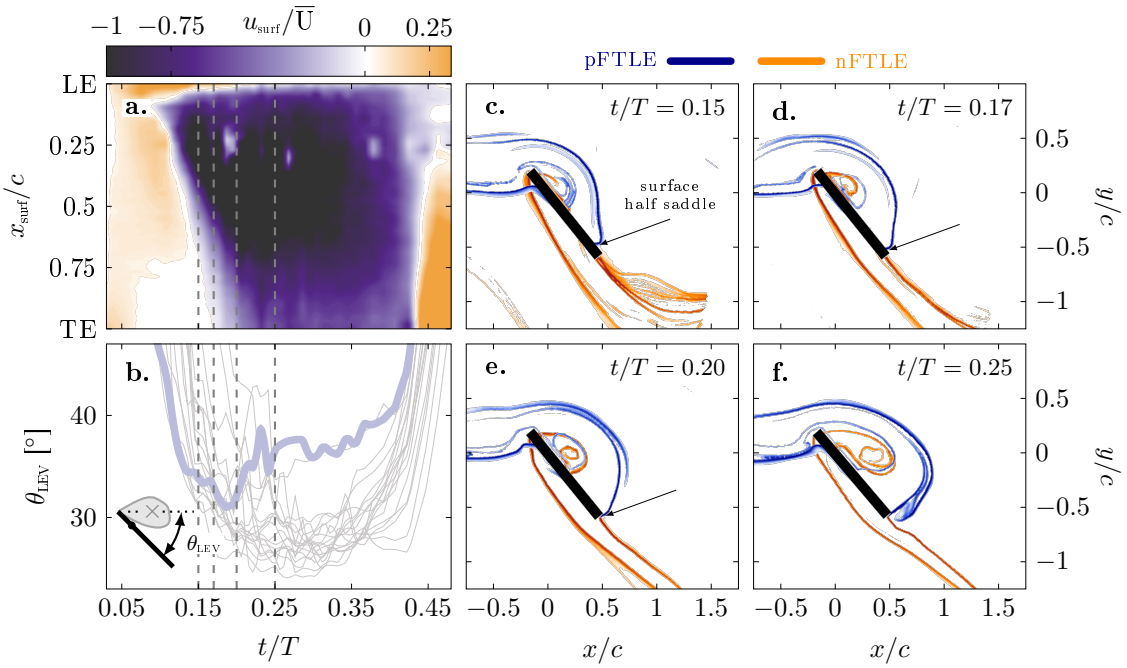

Figure 2.7 – a. Space-time representation of the surface velocity, b. evolution of the angular location of the leading edge vortex with respect to the wing and the leading edge. The grey lines in b represent all Pareto optimal solutions as reference. The bold line represents the highest lift generating Pareto front kinematics ($\overline{C}_L = 2.09, \eta = 0.60$). c.-f. Snapshots of the FTLE ridges for selected time instants indicated by the vertical dashed lines in a and b.

edge and do not lift off (fig. 2.9c-f). Due to the close proximity of the leading edge vorticity to the wing, the calculation of the vortex position is more sensitive and the evolution of θ_{LEV} is a little more noisy. Yet, the angle does not really start to increase before the end-of-stroke rotation confirming the absence of vortex lift off and the associated penalty on the power coefficient.

2.3.2 Quantitative analysis and scaling

In the previous section, we qualitatively linked three characteristic flapping wing pitch angle kinematics along the Pareto front to their aerodynamic response based on the spatiotemporal evolution of the leading edge vortices that are created. In the reminder of the paper, we aim to quantitatively describe and scale the temporal evolution of the vortex development and the aerodynamic forces and efficiency for all solutions along the Pareto front. First, we will extract characteristic velocity and time scales directly from the kinematic input. Second, we will demonstrate how these characteristic parameters allow us to scale the leading edge vortex circulation and the aerodynamic performance.

The leading edge vortex formation on plunging and translating plates rapidly accelerating from rest is well described based on the effective velocity of the leading edge shear layer [103].

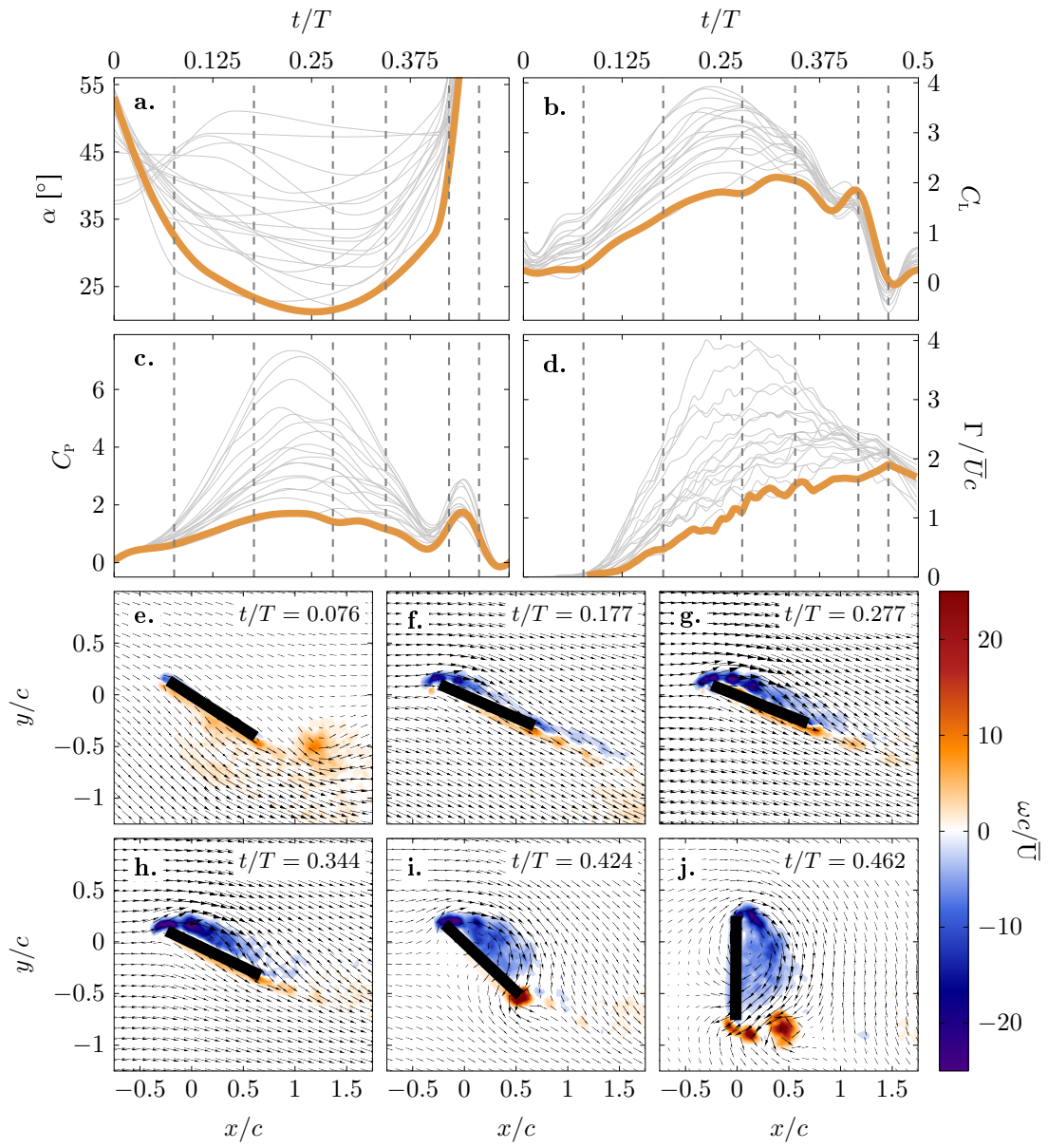

Figure 2.8 – Overview of the most efficient Pareto front kinematics and their aerodynamic performance ($C_L = 1.20, \eta = 1.17$). a. Temporal evolution of the angle of attack α, b. lift coefficient $\overline{C}_L$, c. power coefficient C_P, and d. leading edge vortex circulation Γ. e.-j. Selected velocity and vorticity fields within a single stroke. The grey lines in a.-d. represent all Pareto optimal solutions for reference. The bold lines represent the results for the most efficient Pareto front kinematics.

The effective shear layer velocity for the leading edge vortex formation on pitching and rotating flat plates can be approximated by the leading-edge-normal velocity due to the motion kinematics [104]. For our flapping wing hovering motion, the time dependent shear layer velocity u_s at the span-wise location corresponding to the second moment of area of the wing

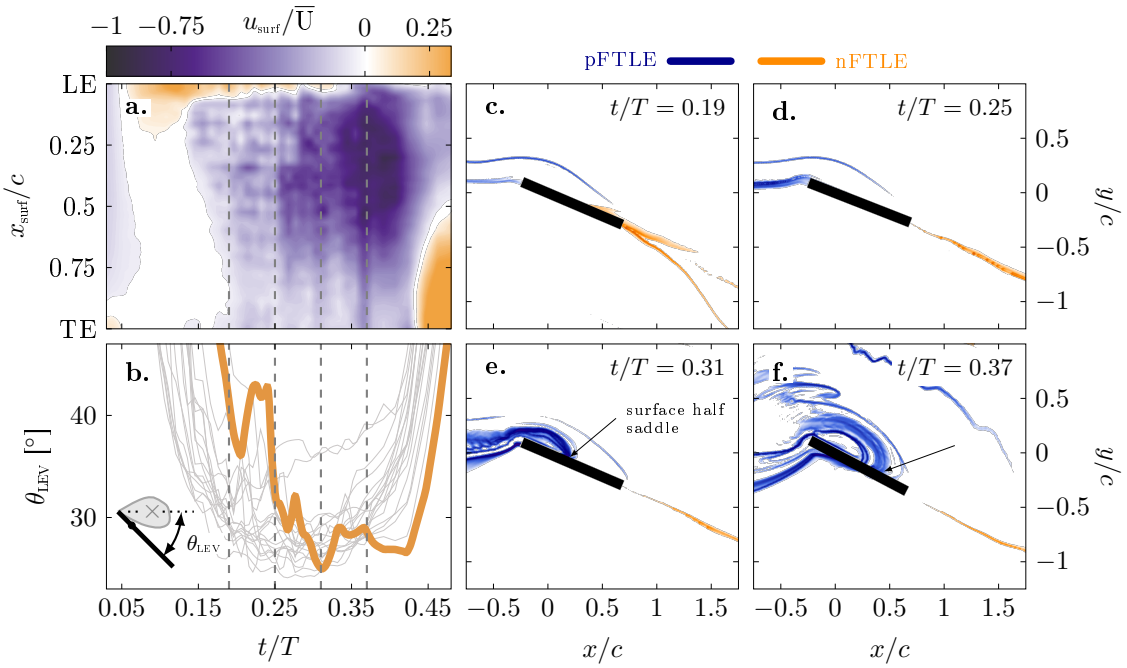

Figure 2.9 – a. Space-time representation of the surface velocity, b. evolution of the angular location of the leading edge vortex with respect to the wing and the leading edge. The grey lines in b represent all Pareto optimal solutions as reference. The bold line represents the most efficient Pareto front kinematics ($C_L = 1.20, \eta = 1.17$). c.-f. Snapshots of the FTLE ridges for selected time instants indicated by the vertical dashed lines in a and b.

(R_2) is calculated using the stroke velocity $\dot{\phi}$ and pitch velocity $\dot{\beta}$ components:

$$u_s(t) = R_2 \dot{\phi}(t) \cos\big(\beta(t)\big) + 0.25c\,\dot{\beta}(t) \quad . \tag{2.5}$$

The second moment of area of the wing R_2 is the span-wise location where the force is applied [88] and the evolution of the shear layer velocity at this location serves as representative velocity for the analysis of the vortex dynamics. By integrating the temporal evolution of the leading edge shear layer velocity u_s defined by equation 2.5 over a time t since the start of the flapping cycle, we obtain the advective time σ:

$$\sigma(t) = \int_0^t u_s(\tau)\,d\tau = \int_0^t R_2 \dot{\phi}(\tau) \cos\big(\beta(\tau)\big) + 0.25c\,\dot{\beta}(\tau)\,d\tau \quad . \tag{2.6}$$

The advective time describes the distance the leading edge has traveled since the beginning of the stroke-cycle [104]. The shear layer velocity is a measure for the instantaneous feeding rate of vorticity into the leading edge vortex. The advective time is a measure for the total amount of vorticity fed into the vortex since the start of the stroke motion and indicates the age of the vortex.

Figure 2.10a summarises the temporal evolution of the leading edge shear layer velocity u_s for

all pitch angle kinematics along the Pareto front in fig. 2.3. The leading edge shear layer velocity is non-dimensionalised by the average stroke velocity $\overline{U}$. The shear layer velocity profiles can again be divided into three characteristic groups based on their form (fig. 2.11). The three groups correspond to the same main middle portion of the Pareto front and the high lift and high efficiency tails. The solutions with trapezoidal pitch angle profiles that yield maximum $\overline{C}_{\mathrm{L}}$ have sinusoidal u_{s}-evolutions. The pitch angle β is approximately constant during large portions of the stroke cycle and the shear layer velocity is mainly driven by the stroke velocity. The most efficient solutions with sinusoidal pitch angle profiles have more trapezoidal shear layer velocity profiles. Here, the pitch angle decreases when the stroke velocity increases and vice versa to obtain an approximately constant value of the shear layer velocity during most of the stroke. The shear layer velocity profiles for the intermediate solutions gradually evolve from the sinusoidal shape with high maximum values around mid stroke to the trapezoidal shapes with a rounded ascending flank and a plateau at lower values.

To scale the aerodynamic performance of the flapping wing hovering motion it is desirable to have a single characteristic velocity which is representative of the input kinematics. We propose to use the root-mean-square value of the shear layer velocity $u_{\mathrm{s,rms}}$ which serves as a fundamental measure of the magnitude of an oscillating signal. The root-mean-square value of the shear layer velocity decreases continuously along the entire Pareto front with decreasing stroke average lift fig. 2.10b. This single kinematic parameter allows for the sorting of the aerodynamic performance of the kinematics in terms of the two objectives of the optimisation: mean lift and efficiency.

The temporal evolution of the advective time σ for all pitch angle kinematics along the Pareto front is summarised in fig. 2.10c. The advective time has the dimension of length and is non-dimensionalised by the chord length. According to equation 2.6, the advective time is zero at the start of the pitching cycle and increases monotonically until the shear layer velocity becomes negative following the initiation of the pitch rotation near the end of the stroke ($t/T \approx 0.42$). The shape of the advective time curves is similar for all solutions. The advective time evolutions of solutions that yield higher mean lift are above those that are more efficient. This is true at any time beyond $t/T = 0.125$. Prior to $t/T = 0.125$, the more efficient kinematics have a higher shear layer velocity due to a faster pitch rotation and higher advective times (fig. 2.10c). The more efficient kinematics typically have lower angles of attack during most of the stroke motions and require a more important pitch rotation around stroke reversal. The sign-reversal of the shear layer velocity at the end of the stroke motion marks the end of the feeding cycle of the current leading edge vortex. The maximum advective time indicates the age of the leading edge vortex at the end of the feeding cycle. The leading edge vortex created by the highest lift generating kinematics reaches a vortex age of 6.11 advective time scales before the pitch rotation sets in. The maximum advective time σ_{max} decreases with decreasing mean lift C_{L} along the entire Pareto front (fig. 2.10d). The leading edge vortex created by the most efficient kinematics only reaches a vortex age of 3.64 advective time scales. Figure 2.10d reveals a direct relationship between the maximum age of the leading edge vortex and the aerodynamic performance of the hovering motion. This inspires us to use to the advective time

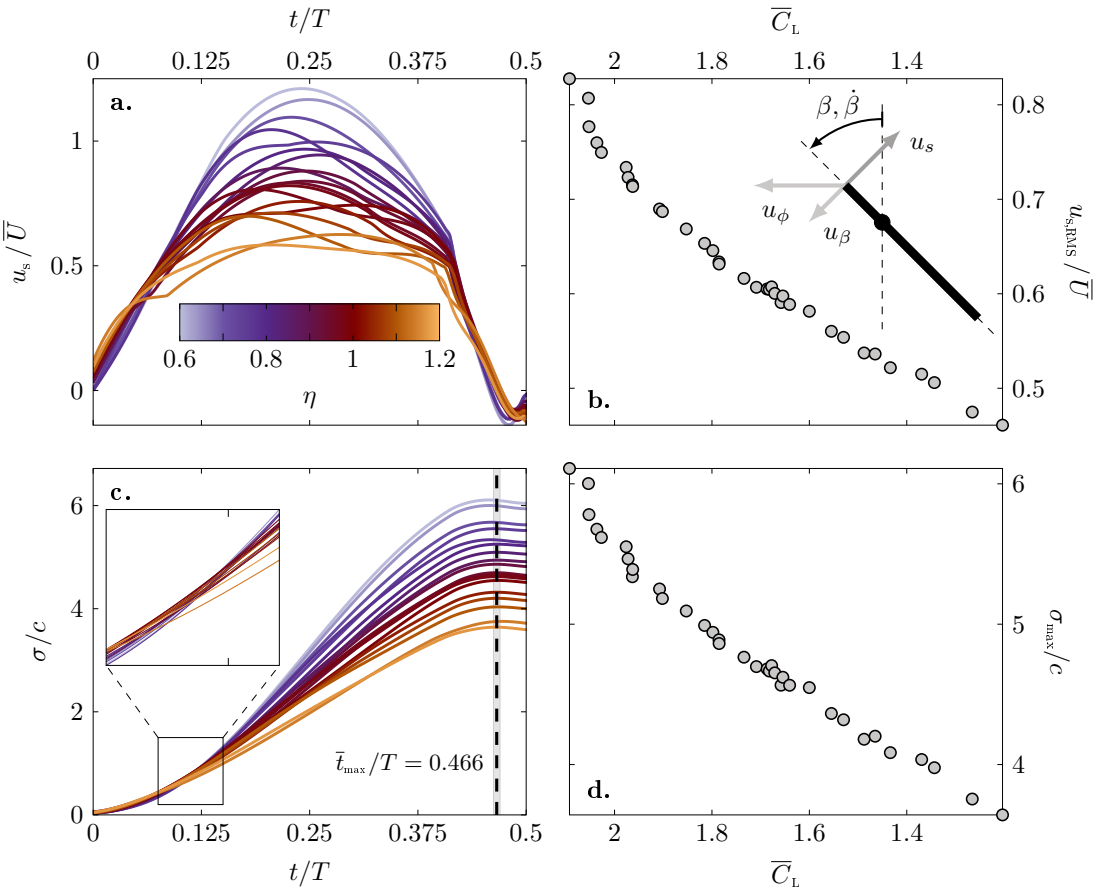

Figure 2.10 – a. Instantaneous shear layer velocity u_s over time t/T, b. RMS of the shear layer velocity $u_{s,RMS}$ over $\overline{C}_L$, and c. chord-normalized advective time σ/c over time t/T, and d. advective time maxima σ_{max} over $\overline{C}_L$. Color-coded is the hovering efficiency η corresponding to the Pareto front individual.

as the characteristic time scale to scale the temporal evolution of the aerodynamic response to the various flapping wing hovering kinematics.

In the following, we will demonstrate how the root-mean-square value of the shear layer velocity and the advective time can be respectively used as characteristic velocity and time to scale the temporal evolution of the leading edge vortex circulation and the aerodynamic performance of Pareto-optimal the flapping wing kinematics.

Leading edge vortex circulation

Figure 2.12 shows a comparison of temporal evolution of the leading edge vortex circulation Γ for all solutions along the Pareto front for two different normalisations. In fig. 2.12a, the circulation is normalised by the stroke average velocity $\overline{U}$ and the chord length and the time axis is normalised by the flapping period. Note that the stroke average velocity and the

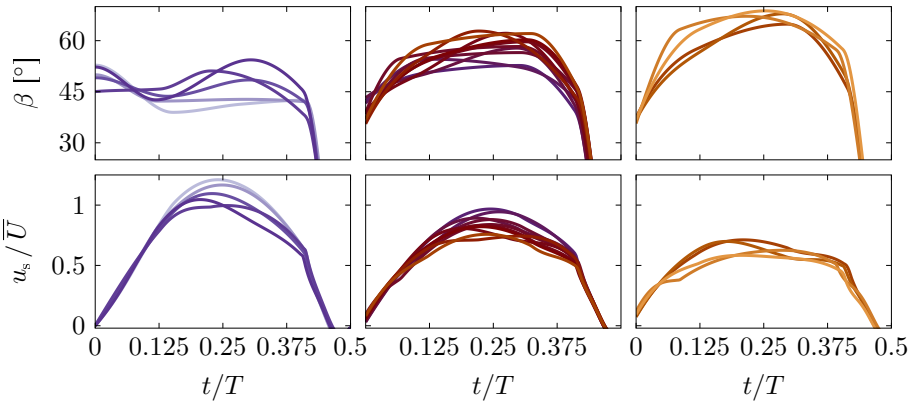

Figure 2.11 – Leading edge shear layer velocity u_s profile groups derived from pitch angle β kinematic groups.

flapping period are the same for all kinematics considered here. In fig. 2.12b, the circulation is normalised by maximum leading edge shear layer velocity $u_{s,max}$ and the chord length and is presented as a function of the non-dimensionalised advective time σ/c.

The leading edge vortex circulation curves all start at zero and start to increases when a new vortex starts to emerge near the wing's leading edge. The circulation increases as the leading edge vortex grows and reaches a maximum value at some point during the second part of the stroke cycle depending on the pitch angle kinematics. Kinematics that yield higher $\overline{C}_L$, generate circulation at a higher rate, reach a higher maximum value of the circulation earlier in the flapping cycle (fig. 2.12a). The peak circulation for the highest $\overline{C}_L$ motion is reached around mid-stroke when the maximum stroke velocity is reached. The circulation for the most efficient motion continues to increase until the pitch rotation sets in at the end of the stroke motion. The peak value gradually decreases and the timing of the peak gradually delays when we move along the Pareto front sacrificing lift for efficiency.

If the circulation is now presented as a function of the advective time as defined in equation 2.6 and normalised by the maximum leading edge shear layer velocity and the chord length, all curves collapse and follow the same trajectory (fig. 2.12b). The newly scaled circulation $\Gamma^* = \Gamma/(u_{s,max}\, c)$ reaches a maximum value of ${\Gamma^*}_{max} \approx 3$ after $\overline{\sigma}/c = 3.90$. For all pitching kinematics along the Pareto front, the maximum leading edge vortex circulation scales with the maximum local shear layer velocity and this maximum circulation is reached after the leading edge has traveled a distance of four chord lengths regardless of the temporal evolution of the pitch angle during the flapping motion.

The optimal kinematics are tailored to reach the maximum circulation right before starting the pitch rotation near stroke reversal. The high lift kinematics continue after the maximum leading edge vortex circulation is reached and cover more advective times during a stroke cycle. For $\sigma/c > 4$, the vortex circulation decreases even though the vortex stays close to the wing. During this part of the motion, vorticity continues to be produced and fed through the

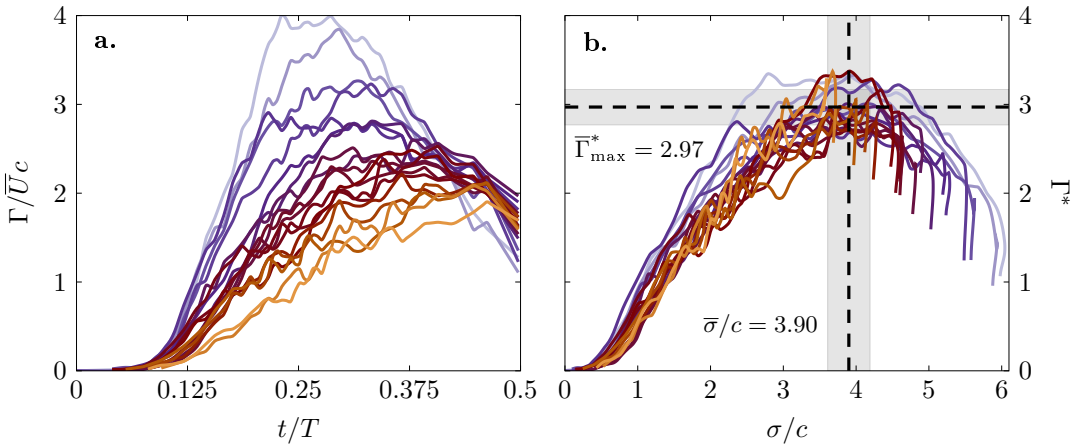

Figure 2.12 – a. Normalized leading edge vortex circulation $\Gamma/\overline{U}c$ over time t/T, b. leading edge vortex circulation $\Gamma/\overline{u}_s c$ scaled with $\hat{u}_s$ over advective time σ/c. Color-coded is the hovering efficiency η corresponding to the Pareto front individual. The dashed lines mark the mean of the scaled circulation Γ^* maxima and the corresponding mean timing $\overline{\sigma}/c$. The gray areas represents +/- one standard deviation around the mean.

leading edge shear layer without increasing the leading edge vortex circulation. This vorticity must be transported either in span-wise direction or dissipates as a consequence of vortex bursting.

This scaling of the leading edge vortex circulation based on the maximum shear layer velocity was previously demonstrated to be effective for two-dimensional starting vortices [105] and swept and unswept pitching wings [106]. The constant vortex formation time of approximately four advective times is also consistent with many examples of optimal vortex formation found in nature [107] and with the many records of vortex formation numbers around four for vortex rings generated by a piston cylinders [108].

Aerodynamic loads

The leading edge vortex provides an important contribution to the aerodynamic forces on unsteadily moving wings [2]. The evolution of the leading edge vortex circulation Γ in the measurement plane at R_2 scales in magnitude with the maximum leading edge shear layer velocity $u_{\mathrm{s,max}}$. Based on this new scaling of the circulation and the Kutta-Joukowski theorem, we can formulate the sectional lift L as:

$$L = \rho \overline{U} \Gamma = \rho \overline{U} \Gamma^* u_{\mathrm{s,max}} c \quad , \tag{2.7}$$

and a rescaled lift coefficient C_{L}^* as:

$$C_{\mathrm{L}}^* = \frac{L}{1/2 \rho \overline{U} u_{\mathrm{s,rms}} R c} \quad . \tag{2.8}$$

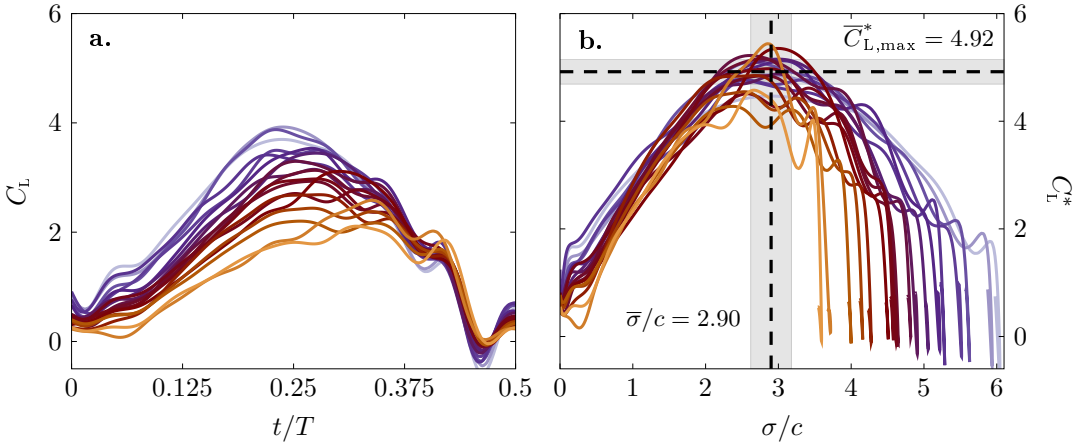

Figure 2.13 – a. Lift coefficient C_L over time t/T and b. scaled lift coefficient C^*_L over advective time σ/c. Color-coded is the hovering efficiency η corresponding to the Pareto front individual. The dashed lines mark the mean of the scaled lift C^*_L maxima and the corresponding mean timing $\overline{\sigma}/c$. The gray areas represents +/- one standard deviation around the mean.

Here, we have replaced the maximum shear layer velocity $u_{\mathrm{s,max}}$ by the root-mean-square value of the shear layer velocity $u_{\mathrm{s,rms}}$ to better account for the span-wise variation of the shear layer velocity.

The comparison of this new scaling of the lift coefficient in comparison to the more standardly used definition $C_\mathrm{L} = L/\left(1/2\rho\overline{U}^2 Rc\right)$ is presented in fig. 2.13 for all solutions along the Pareto front. The maximum values of lift coefficient C_L in fig. 2.13a decrease and occur later in the cycle for kinematics that are more efficient. When the lift coefficient is normalised according to equation 2.8 and presented as a function of the non-dimensionalised advective time σ/c in fig. 2.13b the increasing lift slopes collapse and the magnitude and timing of the lift coefficient maxima align. With the proposed scaling, the lift coefficient reaches a maximum value around $C^*_{\mathrm{L,max}} = 4.92$ for $\sigma/c = 2.90$ for all Pareto-optimal kinematics. The lift coefficient maximum is reached one advective time before the leading edge vortex circulation Γ reaches its maximum value. This indicates that $C^*_{\mathrm{L,max}}$ depends not only on the strength of the leading edge vortex, but also on its position with respect to the wing. The timing of both scales with the advective time for all kinematics considered here.

Hovering efficiency

Analogous to the leading edge vortex circulation Γ and the lift coefficient C_L, the drag C_D and power coefficient C_P can be renormalised using the leading edge shear layer velocity to:

$$C^*_\mathrm{D} = \frac{D}{\frac{1}{2}\rho\overline{U}u_{\mathrm{s,rms}}Rc} \quad \text{and} \quad C^*_\mathrm{P} = \frac{P}{\frac{1}{2}\rho\overline{U}u^2_{\mathrm{s,rms}}Rc} \tag{2.9}$$

Using the coefficients C_{L}^* and C_{P}^*, we rescale the stroke average hovering efficiency η:

$$\eta^* = \frac{\overline{C}_{\mathrm{L}}^*}{\overline{C}_{\mathrm{P}}^*} = \frac{\overline{L}}{\overline{P}}\, u_{\mathrm{s,rms}} \quad . \tag{2.10}$$

Figure 2.14 shows the comparison of the newly scaled stroke average lift, power, and the efficiency with the standard normalisation for all solutions along the Pareto front. The stroke average lift and power coefficients $\overline{C}_{\mathrm{L}}$ and $\overline{C}_{\mathrm{p}}$ normalised based solely on the stroke average velocity $\overline{U}$ in fig. 2.14a,b increase with increasing $\overline{C}_{\mathrm{L}}$. Note that we have kept the y-axis inverted here to match the Pareto front representation in fig. 2.14c. When we normalise the coefficients as proposed in eqs. (2.8) and (2.9) using the root-mean-square value of the shear layer velocity, the scaled coefficients collapse and we obtain mean values of $\overline{C}_{\mathrm{L}}^* = 2.74$ and $\overline{C}_{\mathrm{P}}^* = 4.90$ across the ensemble of Pareto-optimal kinematics. The rescaled hovering efficiency η^* reaches an average value of $\overline{\eta}^* = 0.56$ for all Pareto front solutions. The standard deviation around these mean values across all kinematics is indicated by the grey shading in fig. 2.14.

The proposed scaling works especially well for the power coefficient. Small deviations from the constant mean values of the lift coefficient and efficiency are observed for the most efficient kinematics and the kinematics that yield the highest lift. The successful scaling of the efficiency with the shear layer velocity confirms the strong correlation between the aerodynamic efficiency and the growth rate of the leading edge vortex for the Reynolds number considered in this work.

Based on this scaling, the shape of the Pareto-front would change from a convex η versus $\overline{C}_{\mathrm{L}}$ shape, to basically a single point in the $\overline{\eta}^*$ versus $\overline{C}_{\mathrm{L}}^*$ plane. The values corresponding to this optimal performance point are expected to vary for different wing planforms, different flow conditions, Reynolds number, and reduced frequency. The solutions that end up in the optimal performance point are not unique, they all create a leading edge vortex of a different size and strength, but do this in the most optimal way. This optimal vortex formation process is governed by the shear layer velocity which serves as the main indicator of the aerodynamic performance. The scaled values of non-Pareto optimal kinematics do not collapse and are lower than the $\overline{C}_{\mathrm{L}}^*$ and $\overline{\eta}^*$ values, and higher than the $\overline{C}_{\mathrm{P}}^*$ values found in fig. 2.14. Higher values $\overline{C}_{\mathrm{L}}^*$ and $\overline{\eta}^*$ and lower $\overline{C}_{\mathrm{P}}^*$ values are not achievable with the given geometric and kinematic boundary conditions and the current values obtained by the scaled coefficients represent target limits for optimal performance. The limiting values can be used to quickly estimate the maximal achievable performance values of new or adapted kinematics using

$$\overline{C}_{\mathrm{L}}(\phi,\beta) = \overline{C}_{\mathrm{L}}^*\, \frac{u_{\mathrm{s,rms}}}{\overline{U}} \quad , \tag{2.11}$$

$$\overline{C}_{\mathrm{P}}(\phi,\beta) = \overline{C}_{\mathrm{P}}^*\, \frac{u_{\mathrm{s,rms}}^2}{\overline{U}^2} \quad , \tag{2.12}$$

$$\eta(\phi,\beta) = \overline{\eta}^*\, \frac{\overline{U}}{u_{\mathrm{s,rms}}} \quad , \tag{2.13}$$

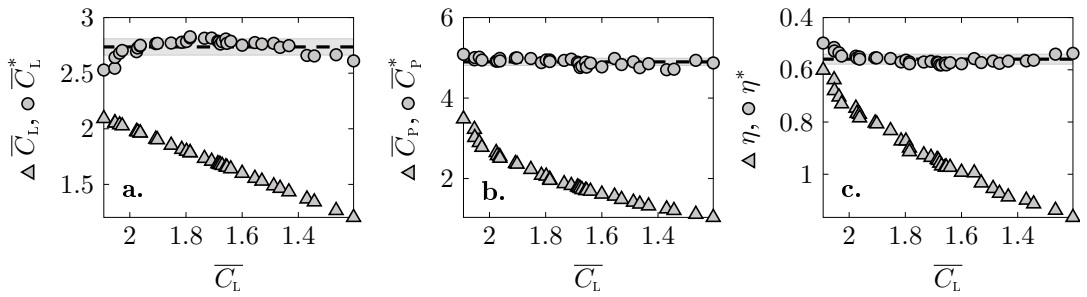

Figure 2.14 – a. Scaled vs. unscaled stroke-average lift coefficient $\overline{C}_L$ over $\overline{C}_L$, b. scaled vs. unscaled stroke-average power coefficient $\overline{C}_P$ over $\overline{C}_L$, and c. scaled vs. unscaled stroke-average hovering efficiency η over $\overline{C}_L$. The triangles represent the normalized aerodynamic coefficients and the circles are the coefficients rescaled with the shear layer velocity $u_{s,rms}$. The dashed lines mark the mean of the scaled values. The grey areas represents +/- one standard deviation around the mean.

with $\overline{C}^*_L = 2.74$, $\overline{C}^*_P = 4.90$ and $\overline{\eta}^* = 0.56$ respectively. This estimation is possible without additional measurements because the shear layer velocity only depends on the input kinematics (ϕ, β). Further investigations are desirable to determine how the values of $\overline{C}^*_L$, $\overline{C}^*_P$, and $\overline{\eta}^*$ vary as function of the Reynolds number and wing geometry.

2.4 Conclusion

We have experimentally optimised the pitch angle kinematics for hovering flapping wing flight using a unique mechanical flapping wing system that allows for robust and repeatable execution of widely varying flapping kinematics. The kinematics yielding maximal stroke average lift and hovering efficiency have been determined with the help of an evolutionary algorithm and in-situ force and torque measurements at the wing root. Additional flow field measurements have been conducted to reveal the phenomenology of the force and flow field response for the Pareto-optimal kinematics.

A Pareto front of optimal solutions is obtained along which the stroke-average lift $\overline{C}_L$ produced by the optimised kinematics ranges from 1.20 to 2.09 and the aerodynamic performance η varies from 0.60 to 1.17. By trading off up to 43 % of its maximum lift capacity, the flapping wing system's efficiency can be increased by 93 % by merely adjusting the pitch angle kinematics.

The Pareto-optimal pitching kinematics are classified into three groups with distinctly different kinematic and dynamic characteristics. The three groups correspond to three sections of the Pareto front: the large central part where the lift increases approximately linearly with decreasing efficiency, and the high lift and high efficiency tails where there is a significantly larger trade off between lift and efficiency. The kinematics in the high-lift tail of the Pareto front have a trapezoidal pitch angle profile with a plateau around $\beta = 45°$ and an additional peak at the beginning of the stroke. These kinematics create strong leading edge vortices

early in the cycle which enhance the force production on the wing. The leading edge vortex circulation and the aerodynamic forces reach their maxima around mid-stroke marking the the end of the growth of the leading edge vortex and the onset of vortex lift-off. The transition between the different phases of the leading edge vortex development are identified based on the surface velocity, the trajectory of the surface half saddles from FTLE ridges, and the position of the leading edge vortex with respect to the wing. The most efficient kinematics have a more rounded, sinusoidal profile with a maximum pitch angle $\beta > 60°$ around mid-stroke and create weaker leading edge vortices that stay close-bound to the wing throughout the majority of the stroke-cycle. The aerodynamic forces and the leading edge vortex circulation grow significantly slower in the high efficiency tail than in the rest of the Pareto front and reach their maxima just before the end-of-stroke rotation. The efficient leading edge vortex development is characterised by the absence of vortex lift-off. The kinematics in the bulk of the Pareto front gradually evolve from the more trapezoidal high lift kinematics toward the almost sinusoidal high efficient kinematics. The aerodynamic forces and leading edge vortex circulation reach maximum values shortly after mid-stroke.

The classification into three groups also applied to the evolution of the shear layer velocity which is directly determined from the input kinematics. Kinematics within the same group yield similar characteristic evolutions of the shear layer velocity that are different from those of the other groups. The integral of time-resolved leading edge shear layer velocity u_s over the cycle time t yields the advective time σ which serves as a normalised time scale for the leading edge vortex growth and aerodynamic force evolution. The root-mean-square value of the shear layer velocity at the leading edge serves to quantitatively characterise the growth of the leading edge vortex and scale the average and the temporal evolutions of the circulation and the aerodynamic forces. The ascending flanks and maxima of the leading edge circulation Γ and lift coefficient C_L collapse when being normalised by the root-mean-square value of the shear layer velocity and presented in function of the advective time for all Pareto front kinematics. The optimal kinematics are tailored to reach the maximum circulation right before starting the end-of-stroke pitch rotation after $\overline{\sigma}/c = 3.9$. The high lift kinematics continue after the maximum leading edge vortex circulation is reached and cover more advective times during a stroke cycle. The vortex formation time of approximately four advective times for the most efficient hovering kinematics is consistent with many examples of optimal vortex formation found in nature.

The leading edge shear layer velocity $u_{s,RMS}$ also serves to renormalise the aerodynamic power coefficient C_P and hovering efficiency η. All cycle-average aerodynamic coefficients normalised by $u_{s,RMS}$ collapse onto their mean-values $\overline{C}_L^* = 2.74$, $\overline{C}_P^* = 4.90$ and $\overline{\eta}^* = 0.56$ for every Pareto front kinematic. The successful newly proposed scaling of the efficiency with the shear layer velocity confirms the strong correlation between the aerodynamic efficiency and the growth rate of the leading edge vortex for the Reynolds number considered in this work. The correlation is based on the underlying physics and we expect the general phenomenology and the scaling based on the shear layer velocity to be valid for different wing shapes and even flexible wings. Furthermore, the shear layer velocity is determined solely on the basis of the input

kinematics and this scaling allows us to estimate the maximally attainable stroke-average lift, power, and efficiency of new or adapted kinematics.

Further investigations are desirable to determine how the values of $\overline{C}_{\mathrm{L}}^{*}$, $\overline{C}_{\mathrm{P}}^{*}$ and $\overline{\eta}^{*}$ vary as function of the Reynolds number, different wing planforms and for non Pareto-optimal kinematics. Taking into account the larger variations of kinematics considered here and the three-dimensionality of the flapping wing motion, the robustness of the proposed scaling is remarkable and can guide the aerodynamic design of human-engineered devices that can automatically adapt their motion kinematics to optimally fit varying flight conditions. The results should also be transferable to other unsteady aerodynamic problems that are vortex dominated and where the vortex is accumulating circulation resulting from an arbitrary relative unsteady motion of an aerodynamic body.

Effects of Wing Flexibility Part II

3 Aeroelastic characterisation of a bio-inspired flapping membrane wing

In this chapter, a novel bio-inspired membrane wing design is introduced and the fluid-structure interactions of flapping membrane wings are systematically investigated. The objective is to characterise the aerodynamic performance at different aeroelastic conditions and relate it to membrane deformation. The extend of this work, shows that combining the effect of variable stiffness and angle of attack variation can significantly enhance the aerodynamic performance of membrane wings and has the potential to improve the control capabilities of micro air vehicles.

The work presented in this chapter has been published in *Bioinspiration & Biomimetics* [109].

3.1 Introduction

Many swimming or flying animals use flexible appendages like fins, tails, and wings for locomotion on land, in water, or in air [110–114]. Natural fliers have flexible wings which turn out to be an efficient means of propulsion that is robust to perturbations [115], lightweight [116], reconfigurable to enhance lift production or reduce drag [117, 118], and silent [119]. By actively controlling their wing's kinematics, flying animals can alternate between flapping wing flight and gliding to conserve energy [120, 121]. In addition to the aerodynamic benefits, the wing's elasticity helps to absorb kinetic energy from collisions [122], and some species can store their wings to protect them when moving through tight spaces on the ground [123].
Flying and gliding mammals, in particular several species of bats, lemurs, and squirrels, use membrane wings to create lift. Bats have a lightweight bone and muscle structure that allows them to precisely control large shape deformations of their thin and compliant membranes. By flapping and deforming their wings, bats can adapt to different flow conditions and perform agile flight manoeuvres [124–126].
Membrane wings have an enhanced aerodynamic performance compared to rigid wings due to their ability to passively camber and reduce their effective angle of attack. The membrane deformation leads to higher lift slopes, a delay in stall onset, improved gust alleviation, and enhanced flight stability relative to rigid wings [127, 128]. These properties make membrane

wings a promising example for advances in the design of micro air vehicles [27, 54, 129–133]. Even though our natural examples exploit the complex fluid-structure interaction between their flexible or membrane wings and the surrounding air with great ease, it is not trivial to replicate and scale the balance between the structural and fluid dynamical parameters for engineering applications. Many theoretical, numerical, and experimental studies have been conducted using flexible and deformable wings to improve our understanding of the impact of fluid-structure interactions on the aerodynamic performance of fixed and unsteadily flapping wings and to provide guidance for the design of micro air vehicles.

Membrane wings at fixed angles of attack have been studied extensively in the past in the context of sailboats, hang gliders, and Cretan type wind mill designs [134–137]. First studies on inextensible membranes were focussed on predicting the shape and aerodynamic performance of sails. Thwaites [134] and Nielsen [135] were among the first to investigate the relation between tension, aerodynamic loads, and deflection of inextensible sails. They found that the equilibrium shape of a passively deformable sail at low angles of incidence α is solely governed by the ratio of the aerodynamic pressure and the tension parameter $\mathscr{T}$ denoted by λ [134]:

$$\lambda = 2\rho \mathrm{U}_\infty^2 c / \mathscr{T} \quad . \tag{3.1}$$

Different models and analytical solutions for inextensible and flexible membranes have since been proposed building upon the early work of Thwaites and Nielsen [134, 135]. An extensive summary of these works can be found in [138].

At higher angles of incidence and for larger excess lengths of the membranes, classical, potential flow based theories fail to predict the equilibrium states of fixed membrane wings and numerical studies coupling the Navier-Stokes equations with an aeroelastic model are desirable. Based on the results of such coupled simulations, Smith and Shyy [139, 140] derived two non-dimensional parameters to characterise the interplay between aeroelastic and aerodynamic effects:

$$\Pi_1 = \left(\frac{Eh}{\frac{1}{2}\rho U_\infty^2 c} \right)^{1/3} \quad \text{and} \quad \Pi_2 = \left(\frac{\epsilon_0 h}{\frac{1}{2}\rho U_\infty^2 c} \right)^{1/3} , \tag{3.2}$$

with E the Young's modulus of the membrane material, h the membrane thickness, ρ the fluid density, U_∞ the freestream velocity, c the chord length, and ϵ_0 the membrane pretension. The two parameters Π_1 and Π_2 control the steady-state, inviscid aeroelastic behaviour of an initially flat membrane at fixed angles of attack. The dimensionless deformation of the membrane wing is inversely proportional to Π_1 in the absence of pretension and inversely proportional to Π_2 in the limit of vanishing material stiffness [55].

If the load distribution on the membrane wing is assumed to be uniform, the maximum camber $z_{\max}$ is entirely characterised by the Weber number We and the membrane pretension ϵ_0 [127]. The Weber number is defined as the ratio between the aerodynamic loading and the effective stiffness of the membrane:

$$We = C_\mathrm{N} \frac{\frac{1}{2}\rho \mathrm{U}_\infty^2 c}{Eh} = \frac{C_\mathrm{N}}{Ae} , \tag{3.3}$$

where Ae is defined as the aeroelastic number [141]:

$$Ae = \frac{Eh}{\frac{1}{2}\rho U_\infty^2 c}, \tag{3.4}$$

and relates to the effective stiffness introduced in equation 3.2 as $Ae = \Pi_1^3$ [139, 141].
The membrane shape characterisation by [127] was extended by Waldman and Breuer [141] who included the Young-Laplace equation for non-linear deformation of the membrane at low angles of attack, assumed a uniform pressure distribution, and incorporated a potential flow model to estimate the aerodynamic loading from the thin membrane airfoil. Their model shows a remarkable agreement with experimental data of the maximum camber of membranes for different material properties, fluid characteristics, and wing angles of attack expressed in terms of the aeroelastic parameters Ae and We. By coupling thin airfoil theory with membrane equations, a new analytical model was derived by Alon Tzezana and Breuer [142] to predict the membrane shape even more accurately than [141] for steady and unsteady membrane wings under various conditions.
The deformation of flexible membrane aerofoils typically manifests in the form of a positive wing camber. The positive camber leads to an increase in the lift coefficient, a decrease in the drag coefficient, and an increase in the lift-to-drag ratio for flexible wings compared to their rigid counterparts especially at angles of attack close to the stall angle of the wing [127, 143]. The curvature of the leading edge of a cambered membrane allows the flow to stay attached at higher angles of attack [144]. The rigid wings at the same angles of attack have larger flow separation regions and are subjected to large-scale vortex shedding accompanied by a loss in lift and an increase in drag [145, 146]. The fluid-structure interaction between the shed vortices and the membrane leads to a reduction in the separation area and lower surface pressure on the wing below the separation area. These changes in flow topology lead to an increase in lift at moderate angles of attack ($\alpha = 10° - 25°$), but the unsteady membrane fluctuations cause a loss in lift-to-drag ratio at the lower angles of attack [147–149]. The dominant membrane vibrations are coupled with the shedding frequency of large-scale flow structures [150]. Membrane wings with lower aspect ratios (≈ 1) experience higher frequency vibrations and higher vibration mode shapes due to an increase in downwash and a delay of vortex shedding to higher angles of attack [132]. The average membrane shape is not very sensitive to changes in angle of attack [145].
In many technical application, the wing kinematics or the flow around flexible wings is highly unsteady and vortex dominated, which further complicates the fluid-structure interactions. Due to unsteady flow conditions and wing kinematics, flapping wings are subject to highly unsteady aerodynamic loadings within each wing stroke [72] and the flow development is governed by the formation and shedding of large-scale coherent leading edge vortices [2, 151, 152]. The large inertial force variations on the wing give rise to unsteady and non-linear wing deformations linking the analysis of fluid and structural dynamics on the flexible wings inevitably together. To explore the shape and force response of membrane wings subjected to an unsteady flow or unsteady wing kinematics, several experimental [153] and numerical [128, 154–156] studies have been conducted in the recent past. Membrane wings have also been

applied and tested in novel flapping wing micro aerial vehicle [125, 133, 157] and flapping wing energy harvester designs [158].
Similar to the steady response, pitching membrane wings experience reduced and delayed flow separation [153, 154, 158]. The flow on the membrane wings remains attached at higher angles of attack and reattaches earlier when pitching down compared to the flow on rigid wings. Analysis of the flow topology revealed that the flow field is dominated by the growth of a strong leading edge vortex which eventually lifts off of the wing for rigid flapping wings. The leading edge vortex stays bound to the wing and spreads over the entire chord when a highly cambering membrane wing is used [154, 158]. This leads to enhanced force production on the membrane wings compared to the rigid wings. The thrust and propulsion efficiency of sinusoidally heaving and flapping membranes was numerically investigated by Jaworski and Gordnier [128, 155] with a high-order Navier-Stokes solver coupled to a non-linear membrane structural model. The maximum performance is achieved for specific sets of membrane pre-strain ϵ_0 and elastic modulus E. The formation and shedding of a large-scale leading edge vortex every half-cycle interact advantageously with the local membrane camber to enhance the propulsive force under the thrust optimal conditions. At efficiency optimal aeroelastic conditions, the vortex shedding reduces the magnitude of the unsteady lift and minimises the pressure drag and required power to perform the flapping motion [155]. The lift and thrust production of a tethered flapping wing vehicle with different membrane flexibilities in forward flight was investigated experimentally by Hu et al. [157]. The rigid wings generate more lift at higher advance ratios $J > 0.6$ ($J = U_\infty/(2fA)$). At lower advance ratios $J < 0.6$, which corresponds to increased flapping frequencies f, the flexible latex wings produce higher lift. The flexible wings produce more thrust than the rigid wings across all frequencies.
These examples reveal a clear potential for flexible membrane wings to out-perform their rigid counterparts but they also indicate that the improvements are not persistent over the entire input parameter space [156]. Systematic investigation on the influence of unsteady fluid-structure interactions on the aerodynamic performance of flapping membrane wings for a large range of flapping motions and membrane properties is highly desirable to provide further guidance to the design of human-engineered flexible wing fliers [159].
Here, we present a novel bio-inspired membrane wing design with self-cambering and flow alignment capabilities to systematically study fluid-structure interactions related to passively deformable flapping wings. We experimentally characterise the force response of membrane wings over a large range of flapping kinematics and wing material properties on a robotic flapping wing mechanism. Additional deformation measurements are conducted to capture the membrane shape throughout the full flapping wing cycle. We demonstrate that the connection between membrane shape and aerodynamic force production can be explained and scaled by two non-dimensional numbers, the aeroelastic number *Ae* and the Weber number *We*. A unique combination of aeroelastic properties and angle of attack is found to achieve either highest lift or most efficient hovering flight. Finally, the implications of our findings for the design of micro air vehicles using membrane wings are discussed.

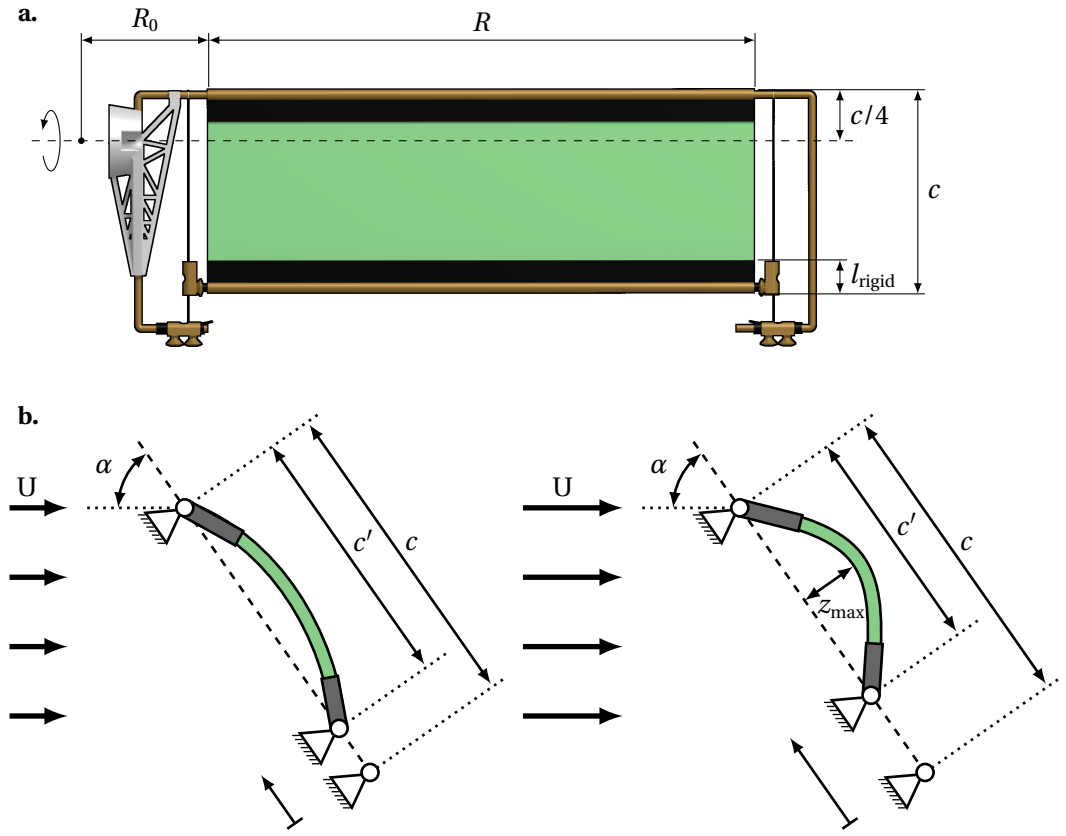

Figure 3.1 – a. Detailed drawing of the novel membrane wing design. b. Side view of the wing during loading indicating the passive deformation mechanism. The angle α is the wing's angle of attack relative to the stroke plane.

3.2 Methods

3.2.1 Membrane wing model

In this study, we present a novel bio-inspired membrane wing design shown in its flat and undeformed shape in fig. 3.1a. The leading and trailing edges of the wing are rigid and have brass bearings which allow the edges to rotate around their span-wise axes. The trailing edge has an additional degree of freedom as it can translate in the chord-wise direction in a frictionless manner. No pre-tension is applied to the membrane or the trailing edge sliders. Depending on the aerodynamic pressure difference between the pressure and suction side of the membrane, the wing passively cambers and the distance between the leading and trailing edge shortens (fig. 3.1b). The adaptive wing is designed to enhance the aerodynamic performance of the wing in two ways: 1) the camber of the wing grows with increasing aerodynamic pressure, and 2) the leading and trailing edges of the wing rotate and align favourably with the flow. The combined effects of these two mechanisms yield higher lift versus angle of attack slopes, higher maximum values of the lift coefficient, and delayed stall to higher angles of attack due to a reduction in the effective angle of attack at the leading edge.

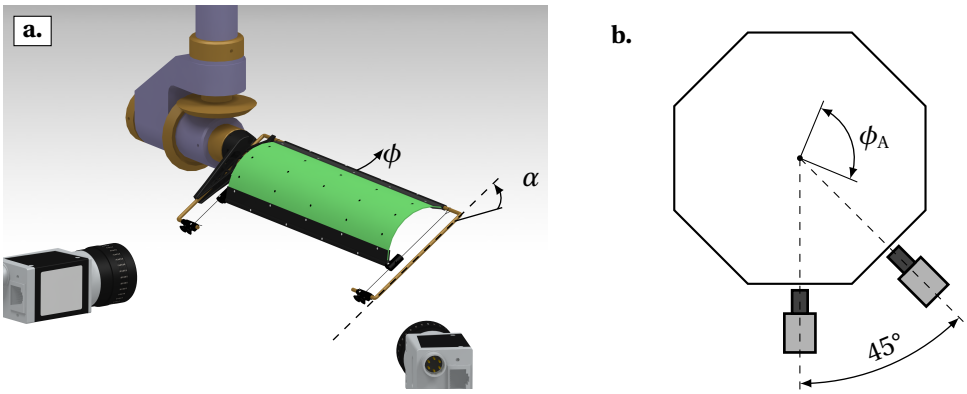

Figure 3.2 – a. Drawing of the membrane wing mounted on the flapping wing apparatus. The angle α is the wing's angle of attack relative to the stroke plane. b. Schematic visualisation of the stereo deformation measurement configuration including the camera positions relative to the peak-to-peak wing stroke amplitude indicated by ϕ_A.

The compliant membranes are made of a silicone-based vinylpolysiloxane polymer (*Zhermack Elite Double 32 shore A*) created by mixing a base and catalyst in a 1:1 ratio and centrifuging the mixture to homogenise it. The mixture is poured into a flat cast to create different silicon sheets of $h = 0.3$ mm to 1.4 mm thickness. The membrane sheets have a density of $\rho = 1160\,\mathrm{kg/m^3}$ and a Young's modulus of $E = 1.22 \pm 0.05$ kPa [160]. Rectangular wings are cut from the silicon sheets and fixed between two thin carbon fibre plates without pre-stretching the membranes (fig. 3.1a). The rigid wings serving as a reference case have a Young's modulus more than three orders of magnitude higher than the membrane wings $E = 1.33$ MPa and a thickness of $h = 1$ mm. The reinforced membranes are glued to hollow, cylindrical brass rods which serve as the outer race of the leading and trailing edge bearings. The wings are mounted on the wing frame which itself is connected to the load cell and the flapping wing mechanism [71]. The membrane wings have a chord length $c = 55$ mm in their undeformed state and a wing span $R = 150$ mm (fig. 3.1a). The root cut-out R_0 is the distance from the stroke-rotation axis to the root of the wing and is constant for all experiments. The pitch rotation axis is at a quarter chord length from the leading edge. The rigid carbon fibre plates and brass bearings make up $l_{\mathrm{rigid}} = 8.5$ mm or 0.15 c at the leading and trailing edges of the wings. A video of the membrane wings in motion and further information about the wing platform can be found in the Gallery of Fluid Motion contribution[1] [161].

3.2.2 Wing kinematics and dynamic scaling

The wing kinematics in hovering flight are described in terms of their stroke angle ϕ, the angle of attack α, and the flap or elevation angle θ (fig. 3.2a). The flap or elevation angle θ moves the wing up or down in stroke-normal direction (not displayed in fig. 3.2). In this study, the elevation angle is not considered and stays constant at $\theta = 0°$. The stroke plane coincides

[1] V0011: *Don't be rigid, be BILLY*

Table 3.1 – Experimental parameters of the flexible membrane wings in this study. The experiments are conducted in water with $\nu_{20\,^\circ\mathrm{C}} = 1.00 \times 10^{-6}\,\mathrm{m}^2/\mathrm{s}$.

Parameters		model wing
Wing chord	c	55 mm
Wing span	R	150 mm
Membrane thickness	h	0.3 mm to 1.4 mm
Wing stroke frequency	f	0.125 Hz to 0.4 Hz
Angle of attack	$\hat{\alpha}$	15° to 75°
Peak-to-peak stroke amplitude	ϕ_A	90°
Reduced frequency	k	0.42
Reynolds number	Re	2800 to 9300

with the horizontal plane in the laboratory's frame of reference and the stroke angle ϕ defines the motion of the wing in the stroke plane. The stroke angle profile varies sinusoidally from $\phi = -45°$ to $\phi = 45°$ and changes in frequency between $f = 0.125\,\mathrm{Hz}$ and $f = 0.4\,\mathrm{Hz}$ (table 3.1). The angle of attack α indicates the wing's rotation relative to the stroke plane and is defined as the angle between the chord length and the horizontal stroke plane as indicated in fig. 3.1b,c. In this study, the wing rotation is symmetric with respect to the stroke motion such that the angle of attack equals 90° at the start and end of the stroke. The angle of attack follows a trapezoidal profile and reaches minimum values ranging from $\hat{\alpha} = 15°$ to $\hat{\alpha} = 75°$. Throughout this paper, we use $\hat{\cdot}$ to denote amplitudes or minimum or maximum values of different quantities. The angle $\hat{\alpha}$ is kept constant during 68 % of the total cycle duration $T = 1/f$. During the remaining 32 % of the cycle, the wing reverses orientation between the symmetric front- and back-strokes, this is often referred to as the flip duration [16, 72].

Non-dimensional numbers characterising the flow around the hovering wing are the Reynolds number Re and the reduced frequency k. The fluid-structure interactions of the compliant membranes are characterised by the Weber number We and the aeroelastic number Ae defined in equations 3.3 and 3.4 [127, 141].

The Reynolds number Re defines the ratio between inertial and viscous forces as a measure for the emergence of flow structures at different length and time scales. In hovering flight, the Reynolds number can be calculated as

$$Re = \frac{\overline{\mathrm{U}}c}{\nu} = \frac{2\phi_\mathrm{A} f c R_2}{\nu} \quad , \tag{3.5}$$

where ν denotes the kinematic viscosity of the fluid and $\overline{\mathrm{U}} = 2\phi_\mathrm{A} f R_2$ is the stroke-average wing velocity at the radius of second moment of area R_2 [71, 72, 88]. The radius of second moment of area is the span-wise position where the sum of all forces apply and is $R_2 = \sqrt{\int_0^R (R_0 + r)^2 dr / R}$ for a rectangular wing planform [71]. The Reynolds number for all presented experiments in table 3.1 varies from $Re = 2800$ to 9300 which is a range where larger flying insects like the Hawkmoth (*Manduca sexta*), small birds like the Rufous Hummingbird (*Selasphorus rufus*), and several bat species like the Pallas's long-tongued bat (*Glossophaga soricina*) take

flight [7, 27].
The reduced frequency k compares the spatial wavelength of the flow disturbance to the chord length c and is a metric for the unsteadiness of the flow:

$$k = \frac{\pi c}{2\phi_A R_2} \quad . \tag{3.6}$$

Here, $\phi_A = 90°$ is the peak-to-peak stroke amplitude. The reduced frequency of all our experiments is $k = 0.42$ which is similar to many hovering flapping wing fliers in nature [27] and is considered to give raise to highly unsteady aerodynamics.

3.2.3 Flapping wing platform

The aerodynamic performances of the different membrane wings and the rigid reference case are evaluated experimentally with a robotic flapping wing device. The experiments are conducted in an octagonal tank with an outer diameter of 0.75 m filled with water at a temperature of 20 °C. The mechanism is controlled by two servo motors (Maxon motors, type RE35, 90 W, 100 N mm torque, Switzerland) which guide the stroke and pitch axis of the system. The motors are equipped with planetary gear-heads of 35 : 1 and 19 : 1 reduction for stroke and pitch respectively and are controlled using a motion controller (DMC-4040, Galil Motion Control, USA). The experimental flapping wing apparatus is designed to be highly repeatable and robust over a large number of experiments. The system allows for complex time-varying kinematics to be executed on both motors and initial tests on all frequencies f and amplitudes $\hat{\alpha}$ show a maximum error of $< 0.1°$ between the motor control signal and the motor response recorded by the encoder throughout the entire stroke.
The aerodynamic loads on the wing are measured using a six-axis IP68 force-torque transducer (Nano17, ATI Industrial Automation, USA) mounted at the wing root with a resolution of 3.13 mN for the force and 0.0156 N mm for torque measurements. The force signals from the load cell are recorded at a sampling frequency of 1000 Hz with a data acquisition module (NI-9220, National Instruments, USA). The instantaneous lift L, drag D and pitch torque T_p are directly retrieved from the load transducer. Here, the lift force L is considered to be the component of the total force vector oriented upwards, perpendicular to the horizontal stroke plane. The drag D is the force component in the stroke plane. The drag component is considered positive when it acts in the direction of the instantaneous velocity U of the flow experienced by wing during its stroke motion (fig. 3.1b and c). The aerodynamic power P is determined as the sum of pitch power P_p and stroke power P_s. The power expended to rotate the wing around its pitch axis with an angular velocity $-\dot{\alpha}$ is determined by $P_p = -T_p\dot{\alpha}$. Analogously, the power required to rotate the wing around its stroke axis is found with the stroke torque T_s and the stroke velocity $\dot{\phi}$ according to $P_s = T_s\dot{\phi}$. We cannot measure the stroke torque directly but instead determine it from the drag force D across the span $T_s = \int_R D(r)\,r\,dr$ [72]. The stroke torque is calculated as $T_s = DR_d$ and the radial position $R_d = \frac{3}{4}\frac{(R_0+R)^4 - R_0^4}{(R_0+R)^3 - R_0^3}$ where the sum of the drag force applies assuming a uniform drag coefficient distribution across the span [71].

Forces and torques are recorded over 16 consecutive cycles. The first 5 cycles are discarded to account for transient effects. The force and torque measurements are averaged over the remaining 11 cycles to obtain phase-averaged temporal evolutions of the results within the flapping period T and to determine the overall mean values of the aerodynamic coefficients. A minimum tip clearance of $3.5c$ is found for a tip-to-tip stroke-amplitude of $\phi_A = 90°$ which has been shown sufficient to avoid wall effects in flapping wing experiments [16, 92]. Initial force measurements at different distances from the wall verify that for the selected stroke amplitude and frequencies no changes in the stroke-average forces are identified for wing tip to wall distances $> 3c$. Initial experiments collecting data for 64 cycles demonstrate that there are some force variations due to recirculation of the tank but these only take effect after the first 16 cycles that are considered here. The influence of the large-scale recirculation in the tank are below 2 % compared to the mean force coefficients presented in this study (see A.1 for more details).
For high-frequency flapping wing flight in air, the wing inertial forces can be as strong as the aerodynamic pressure forces [154]. We quantified the effect of the wing inertia on the total forces by conducting additional experiments in air (A.2). Here, the aerodynamic forces become negligible and the inertial forces dominate the force measurements. The average lift and drag coefficients measured in air are largest for the high frequency cases but remain at least one order of magnitude lower than the results measured in water. For low flapping frequencies the dimensional inertial lift and drag are even lower and drop below the load cell resolution (3.13 mN). The inertial forces are therefore deemed negligible in this study.

3.2.4 Stereo photogrammetry

In this work, we also perform stereo deformation measurements of the flexible wing platform to quantify the membrane shape and its influence on the aerodynamic forces. Deformation and load measurements are conducted simultaneously for selected experimental conditions to allow for direct comparison of deformation and aerodynamic force response. Two CCD cameras (*pco.pixelfly usb*, ILA_5150 GmbH/PCO AG, Germany) at a 45° stereo angle and equipped with 12 mm focal length lenses are used to perform marker tracking on the membrane wing throughout the entire flapping wing cycle (fig. 3.2b). With a camera resolution of 1392 px × 1040 px, the deformation measurements have a spatial resolution between 0.13 mm/px, when the wing is closest to the cameras, and 0.23 mm/px, when the wing is farthest away from the cameras. We record stereo images over 20 cycles. The first 5 cycles are discarded to remove transient effects. The deformation measurements of the remaining 15 cycles are phase-averaged over one half-cycle, using the symmetry between front- and back-stroke of the flapping motion [71]. The images are recorded at an acquisition frequency of 6.17 Hz uncorrelated to the flapping frequency f. In consecutive cycles the images correspond to different phase-times t/T within one full cycle T. After sorting the frames by their relative phase-time we achieve an increased image acquisition rate of 186 Hz per half-cycle or between 465 and 1488 times the flapping frequency f.
The membrane is covered with black markers and the carbon fibre and structural parts with

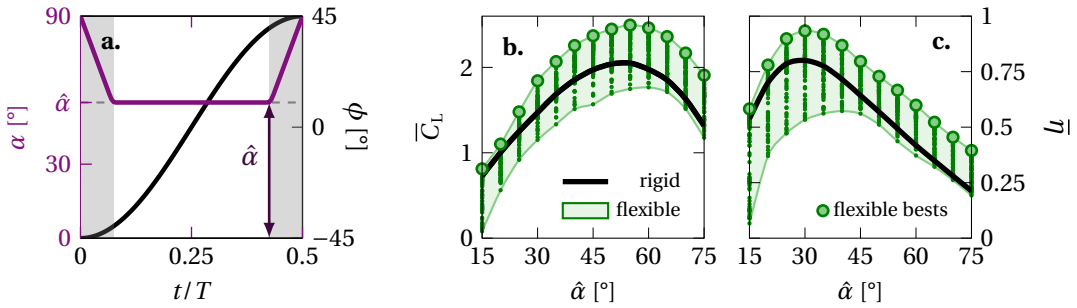

Figure 3.3 – a. Temporal variation of the angle of attack α and stroke angle ϕ over one half-cycle, b. stroke-average lift coefficient as a function of the angle of attack, and c. hovering efficiency as a function of the angle of attack. The shaded envelopes in b. and c. cover all conducted experiments.

white markers to ensure high contrast (fig. 3.2a). The markers are tracked using the software tool *XMALab*, an open-source software for marker-based X-ray reconstruction of moving morphologies [162]. The stereo camera configuration is calibrated using a chequerboard recorded at different positions and rotation angles for both cameras. The calibration procedure determines all camera intrinsic parameters, calibration coefficients and the image distortion matrix. The markers are tracked at each time step in the undistorted stereo images and their position in three-dimensional space reconstructed using linear triangulation [163]. The orientation and position of the rigid parts of the wing platform are determined through rigid body transformation. Finally, we determine the membrane shape with a two-dimensional polynomial which fits best the membrane markers and the angle between the membrane and the rigid edges of the wing in a least-square sense.

3.3 Results

The aerodynamic performance of the new adaptive membrane wing is evaluated in terms of the stroke-average lift coefficient $\overline{C}_L$ and its hovering efficiency $\overline{\eta}$ [71, 86]:

$$C_L = \frac{L}{\frac{1}{2}\rho R c \overline{U}^2}, \quad C_P = \frac{P}{\frac{1}{2}\rho R c \overline{U}^3}, \quad \overline{\eta} = \frac{\overline{C}_L}{\overline{C}_P} \quad , \tag{3.7}$$

where L and P are the dimensional lift and power respectively. Here, $\bar{\cdot}$ denotes stroke-average quantities and $\overline{U} = 2\phi f R_2$ is the stroke-average wing velocity computed at the radius of the second moment of area R_2. The average lift coefficient determines how much weight the flapping wing system can support or how fast it can climb in altitude. The hovering efficiency limits the total flight time of the vehicle.

3.3.1 Overview of the phase-average performance of the membrane and rigid wings

The flapping wing kinematics in all experiments are defined by the stroke and pitch angle profile presented in fig. 3.3a. Here, only the first half of the cycle is presented as the front- and back-strokes of the flapping wing motion are symmetric. At the beginning and end of each half-cycle the wing rotates to keep the leading edge ahead of the trailing edge. The duration of the wing rotation is indicated by the grey area in fig. 3.3a. During the majority of the cycle, the angle of attack remains at a constant value of $\hat{\alpha}$. For brevity, we will refer to the constant minimum angle of attack during the stroke motion simply as the angle of attack. The system's base frequency f and the angle of attack $\hat{\alpha}$ are varied over a wide range shown in table 3.1 to characterise the aerodynamic performance of the different membrane wings in comparison to rigid reference cases.
The stroke-average lift coefficient $\overline{C}_\mathrm{L}$ and hovering efficiency $\overline{\eta}$ for all tested flapping frequencies f, wing thicknesses h, and angles of attack $\hat{\alpha}$ are presented in fig. 3.3b and c. The black curve connects the results for the rigid reference case averaged over all stroke frequencies f. As the rigid wings do not deform, low variance in $\overline{C}_\mathrm{L}$ and $\overline{\eta}$ is observed for each angle of attack $\hat{\alpha}$ compared to the membrane wings. The results of the best performing membrane wings are highlighted by the large green markers. The small markers indicate individual test cases. In general, the membrane wings reach maximum stroke-average lift $\overline{C}_\mathrm{L}$ and efficiency $\overline{\eta}$ values in a range around the values attained by the rigid reference cases for the same angle attack $\hat{\alpha}$. By varying the thickness of the membranes, we cover a relevant parameter range in terms of membrane stiffness. Our set of tested membrane wings include membranes that perform better and some that perform worse than their rigid counterparts. For the lowest angle of attack $\hat{\alpha} = 15°$, all membrane wings tested at best match the performance of the rigid wing. For the highest angle of attack $\hat{\alpha} = 75°$, all membrane wings perform equally well or better than the rigid wing.
The highest stroke-average lift is found at $\hat{\alpha} = 55°$ with $\overline{C}_{\mathrm{L,max}} = 2.43$ for the membrane wings and at $\hat{\alpha} = 50°$ with $\overline{C}_{\mathrm{L,max}} = 2.06$ for the rigid wing. The variance in aerodynamic performance of the membrane at each angle of attack $\hat{\alpha}$ in fig. 3.3a and b is due to the deformation of the membrane which depends on the ratio between the dynamic pressure on the wing as a function of the flapping frequency f and the rigidity or bending stiffness of the membrane which varies with membrane thickness h. The aeroelastic number Ae (equation 3.4) represents the ratio between membrane compliance and the dynamic pressure and is used to further characterise the influence of the fluid-membrane interaction on the aerodynamic performance of the membrane wings. Note that no additional pre-tension is applied to the membrane or the trailing edge sliders that could influence the effective stiffness of the system.

3.3.2 Lift enhancement through deformation

The lift produced in hovering flight is presented in fig. 3.4 as a function of the aeroelastic number Ae (equation 3.4) for all conducted experiments. Overall, the stroke-average lift of the membrane wings increases with increasing angle of attack for $\hat{\alpha} \leq 50°$ and decreases for

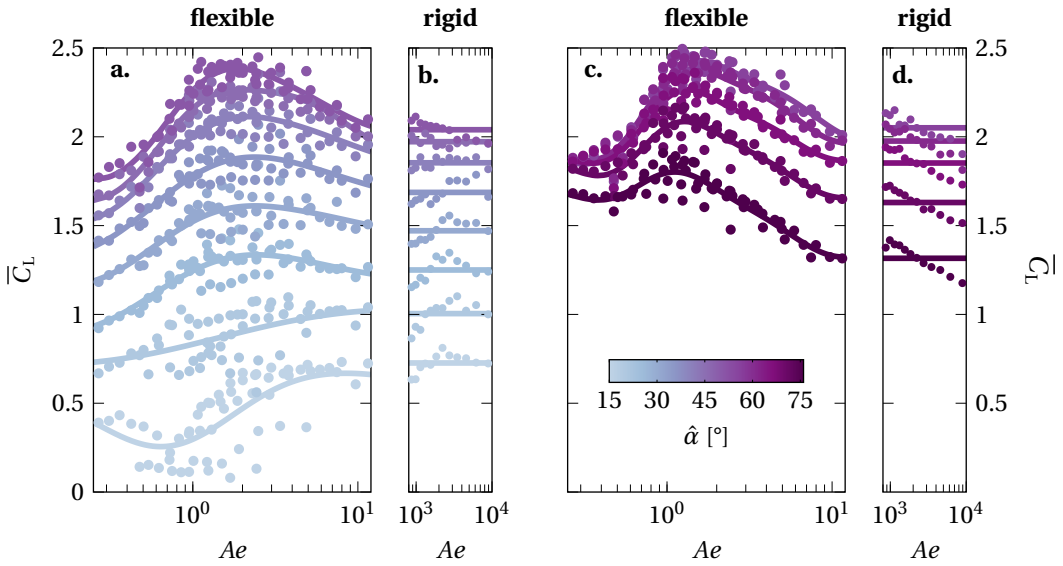

Figure 3.4 – Stroke-average lift coefficient $\overline{C}_L$ for different angles of attack $\hat{\alpha}$ as a function of the aeroelastic number *Ae*. Results for angles of attack ranging from $\hat{\alpha} = 15°$ to 50° are presented in a and b. Results for higher angles of attack ranging from $\hat{\alpha} = 55°$ to 75° are presented in c and d. Each dot represents an individual experiment. The solid lines indicate the average variation of $\overline{C}_L$ as a function of *Ae* for each angle of attack.

$\hat{\alpha} \geq 55°$. For visual clarity, the results are split in different panels in fig. 3.4. The two panels to the left (fig. 3.4a and b) include all experiments with angles of attack ranging from $\hat{\alpha} = 15°$ to 50° for the flexible membrane wings ($Ae = 0.25$ to 12 in fig. 3.4a) and the rigid wings ($Ae = 870$ to 8900 in fig. 3.4b). The markers represent individual experiments. The solid lines indicate the average variation of $\overline{C}_L$ as a function of *Ae* and are obtained by training a Gaussian process regression model at each angle of attack $\hat{\alpha}$ and predicting the response over the *Ae* range of the experiments. The stroke-average lift coefficient $\overline{C}_L$ for $20° \leq \hat{\alpha} \leq 50°$ increases with increasing *Ae* until it reaches a maximum between $Ae = 1$ and $Ae = 5$. The maximum stroke-average lift coefficient $\overline{C}_L$ is reached at slightly lower values of the aeroelastic number at higher angles of attack. For $Ae > 5$ and $\hat{\alpha} > 20°$, the stroke-average lift decreases with increasing *Ae* and asymptotically converges to the average lift produced by the rigid wings (fig. 3.4b).

At lower angles of attack $\hat{\alpha} \leq 20°$, the maximum stroke-average lift values are obtained for the stiff wings and the flexible wings with the highest values of *Ae*. For the lowest angle of attack $\hat{\alpha} = 15°$, the stroke-average lift initially decreases with increasing *Ae* for $Ae < 1$ and we notice larger variations among individual experiments. Observations of the experiments showed that the cambering of the membrane wings started later into the cycle compared to higher angles of attack and that the amount of camber showed more variability between consecutive strokes. Additional experiments at the lower angles of attacks are required to determine if this effect is caused by unsteady aeroelastic effects or limitations of the experimental system. For higher angles of attack $\hat{\alpha} > 50°$, the overall stroke-average lift decreases with increasing

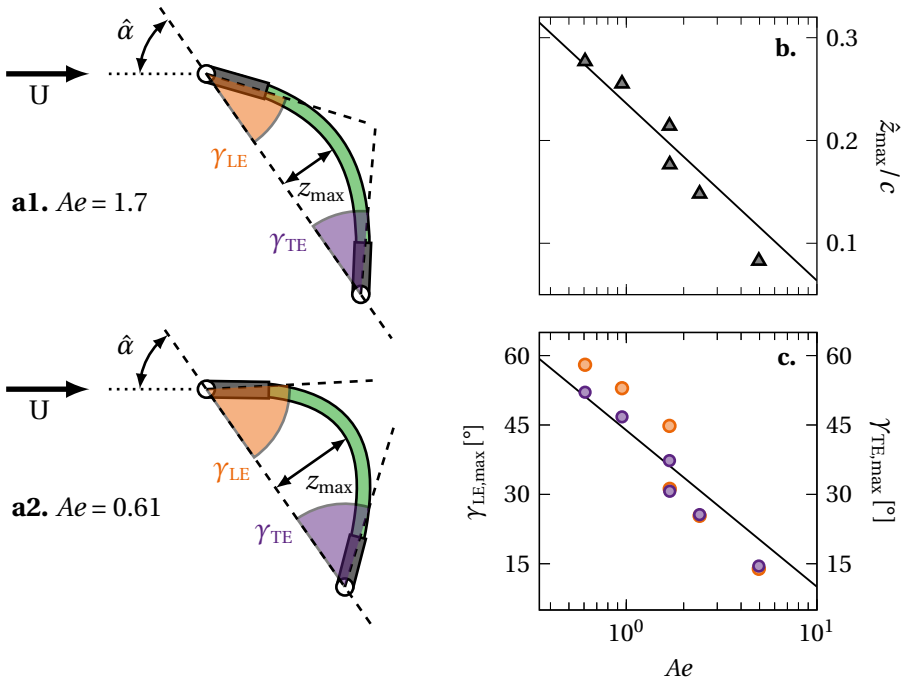

Figure 3.5 – a. Schematic of the wing deformation indicating the definition of the wing camber $\hat{z}$, the leading and trailing edge rotation angles γ_{LE} and γ_{TE} for $Ae = 1.7$ (a1) and $Ae = 0.61$ (a2). b. Stroke-maximum camber $\hat{z}_{max}$ as a function of the aeroelastic number for $\hat{\alpha} = 55°$. c. Stroke-maximum leading and trailing edge rotation angles $\gamma_{LE,max}$ and $\gamma_{TE,max}$ as a function of the aeroelastic number for $\hat{\alpha} = 55°$.

angles of attack (fig. 3.4c and d). At these high angles of attack, the flexible wings attain values of the stroke-average lift above those attained by their solid counterparts for all values of the aeroelastic number. The aeroelastic number at which the overall maximum stroke-average lift coefficient is reached remains around $Ae \approx 1$ and continues to decreases with increasing angles of attack.

To explain the differences observed among the stroke-average lift and efficiency measured of the flapping membrane and rigid wings, we have extracted the membrane shape deformation for selected wings. The membrane wings passively deform when flapping. The main characteristics of the passive deformation are the passive cambering of the membrane, the rotation of the leading edge and the rotation of the trailing edge (fig. 3.5a). The stroke-maximum camber $\hat{z}_{max}$ and the stroke-maximum rotation angles of the leading and trailing edges with respect to the chord, denoted by $\gamma_{LE,max}$ and $\gamma_{TE,max}$, respectively, are presented as a function of the aeroelastic number in fig. 3.5b-c for $\hat{\alpha} = 55°$. Positive angles of γ are associated with a positive camber $\hat{z}$ following the convention indicated in fig. 3.5a. The stroke-maximum values reveal a clear variation with the aeroelastic number which relates the stiffness of the membrane and the aerodynamic pressure. At low values of the aeroelastic number, a relatively smaller amount of aerodynamic pressure is required to deform the wing. This results in large values of the stroke-maximum camber and the stroke-maximum leading and trailing edge rotation

angles. With increasing values of the aeroelastic number, the effective stiffness of the wing increases and the maximum camber and maximum leading and trailing edge rotation angles decrease towards zero for values of $Ae \gg 1$.
The decrease of the stroke-maximum camber $\hat{z}_{\max}$ with increasing aeroelastic number follows an exponential decay as evidenced by the linear evolution in the semi-log space. Exponential fits in form of straight lines are included in the semi-logarithmic plots as a reference. The decrease of the leading and trailing edge rotation angles also appear close to linear in the semi-log space at first glance, but a closer look reveals a more complicated variation. The leading and trailing edge rotation angles are identical for $Ae \geq 1.68$, indicating symmetric cambering at higher values of the aeroelastic number. For lower values of the aeroelastic number and thus reduced effective membrane stiffness, the fluid-membrane interaction leads to asymmetric bending of the membrane and a shift of the maximum camber position towards the leading edge where the rotation angle is largest. The asymmetric bending is the result of a more complex fluid structure interaction between the aerodynamic pressure due to the stroke motion and a prominent leading edge vortex. The change between symmetric and asymmetric camber lines occurs between $Ae = 1$ and $Ae = 2$ which corresponds to the range of aeroelastic numbers where we observe a maximum in the stroke-average lift coefficient for this angle of attack ($\hat{\alpha} = 55°$). The lift-optimal stroke-maximum camber in this case is $\hat{z}_{\max} \approx 0.2c$. An increase in the maximum camber $\hat{z}_{\max}/c$ beyond 0.2 results in a decrease of the stroke-average lift. To better understand why, we will now look at the orientation of the leading and trailing edges with respect to the stroke plane.

The passive cambering of the membrane wings and the rotation of the leading and trailing edges lead to a decrease in the leading edge angle of attack with respect to the stroke plane and a decrease in the angle between the trailing edge and the stroke plane as defined in fig. 3.6a. The stroke-minimum leading and trailing edge angles $\alpha_{\text{LE,min}}$ and $\alpha_{\text{TE,max}}$ are presented as a function of the aeroelastic number in fig. 3.6b,c for $\hat{\alpha} = 55°$. As expected based on the measured decay of the maximum camber, the minimum leading and trailing edge angles both increase with increasing aeroelastic number in an approximately exponential manner. For the higher values of the aeroelastic number, where the deformation is symmetric, the angles lie above the fitted approximations. For the lower values of the aeroelastic number, where the deformation is no longer symmetric, we find angles below the fitted approximation.
The maximum stroke-average lift coefficient and the onset of asymmetric membrane deformation occur at the same aeroelastic number of $Ae \approx 1.7$. The measured membrane shape at these lift-optimal aeroelastic conditions is shown in fig. 3.6a1. The rotation of the leading edge has reduced the effective angle of attack at the leading edge to a more moderate angle and the trailing edge is oriented vertically with respect to the stroke plane. The reduced leading edge angle of attack allows the flow to accelerate smoothly around the leading edge and the trailing edge orientation directs the flow straight downwards in the near wake increasing the vertically upward force on the wing itself.
By decreasing the aeroelastic number Ae for the same angle of attack $\hat{\alpha}$, the deformation of the membrane increases but the stroke-average lift decreases. This is attributed to the trailing

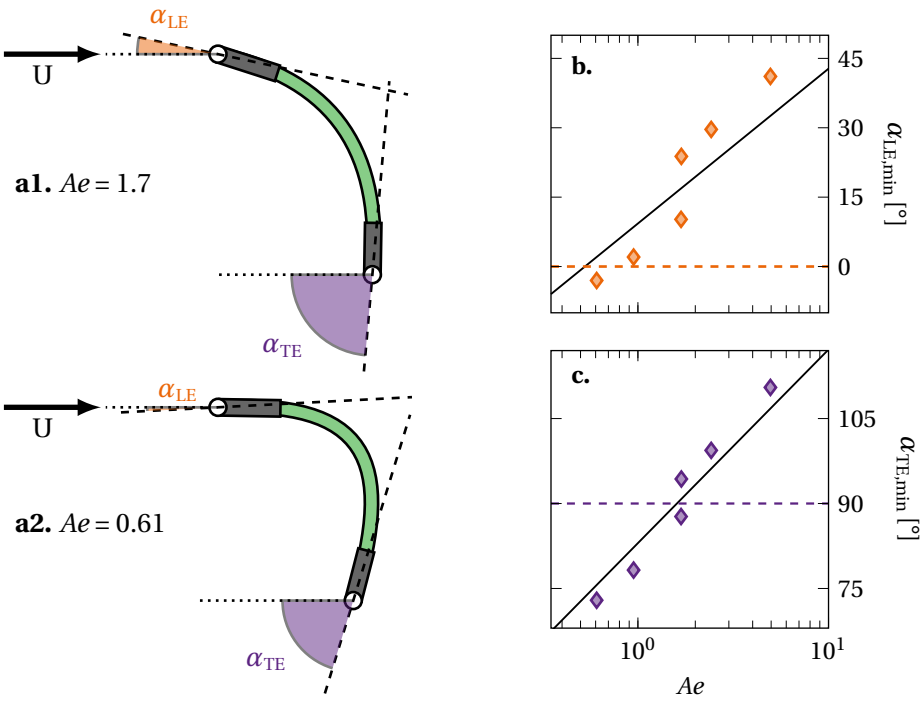

Figure 3.6 – a. Schematic of the wing deformation indicating the definition of the leading and trailing edge angles with respect to the stroke plane, α_{LE} and α_{TE} for $Ae = 1.7$ (a1) and $Ae = 0.61$ (a2). b. Stroke-minimum leading edge angle $\alpha_{LE,min}$ as a function of the aeroelastic number for $\hat{\alpha} = 55°$. c. Stroke-minimum trailing edge angle $\alpha_{TE,min}$ as a function of the aeroelastic number for $\hat{\alpha} = 55°$.

edge angle decreasing below $\alpha_{\mathrm{TE,min}} < 90°$ (dashed line in fig. 3.6c) and the leading edge angle decreases to values below the static stall angle of a flat plate which delays flow separation and the formation of a strong leading edge vortex. The stroke-maximum membrane deformation at $Ae = 0.61$ is presented in fig. 3.6a2. At this low value of the aeroelastic number, the chord-normalised camber becomes as high as 30 % and the leading edge angle even becomes negative which causes the lift coefficient to drop below the values of their stiff counterparts. The stroke-average lift of our flapping wings is increased when they are deformed up to a point when they over-camber. Here, we consider a membrane to be over-cambered when its minimum leading edge angle $\alpha_{\mathrm{LE,min}}$ becomes negative or its minimum trailing edge angle $\alpha_{\mathrm{TE,min}}$ rotates below 90° as marked by the dashed lines in fig. 3.6b,c. The performance of over-cambering wings rapidly falls with decreasing aeroelastic number.

3.3.3 Temporal evolution the wing deformation and aerodynamic performance

We further explore the relationship between the aeroelastic properties and their contribution to the force production on the wing by analysing the temporal evolution of the lift and power coefficients for the highest lift producing angle of attack $\hat{\alpha} = 55°$ in fig. 3.7c,d. The colours indicate the range of aeroelastic numbers from $Ae = 0.61$ to 4.96. Here, all quantities are phase-averaged over one half-cycle ($t/T = 0$ to 0.5) exploiting the symmetry between the front- and back-stroke of the hovering cycle [71]. The results of the rigid wing are presented by the black dashed line. The phase-averaged temporal evolutions of the lift and power were filtered using a 5th-order Butterworth filter with no phase delay at a cut-off frequency 12 times higher than the flapping frequency f.

The overall temporal evolution of the lift and the power coefficient for all wings is dominated by the evolution of the stroke velocity $\dot{\phi}$ (fig. 3.7b). Lift and power increase or decrease with increasing or decreasing stroke velocity and reach a maximum value around $t/T = 0.25$. Interesting differences are observed when the aeroelastic number varies. The main differences in the lift coefficient evolution occur towards the end of the first half and during the second half of the stroke ($t/T > 0.2$) (fig. 3.7c). The flexible wings all reach a higher maximum lift coefficient than their rigid counterpart. The highest value of C_{L} is measured for an aeroelastic number of $Ae = 1.64$. The higher lift values for the flexible wings are maintained during the second half of the stroke. The competition for the top rankings among different aeroelastic numbers is decided in the second half of the stroke. This holds true for all angles of attack as evidenced by the contour plots of the average lift coefficient across the first and second half of the stroke (fig. 3.7e1,e2). The average lift coefficient is consistently lower during the first half of the stroke than during the second half for all values of the aeroelastic number and all angles of attack. The average lift coefficient during the first half does not vary substantially with the aeroelastic number for $\hat{\alpha} < 45°$. For $45° < \hat{\alpha} < 70°$, the average lift increases with increasing aeroelastic number for $Ae < 1$ and reaches a plateau for $Ae > 1$. The average lift coefficient during the second half shows a clear global maximum for $\hat{\alpha} \approx 50°$ and $Ae \approx 1.7$. This corresponds to conditions that yield the overall best performance.

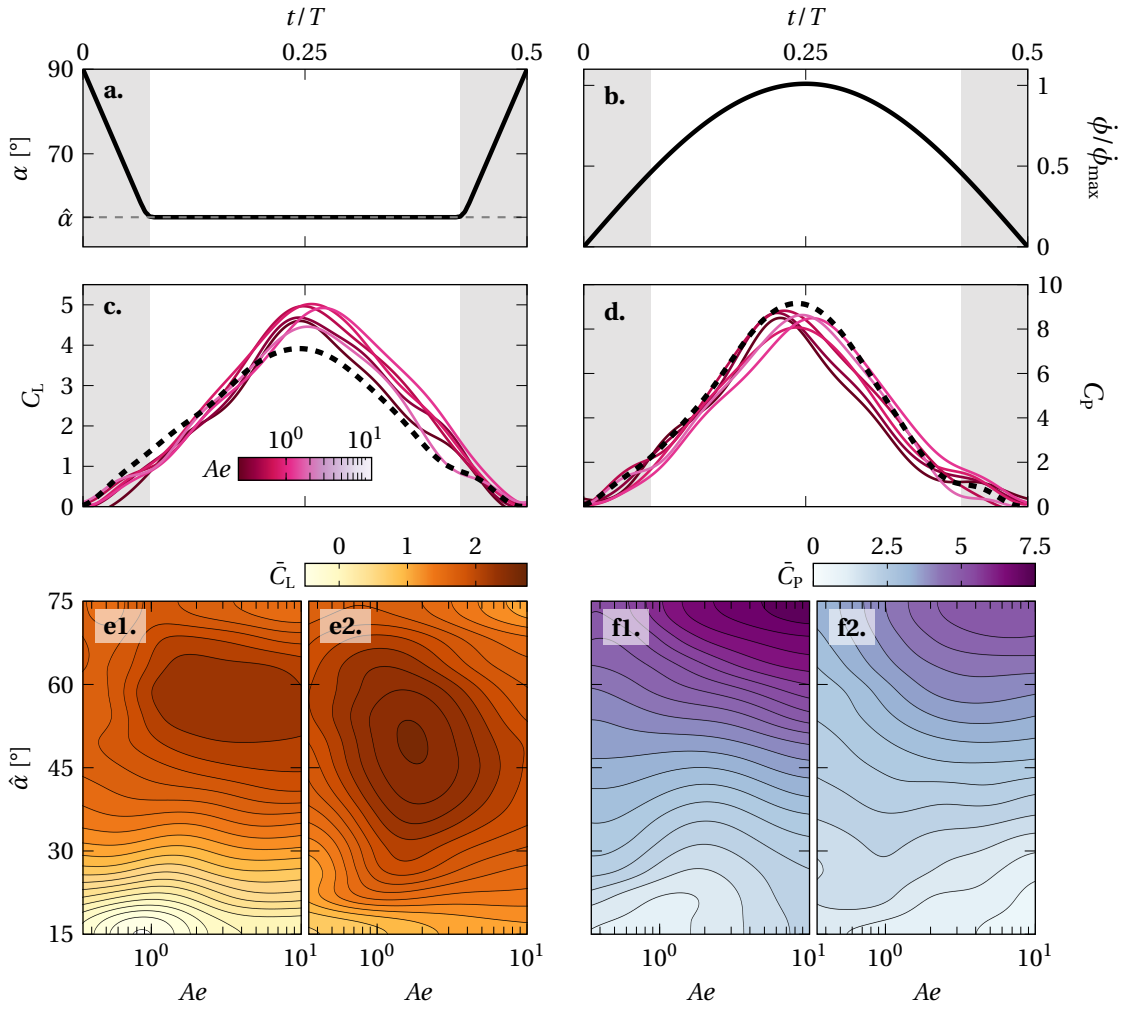

Figure 3.7 – Temporal evolution of the flapping kinematics in terms of the angle of attack (α) (a.) and stroke rate ($\dot{\phi}$) (b.), and the lift (c.) and power coefficient (d.) for $\hat{\alpha} = 55°$. As the motion is symmetric, only one half cycle $0 \leq t/T \leq 0.5$ is shown. The dashed black lines represents the rigid reference case with no deformation. The grey shaded areas indicate the duration of the wing rotation between strokes. Contour plots showing the averaged lift/power coefficient generated during the first half of the stroke (e1./f1.) and during the second half of the stroke (e2./f2.) for all variations of the angle of attack and aeroelastic number tested.

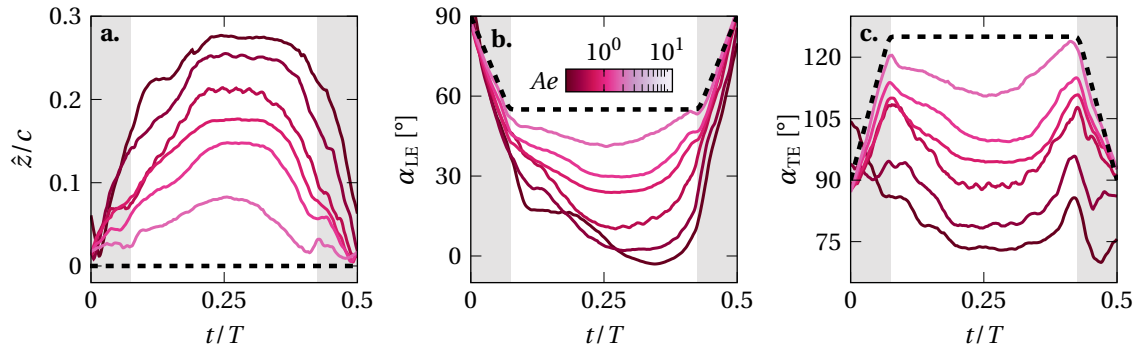

Figure 3.8 – Temporal evolution of the wing deformation in terms of the wing camber ($\hat{z}$) and the leading and trailing edge angles with respect to the stroke plane (α_{LE} and α_{TE}) for $\hat{\alpha} = 55°$. As the motion is symmetric, only one half cycle $0 \leq t/T \leq 0.5$ is shown. The dashed black lines represents the rigid reference case with no deformation. The grey shaded areas indicate the duration of the wing rotation between strokes.

The analysis of the power coefficient C_P leads to the same conclusion that the performance difference by the deformable wings is made in the second half of the stroke (fig. 3.7d,f). All power curves follow a similar increase in power with increase in the stroke velocity in the first part of the stroke (fig. 3.7d). A maximum in C_P is reached slightly before mid-stroke. The highest peak in power belongs to the rigid wing. In the second half of the cycle, the aerodynamic power curves associated with the deformable wings remain below the rigid wing curve for most of the second part of the stroke. The least amount of power is required by the lowest value of the aeroelastic number which is the most deformable wing. The least deformable wing with the highest value of *Ae* requires approximately the same amount of power as the rigid wing. For all tested angles of attack $\hat{\alpha}$ and aeroelastic numbers, the first half of the stroke requires more power than the second (fig. 3.7f1,f2). The strongest dependence on the aeroelastic number is observed for angles $\hat{\alpha} > 45°$ in the second half of the stroke (fig. 3.7f2). Here, the power is drops significantly with decreasing values of *Ae*. At low *Ae*, the stronger cambering of the membrane leads to a decrease in the frontal area which leads to reduced drag and power coefficients.
To explain the higher aerodynamic performance at moderate *Ae* and the variations during the second half of the stroke, we analyse the temporal evolution of the passive membrane deformation characterised by the camber $\hat{z}$ and the leading and trailing edge angles α_{LE} and α_{TE} in fig. 3.8. The data is presented for the lift-optimal angle of attack $\hat{\alpha} = 55°$ over one stroke or half the flapping cycle. The results of the rigid wing are presented by the black dashed line. The line colour of the solid lines indicates the value of the aeroelastic number.
The temporal evolutions of the membrane camber $\hat{z}$ for the deformable wings roughly follow a trapezoidal shape in response to the trapezoidal variation in their geometric angle of attack α (fig. 3.8a). The camber for the lowest values of *Ae* reaches the highest camber of $\hat{z}/c = 0.28$ just before mid-stroke and keeps a steady camber over a larger portion of the second half of the stroke. We refer to the time interval during which the camber remains at its maximum value as the camber plateau time. The time at which the maximum camber is reached does not vary significantly with effective membrane stiffness expressed by the aeroelastic number.

The deformation seems to continue as long as the stroke velocity increases. Yet, the rate of change of the camber during the first part of the stroke does not vary consistently with the stroke velocity and the response strongly depends on the value of *Ae*. For the lowest values of *Ae*, we measure an immediate increase of the camber already during the rotation phase. For the higher values of *Ae*, the increase in camber becomes more prominent after the wing rotation has ended. This suggests that the rotational acceleration affects the initial response of the membrane, but we believe that it does not affect the maximum camber which was shown to scale well with the aeroelastic number (fig. 3.5a). The maximum camber decreases with increasing values of *Ae* and this holds try for any value of the camber $\hat{z}$ at all times during the stroke. The camber plateau time also reduces with increasing values of *Ae*. At the highest presented aeroelastic number, the membrane cambers up to $\hat{z}/c = 0.08$ and immediately reduces again during the second part of the stroke. A plateau of constant camber is no longer observed. The persistence of the higher camber during the second part of the stroke at lower aeroelastic numbers leads to higher lift and a reduction of the power during that time (fig. 3.7). The temporal evolution of the phase-average leading and trailing edge angles with respect to the stroke plane are presented in fig. 3.8b,c. When the membrane cambers more at lower *Ae*, the leading and trailing edges angles drop below the corresponding reference values imposed on the rigid wing. All leading edge angles of attack α_{LE} in fig. 3.8b reach a minimum angle during the wing's camber plateau time fig. 3.8a. With increasing deformation at lower *Ae*, the leading edge angle of attack minima decrease and are attained later in the second half of the stroke. At the lowest *Ae*, the leading edge angle of attack becomes negative $\alpha_{\mathrm{LE}} = -3°$ at $t/T = 0.35$ in fig. 3.8b. The excessive rotation of the leading edge due to over-cambering is accompanied by a decrease in lift coefficient C_{L} but also by reduction in power C_{P} (fig. 3.7c,d). The trailing edge angle α_{TE} evolves differently than the leading edge angle (fig. 3.8c). The trailing edge orientation appears symmetric around mid-stroke and all curves of α_{TE} follow an M-shape evolution. Two peaks emerge at the end and the start of the wing rotations. After the first peak, the trailing edge angle decreases and the trailing edge rotates in the direction of the motion. For moderate to high values of *Ae*, the angle remains constant for a part of the stroke and the duration of this constant angle phase increases again with decreasing aeroelastic number, similar to the behaviour of the camber plateau time. At lift-optimal aeroelastic conditions, the trailing edge orientation is perpendicular to the flow with $\alpha_{\mathrm{TE}} = 90°$. Further increase in the camber $\hat{z}$, by lowering *Ae*, causes the trailing edge to rotate into the flow at angles down to $\alpha_{\mathrm{TE}} = 70°$. The trailing edge rotation $\alpha_{\mathrm{TE}} < 90°$ indicates over-cambering and coincides with a decrease in lift production by the membrane wings.

3.3.4 Global optima of lift and efficiency

In the previous sections, we analysed the relationship between lift coefficient C_{L}, aeroelastic number *Ae* for the lift-optimal angle of attack $\hat{\alpha} = 55°$. In fig. 3.9, we summarise the results of the stroke-average lift coefficient $\overline{C}_{\mathrm{L}}$ and hovering efficiency $\overline{\eta}$ (equation 3.7) for the entire experimental parameter range covered in this study. The input parameter space is spanned by

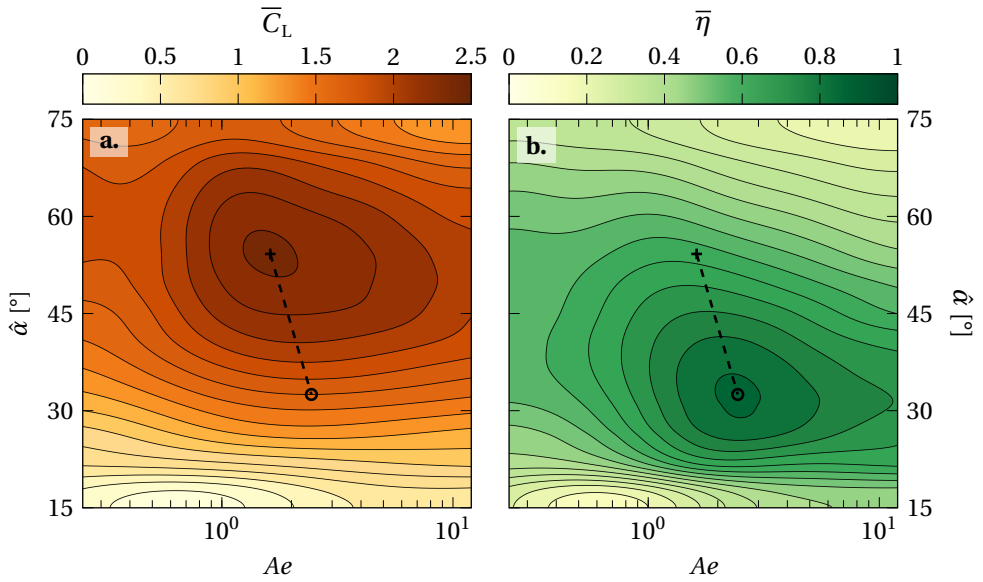

Figure 3.9 – a. Lift coefficient over aeroelastic number and angle of attack, and b. hovering efficiency over aeroelastic number and angle of attack.

the angle of attack $\hat{\alpha}$ and the aeroelastic number Ae. The two markers in the contour plots indicate the optimal-lift (×) and optimal-efficiency (∘) points which lie at different locations. The maximum lift $\overline{C}_{L,max} = 2.43$ is found at $Ae = 1.68$ and $\hat{\alpha} = 55°$ (fig. 3.9a). The most efficient hovering $\overline{\eta} = 0.858$ occurs at a higher aeroelastic number $Ae = 2.44$ and a lower angle of attack $\hat{\alpha} = 33°$ than the lift optimum (fig. 3.9b). In literature, we found an experimental study using compliant flat plate wings with a stiff leading edge that reports an enhancement of the aerodynamic performance of these flexible flapping wings in hover compared to rigid wings for a range of effective stiffness from $\Pi_1 = 0.5$ to $\Pi_1 = 10$ [164]. The maximum lift production in [164] was found at $\Pi_1 = 3.5$. We find maximum lift production at a lower value of $\Pi_1 = 1.17$ using $Ae = \Pi_1^3$. The highest efficiency for our wings occurs at $\Pi_1 = 1.34$. Both optima still fall within the range of effective stiffness values that are reported to enhance aerodynamic performance by [164]. Compared to different insect species, the optimum chord-wise effective stiffness in our study matches with the tarantula-hawk wasp (*Pepsis grossa*) which has similar aspect ratio wings than the membrane wings in our study [42, 164]. A recent study on membrane wings for energy harvesting applications discovered highest energy extraction at their lowest tested aeroelastic number $Ae = 5$ ($\Pi_1 = 1.71$) [158].

Rigid flapping wings at lower angles of attack promote the stable growth of a leading edge vortex and a lift favouring orientation of the normal force vector leading to more efficient hovering flight [71]. A shift of the most efficient hovering conditions to larger value of Ae indicates a higher relative stiffness of the membrane and lower camber. The same leading edge deflection of up to $\gamma_{LE,max} = 45°$ observed at $\hat{\alpha} = 55°$ and lift-optimal aeroelastic number $Ae = 1.68$ would lead to over-cambering and negative leading edge angles of attack α_{LE} at a geometric angle of attack $\hat{\alpha} = 33°$ of most efficient hovering.

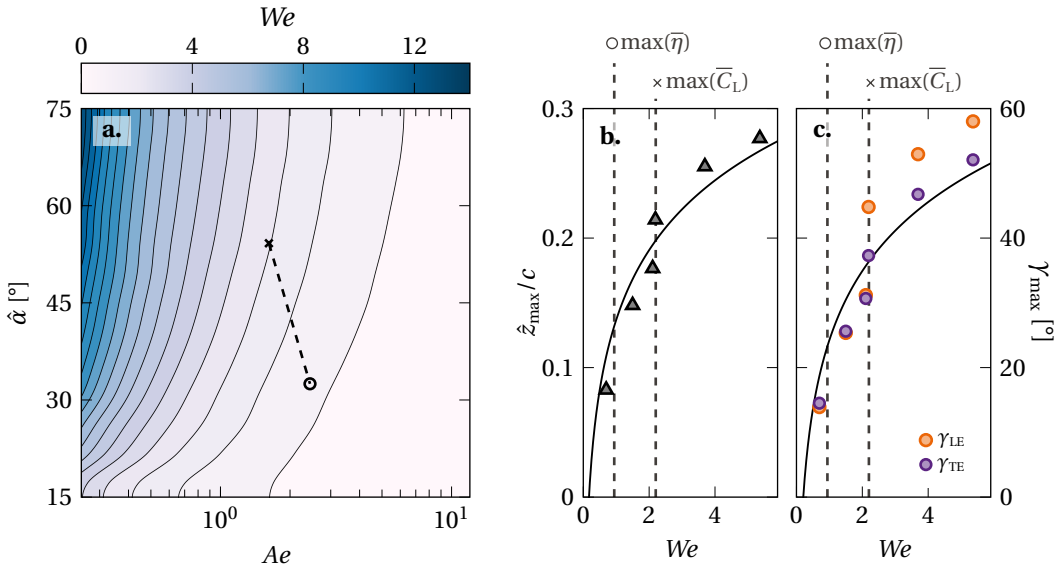

Figure 3.10 – a. Weber number over aeroelastic number and angle of attack, b. stroke-maximum camber $\hat{z}_{max}$ as a function of the Weber number for $\hat{\alpha} = 55°$, and c. stroke-maximum leading and trailing edge rotation angles $\gamma_{LE,max}$ and $\gamma_{TE,max}$ as a function of the Weber number for $\hat{\alpha} = 55°$.

To quantify the relationship between aerodynamic performance and membrane deformation over the entire experimental parameter range, a Weber number is calculated, $We = C_N/Ae = N/(EhR)$ (equation 3.3) [127, 141]. The Weber number represents the ratio between inertial forces, e.g. lift and drag on the wing, and the membrane tension. Previous work on membranes at a steady free-stream velocity and angle of attack demonstrated that the maximum membrane camber $\hat{z}_{max}$ increases with increasing Weber number We for a pre-strain parameter ϵ_0 (equation 3.3) [127, 141]. The trailing edge of the membrane wing in this study can move freely in chord-wise direction and a pre-strain of $\epsilon_0 = 0$ can be assumed. The Weber number is presented in fig. 3.10a for all our experiments in the parameter space spanned by Ae and $\hat{\alpha}$. The two markers indicate the global lift-optimum (×) and efficiency-optimum (○) found in fig. 3.9. The Weber number decreases from $We = 2.20$ to 0.94 between the lift and the efficiency optimum. With a reduction in Weber number the pressure and lift pulling on the membrane decrease relative to the stiffness of the membrane and less deformation is expected. Assuming the membrane camber is a direct function of the Weber number [127, 141], we can infer the change in maximum membrane camber $\hat{z}_{max}$ and deflection angle γ_{max} from the deformation measurements at $\hat{\alpha} = 55°$ in fig. 3.10b and c. For most efficient hovering at $We = 0.94$ the camber is predicted to drop below $\hat{z}_{max} < 0.15c$ and limiting $\gamma_{max} < 25°$ preventing over-cambering and negative angles of attack at the leading edge. The relationship between the increase in the maximum camber $\hat{z}$ and the Weber number in fig. 3.10b agrees qualitatively with experiments conducted for fixed membrane wings without pre-strain [127, 141]. Compared to the results under steady flow conditions, the Weber number in our study is one order of magnitude higher. This difference in Weber number is attributed to the change to unsteady flapping wing flight

and to a difference in the mechanism that causes the membrane deformation. In [127,141], the membrane deformation is dominated by stretching. In our study it is dominated by bending. Two distinct regions of maximum lift production and hovering efficiency are identified in the full experimental parameter range. The ability to move from high lift production to efficient hovering by modifying the angle of attack or the aeroelastic properties makes the membrane wing platform a promising model for the design of novel micro air vehicles. Many natural fliers already modify their wings' angle of attack and stiffness in flight to adjust to different flight situations, for example when performing manoeuvres or to alleviate a gust encounter. Different types of flapping wing vehicles have already incorporated angle of attack variation in their designs and progress has been made recently in developing membrane wings with variable stiffness [165, 166]. Our results show that combining both effects, variable stiffness and angle of attack variation, enhances the aerodynamic performance and has the potential of improved control capabilities of micro air vehicles.

3.4 Conclusion

We have introduced a novel bio-inspired membrane wing design for systematic investigation of the fluid-structure interactions of flapping membrane wings. The wing platform allows for passive cambering of the membrane and for the rotation of the leading and trailing edges with respect to the stroke plane. A wide range of kinematic and membrane material parameters were tested on an experimental flapping wing platform and the aerodynamic performance in terms of the stroke-average lift coefficient $\overline{C}_{\mathrm{L}}$ and hovering efficiency $\overline{\eta}$ was evaluated. Additional deformation measurements were conducted over the full stroke duration to capture the temporal evolution of the membrane camber and the orientation of the leading and trailing edges relative to the flow for selected parameter variations.

Across the entire range of angles of attack tested, we found membrane wings that can produce up to 18 % more lift and reach 16 % higher lift to power coefficient ratios than the rigid reference wing. At the lowest tested angles of attack $\hat{\alpha} < 25°$, the rigid wings perform equally well as the highest performing membrane wings. With increasing angles of attack, the rigid wings loose terrain with respect to the membrane wings. At the highest angle of attack $\hat{\alpha} = 75°$, the rigid wings have similar performance to the lowest-performing membrane wings.

We computed an aeroelastic number *Ae*, typically used for fixed wings, to characterise the balance between the membrane stiffness and the dynamic pressure on the wing and confirm that it is also suitable to characterise unsteady flapping wings. At low *Ae*, the dynamic pressure of the flow on the wing is relatively high compared to the stiffness of the membrane and we observe larger membrane deformations. With increasing *Ae*, the effective stiffness of the membrane increases and the membrane deforms less. At the highest *Ae*, the membrane behaves the same as a rigid plate. For most angles of attack, the stroke-average lift coefficient $\overline{C}_{\mathrm{L}}$ increases with increasing *Ae* until a maximum is reached at aeroelastic numbers *Ae* ranging from 1 to 2. Further increasing *Ae* beyond the lift optimal aeroelastic conditions leads to a decrease in the lift produced by the membrane wings and their $\overline{C}_{\mathrm{L}}$ values asymptotically converge to the

average lift produced by the rigid wings at the highest *Ae*.
To understand the relationship between effective membrane compliance expressed by the aeroelastic number *Ae* and the aerodynamic force production on the wing, we measured and quantified the membrane deformation throughout the entire wing stroke. The stroke-maximum camber $\hat{z}_{\max}$ grows exponentially with decreasing *Ae* for a given angle of attack. As the camber increases, the rotational angle of the leading and trailing edges increase. The stroke-average lift coefficient does not increase indefinitely with increasing stroke-maximum camber, but reaches an optimal value near $\hat{z}_{\max}/c \approx 0.2$ for $\hat{\alpha} = 55°$. The lift optimal membrane shape displays two features that enhance the lift production: moderate angles of attack at the leading edge which lead to stall delay and a vertical orientation of the trailing edge which deflects the fluid downwards and enhances the upward reaction force on the membrane. For lower *Ae*, the membrane over-cambers and the lift decreases. We identify thresholds for over-cambering when either the leading edge angle becomes negative $\alpha_{\text{LE,min}} < 0°$ or when the trailing edge angle drops below $\alpha_{\text{TE,min}} < 90°$.
The temporal evolutions of the aerodynamic forces reveal that most of the lift gain of the membrane wings relative to the rigid wings is achieved in the second half of the stroke. The power consumption in the second half of the stroke is lower across all tested angles of attack and aeroelastic numbers. The membrane camber $\hat{z}$ reaches a maximum around mid-stroke ($t/T = 0.25$), when the stroke velocity $\dot{\phi}$ is highest, and maintains the maximum camber during most of the remainder of the stroke for *Ae* equal or lower than the lift optimal *Ae*.
Across the entire parameter space considered, we identified global maxima for either maximum lift or most efficient hovering at different angles of attack $\hat{\alpha}$ and aeroelastic numbers *Ae*. The maximum lift is found at $Ae = 1.7$ and $\hat{\alpha} = 55°$ and the most efficient hovering occurs for a higher effective membrane stiffness, $Ae = 2.4$, and at a lower angle of attack $\hat{\alpha} = 33°$. The aeroelastic numbers we find are in line with previous results reported in literature for flexible hovering wings, membrane energy harvesting applications, and insect species with matching aspect ratio wings. In hovering flight, a lower angle of attack typically enhances the lift to drag ratio. The same deformation and leading edge rotation angle observed at the lift optimal *Ae* would lead to over-cambering and a negative leading edge angle at the efficiency optimal angle of attack. This explains the increase in *Ae* to limit camber and rotation of the leading edge at the efficiency optimum.
Finally, we quantified the relationship between membrane camber, force production, and the relative stiffness of the membrane wing using the Weber number *We*. For the lift and the efficiency optimal cases, the Weber number decreases from $We = 2.20$ to 0.94 suggesting a reduction in membrane tension and membrane deformation. With a reduction in Weber number, the pressure and force pulling on the membrane decrease relative to the stiffness of the membrane. The lower *We* is associated with a decrease in membrane camber which limits the leading edge rotation angle $\gamma_{\max} < 25°$ preventing over-cambering and negative angles of attack at the leading edge.
The ability to move from high lift production to efficient hovering by modifying the angle of attack or the aeroelastic properties makes the membrane wing platform a promising model for the design of novel micro air vehicles. Our results show that combining both effects, variable

stiffness and angle of attack variation, enhances the aerodynamic performance of membrane wings and has the potential to improve control capabilities of micro air vehicles.

4 Vortex dynamics of highly deformable flapping wings

In this chapter, the effects of chord-wise flexibility on the vortex topology of a flapping membrane wing in hover are investigated. The objective is to describe the flow characteristics of the highly deformable membranes at optimal and sub-optimal aeroelastic conditions. The extend of this work, explains certain flight behaviours of bats and provides a flow control application for flapping membrane wing. This chapter is a direct extension of the previous chapter 3 [109] and does only provide a short introduction and no methods section.

4.1 Introduction

In the previous chapter 3, we identified two global optima of the stroke-average lift coefficient $\overline{C}_\mathrm{L}$ and hovering efficiency $\overline{\eta}$ (fig. 4.1) according to [71, 86]:

$$C_\mathrm{L} = \frac{L}{\frac{1}{2}\rho R c \overline{U}^2}\,, \quad C_\mathrm{P} = \frac{P}{\frac{1}{2}\rho R c \overline{U}^3}\,, \quad \overline{\eta} = \frac{\overline{C}_\mathrm{L}}{\overline{C}_\mathrm{P}}\,. \tag{4.1}$$

The optima are obtained at different aeroelastic conditions quantified by the aeroelastic number Ae and at different angle of attack amplitudes $\hat{\alpha}$. We explain the two global maxima by correlating the leading and trailing edge angles of attack with the flow at various Ae with the aerodynamic loads on the wing. The membrane wings have the highest aerodynamic performance when the angle at the leading edge is aligned with the flow and the trailing edge angle is directed downwards relative to the stroke plane. This wing configuration promotes flow attachment and a delay in stall due to moderate angles of attack and reaches high lift coefficients due to the redirection of the flow downwards [109]. The effect of the wing geometry on aerodynamic loads is consistent throughout different aeroelastic conditions Ae and angle of attack amplitudes $\hat{\alpha}$.

In this chapter, we want to focus on the velocity flow field around the unsteady flapping membrane wings. Our main objective is to characterize the flow development around the flexible wings and relate it to the membrane deformation and aerodynamic forces. Especially the

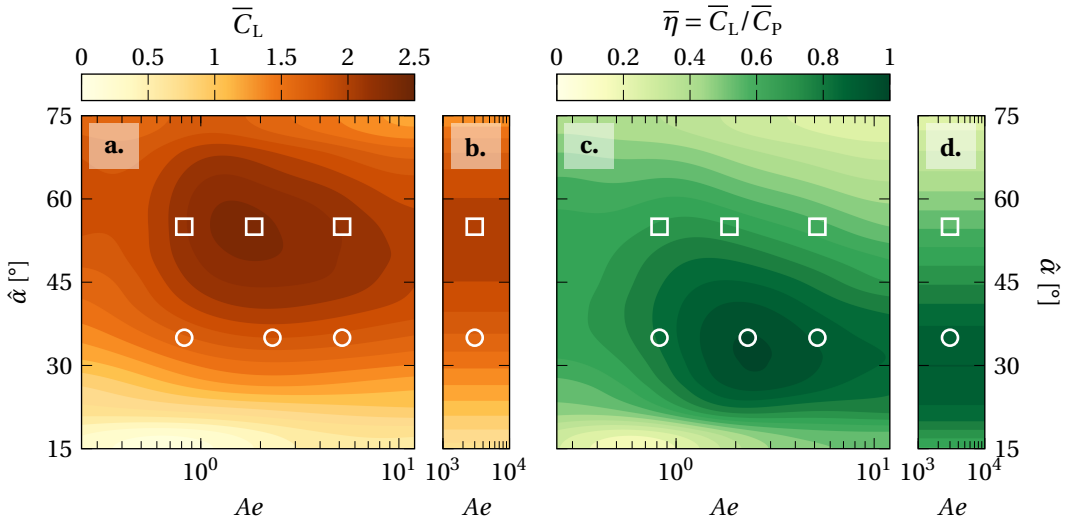

Figure 4.1 – a. Stroke-average lift coefficient $\overline{C}_L$ for the membrane and b. rigid wing, c. stroke-average hovering efficiency $\overline{\eta}$ for the membrane and d. rigid wing over aeroelastic number Ae and angle of attack amplitude $\hat{\alpha}$. The white markers indicate where flow field measurements are conducted. (adopted from [109])

leading edge vortex formation and its position relative to the wing are crucial in understanding the lift and drag production over the cycle [71, 167, 168], and have received less attention in previous studies.

4.2 Results

4.2.1 Membrane and vortex dynamics

We conduct flow field measurement for eight different cases (highlighted by the white markers in fig. 4.1). The PIV measurements are taken normal to the span-wise direction at radius of the second moment of area R_2. Two different angle of attack amplitudes are considered, $\hat{\alpha} = 55°$ and 35° for the highest lift production and highest hovering efficiency respectively. The optimal aeroelastic conditions selected are $Ae = 1.86$ for $\overline{C}_L$ and $Ae = 2.30$ for $\overline{\eta}$ [1]. Additional flow field measurements are taken where the effective stiffness is significantly lower ($Ae = 0.825$) or higher ($Ae = 5.17$) than the global optima. Finally, two sets of velocity field measurements are conducted for the rigid reference wings.

The time-resolved velocity flow field measurements are presented for the high lift angle of attack amplitude $\hat{\alpha} = 55°$ in fig. 4.2 and for the high efficiency angle $\hat{\alpha} = 35°$ in fig. 4.3. The panels (a-d) show snapshots of the wing's cross-section and the vorticity field around them for the rigid wing (a), too stiff membrane (b), optimal stiffness membrane (c), and the too flexible

[1] Note that the experimental parameters closest to the global optima in fig. 4.1 are selected for the flow field measurements based on the parameter sweep in [109].

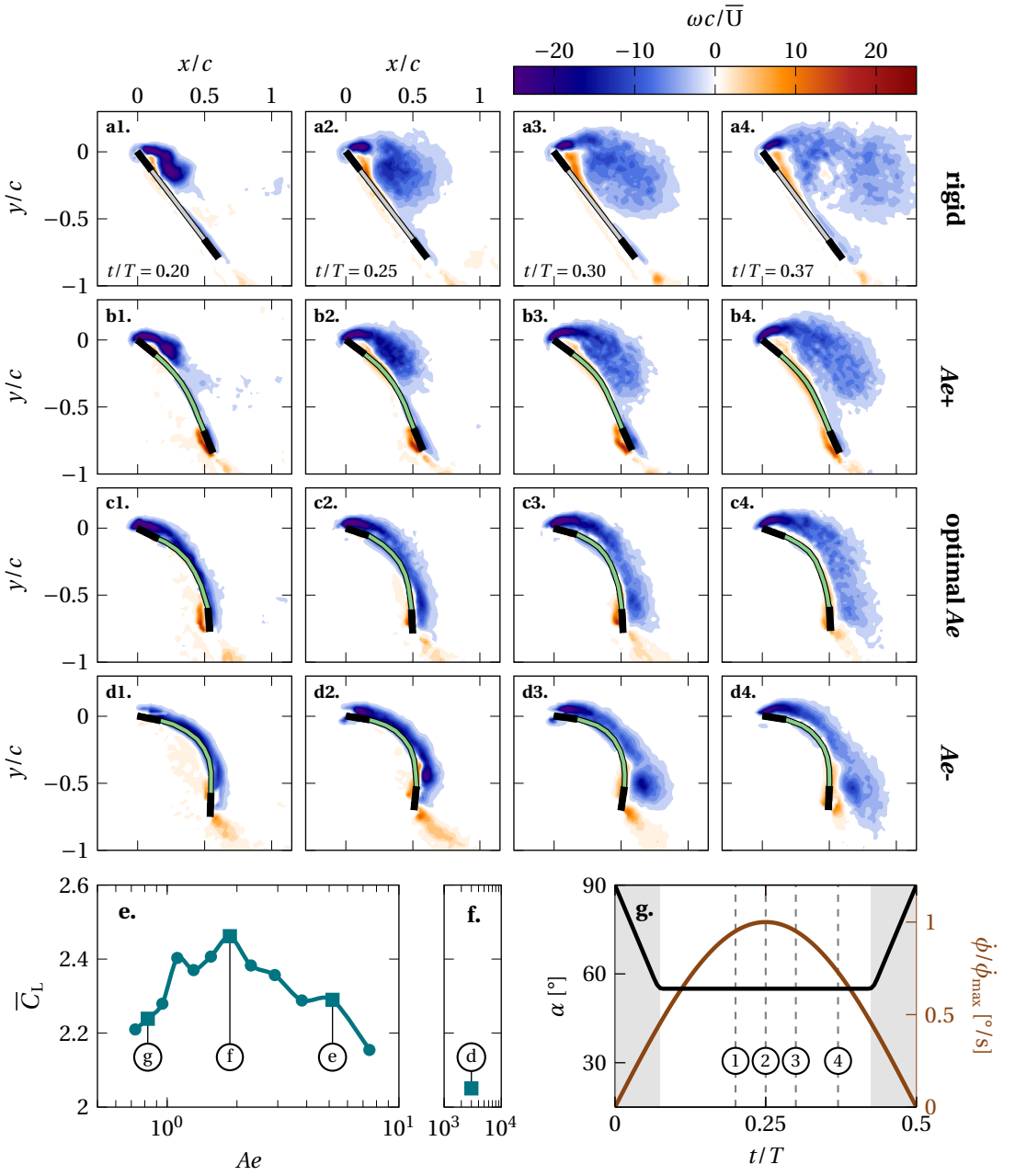

Figure 4.2 – a.-d. Vorticity field snapshots, e./f. stroke-average hovering efficiency $\overline{\eta}$ as function *Ae* for membrane and rigid wings, g. flapping wing angle of attack α and stroke velocity $\dot{\phi}$.

membrane (d) at four different stroke-cycle times t/T indicated by the markers in panel (g). Figure 4.2 also shows the stroke-average lift coefficient $\overline{C}_L$ as function of the aeroelastic number Ae for the flexible membrane and the rigid wing in panels (e) and (f), and the pitch angle α and stroke-velocity $\dot{\phi}$ as function of time in panel (g).

Lift optimal angle of attack

The rigid wing presented in fig. 4.2 panels a1-a4 features the formation of a coherent leading edge vortex, typical for a flapping wing in hovering flight [2, 11, 16, 26]. The vortex grows strongly in strength and size early in the cycle (fig. 4.2 a1 and a2). It stretches over the entire wing chord c around $t/T = 0.3$ (a3), and finally loses coherency and breaks down towards the end of the cycle when the wing is decelerating (a4). When flexibility is introduced, the wing starts to deform in the first half of the cycle in fig. 4.2b1 for the stiffest membrane wing. The airfoil camber leads to lower leading edge angles and a reduction in shear at the leading edge. Consequently, a vortex of smaller size and strength is formed at the leading edge of the stiff membrane than on the rigid wing. A maximum camber is reached around mid-stroke (fig. 4.2b2) when the highest stroke velocity $\dot{\phi}$ is experienced by the wing. The leading edge vortex has grown less in size compared to the rigid wing, but it has a stronger core and stays closer to the wing. The vortex grows consistently while staying coherent and close-bound to the wing until late into the stroke cycle (fig. 4.2b4) when the leading edge vortex on the rigid wings starts to break down. The membrane camber keeps the vortex closer to the wing and more coherent, which leads to a significant improvement in stroke-average lift production of the stiff membrane over the rigid wing (fig. 4.2e,f).

At lift optimal aeroelastic conditions, the flow topology around the membrane wings changes (fig. 4.2c). The membrane deforms much stronger due the decreased Ae in the first half of the cycle (fig. 4.2c1). As a result, the leading edge aligns with the flow and no coherent leading edge vortex is formed. Instead, the flow stays attached to the wing and a thin shear-layer spreads over the chord. At mid-stroke (fig. 4.2c2) the wing reaches its maximum camber. Even this far into the stroke-cycle, no conventional leading edge vortex has rolled up whereas the stiffer membrane and rigid wing feature pronounced, round vortices. The shear-layer remains bound to the wing and grows in strength and height over the chord in fig. 4.2c2,c3. Towards the end of the cycle (fig. 4.2c4) the shear-layer loses coherence and its height grows to about 1/3 of the chord length c. The vorticity still stays bound to the membrane, in contrast to the stiffer membrane and rigid wing where the leading edge vortices lift off of the wing at the end of the cycle. The membrane wing at optimal aeroelastic conditions keeps the flow attached and suppresses the formation of a leading edge vortex over the entire stroke-cycle. This leads to highest stroke-average lift coefficients in all presented experiments and more than 20 % increased $\overline{C}_L$ over the rigid wing despite the absence of a leading edge vortex. Similar improvements in lift production have been observed for active stiffness controlled membrane wings at steady flow conditions [166].

Finally, we present in fig. 4.2d the membrane wing that hovers at a lower aeroelastic number

Ae than the lift optimal case. The highly flexible membrane experiences strong deformation right from the start of the stroke (fig. 4.2d1). No vortex formation is observed in the first half of the cycle. Instead, a thin layer of vorticity stretches over the chord, similarly as seen for the lift optimal aeroelastic conditions. At mid-stroke, a transition in the flow topology is observed (fig. 4.2d2). The leading edge shear-layer rolls up close to the trailing edge as it separates over the high curvature of the membrane. In the second half of the cycle, the vortex grows in size and stays attached to the leading edge shear-layer (fig. 4.2d3). At the same time, a trailing edge vortex of counter-clockwise rotation rolls up and forms a pair with the first vortex. Both vortices persist until the late stages of the stroke-cycle (fig. 4.2d4). The clockwise rotating vortex then loses its coherency, akin to the vortex evolution for the stiffer membranes and the rigid wing. The highly flexible membrane experiences very strong deformations which cause the flow to separate over the high camber at mid-chord. Additionally, the trailing edge rotates into the flow which causes flow separation and the formation of a strong trailing edge vortex. At these high membrane deformation the average lift production of the membrane wings falls sharply compared to the optimal aeroelastic conditions, but yields more lift than the rigid reference case (fig. 4.2e,f).

Efficiency optimal angle of attack

The vorticity flow fields at the maximum efficiency ($\overline{\eta} = \overline{C}_L/\overline{C}_P$) angle of attack amplitude $\hat{\alpha} = 35°$ are presented in fig. 4.3 for four aeroelastic conditions. The four cases correspond to the rigid wing (a), the stiff membrane (b), efficiency optimal aeroelastic conditions (c), and the highly flexible membrane (d) indicated by the circular markers in fig. 4.1.

The flow field around the rigid wing at $\hat{\alpha} = 35°$ in fig. 4.3a1-a4 shows the formation, growth and breakdown of a coherent leading edge vortex. The strength and size of the vortex is reduced and it stays closer to the wing compared to the rigid wing at higher angle of attack $\hat{\alpha} = 55°$ (fig. 4.2a). The vortex stays attached to the wing even towards to the end of the cycle (fig. 4.3a4) where at higher angles of attack the vortex lifts off of the wing and breaks down. Maintaining a coherent and close-bound leading edge vortex over large parts of the stroke-cycle was shown to promote energy efficient hovering flight for rigid flapping wings [71].

As wing flexibility is introduced, the stiff membrane wing begins to deform in fig. 4.3b1,b2. The membrane camber reaches a maximum shortly after mid-stroke, after which the camber reduces again (fig. 4.3b3,b4). The camber of the membrane leads to a rotation of the leading and trailing edges of the wing platform and reduced the effective angles with the flow. The leading edge vortex grows slower in size and strength (fig. 4.3b1-b3) compared to the rigid wing due to the reduced shear at the leading edge. The leading edge vortex stays close to the wing and coherent until the end of the stroke-cycle (fig. 4.3b4). With increased wing flexibility at lower *Ae*, the lift to power ratio $\overline{\eta}$ increases, but the highlighted stiff membrane wing only just reached the same $\overline{\eta}$ in fig. 4.3e as the rigid wing in fig. 4.3f.

The wing section and flow field snapshots at efficiency optimal aeroelasticity are presented

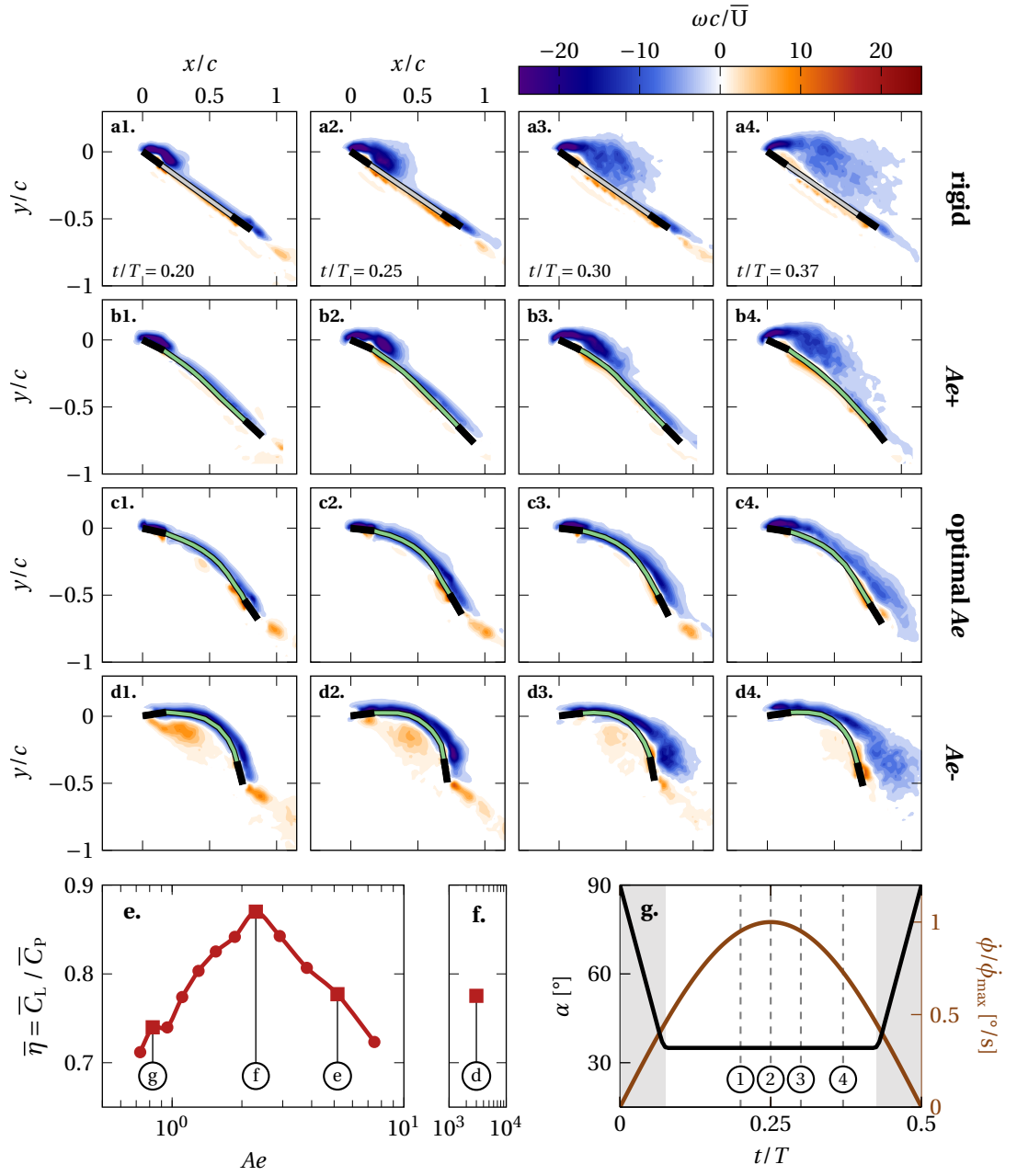

Figure 4.3 – a.-d. Vorticity field snapshots, e./f. stroke-average hovering efficiency $\overline{\eta}$ as function Ae for membrane and rigid wings, g. flapping wing angle of attack α and stroke velocity $\dot{\phi}$.

in fig. 4.3c1-c4. The vortex topology changes considerably compared to the stiff membrane. No leading edge vortex is formed. Instead, a thin layer of vorticity spreads over the chord and grows slightly in height and strength over the cycle. The membrane cambers strongly early in the cycle in fig. 4.3c1. At mid-stroke and shortly thereafter (fig. 4.3c2,c3) the leading edge is aligned with the flow which suppresses the formation of a leading edge vortex. The same flow topology is found at lift optimal aeroelastic conditions in fig. 4.3c. Keeping the flow attached to the membrane and suppressing the leading edge vortex growth leads to the most power efficient hovering flight and to improvements of more than 12 % in $\overline{\eta}$ over the rigid wing (fig. 4.3e,f).

Figure 4.3d1-d4 display the membrane shape and vorticity field snapshots for the most flexible wing at $\hat{\alpha} = 35°$ over one stroke-cycle. The membrane reaches already a very high camber early in the cycle (fig. 4.3d1). The deformation leads to strong rotations of the leading edge and trailing edges, and a negative leading edge angle (of attack). The flow stays attached on the suction side, above the wing but the negative leading edge angle leads to the formation of a leading edge vortex on the pressure side, below the wing. The vortex grows until mid-stroke (fig. 4.3d2) and moves below the maximum camber at the mid-chord position. At the same time, the flow separates over the high curvature on the suction side and a vortex forms behind the wing, close to the trailing edge. The vortex behind the wing grows rapidly in size in the second half of the cycle (fig. 4.3d3) and reaches a similar size as the leading edge vortex on the stiff membrane wing (fig. 4.3b3). The vortex below the wing begins to dissipate after mid-stroke in fig. 4.3d3, and disappears almost entirely towards the end of the cycle in fig. 4.3d4. The strong membrane deformation at the lowest *Ae* gives rise to the formation of two strong vortices below and behind the wing. These vortices induce a higher drag and for the vortex below the wing contribute even negatively to the lift. Both effects cause a sharp decrease in stroke-average hovering efficiency $\overline{\eta}$ compared to the optimal aeroelasticity in fig. 4.3e.

Wing shape and vortex phenomenology

The different emerging membrane deformation and vortex topologies are summarized for all flow field measurements in fig. 4.4 for the membrane wings and rigid reference cases. The upper half of the contour plot corresponds to the stroke-average lift coefficient $\overline{C}_\mathrm{L}$ and the lower half of the contour plot corresponds to the hovering efficiency ($\overline{\eta} = \overline{C}_\mathrm{L}/\overline{C}_\mathrm{P}$) as function of the angle of attack amplitude $\hat{\alpha}$ and the aeroelastic number *Ae*. The icons represent the membrane shape and flow field at mid-stroke ($t/T = 0.25$) when the wing is at the highest stroke velocity $\dot{\phi}_\mathrm{max}$. The flow structures and deformation change in a similar way for the two tested angles of attack ($\hat{\alpha} = 35°$ and 55°). The rigid wings in fig. 4.4b do not deform and have large scale coherent leading edge vortices. The leading edge vortex is a common occurrence in many flapping wing applications and is attributed to the high lift coefficient produced by natural fliers.

As flexibility is introduced in fig. 4.4a, the wings camber, and their leading and trailing edges rotate with respect to the flow. The leading edge vortices reduce in size and strength, and

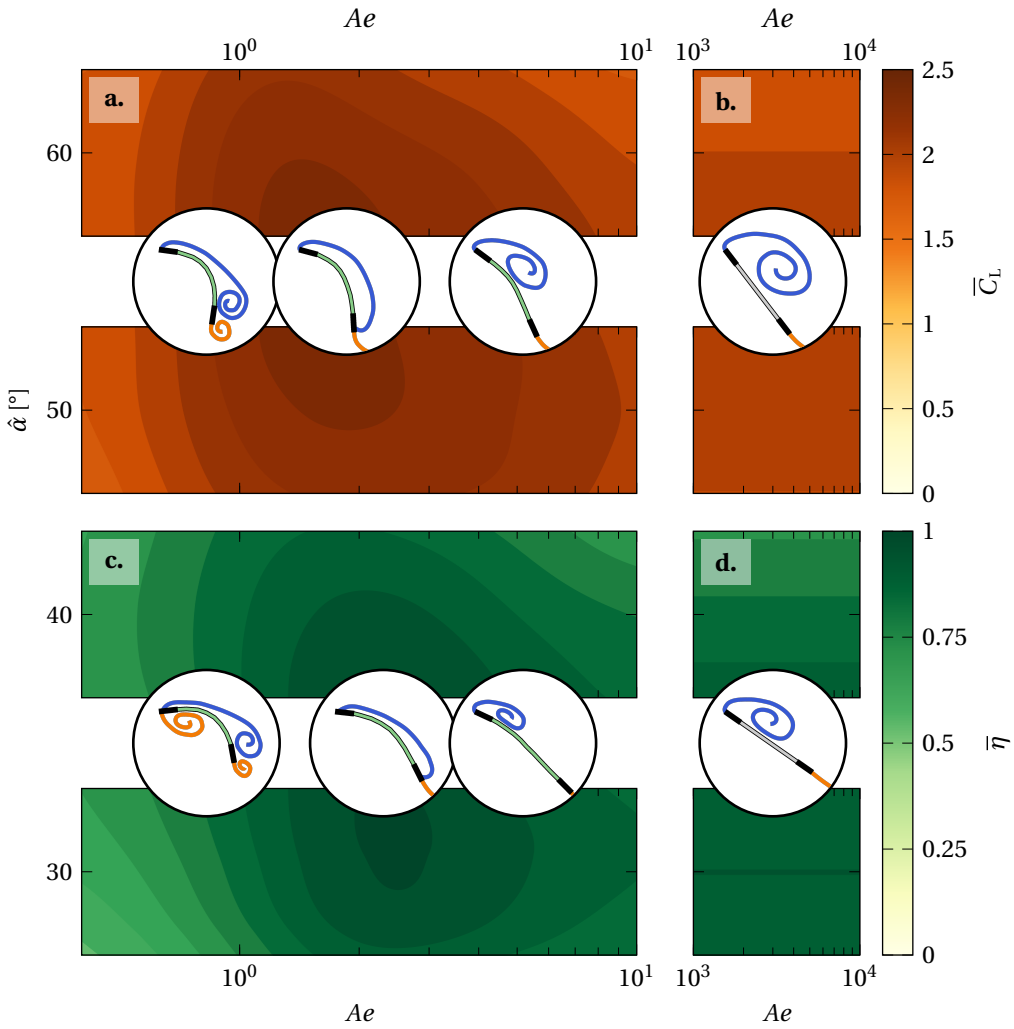

Figure 4.4 – Membrane deformation and flow field phenomenology. a. Stroke-average lift coefficient $\overline{C}_L$ for the membrane and b. rigid wing, c. stroke-average hovering efficiency $\overline{\eta}$ for the membrane and d. rigid wing over aeroelastic number Ae and angle of attack amplitude $\hat{\alpha}$. The graphs are split at $\hat{\alpha} = 35°$ and $55°$ to include depictions of the membrane and flow topologies (icons).

stay closer to the wing for the stiffest membrane wings ($Ae = 5.17$). The stiff membrane wings reach higher stroke-average lift coefficient and have an increased efficiency $\overline{\eta}$ compared to the rigid wing. The flow stays fully attached and no leading edge vortex is formed at optimal aeroelasticity and both angles $\hat{\alpha}$. Despite forming no leading edge vortex at all, the highest lift coefficients and the most energy efficient hovering is achieved. Further decreasing the effective membrane stiffness to $Ae = 0.825$ leads to even higher wing camber and rotation of the leading and trailing edges. The high membrane deformation leads to two important changes in the flow topology. Firstly, a vortex is forming on the suction side of the wing, but its shear-layer is separating over the high membrane curvature instead of at the leading edge.

Secondly, the leading edge rotates to negative angles of attack and a vortex of opposite sign vorticity is formed below the wing for the lower angle of attack amplitude ($\hat{\alpha} = 35°$). Both vortices are detrimental to the aerodynamic performance of the wing and cause losses in stroke-average lift production and power efficiency.

4.2.2 Membrane dynamics

The membrane shapes and corresponding flow fields around the wing presented in the previous section demonstrate the strong influence the wing deformation has on the formation of different vortical structures. Especially the timing of maximum deformation and when it is achieved has a great influence on the vortex formation. In the following section, we quantify the membrane deformation dynamics in time, and relate them to the vortex evolution and aerodynamic loading on the wing.

The membrane deformation as function of time is presented in fig. 4.5 for $\hat{\alpha} = 55°$ (a,c,e) and $\hat{\alpha} = 35°$ (b,d,f). The sketch on the left shows the definition of the wing camber $z_{\max}$, leading edge angle α_{LE}, and trailing edge angle α_{TE} relative to the flow velocity U. The membrane deformations are presented at three different aeroelastic numbers, corresponding to the PIV cases: too stiff, optimal stiffness, and too flexible membrane wing (coloured lines)[2]. The rigid reference case follows the input kinematics as it does not deform (black line).

The membrane camber $\hat{z}_{\max}$ in fig. 4.5a,b increases at the beginning of the stroke-cycle until it reaches a maximum. The maximum is maintained for a while before the camber of the membrane decreases again. We refer to the time of constant camber as the plateau time. With lower *Ae*, which corresponds to increasing relative flexibility, the value of maximum camber increases and the maximum is reached earlier in the cycle. The plateau of the camber maximum widens with a decrease in *Ae*, until for the most flexible case the camber is maintained throughout most of the cycle apart from the wing rotation at the beginning and end of each stroke-cycle. At lift optimal aeroelastic conditions in fig. 4.5a the membrane cambers up to $\hat{z}_{\max} = 0.27c$. The camber maximum for the highest hovering efficiency is at $\hat{z}_{\max} = 0.23c$ in fig. 4.5b. The camber peaks are attained around mid-stroke for both optimal aeroelasticities.

The wing's leading edge angle α_{LE} due to the membrane deformation in fig. 4.5c,d shows many similarities to the dynamics of the membrane camber. Here, the leading edge rotates and causes a reduction in α_{LE} until a minimum is reached. The minimum angle α_{LE} is lowest for the highly flexible case and increases for higher effective stiffness. The angle α_{LE} follows the rigid, imposed angle of attack α of the wing frame in the beginning and end of the stroke-cycle. For the highest lift coefficient $\overline{C}_{\mathrm{L}}$, the leading edge angle is reduced by 45° at mid-stroke and arrives at a minimum angle $\alpha_{\mathrm{LE}} = 9.3°$, which is close to the stall angle of a flat plate. For the highest hovering efficiency $\overline{\eta}$, the leading edge aligns with the flow $\alpha_{\mathrm{LE}} = 1.0°$ at $\hat{\alpha} = 35°$ (fig. 4.5d). A minimal angle at the leading edge reduces the shear at the leading edge and suppresses the

[2]Note that some data points of the most flexible case are missing. During the rotation phase of the wing the marker tracking algorithm could not follow the markers properly due to very high gradients of deformation.

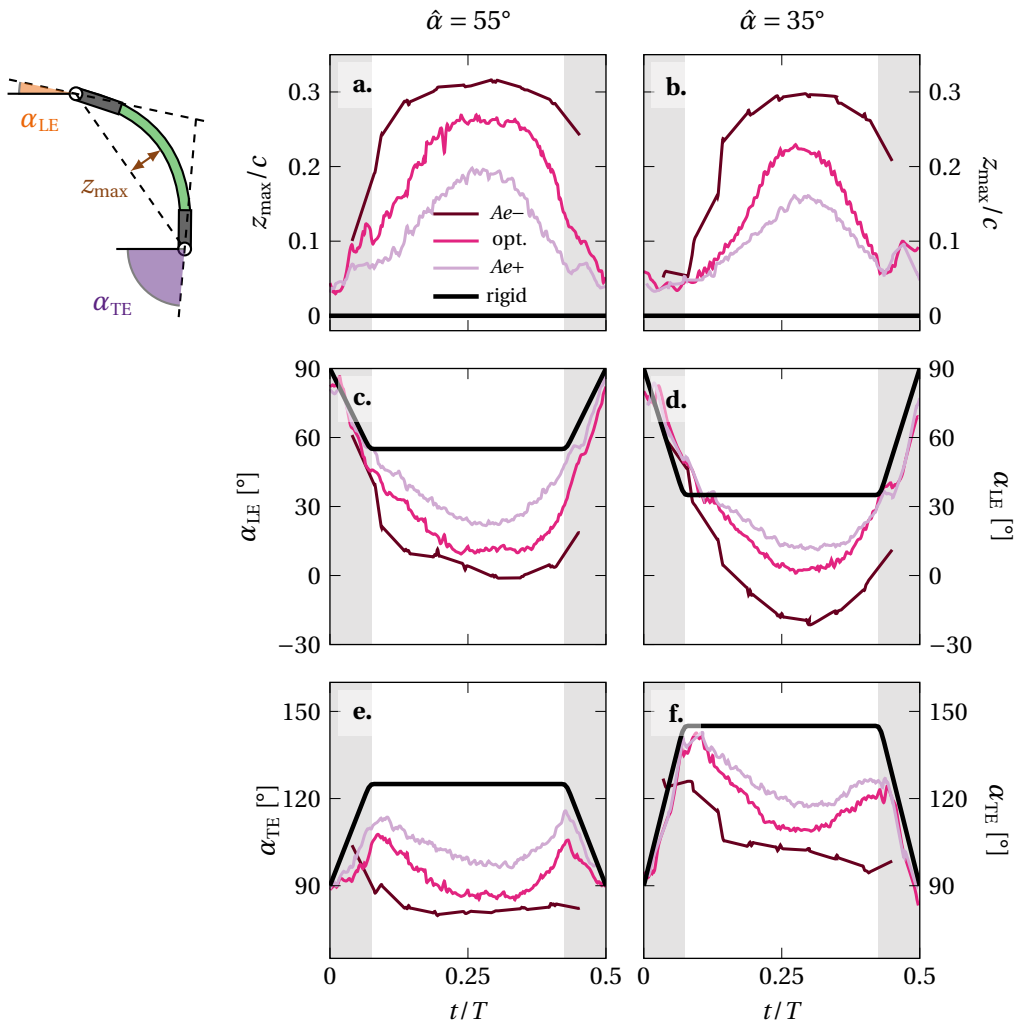

Figure 4.5 – a. Membrane camber z_{max}, b. leading edge angle α_{LE}, and c. trailing edge angle α_{TE} over one stroke-cycle $t/T = 0$ to 0.5.

formation of a leading edge vortex. In addition, it allows the flow to stay attached to higher geometric angles of attack α.

We consider the trailing edge angle α_{TE} as another important quantity in understanding the flow dynamics around the flexible membrane wing. The trailing edge redirects the flow downwards and controls the trailing edge vortex formation. If the trailing edge rotates too far, it turns into the flow causing strong flow separation and a loss in overall aerodynamic performance [109]. The trailing edge angle α_{TE} in fig. 4.5e,f reaches a minimum, remains at that angle for a certain plateau time, and finally returns to the wing frame angle at the end of the stroke cycle, akin to the observations about the leading edge angle α_{LE}. The minima increase in value and have a wider plateau for lower *Ae*. At the lift optimal aeroelasticity the trailing edge angle reaches a minimum of $\alpha_{TE} = 90°$. This corresponds to a 35° decrease in effective trailing edge angle. The difference between leading and trailing edge angles is due to

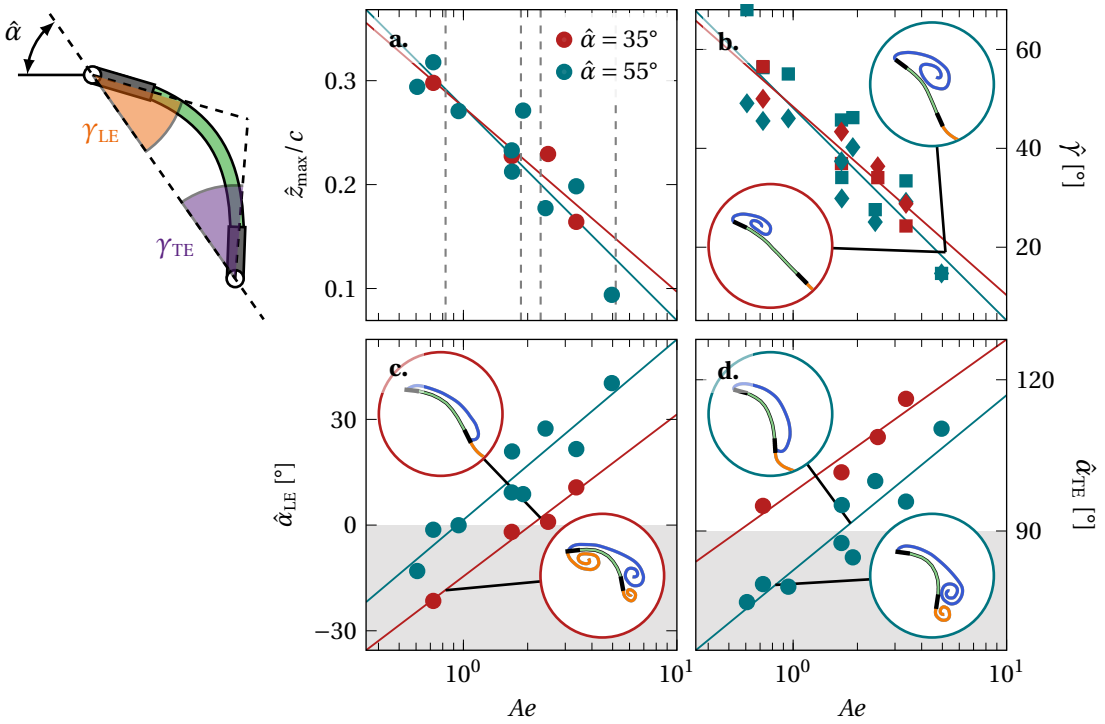

Figure 4.6 – a. Wing camber maxima $\hat{z}_{max}$, b. rotation angle maxima $\hat{\gamma}_{LE}$ at the leading edge and $\hat{\gamma}_{TE}$ at the trailing edge, c. leading edge angle minima $\hat{\alpha}_{LE}$, and d. trailing edge angle minima $\hat{\alpha}_{TE}$ as function of the aeroelastic number *Ae*. The lines represent the general trend of the deformation data and are obtained by a least-square fit to the individual markers.

a shift in maximum camber towards the leading edge, which has been reported in previous membrane wing studies and has also been observed in bats during flight [43, 142]. The trailing edge rotates further below < 70° for the highly flexible case, which is detrimental for its lift production.

4.2.3 Membrane deformation and aerodynamic loads as function of *Ae*

In the previous section, the membrane deformation was presented as a function of time. The wing camber, the leading edge angle, and the trailing edge angle reach different extrema in the stroke-cycle based on the relative stiffness defined by *Ae*. We extract the membrane deformation extrema for both processed angle of attack amplitudes $\hat{\alpha}$ at different *Ae*. In fig. 4.6 the wing camber maxima $\hat{z}_{max}$, rotation angle maxima $\hat{\gamma}$, leading edge angle minima $\hat{\alpha}_{LE}$, and trailing edge angle minima $\hat{\alpha}_{TE}$ are presented as function of the aeroelastic number *Ae*. The icons depict the membrane shape and flow field at mid-stroke. The rotation angle γ is defined as the edge's rotation relative to the undeformed wing and relates to the leading and trailing edge angles of attack as follows:

$$\alpha_{LE} = \alpha - \gamma_{LE}, \quad \alpha_{TE} = 180° - \alpha - \gamma_{TE}. \tag{4.2}$$

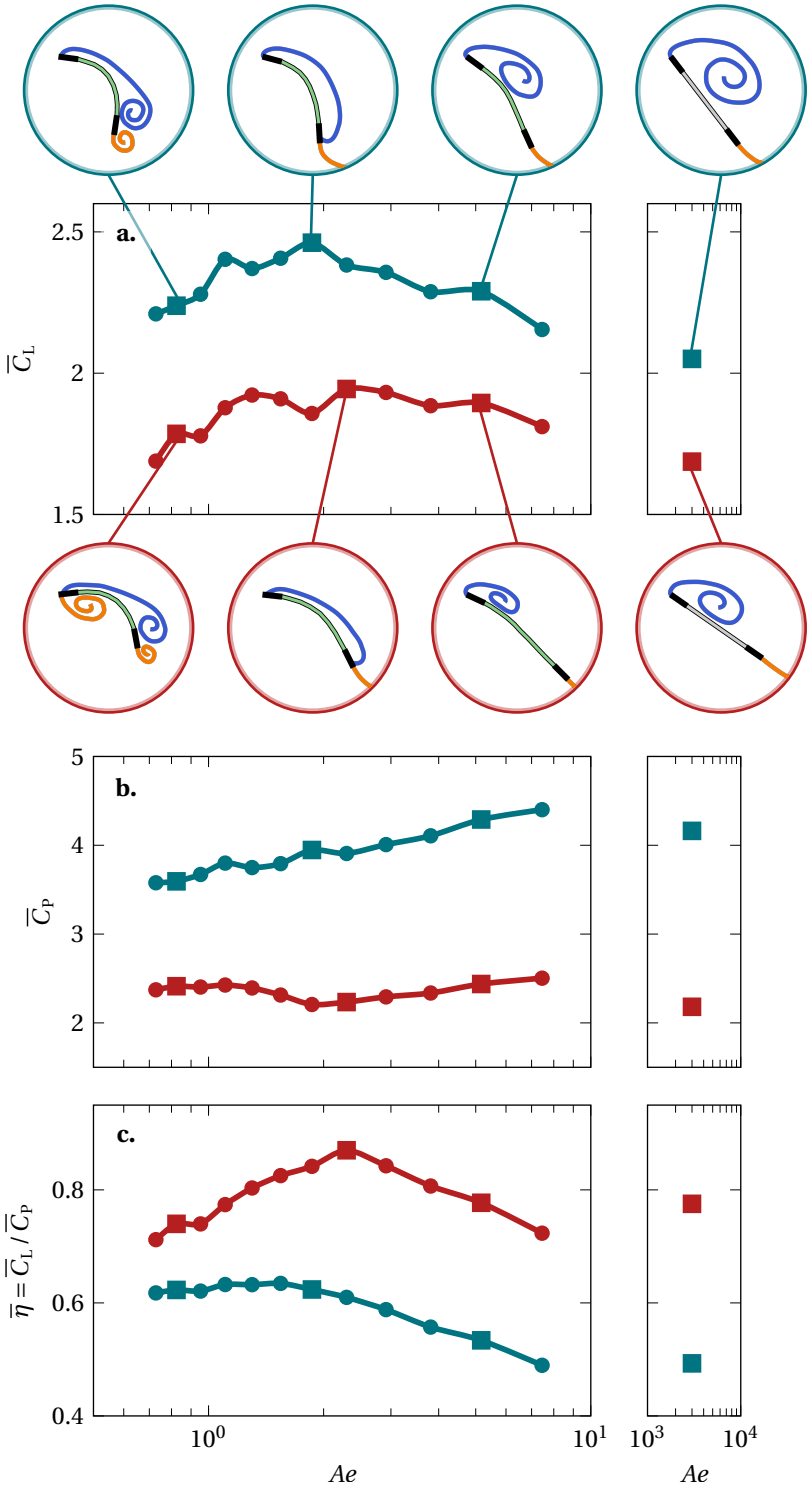

Figure 4.7 – a. Stroke-average lift coefficient, b. stroke-average power coefficient, and c. stroke-average hovering efficiency as a function of the aeroelastic number. The colours correspond to measurements at 35° (●) and 55° (●). The squares (■/■) indicate cases where additional PIV measurements were conducted.

The maximum camber $\hat{z}_{max}$ (fig. 4.6a) decreases approximately linearly with increasing *Ae* in the logarithmic scale regardless of the angle of attack amplitude $\hat{\alpha}$ indicated by the (●) and (●) markers. This corresponds to an exponential relationship relation between $\hat{z}_{max}$ and *Ae*, also referred to as a power law in the general sense. We find maximum membrane camber values that range from $0.1c$ for the stiffest membrane, up to $0.3c$ for the most flexible membranes. The lift and efficiency optimal cases reach a camber around and slightly above $0.2c$. The highest possible wing camber is $0.5c$ considering only bending deformation and no membrane stretching.

The rotation angle maxima $\hat{\gamma}$ in fig. 4.6b relate to log(*Ae*) linearly independent of the angle of attack amplitude $\hat{\alpha}$, similar to the wing camber. Here, no distinct differences between the rotation angle at the leading (■/■) and trailing edge (◆/◆) are observed for most of the cases. Only for the lowest stiffness ($Ae < 1$), the leading edge rotates to higher angles $\hat{\gamma}$ compared to the trailing edge. This indicates that the maximum camber location is shifted closer towards the leading edge. An asymmetry in the membrane shape has been observed for membrane wings under various steady and unsteady conditions [109,142,158]. The asymmetry stems from pressure distribution along the camber which is subject to different steady and unsteady effects like vortex formation and shedding. We consider the shape asymmetry to be a secondary effect and to not have a major impact on the aerodynamic performance.

The functional relationship between camber $\hat{z}_{max}$ and rotation angle $\hat{\gamma}$ maxima allows us to a priori estimate the membrane deformation from the prescribed kinematics, but it does not directly relate to the vortex dynamics nor the aerodynamic loading on the wing. To understand the impact of the membrane deformation on the flow, we quantify the minimum leading $\hat{\alpha}_{LE}$ and trailing edge angles of attack $\hat{\alpha}_{TE}$ within the stroke-cycle (fig. 4.6c,d). In fig. 4.7a the stroke-average lift coefficient $\overline{C}_L$ as a function of the aeroelastic number *Ae* is presented for the flexible membrane wings and the rigid reference case. The coloured markers represent results at two different angles of attack, $\hat{\alpha} = 35°$ (●) and $\hat{\alpha} = 55°$ (●), and the square markers (■/■) correspond to the PIV measurements illustrated by the icons. Both angles $\hat{\alpha}_{LE}$ and $\hat{\alpha}_{TE}$ have the same linear relationship with log(*Ae*) but they are shifted relative to $\hat{\gamma}$ in equation 4.2. The two different coloured datasets (●/●) are separated by a constant 20°, the difference in angle of attack amplitude of the input kinematics $\hat{\alpha} = 35°$ and 55°. The grey shaded areas indicate angles where the membrane is over-rotating or over-cambering. If either negative angles of attack are reached at the leading edge $\hat{\alpha}_{LE} < 0°$ or the trailing edge rotates into the flow $\hat{\alpha}_{TE} < 90°$, the wing is over-cambering and its aerodynamic performance decreases (fig. 4.7) [109].

The leading edge angle maxima $\hat{\alpha}_{LE}$ in fig. 4.6c decrease with a decrease in the aeroelastic number *Ae*. At $\hat{\alpha} = 35°$ (●), $\hat{\alpha}_{LE}$ gets close to 0° which corresponds to the leading edge being aligned with the flow and leads to the lowest power consumption and highest aerodynamic efficiency (fig. 4.7b,c). The low angle at the leading edge promotes flow attachment and a reduced projected frontal wing area compared to the stiffer membranes or the rigid wing. Further reduction in effective stiffness *Ae* causes the power consumption to rise again and

the efficiency to decline. The increase in membrane flexibility causes $\hat{\alpha}_{\mathrm{LE}}$ to over-rotate and become negative (fig. 4.6c). Eventually, the stall angle is crossed in the negative $\hat{\alpha}_{\mathrm{LE}}$ which leads to the formation of a vortex below the wing and a sharp decline in aerodynamic performance. The flow is separating over the high membrane curvature and the negative angle of attack at the leading edge. The increase in power (fig. 4.7b) is caused by the growth of a strong vortex that forms near the trailing edge and a second vortex below the wing. The vortex at the trailing edge produces additional pressure induced drag due to its position behind the wing.

The trailing edge angle minima $\hat{\alpha}_{\mathrm{TE}}$ in fig. 4.6d decrease with decreasing *Ae* as the trailing edge rotates into the flow with increasing wing camber. At $\hat{\alpha} = 55°$ (●), the highest stroke-average lift (fig. 4.7a) is reached by the membrane wing as a minimum angle of roughly $\hat{\alpha}_{\mathrm{TE}} = 90°$ is attained. The trailing edge at this angle directs the flow downwards, perpendicular to the stroke-plane in the negative lift direction. The trailing edge rotates to lower trailing edge angles of attack for lower *Ae*. The flow separates and a vortex forms behind the high camber curvature for the lowest *Ae* tested at $\hat{\alpha} = 55°$ (●). All cases within in the grey shaded region in fig. 4.6d suffer losses in lift production compared to the optimal aeroelastic conditions (fig. 4.7a).

The membrane deformation data presented as function of the aeroelastic number *Ae* highlights two important findings. Firstly, the wing camber and rotation angle maxima grow exponentially over the observed parameter space. This allows to predict the membrane shape from the input kinematics in first approximation and infers that the fluid-structure interaction is mainly driven by the structural and fluid inertia. Secondly, two conditions for over-rotation or over-cambering can be defined when the rotation angle γ is decomposed into a leading and trailing edge angle (equation 4.2). The highest aerodynamic performance is achieved when the membrane deformation is just at the edge of one of the conditions, for highest lift coefficient $\hat{\alpha}_{\mathrm{TE}} = 90°$ and for most energy efficient hovering $\hat{\alpha}_{\mathrm{LE}} = 0°$. When these thresholds are exceeded the aerodynamic performance decreases.

Bats and other natural fliers using compliant membrane wings have been observed to favour lower angles of attack ($\alpha < 40°$) for power efficient flight [43, 169]. Bats control the camber of their wings by increasing the tension during flight with their muscles to adapt the wing shape to different flow conditions. When their muscles are paralysed they regulate their flight speed instead to control the wing camber [43]. Controlling either the wing flexibility Eh or the flight speed U regulates the effective aeroelastic number *Ae*. Our findings demonstrate that these are effective means of controlling flow separation over membrane wings and limiting vortex formation. Based on the observed aeroelastic phenomena active flow control schemes of artificial flapping wing vehicles can be realized. Optimal aeroelastic conditions can be maintained in flight by modulating either the wing's angle of attack α, membrane stiffness Eh, or flow velocity U using the leading and trailing edge angles as indicators for the flow state and membrane shape.

4.3 Conclusion

In this chapter, we investigated different emerging flow topologies of flapping membrane wings, and how they relate to the aerodynamic performance and wing deformation. We present results from flow field measurements for the optimal aeroelastic conditions and three reference cases where the membrane is either too flexible or too stiff, and a rigid reference wing. We identify several new flow characteristics previously not observed in rigid flapping wing flight or other flexible wing studies. The flow topology around the wing is similar to the rigid wing, when the membrane wing is too stiff but the leading edge vortex stays closer to the wing and is more coherent.

At the optimum aeroelastic conditions the wing is deformed such that the leading edge is aligned with the incoming flow and the trailing edge oriented downwards. The flow stays close-bound to the wing and no coherent leading edge vortex is formed in the first half of the cycle. In the second half of the cycle, the vorticity stays close to the membrane but the flow separates over the high curvature of the membrane and a vortex forms in the second half of the wing chord for all observed cases. The membrane wings produce the highest lift coefficients despite suppressing the leading edge vortex formation entirely. These results challenge the claim that a leading edge vortex is always required to generate high lift in flapping wing flight [2, 11, 26].

If the membrane wing is too flexible, the membrane curvature increases rapidly early in the cycle. The flow separates over the high curvature of the membrane and causes a strong vortex to form behind the wing, close to the trailing edge. This vortex reaches a similar strength compared to the rigid case, but the wing experiences a dramatic loss in lift and hovering efficiency due to the vortex' position behind the wing. The high membrane curvature eventually leads to negative angles of attack at the leading edge for the lowest observed angle of attack amplitude $\hat{\alpha} = 35°$ and causes a vortex to grow at the pressure side, below the wing. The vortex formation induces additional drag forces and even impacts the lift negatively as it creates a low pressure below the wing.

Bats and other natural fliers using compliant membranes actively control the shape of their wings in flight by increasing the tension in their muscles or varying the flight speed, both of which regulate the aeroelastic number [43, 169]. We suggest using active flow control for artificial flapping wing vehicles by modulating either the wing's angle of attack α, membrane stiffness Eh, or flow velocity U. Using the leading and trailing edge angles as indicators for the flow state and membrane shape allows to maintain optimal aeroelastic conditions without further sensory input.

Effects of Wing Planform Part III

5 Hawk moth wing morphology and the leading edge vortex

In this chapter, the effects of different wing planforms and wing shapes on the leading edge vortex formation and aerodynamic performance are investigated. The objective is to identify key morphological traits which govern the leading edge vortex formation on hawk moth wings and explain the diversification of different wing planforms found in nature. The extend of this work, provides guidelines for the design of different wing planforms for flapping wing vehicles.

The work presented in this chapter has been done in collaboration with Megan Matthews, Marc Guasch, Simon Sponberg, and Karen Mulleners.

5.1 Introduction

Flight is a key evolutionary trait which augmented the abilities of various species of birds, insects, and mammals to forage, hunt, evade predators, migrate, find mates, and more [170]. Strong selective pressure is put on the aerodynamic performance of natural fliers to perform the different activities with highest proficiency. The aerodynamic performance in flapping wing flight is greatly influenced by the functional wing morphology and the wing motion [25–27]. The success of aerial organisms gave rise to a large variety in different wing sizes and shapes which each fill their biological niche from the micron to the meter scale [171, 172]. In particular, flying insects present one of the highest diversities in wing morphology, kinematics, and behaviour with nearly one million species discovered to date [42, 110, 173–176]. Even though there are many similarities shared across the different flapping wing fliers, there are distinct differences in the wing morphology and actuation between species. To understand which traits were key in the diversification of species, it is important to distinguish if these differences are mainly providing aerodynamic advantages or other, functional benefits [176–178].

The leading edge vortex is one important aerodynamic characteristic, which gives rise to the high lift production required by flapping wing fliers at the insect-scale [11, 26, 76, 151]. The leading edge vortex is a large scale coherent flow structure which arises when a wing operates

at high angles of attack, above its static stall angle, typical for insect flight. The strong shear will cause the flow to separate over the leading edge and roll-up into a vortex. The bound leading edge vortex produces a low pressure area on the suction side of the wing and greatly augments the aerodynamic forces and torques. The vortex grows in size to cover the entire wing and eventually lifts off of the wing and sheds into the wake. The life cycle of the leading edge formation and breakdown is repeated during each wingbeat and leads to high transient lift coefficients [2, 16].

Different insect species have developed their own strategies to manipulate the flow around their wings and in particular the formation of the leading edge vortex. Honeybees and mosquitos for example flap their wings with low amplitude at extremely high frequencies and perform well-timed, rapid wing rotations which create strong vorticies at every stroke-cycle [81, 179]. Butterflies in contrast have lower aspect ratio wings and flap at reduced wingbeat frequencies. Their bodies undergo large angle rotations which helps to direct the trajectories of their shed vorticies and reduce drag force [44, 45]. Some of the smallest flying insects, like the fairyflies [180] or thrips [181], use bristled wings to fly. At very low Reynolds numbers $Re = 10$, the bristled wings generate large and coherent leading edge vorticies which yields similar lift but greatly reduced drag production compared to rigid wings, especially when *flinging* their wings apart [171, 182].

Even within sister-families, like the hawk moths and silk moths (Sphingidae and Saturniidae), large diversity in wing morphology and behaviour are observed [176, 177]. Many Sphingidae, like the hawk moth, evolved a controlled and agile flight with small, high aspect ratio wings. Their flight is power efficient and allows them to navigate and feed in hover even in the unsteady wakes of flowers [8, 183]. The Saturniidae developed an entirely different wing morphology and motion in comparison. Silk moths lose their functional mouth parts and do no longer feed during their adult life which limits their available energy budget. They evolved large, low aspect ratio wings and adopted an erratic flight trajectories which could help in evading predators [176, 177].

These examples demonstrate the close relation between wing morphology and wing kinematics which are both adapted to the animal's aero-ecological niche. In this part, the hypothesis is tested if the morphology of hawk moth wings evolved to accommodate the formation a strong and coherent leading edge vortex. The aerodynamic performance and three-dimensional flow fields around scaled hawk moth wing models and basic reference wing shapes are investigated. From the velocity flow fields, the leading edge vortex strength in terms of its circulation is extracted over the entire wing span. To explain the differences in aerodynamic performance and leading edge vortex circulation, the wing geometries are quantified in terms of the spanwise chord length, camber, twist, and dihedral angle. The local wing geometry parameter are used to define a leading edge vortex scaling over the wing span. Finally, the implications of the leading edge vortex scaling and its contribution to the aerodynamic performance are discussed in the context of wing morphology evolution of hawk moth wings.

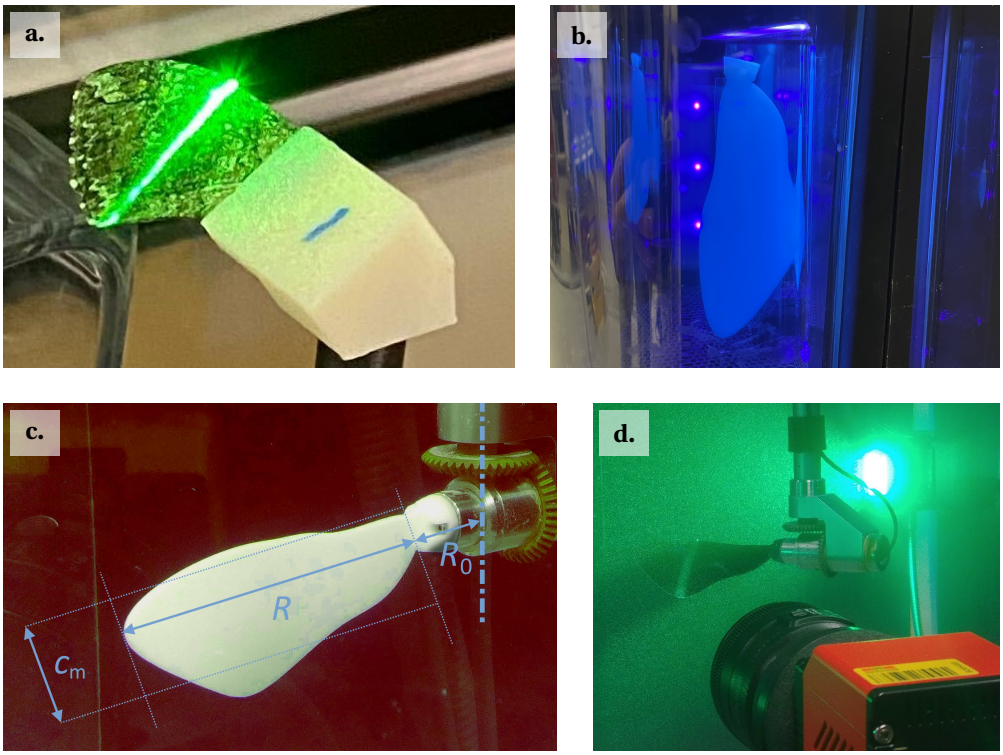

Figure 5.1 – An overview of the different parts of the study: a. Hawk moth wing deformation measurements, b. 3D printing of scaled hawk moth wing models, c. scaled hawk moth wing model mounted on the flapping wing apparatus, d. PIV on the scaled hawk moth wing model.

5.2 Materials and Methods

Measuring the aerodynamic loads on natural insect wings experimentally is an extremely challenging task. The forces produced even by larger insects like bumblebees, hawk moths or dragonflies are only on the order of $\mathcal{O}(10^{-4}\,\mathrm{N})$ to $\mathcal{O}(10^{-2}\,\mathrm{N})$ [87, 184, 185]. To measure the aerodynamic performance by the different hawk moth wings in this study, scaled wing models are constructed and tested on a flapping wing mechanism submerged in water. An overview of the different stages of the study is given in fig. 5.1. First, the three-dimensional wing shape is extracted from deformation measurements on real hawk moth wing samples (fig. 5.1a) conducted by our collaborators from the *Agile Systems Lab* at the *Georgia Institute of Technology, USA* [8, 183, 186, 187]. Then, the geometric dimensions of the wing are scaled up in size to reach the same Reynolds number ($Re = 5000$) in our water tank as the original experiments in the wind tunnel. For PIV experiments the wings are painted in black. Finally, the wings are mounted on the flapping wing mechanism and the forces (fig. 5.1c.) and flow fields (fig. 5.1d.) around the wings are recorded. We test four different wing shapes in this study. The shape of a fresh hawk moth wing sample, the shape of an aged hawk moth wing sample, a flattened hawk moth wing sample and a rectangular planform. All four wings have the same wing surface area, span-length R, and mean chord length ($c_m = \textit{surface area}/\textit{span}$).

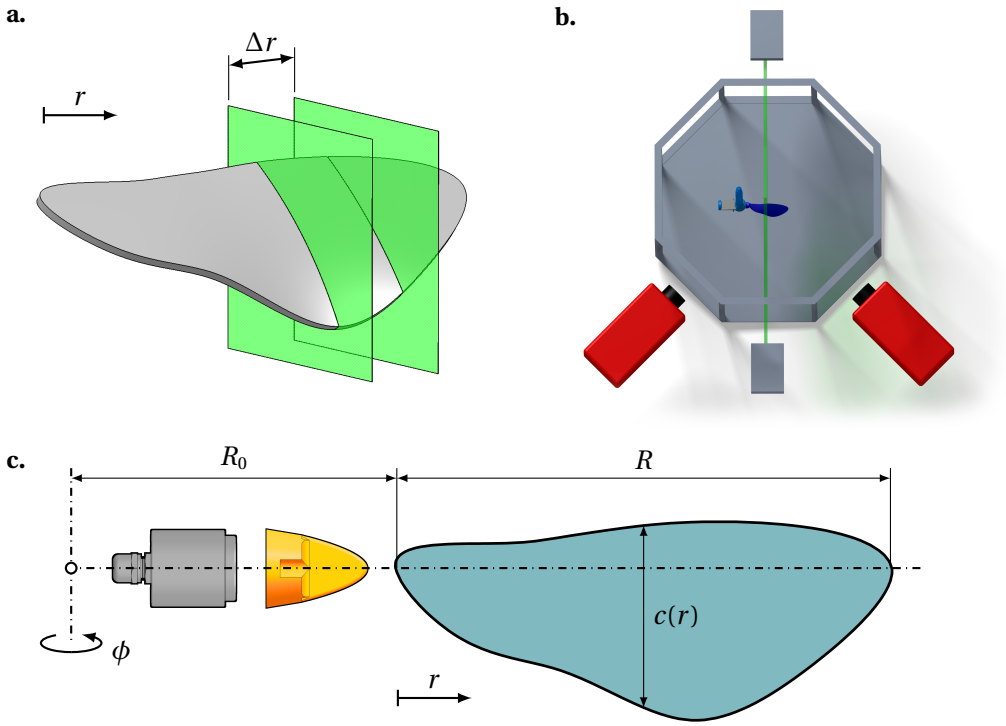

Figure 5.2 – a. Hawk moth wing model mounted on the flapping wing apparatus, b. stereo PIV configuration, and c. load cell, holder and wing assembly.

5.2.1 Kinematics and dynamic scaling

The different length- and time-scales of many technical and biological flows are often characterized with the Reynolds number *Re*. The Reynolds number *Re* is defined as the ratio between the inertial and viscous forces and is calculated for given wing geometries and kinematics in this study as [188]:

$$Re = \frac{U_{\text{ref}}\, l_{\text{ref}}}{\nu} = \frac{\dot{\phi} R_{3b/4}\, c_{\text{m}}}{\nu}, \tag{5.1}$$

where $\dot{\phi}$ is the stroke velocity, $R_{3b/4}$ the radial position at 3/4 the wing span (fig. 5.2c), c_{m} the mean wing chord length, and ν the kinematic viscosity. Here, the reference velocity is calculated at a fixed 3/4-span position. The radius of the second moment of area R_2 used in the previous chapters, changes the reference velocity between the hawk moth and rectangular planform and would not allow a direct comparison of the wings. To ensure dynamic similarity, a Reynolds number $Re = 5000$ is chosen to match the hawk moth (*Manduca sexta*) in hovering flight and the deformation measurements in the wind tunnel [8, 183, 186, 187]. All wing models have a fixed span length and the aspect ratio of the wings is preserved (table 5.1).

The kinematics of a flapping wing in hovering flight are defined by three Euler angles and their variation in time. The stroke angle ϕ determines the wing's position in the horizontal lab frame, or the stroke-plane. The stroke velocity profile is a smoothed linear ramp given by the

following equation [188]:

$$\dot{\phi}(t) = \frac{\dot{\phi}_{\max}}{2a\Delta t} \ln \left[\frac{\cosh\left[a\left(t-t_1\right)\right] \cosh\left[a\left(t-t_4\right)\right]}{\cosh\left[a\left(t-t_2\right)\right] \cosh\left[a\left(t-t_3\right)\right]} \right], \tag{5.2}$$

where the amplitude is defined by the maximum angular velocity $\dot{\phi}_{\max}$ to match the Reynolds number to the experiments in air ($Re = 5000$). The parameters t_1 to t_4 define the beginning and end of the ramp up or ramp down time, and a is the smoothing parameter (fig. 5.3a). The timing parameter in this work are set so the first quarter of the cycle $\Delta t / T = 0.25$ is used to ramp up to the maximum angular velocity and successively ramp down to rest at the end of the cycle. The angle of attack α relates to the rotation of the wing around its span-wise axis. A fixed angle of attack of $\alpha = 40°$ is used in all experiments to match the deformation measurements. The flap angle ψ determines the elevation of the wing relative to the stroke plane. In this study, the elevation angle is kept constant at $\psi = 0°$. A summary of all relevant wing geometry and kinematic parameters is provided in table 5.1.

5.2.2 Experimental platform

The different wing shapes are extracted in wind tunnel experiments on hawk moth wings collected from live specimen by our collaborators from the *Agile Systems Lab* at the *Georgia Institute of Technology, USA* [8, 183, 186, 187]. The fresh wings are first tested and then left to age. The same experiment is repeated with the aged wings and the new wing shape is extracted. The aged wings are deformed by the drying process and become stiffer. Each hawk moth wing model is scaled in size, manufactured and tested on our flapping wing system submerged in an octagonal water tank with an outer diameter of 0.75 m.

The kinematics of the wing are controlled by two servo motors (Maxon motors, type RE35, 90 W, 100 N mm torque, Switzerland) with a transmission of 35 : 1 for the stroke angle and 19 : 1 for the angle of attack. The flapping wing platform is designed to produce highly repeatable results and precise actuation of the attached wings with errors of less than 0.1° between motor controller input (DMC-4040, Galil Motion Control, USA) and the encoder output signal

Table 5.1 – Summary of the experimental parameters of the dynamically scaled wing used for the force measurements. The working fluid in the experiments is water at 20° with a density of $\rho = 998.23\,\mathrm{kg/m^3}$ and a kinematics viscosity of $\nu = 1.00 \times 10^{-6}\,\mathrm{m^2/s}$.

Parameters		hawk moth sample	model wing
Reynolds number	Re	5000	5000
Wing span	R	54.8 mm	120 mm
Mean wing chord	c_m	12.4 mm	33.8 mm
Root cutout	R_0		32.5 mm
Wing thickness	h		2 mm
Stroke amplitude	ϕ_A	180°	180°
Smoothing parameter	a	167	167

measured over multiple cycles in a previous study [71]. The aerodynamic forces and torques are measured with a six-axis IP68 force-torque transducer (Nano17, ATI Industrial Automation, USA) located at the wing root in fig. 5.2a. The load cell has a resolution of 3.13 mN for force and 0.0156 N mm for torque measurements which are recorded at a sample frequency of 1000 Hz with a data acquisition card (National Instruments, USA). The force and flow field measurements are repeated 64 times for each wing and the resulting force signals are ensemble averaged. The time-resolved force data plots are filtered with a zero phase delay low-pass 5th order digital Butterworth filter and a cut-off frequency 10 times higher than the cycle frequency $1/T = 1/(t_4 - t_1)$.

Two high-power light-emitting diodes (LED) (LED Pulsed System, ILA_5150 GmbH, Germany) and cylindrical lenses are used to produce 4 mm-thick light-sheets from opposite sides of the wing (fig. 5.2b). Two sCMOS cameras (ILA_5150 GmbH / PCO AG, Germany) with 2560 px × 2160 px resolutions at a 90° stereo angle are used to record the illuminated plane. Both cameras are equipped with Scheimpflug tilt adapters (ILA_5150 GmbH, Germany) to focus on the tilted plane of interest. Phase-locked three component particle image velocimetry (PIV) is performed by simultaneously triggering the two cameras and LEDs to record individual image pairs for a specific phase angle ϕ and relative spanwise position r/R. In this study, all images are recorded on the plane normal to the span-wise direction at mid-stroke $\phi = 90°$ or $t/T = 0.5$. We use a motorized linear traverse system to move the flapping wing mechanism with the wing attached in span-wise direction r relative to the fixed camera and LED optics. At every span-wise position, the experiment is repeated to capture the flow fields successively over the entire wing span R (fig. 5.2a). We record a total of 21 span-wise positions or $\Delta r = 0.05R$ for the fresh and aged hawk moth wings and 11 span-wise positions or $\Delta r = 0.10R$ for the flat hawk moth and rectangular wing models. The three component flow fields are reconstructed from the stereo PIV image pairs and the camera intrinsic parameters obtained during the stereo calibration procedure. A multi-grid algorithm with a final interrogation window size of 64 px × 64 px and an overlap of 62 % is employed to correlate the raw images and produce the three component velocity flow fields with a spatial resolution of 1.85 mm or 0.055 c. Finally, the velocity flow fields are ensemble-averaged over the 64 consecutive experiments. More details about the experimental setup and measurement procedures of the force and flow field measurements can be found in [71].

5.3 Results

In the following section the aerodynamic performance of the different wing models is evaluated in terms of their force production and the leading edge vortex evolution over the wing span. Finally, we quantify the three-dimensional wing geometry to explain the force variation between the different wings and to identify proper scaling parameters for the leading edge vortex circulation.

5.3.1 Aerodynamic forces

The dimensional lift L and drag D obtained with the force and torque transducer are normalized using the following expression [188]:

$$C_L = \frac{L}{0.5\rho\left(\dot{\phi}_{\max} R_{3b/4}\right)^2 c_{\mathrm{m}} R} \quad \text{and} \quad C_D = \frac{D}{0.5\rho\left(\dot{\phi}_{\max} R_{3b/4}\right)^2 c_{\mathrm{m}} R}, \tag{5.3}$$

where ρ is the density of water, $(\dot{\phi}_{\max} R_{3b/4})$ is the reference velocity, and $(c_{\mathrm{m}} R)$ the surface area of the wing (fig. 5.2c).

In fig. 5.3 the stroke velocity $\dot{\phi}$ profile (a), the ensemble-averaged lift coefficient C_{L} (b), and the ensemble-averaged drag coefficient C_{D} (c) for the four different wings in function of time (t/T) and convective time $(\int_0^t \dot{\phi}(t) R_{\mathrm{tip}}/c_{\mathrm{m}}\,\mathrm{d}\tau)$ are presented. Panels (d) and (e) show box plots of the lift and drag coefficients measured at mid-stroke.

The lift and drag coefficients (fig. 5.3b,c) of all four wings closely follow the timing of the stroke velocity profile (fig. 5.3a). During the acceleration phase of the motion, the lift and drag rise continuously. Once the wings have reached the maximum velocity $\dot{\phi}_{\max}$ only minor force variations are measured. During the deceleration phase, the lift and drag coefficients fall sharply until they return to zero at the end of the motion. The fresh hawk moth wing reach the highest lift and drag coefficients of the four wings at mid-stroke with median force coefficients of $C_{\mathrm{L,mid}} = 1.17$ and $C_{\mathrm{D,mid}} = 1.03$ respectively. The aged wing and flat wing model produce 12 % and 7 % lower lift coefficients but both wings also produce 18 % lower drag coefficients. This gives the flat wing a higher lift-to-drag ratio. The rectangular wing generates significantly lower forces than the hawk moth planform wings. All wings have the same surface area and aspect ratio, but the rectangular wing produces only half the lift and drag coefficients compared to the fresh wing. The difference in planform in our experiments has the highest impact on the aerodynamic forces. The hawk moth planform has a larger local wing area outboards of the wing, where the flow velocities are higher, which has been shown to produce higher wing loadings [91]. The difference in lift and drag production between the fresh, aged and flat hawk moth wing in our study is due to the the wing's deformation in camber, twist and dihedral angle which will be quantified in section 5.3.3.

During the phase of constant stroke velocity the lift and drag coefficients slightly increase until they reach a maximum value just before or around mid-stroke (fig. 5.3b,c). After reaching the peak value the lift and drag coefficients fall slightly again. The global force peak during the unsteady rotary motion is attributed to the growth-cycle of the leading edge vortex, or the vortex circulation and the rate of change of the vortex circulation [2, 188]. In the following section, the three dimensional flow fields around the wings are presented. The leading edge vortex circulation is quantified and related to the force production on the wing.

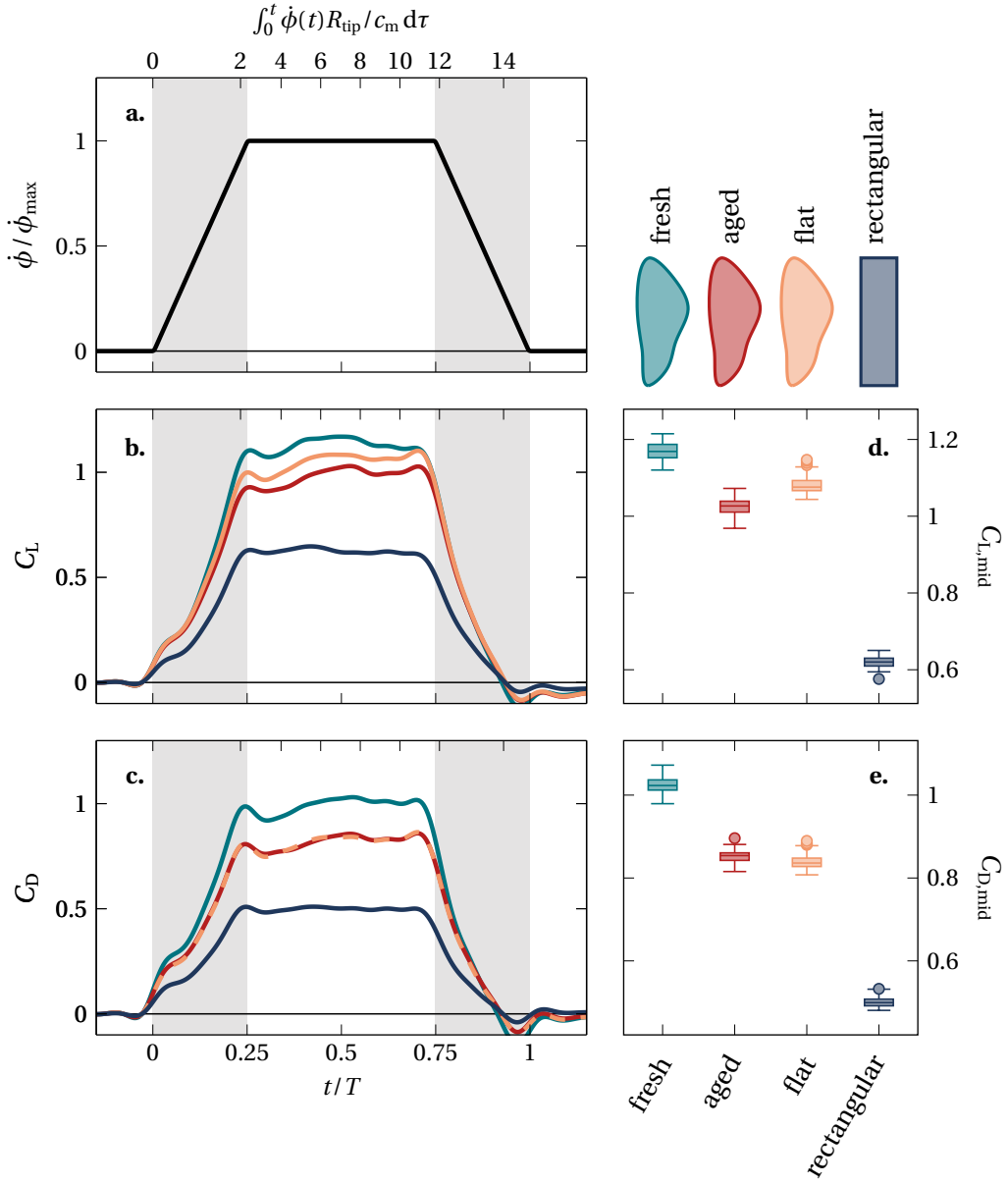

Figure 5.3 – a. Stroke velocity profile, b. lift coefficient, and c. drag coefficient as function of time t/T and convective time $\int_0^t \dot{\phi}(t) R_{\mathrm{tip}} / c_{\mathrm{m}} \, \mathrm{d}\tau$. The grey shaded areas show the acceleration and deceleration phases of the motion. d. Boxplots of the lift coefficient, and e. drag coefficient measured at mid-stroke ($t/T = 0.5$). The box spans the interquartile range of all recorded values. The median of the data is represented by the horizontal line inside the box. The whiskers enclose the minimum to the maximum values measured in all experiments excluding the outliers which are indicated by the circles.

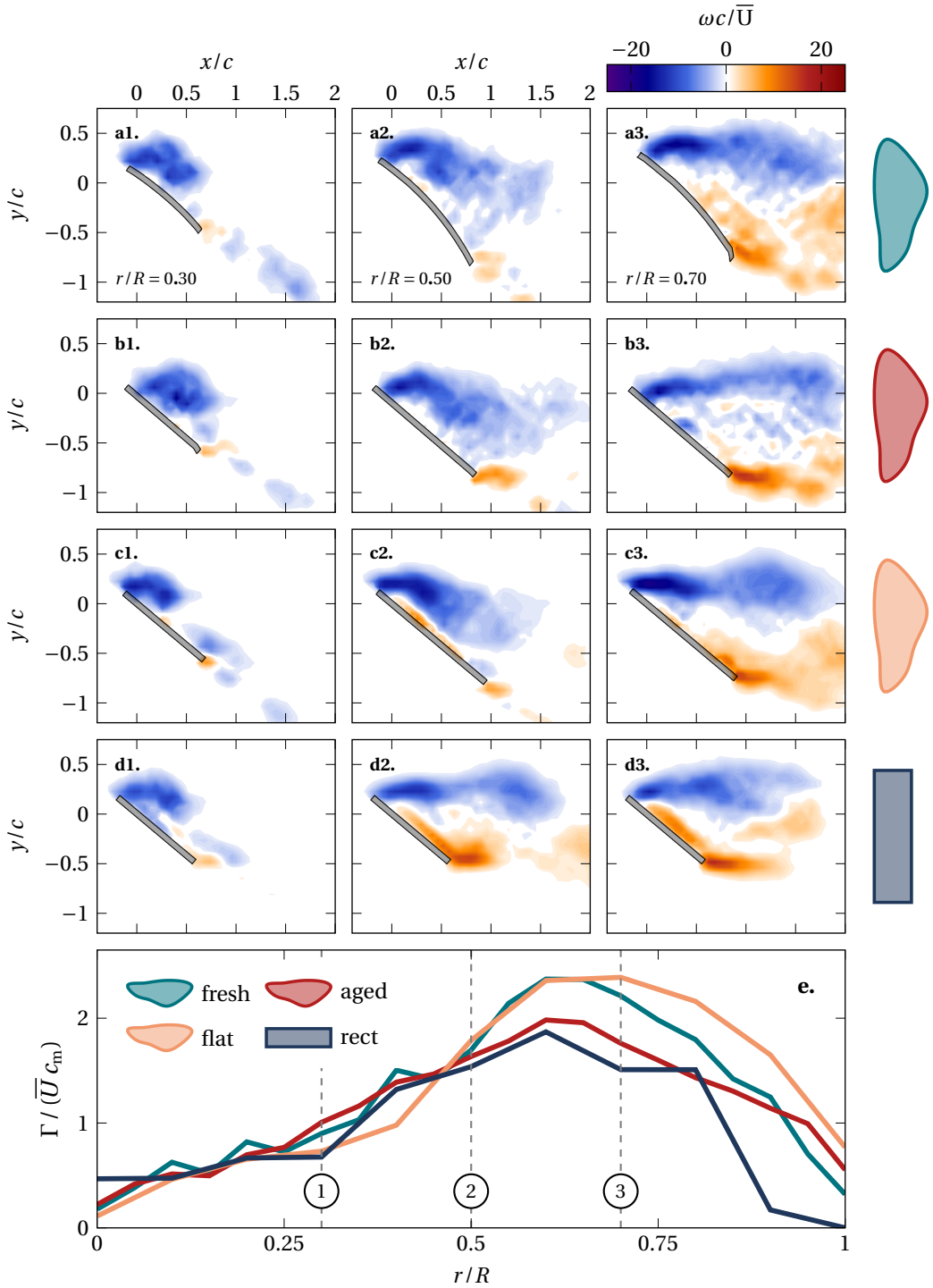

Figure 5.4 – a.-d. Vorticity field snapshots at $t/T = 0.5$ for the fresh, aged, flat and rectangular wing, e. leading edge vortex circulation for the four wings. The span-wise locations of the PIV snapshots are indicated by the number icons.

5.3.2 Three dimensional flow fields

In flapping wing flight at insect scale, the leading edge vortex plays a crucial role in the aerodynamic force production. In this section, the flow fields around the different wings are presented over the full wing span R at mid-stroke ($t/T = 0.5$). The vorticity flow fields at three radial positions normal to the span-wise direction are presented in fig. 5.4a-d for the fresh, aged, flat and rectangular wing. The normalized leading edge vortex circulation associated to the four cases is shown in fig. 5.4e.

The first column in fig. 5.4 displays the vorticity snapshots for all wings at $r/R = 0.3$. A coherent leading edge vortex is present for all four wing shapes. The leading edge vortex stays close to the wing and fills only 1/2 to 2/3 of the wing chord. The leading edge vortex grows along the span in the first half of the wing $r/R < 0.5$ for all wings (fig. 5.4a-d, panels 1,2). The leading edge vortex stays close to the wing and fills the entire chord for the hawk moth planform wings (fig. 5.4a2,b2,c2). In contrast, the leading edge vortex of the rectangular wing lifts off of the wing and stretches in flow direction (fig. 5.4d2). A trailing edge vortex forms and secondary, counter-clockwise vorticity spreads from the trailing edge across the chord. Despite the different wing shapes and planforms, the leading edge vortex circulation in the first half of the wing grows at a similar rate to $\Gamma/\bar{U}c_{\mathrm{m}} = 1.5$ for all wings (fig. 5.4e). The rectangular wing has a lower local chord length $c(r)$ compared to the hawk moth planform and cannot maintain a compact and coherent leading edge vortex of the same size.

All four wings reach the maximum leading edge vortex circulation around $r/R = 2/3$ (fig. 5.4e). The fresh and flat hawk moth wings attain the highest non-dimensional circulation $\Gamma/\bar{U}c_{\mathrm{m}} = 2.4$ The aged hawk moth wing and rectangular planform reach lower circulation peaks of $\Gamma/\bar{U}c_{\mathrm{m}} = 1.9$. In the second half of the span, the leading edge vortex of the hawk moth wings loses coherence and lifts off of the wing (fig. 5.4a3,b3,c3). The leading edge vortex stretches in stream-wise direction and a trailing edge vortex forms. Secondary vorticity develops over the chord albeit not to the extend as seen for the rectangular wing (fig. 5.4d2,d3). The flow state of the hawk moth wings at $r/R = 0.7$ resembles the flow field of the rectangular wing at $r/R = 0.5$, especially for the flat hawk moth wing (fig. 5.4c3). The flow fields between hawk moth wings and the rectangular planform are self-similar to some extend, but the near wake of the hawk moth wings is increased in size relative to the local chord length. The leading edge vortex circulation past $r/R > 0.7$ decreases for all four wings(fig. 5.4e). The circulation of the hawk moth wings stays above the rectangular wing which goes to zero at the wing tip. The hawk moth planforms do not reach zero circulation at the wing tip, indicating that the vortex extends slightly past the wing tip. Compared to the rectangular planform wings, no strong tip vortex growth causes the core flow within the leading edge vortex to decelerate [188, 189]. No additional shear-layer vorticity is produced passed the wing tip but vorticity from the leading edge core is transported in span-wise direction outboards through rotational acceleration [75, 190]. Eventually the vorticity will tilt in down-stream direction and the leading edge vortex does not expand further outboards [191].

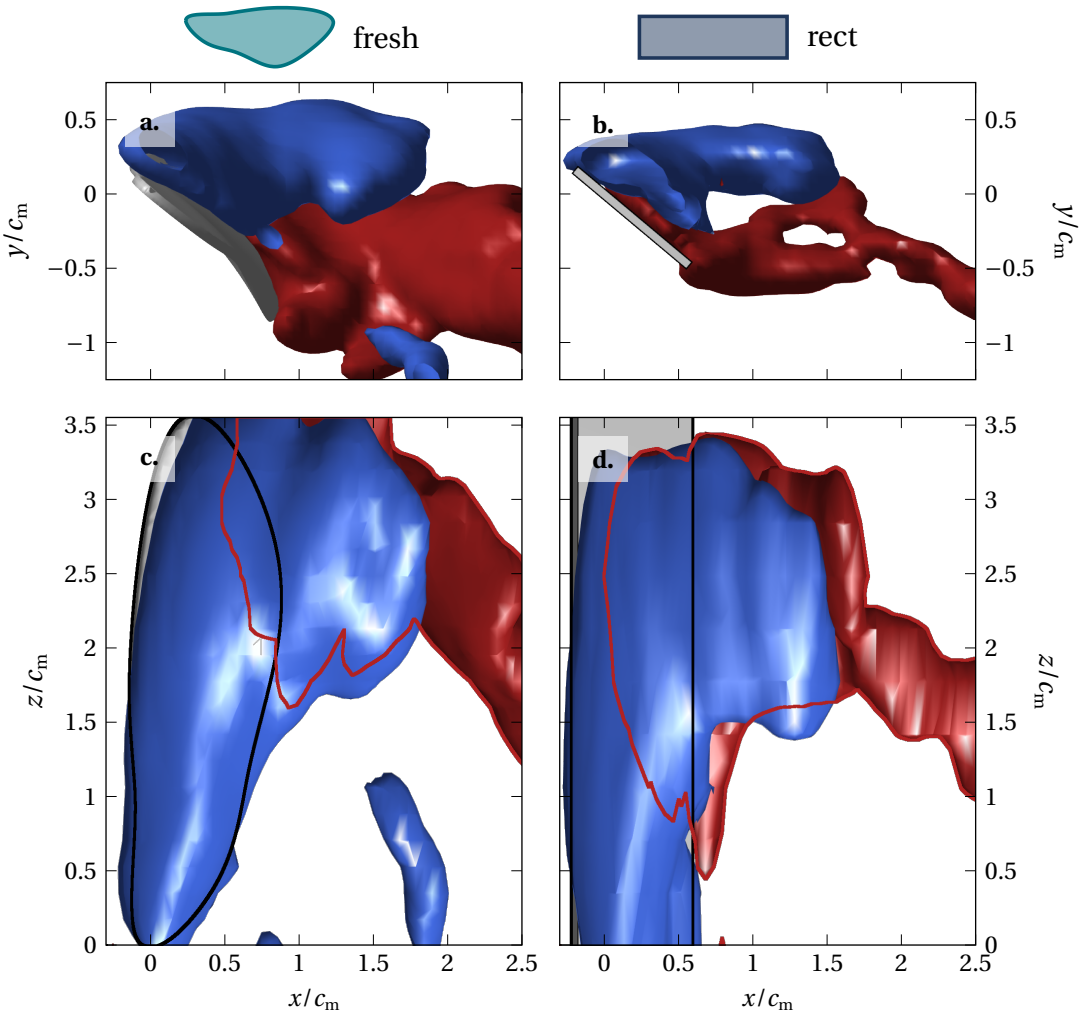

Figure 5.5 – Iso-surfaces of the leading edge vorticity ($\omega_{LEV} = 1/2$) and the trailing edge vorticity ($\omega_{TEV} = 1/3$) for the fresh (a/c) and rectangular wing (b/d). The red contours show the outline of the counter-clockwise vorticity underneath the leading edge vortex.

The entire vortex system around the fresh hawk moth wing and the rectangular wing is visualised with vorticity iso-surfaces in fig. 5.5. Panels (a,b) show a side view of the wing where the wing is seen in span-wise direction analogous to the vorticity snapshots in fig. 5.4. Panels (c,d) display the wing and the vortex system from the top view[1]. The red contours in fig. 5.4c,d show the extend of the secondary vorticity over the wing.

The near wake seen in the side-view is wider for the fresh hawk moth wing compared to the rectangular wing (fig. 5.4a,b) due to the local increase in chord length. The leading edge vortex of the fresh hawk moth wing stays close to the wing for most of the span whereas the leading edge vortex over the rectangular wing lifts off of the wing and secondary edge vorticity spreads over the chord. The extent of the secondary vorticity spread over the wing is revealed by the red contour lines in fig. 5.4c,d. On the hawk moth wing, the secondary vorticity extends only over a small part in the second half of the wing near the trailing edge. The secondary vorticity on the rectangular planform reaches from the first quarter of the span all the way to the wing tip. It reaches far up the chord and only the section directly behind the leading edge is devoid of counter-clockwise rotating vorticity. No span-normal vorticity is present near the wing tip for the rectangular wing attributed to the presence of a strong tip vortex [188]. The hawk moth wing planform and in particular the reduction in chord-length towards the wing tip limits the formation of the tip vortex and allows the leading edge vortex to grow further along the span.

The different wing geometries have a strong impact on the leading edge vortex formation and aerodynamic force production. Often fixed wing positions and average wing geometry quantities are used to define non-dimensional scaling parameters. In the following section, the wing shape is quantified and local scaling parameters are derived.

5.3.3 Wing geometry analysis and leading edge vortex circulation scaling

In the previous sections, the aerodynamic forces and the leading edge vortex evolution over the span was discussed for the four different wing shapes. In this study, all four wings have the same aspect ratio AR, mean chord length c_m, and reference velocity U. Using only the mean chord length c_m and the velocity U at 3/4 of the wing span R to scale the aerodynamic performance does not capture the planform and wing deformation effects. First, the wing geometry is quantified for the four different wings. Then, we apply the local wing geometry to scale the circulation over the span.

The geometry of a wing over the span can be described by the chord length, the camber, the wing twist, the sweep angle, and the dihedral angle. The local chord length c is the distance between leading and trailing edge as illustrated in fig. 5.2c. For a rectangular wing, the chord length is constant over the entire span. The local camber κ is used to describe the asymmetry between the lower and upper surface, or the pressure and suction side, of an airfoil (fig. 5.6a). A positive camber is referred to the suction side being more convex than the pressure side. For a thin deformed foil the camber relates directly to the curvature of the structure. The wing twist

[1] Note that the wings appear skewed from the top view due to the wing's angle of attack.

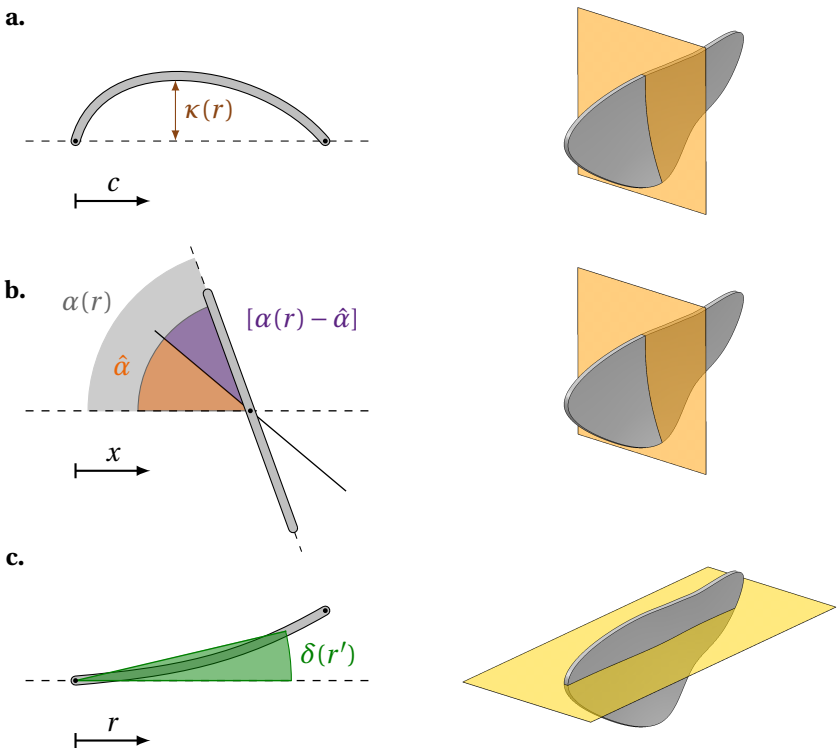

Figure 5.6 – Definitions of a. wing camber κ, b. wing twist $(\alpha - \hat{\alpha})$, and c. dihedral angle δ as function of the local spanwise position r.

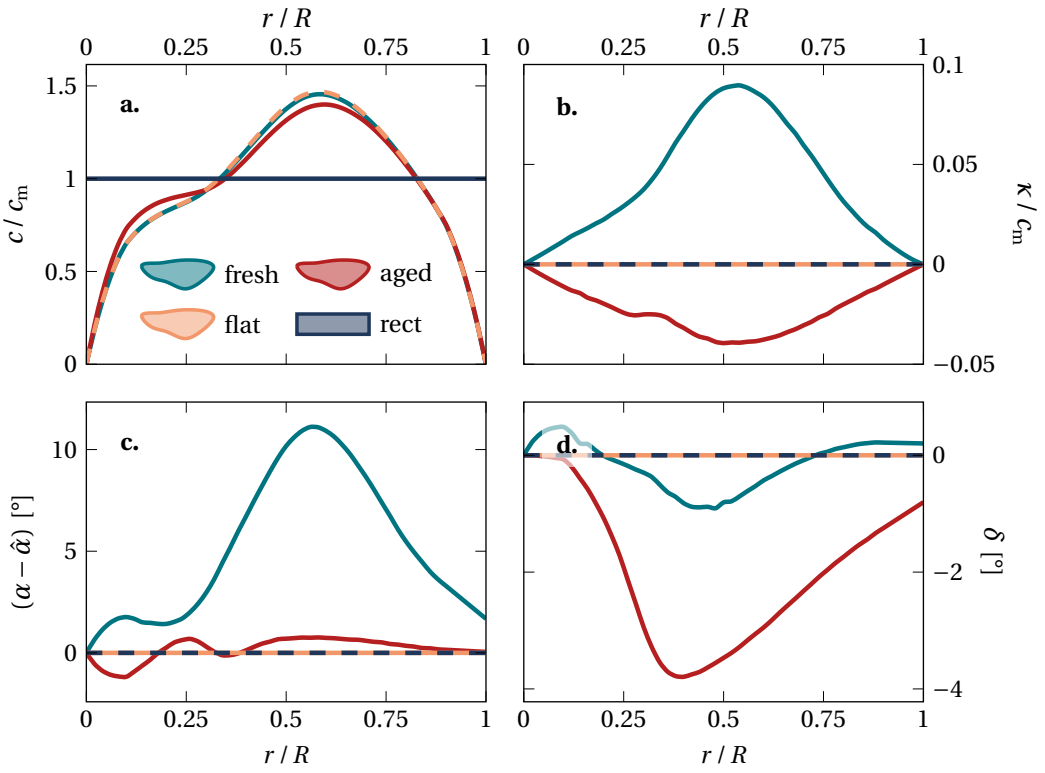

Figure 5.7 – a. Chord length, b. wing camber, c. angle of attack variation, and d. dihedral angle over the span.

is the local angle of attack variation from the imposed geometric angle of attack $\hat{\alpha}$ (fig. 5.6b). A positive twist refers to a local increase in angle of attack α. A wing is considered swept when its centreline is angled relative to the span-wise direction. The rectangular wings are unswept and the hawk moth planform wings have a sweep $< 5°$ over the span. Due to the low angles, the sweep is not further considered in the analysis. The wing's dihedral angle δ describes the local deflection of a wing upwards in the wing's reference frame of view (fig. 5.6c). Here, r' refers to the relative span-wise position if the wing was flattened. Flattening the wing or integrating the local arc-length results in obtaining the full span-length R of the undeformed wingform.

The wing geometries in terms of normalized chord length, normalized camber, wing twist, and dihedral angle for the four different wing shapes are presented in fig. 5.7. The rectangular wing is considered the reference case and has the most basic wing shape. The rectangular wing has a fixed chord length of $c/c_m = 1$, and zero camber, twist, and dihedral angle over the full span length R. The three hawk moth planform wings have the same chord length distribution as they inherently refer to the same wing (fig. 5.7a). The hawk moth wings have zero chord length at the wing root, increase sharply to $c_m = 0.75$ at $r/R = 0.1$. Then, the chord length increases at a lower rate to $c_m = 1.0$ at $r/R = 0.3$. The hawk moth wings have a strong increase in local chord length and reach their maxima $c_m = 1.5$ shortly after mid-span ($r/R = 0.6$). After

the maximum the chord length decreases sharply and goes down to zero at the wing tip. The aged hawk moth wing slightly differs from the fresh and flat wing (fig. 5.7a). The difference in local chord length is due to drying during the ageing process and measurement uncertainties between the two sets of deformation measurements.

The local wing camber are zero at the wing root and tip, and have one clear extremum around mid-span. The fresh wing has a positive camber of $\kappa = 0.09c_m$, whereas the aged wing has a negative camber of $\kappa = -0.04c_m$. The positive wing camber augments the force production on the wings which leads to higher lift but also higher drag coefficients. The aged hawk moth wings have a negative camber which explains in part the lower lift yield compared to the fresh and flat hawk moth wings.

The wing twist or local angle of attack variation is mainly affecting the fresh wing (fig. 5.7c). The aged wing does not exceed |1°| over the full span and the flat and rectangular wing have zero twist. The fresh wing maintains a twist around 2° in the first quarter of the wing span. Then, the local twist increases to reach a maximum of 11° slightly after mid-span. Finally, the twist reduces again down to 2° at the wing tip. The positive wing twist of the fresh hawk moth wings leads to higher local normal forces acting on the wing, which brings about higher lift coefficients but also additional drag. A higher local angle of attack increases the shear at the leading edge. The leading edge vortex gets fed with increases shear which can aid in keeping a coherent leading edge vortex close to the wing along the outboard parts of the wing span.

The dihedral angle δ as defined in fig. 5.6d is presented in fig. 5.7d. The fresh and aged hawk moth wings have only minor peaks of $\delta = -1°$ and $\delta = -4°$ just before mid-stroke. Due to relatively low values of the dihedral angles they are most likely negligible compared to the other geometric features of the different wings.

The wing geometry analysis highlighted two important distinctions between the different wing shapes. Firstly, the wing chord variation or wing planform has the strongest impact on the aerodynamic performance and leading edge vortex evolution over the span in our study. The hawk moth wings start at a low chord length which grows steadily until mid-span. Then, the local chord length grows strongly to a maximum in the second half the wing-span, and finally goes down to zero. This chord length profile matches qualitatively the strength of the leading edge vortex previously discussed (fig. 5.4e). Secondly, The difference in performance of the three hawk moth wing planforms is most likely explained to the presence of a positive camber for the fresh wing, no camber for the flat wing, and a negative camber for the aged wing. The fresh wing also has a positive wing twist around mid-span which provides additional normal force and shear at the leading edge.

The local chord length variation has the strongest impact on the aerodynamic forces and leading edge vortex circulation. To provide additional geometric scaling parameters, we compare now the global wing scaling of the circulation with local, span-wise scaling of the circulation. For the global scaling, we used previously the velocity wing velocity at 3/4 the wing span $\dot{\phi}_{max} R_{3b/4}$ and the mean chord length c_m (fig. 5.4e) [188]. As part of the span-wise

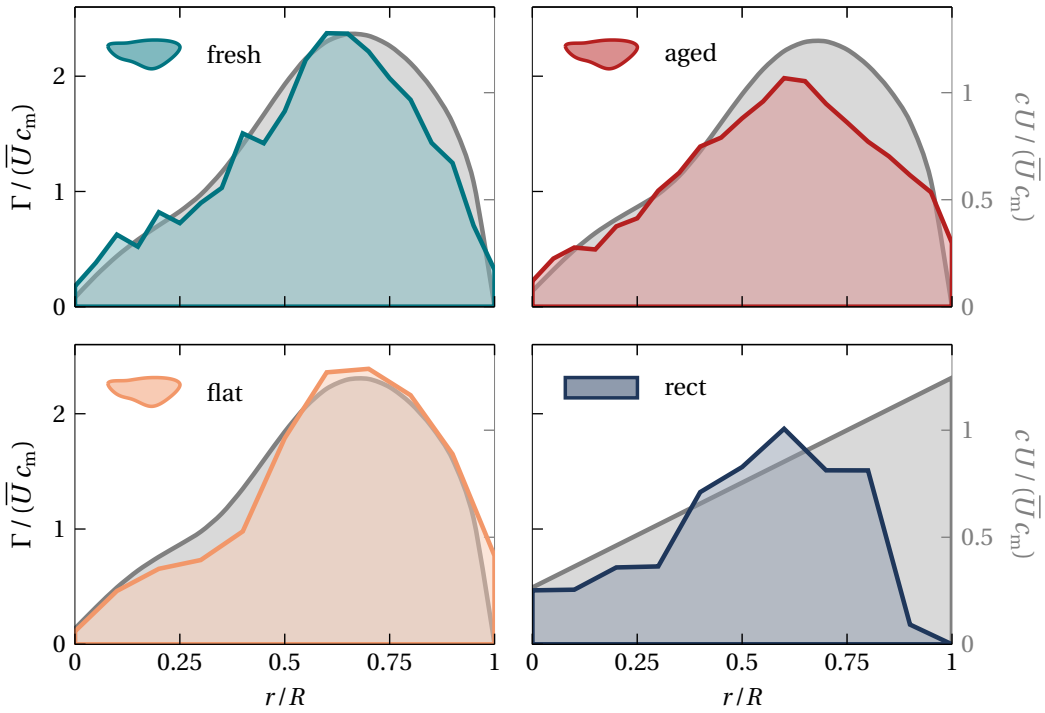

Figure 5.8 – Leading edge vortex circulation Γ and scaling parameter ($c\,U$) over the span for all four tested wings.

circulation scaling, the local chord length $c(r)$ and wing velocity $U(r) = \dot{\phi}_{max}(R_0 + r)$ will now be used. In fig. 5.8, the local scaling parameter variation over the span is overlayed with the leading edge vortex circulation for all four wing shapes. All figures have the same axis limits for comparison. The local scaling for the three hawk moth wing shapes matches their leading edge vortex circulation distributions over the span for most parts. The local scaling of the hawk moth wings captures the rise in circulation up to the maxima particular well for the fresh and flat wings (fig. 5.8a,b). The aged wing does not reach the same maximum values as the fresh and flat wing which is likely tied to the negative camber and dihedral angle at that span-wise position. The local chord and velocity matches the circulation of the rectangular wing only partially. The leading edge vortex circulation would need to increase linearly from the wing root to the wing tip to equal the scaling. However, the velocity field measurements reveal that the leading edge vortex grows in diameter higher than the local chord length past the mid-span (fig. 5.4d2). The vortex is no longer supported by the chord length and lifts off of the wing. Further outboards, the vortex loses almost all of its strength and coherence as the vortex bursts and the tip vortex impedes on the leading edge vortex formation [188].

The leading edge vortex circulation of the rectangular wing does not match its local chord length and velocity scaling well, it resembles the circulation distribution of the hawk moth wings if it were scaled down. This suggests that there is a general leading edge vortex shape for flapping and rotating wings, and the hawk moth wings are adapted to fit the leading edge vortex distribution. For a given wing area, the hawk moth wing planform maintains the strongest

leading edge vortex and produces the highest force coefficients. The rectangular planform utilizes only parts of its wing area which results in lower leading edge vortex circulation and aerodynamic forces in comparison.

5.4 Conclusion

Different insect species have developed their own strategies to manipulate the flow around their wings and in particular the formation of the leading edge vortex. In this part, the hypothesis is tested if the morphology of hawk moth wings evolved to accommodate the formation of a strong and coherent leading edge vortex over the full wing span. We investigate four different wing shapes collected of real hawk moth wings provided by our collaborators. Fresh and then aged hawk moth wing samples are compared with a flat hawk moth wing model and a rectangular planform. The four different wings are dynamically scaled and manufactured for force and span-wise resolved stereo flow field measurements in a water tank. Successively, we analyse the impact of suboptimally deformed hawk moth wings, undeformed hawk moth wings, and the effect of the hawk moth planform relative to a rectangular planform.

The fresh wing produces the highest lift but also the highest drag coefficients. The aged and flat wing produce 12 % and 7 % lower lift coefficients but both wings also produce 18 % lower drag coefficients. The rectangular planform wing has significantly lower aerodynamic forces than the hawk moth wings. While all wings have the same surface area and aspect ratio, the rectangular wing produces only half the lift and drag coefficients compared to the fresh hawk moth wing.

We perform stereo PIV measurements over the full wing span to analyse the leading edge vortex formation and to explain the aerodynamic forces produced by the different wings. The leading edge vortex grows over the span until it reaches a maximum in size and strength around the 2/3 wing span location. The fresh and flat wings reach similar values of the circulation maxima $\Gamma/(\bar{U}c_{\mathrm{m}})$. The aged and rectangular wings have circulation maxima reduced by up to 20 %. In addition, the leading edge vortex stays close to the wing over the majority of the span ($r/R < 2/3$) for the hawk moth planform wings, whereas the vortex lifts off of the wing after mid-span for the rectangular planform. The vortex lift-off coincides with secondary vorticity spreading from the trailing edge over the chord. For the rectangular wing, the secondary vorticity covers large parts of the wing whereas for the fresh hawk moth only a small portion in the second half of the wing is covered.

To further explain the difference in aerodynamic performance and leading edge vortex formation, the wing geometry is quantified in terms of the local chord length, camber, twist, and dihedral angle. The three hawk moth planform wings have a maximum in chord length around $r/R = 2/3$, which coincides with the maximum in leading edge vortex size and strength. Furthermore, the fresh hawk moth wing has positive camber and twist maxima close to mid-span. The positive camber provides additional lift force and the wing twist increases the shear feeding the leading edge vortex.

Based on the wing geometry analysis, the local chord length and wing velocity are selected to scale the leading edge vortex circulation over the full wing span. The new scaling parameter matches the span-wise leading edge vortex circulation closely for the hawk moth planform wings. The local scaling parameter predicts a linear increase in circulation from the wing root to the wing tip for the rectangular wing. This circulation distribution can only be maintained until the circulation maximum $r/R < 2/3$. Then, the vortex breaks down and its circulation decreases to zero towards the wing tip where a strong tip vortex impedes further on the leading edge vortex formation and span-wise vorticity transport. The geometric scaling reveals that the leading edge vortex forms only over parts of the rectangular wing planform area. Its circulation distribution looks qualitatively like a scaled down version of the hawk moth wing circulation.

The self-similar shape of the leading edge vortex circulation indicates that there exists a common leading edge vortex shape for flapping and rotating wings at these Reynolds numbers and aspect ratios. The local wing geometry scaling suggests that the hawk moth wing shape could have evolved to maintain a strong and coherent leading edge vortex over the full span. Where the leading edge vortex expands beyond the mean chord length and breaks down for the rectangular wing, the hawk moth planform has an increased chord length to support the growing vortex. Towards the wing tip, the rectangular planform leads to the formation of a strong tip vortex which impedes on the leading edge vortex formation and span-wise vorticity transport. On the hawk moth wing planform the local chord length reduces greatly towards the tip and eventually reaches zero. This counter-acts the tip vortex formation and allows the leading edge vortex to expand over the full wing span. In consequence, the hawk moth wings achieve double the wing loading compared to rectangular wings. A higher wing loading improves the flight control and escape capabilities of the flapping wing flier [192], and allows the smaller, high aspect ratio wings of the hawk moth to produce sufficient lift to stay in hover [176, 177].

6 Conclusions

Flapping wing flight is an alternative to fixed and rotary wings to produce lift used predominately in nature by flying insects, birds, and mammals. The flight performance of natural and human-made flapping wing fliers at low Reynolds numbers generally has a higher performance in terms of lift production and energy efficiency than rotary or fixed wing micro air vehicles. The formation of a leading edge vortex under unsteady flow conditions produces transient high lift coefficients greatly augmenting the performance for flapping wing fliers at low Reynolds numbers. The reason flapping wing micro air vehicles are not as widely used as their rotary wing counter-parts, is due to the great complexity the bio-inspired flight system presents. Successful flapping wing flight in nature is the interplay of wing and body morphology, muscle actuation, and sensory control which is not yet met by engineered flapping wing systems.

In this thesis, the aerodynamic challenges in flapping wing flight were addressed. In particular, the effects of different wing kinematics, flexibilities, and planforms on the the leading edge vortex development and aerodynamic performance were investigated experimentally on a robotic flapping wing platform. The objective of the thesis was to gain an understanding of the underlying fluid dynamic phenomena in flapping wing flight, and to explore different methods for improving the aerodynamic performance in terms of lift production and energy efficiency. The findings of this thesis aim to explain morphological and behavioural traits in natural fliers, and to provide guidelines for the design and control of engineered flapping wing vehicles.

In part I, the effects of wing kinematics on the vortex formation and aerodynamic performance of flapping wing flight were investigated. We experimentally optimised the kinematics of a flapping wing system in hover with the objective to maximise the average lift production and hovering efficiency. In chapter 1, different parametrisations of the wing kinematics were explored using spline interpolation, Fourier series, and modal reconstruction. The performance of the different approaches was analysed by comparing the diversity of the solutions and coverage of the motion space, the optimisation process and the convergence. Each of the parametrisation approaches is fit for specific applications ranging from the optimisation of

intermittent kinematics (control points), to energy harvesters (Fourier series), and complex animal like locomotion (modal reconstruction).

Due to its robustness in handling experimental constraints and high interpretability of the optimisation parameters, the control point approach was chosen for the flapping wing optimisation in chapter 2. Additional flow field measurements were performed to link the vortical flow structures to the aerodynamic performance for the Pareto-optimal kinematics. We obtain Pareto-optimal kinematics which promote the formation of a strong leading edge vortex and yield high lift coefficients, and kinematics which promote leading edge vortex attachment and are more power efficient. In all cases, a leading-edge vortex is fed by vorticity through the leading edge shear layer which makes the shear layer velocity a good indicator for the growth of the vortex and its impact on the aerodynamic forces. We estimated the shear layer velocity at the leading edge solely from the input kinematics and use it to scale and predict the average and the time-resolved evolution of the circulation and the aerodynamic forces. The experimental data agree well with the shear layer velocity prediction, making it a promising metric to quantify and predict the aerodynamic performance of the flapping wing hovering motion for the design and control of micro air vehicles.

In part II, the effects of wing flexibility on the aerodynamic performance and flow field development in flapping wing flight were investigated. A novel bio-inspired membrane wing design is introduced in chapter 3 and used to study the fluid-structure interactions of flapping membrane wings. We find optimal combinations of the membrane properties and flapping kinematics that out-perform their rigid counterparts both in terms of increased stroke-average lift and efficiency, but the improvements are not persistent over the entire input parameter space. The lift and efficiency optima occur at different angles of attack and effective membrane stiffnesses which we characterised with the aeroelastic number. At optimal aeroelastic numbers, the membrane has a moderate camber between 15% and 20% and its leading and trailing edges align favourably with the flow. Higher camber at lower aeroelastic numbers leads to reduced aerodynamic performance due to negative angles of attack at the leading edge and an over-rotation of the trailing edge.

In chapter 4, we investigated the impact of the membrane deformation on the leading edge vortex formation at different aeroelastic conditions. We identified several new flow characteristics previously not observed in rigid flapping wing flight or other flexible wing studies. The flow topology around the wing is similar to the rigid wing, when the membrane wing is too stiff but the leading edge vortex stays closer to the wing and is more coherent. At lift and efficiency optimal aeroelastic conditions the wing is deformed such that the leading edge is aligned with the incoming flow and the trailing edge oriented downwards. The flow stays attached to the wing and no coherent leading edge vortex is formed in the first half of the cycle. In the second half of the cycle, the vorticity stays close to the membrane but the flow separates over the high curvature of the membrane and a vortex forms in the second half of the wing chord. The membrane wings produce the highest lift coefficients despite suppressing the leading edge vortex formation. These results challenge the claim that a leading edge vortex is always

required to generate high lift in flapping wing flight [2, 11, 26]. If the membrane wing is too flexible, the flow separates over the high curvature of the membrane, and the wing experiences great losses in lift and hovering efficiency. The high membrane curvature eventually leads to negative angles of attack at the leading edge for the lowest observed angle of attack amplitude $\hat{\alpha} = 35°$, and causes a vortex to grow at the pressure side, below the wing. Bats and other natural fliers using compliant membranes actively control the shape of their wings in flight by increasing the tension in their muscles or varying their flight speed, both of which regulate the aeroelastic number we use to characterize the fluid-structure interaction [43, 169]. We suggest using active flow control for artificial flapping wing vehicles by modulating either the wing's angle of attack, membrane wing stiffness, or flow velocity. Using the leading and trailing edge angles as indicators for the flow state and membrane shape allows to maintain optimal aeroelastic conditions without further sensory input.

In part III, the effects of different wing planforms on the leading edge vortex formation and aerodynamic performance in flapping wing flight were explored. Chapter 5 investigates if the morphology of hawk moth wings evolved to accommodate the formation a strong and coherent leading edge vortex over the full wing span for aerodynamic benefits. We extract three-dimensional wing shapes from hawk moth wing samples in wind tunnel experiments, and scale them to the same Reynolds number on a robotic flapping wing system submerged in water. Four different wing shapes were investigated: A Fresh and then aged hawk moth wing sample, a flattened hawk moth wing model, and a rectangular planform. We performed stereo PIV measurements over the full wing span at mid-stroke to analyse the leading edge vortex formation, and recorded the aerodynamic forces produced by the four different wings. The fresh hawk moth wing has the highest wing loading and produces the largest lift but also drag coefficients. The aged and flat wing generate 12 % and 7 % lower lift coefficients but both wings also generate 18 % lower drag coefficients. While all wings have the same surface area and aspect ratio, the rectangular wing produces only half the lift and drag coefficients compared to the fresh hawk moth wing. The difference in force production is also reflected in the leading edge vortex formation on the wings. The hawk moth planform wings have a strong and coherent vortex forming over large parts of the span. The leading edge vortex on the rectangular planform lifts off of the wing after mid-span and its strength is greatly reduced in comparison. We quantified the geometry of the different wings and found that the planform, or chord-length variation has the strongest impact on the aerodynamic performance, followed by the camber and wing twist. Based on the wing geometry analysis, the local chord length and wing velocity are selected to define a span-wise scaling of the leading edge vortex circulation over the full wing.

The new scaling parameter matches the span-wise leading edge vortex circulation closely for the hawk moth planform wings, whereas it can only be maintained until 2/3 of the span for the rectangular planform. The matching of the local wing geometry scaling suggests that the hawk moth wing shape could have evolved to maintain a strong and coherent leading edge vortex over the full span. Where the leading edge vortex expands beyond the mean chord length and breaks down for the rectangular wing, the hawk moth planform has an increased chord

length to support the growing vortex. Towards the wing tip, the rectangular planform leads to the formation of a strong tip vortex which impedes on the leading edge vortex formation and span-wise vorticity transport. On the hawk moth wing planform the local chord length reduces greatly towards the tip and eventually reaches zero. This counter-acts the tip vortex formation and allows the leading edge vortex to expand over the full wing span. In consequence, the hawk moth wings generate double the wing loading compared to rectangular wings. A higher wing loading improves the flight control and escape capabilities of the flapping wing flier [192], and allows the smaller, high aspect ratio wings of the hawk moth to produce sufficient lift to stay in hover [176, 177].

Our investigations of wing kinematics, flexility, and planform in parts I to III demonstrate the strong connection between the leading edge vortex formation and the aerodynamic performance in flapping wing flight. By adapting the kinematics, the vortex formation is directly influenced by a change in the shear-layer velocity feeding the vortex. A constant influx of vorticity provided to the vortex over the full cycle, keeps the vortex attached to the wing and yields the most efficient hovering at vortex formation times around 4. Additional vorticity fed to the vortex generates more lift, but at the cost of increased power consumption. The effects of chord-wise wing flexibility in flapping wing flight can be characterised with the aeroelastic number. A variation in flow velocity or material properties, changes the aeroelastic number and the dynamics of the wing deformation. On a membrane wing hinged at the leading and trailing edges, lower aeroelastic numbers lead to an increase in camber, and lower angles of the leading and trailing edges relative to the flow. The shear at the leading edge is reduced at lower angles and leading edge vortices of lower strength grow close-bound to the wing. At lift and efficiency optimal aeroelastic number, the leading edge is aligned with the flow. The flow stays attached to the wing, and the leading edge vortex is fully suppressed in the first half of the stroke cycle at geometric angles of attack up to $\hat{\alpha} = 55°$. Finally, we find that the span-wise growth of the leading edge vortex is governed by the local chord length and wing velocity distribution. The hawk moth wing planform and shape is adapted such that it provides the growing vortex with enough local wing area to support its size. Towards the wing tip, the local chord of the hawk moth wing shrinks and prevents the formation of a strong tip vortex. This allows the leading edge vortex to form over the entire wing span, and achieve double the wing loading compared to rectangular wings.

A Cycle-average force measurements

A.1 Convergence of the mean force coefficient

Large-scale recirculation of the fluid within the tank due to the down-wash created by the wing can affect the force measurements when repeating many flapping cycles in a closed vessel. In the following section we present a quantitative study to determine the influence of the tank confinement on the average force data for the membrane wing experiments presented in chapter 4 [109]. Figure A.1a summarises the experimental results for two different cases with each three repetitions conducted over 66 cycles. This is equivalent to an experimental time of 5 minutes or more than 4 times the number of cycles of the main study for the higher lift producing case with a frequency of $f = 0.225\,\mathrm{Hz}$. The markers show the cycle-average lift coefficient for the individual cycles and the solid lines represent the cumulative average lift starting from the sixth cycle. The grey area indicates the first five cycles which are being removed from the averaging and the vertical dashed line marks the end of 16 cycles which is the number of cycles considered in the main study. Figure A.1b shows a close-up view with only one out of the three cases for visual clarity. Here, the dashed lines show a moving average over 5 cycles to highlight potential long term drift of the forces due to recirculation in the tank. Even though we see some variation in the moving average lift, the cumulative average values do not change substantially after the first 16 cycles. The largest relative observed drift in the cumulative mean is found for the top case in fig. A.1b which varies from $\overline{C}_{\mathrm{L,n=16}} = 2.449$ to $\overline{C}_{\mathrm{L,n=37}} = 2.496$ which corresponds to a 1.9 % increase.

A.2 Wing inertia

Depending on the mass ratio between the wing and the fluid, inertial forces can be of the same order of magnitude as the aerodynamic forces for flapping wings in air [154]. Our experiments are conducted in water which allows us to achieve low density ratios between the membrane wing and the fluid $\rho_{\mathrm{m}}/\rho_{\mathrm{water}} = 1.20$. We conducted additional experiments in air where the inertial forces dominate the measurement loads on the membrane wings

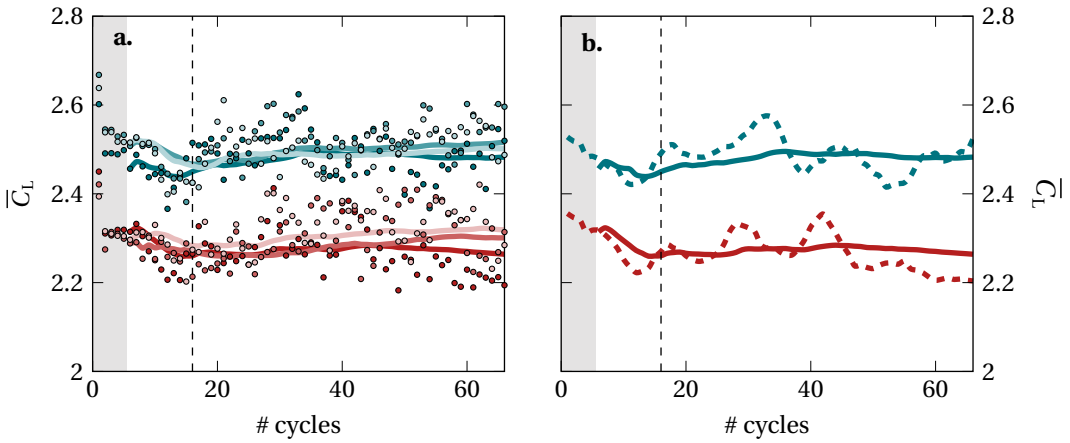

Figure A.1 – Average lift coefficient recorded over 66 cycles for two different frequencies. The different colours refer to different cases and the different shades indicate the different repetitions of the same parameter frequency. The markers indicate the cycle-average lift coefficient for the individual cycles and the solid lines represent the cumulative average lift starting from the sixth cycle.

presented in chapter 4 [109] . In fig. A.2 we present the dimensional average lift force $\overline{L}$ and the average of the absolute drag force $|\overline{D}|$ for the heaviest membrane wing with thickness $t = 1.4\,\text{mm}$, which has the highest contribution of the inertial forces to the total measured force. The open markers show the stroke-average forces in water and the filled markers show the results in air. The first row of images shows an overview of the entire measurement set and the second row of images shows a zoomed in version on the experiments in air. The grey areas highlight the force transducer resolution of 3.13 mN around zero. The inertial forces recorded in air increase with increasing frequency but are close to or even below the resolution of the load cell. For our set-up, the inertial forces are much lower than the fluid mechanics forces and the former are deemed negligible.

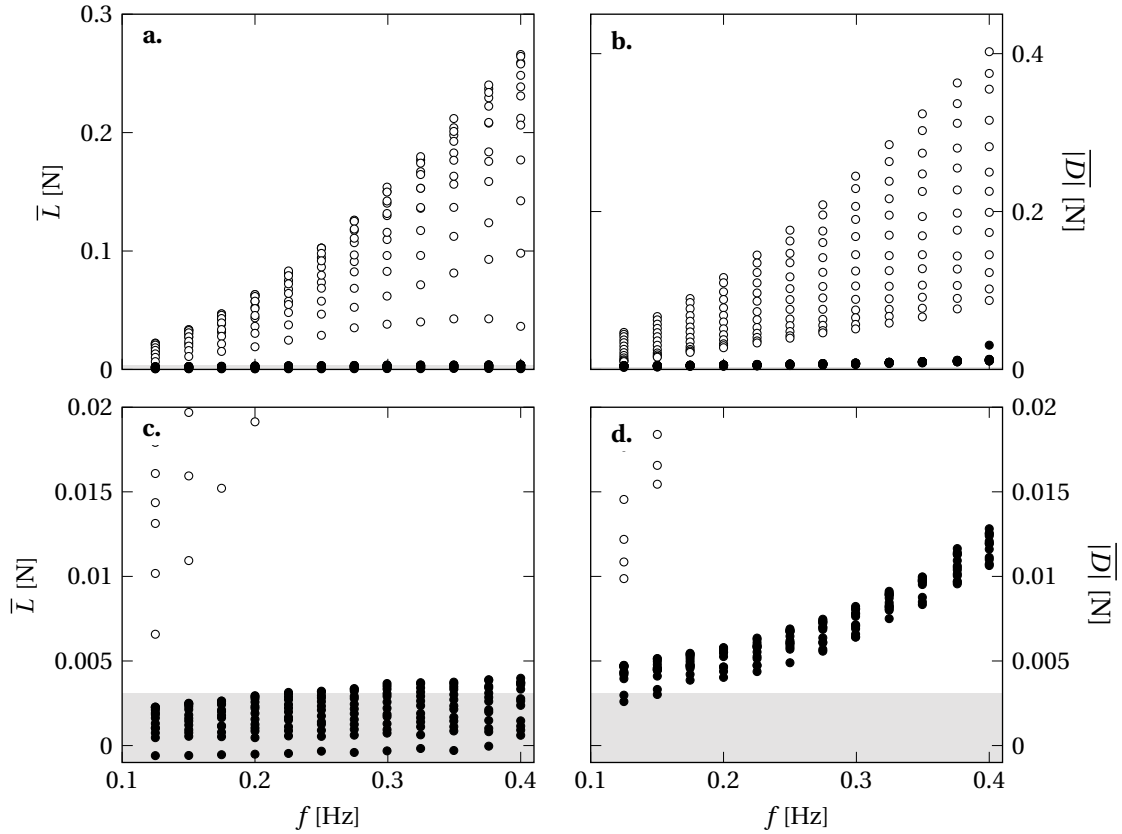

Figure A.2 – Dimensional average lift force $\overline{L}$ and average of the absolute drag force $\overline{|D|}$ for the membrane wing with thickness $t = 1.4\,\text{mm}$. The open markers show the stroke-average forces in water and the filled markers show the results in air.

Bibliography

[1] J. D. Anderson, *Introduction to flight*. New York, NY: McGraw-Hill Education, eighth edition ed., 2016.

[2] J. D. Eldredge and A. R. Jones, "Leading-Edge Vortices: Mechanics and Modeling," *Annual Review of Fluid Mechanics*, vol. 51, Jan. 2019. Number: 1.

[3] A. R. Jones and H. Babinsky, "Unsteady Lift Generation on Rotating Wings at Low Reynolds Numbers," *Journal of Aircraft*, vol. 47, pp. 1013–1021, May 2010. Number: 3.

[4] K. Mulleners and M. Raffel, "The onset of dynamic stall revisited," *Experiments in Fluids*, vol. 52, pp. 779–793, Mar. 2012.

[5] C. Chengguang, "An osprey diving to catch its prey," 2019. https://www.instagram.com/p/B6Ny93RBBt4 (Accessed: 26.10.2022).

[6] T. Houette, E. Gjerde, and P. Gruber, "Unfolding Crease Patterns Inspired by Insect Wings and Variations of the Miura-ori with a Single Vein," *Biomimetics*, vol. 4, p. 45, July 2019.

[7] F. T. Muijres, L. C. Johansson, R. Barfield, M. Wolf, G. R. Spedding, and A. Hedenstrom, "Leading-Edge Vortex Improves Lift in Slow-Flying Bats," *Science*, vol. 319, pp. 1250–1253, Feb. 2008. Number: 5867.

[8] M. Matthews and S. Sponberg, "Hawkmoth flight in the unsteady wakes of flowers," *Journal of Experimental Biology*, p. jeb.179259, Jan. 2018.

[9] U. Pesavento and Z. J. Wang, "Flapping Wing Flight Can Save Aerodynamic Power Compared to Steady Flight," *Physical Review Letters*, vol. 103, p. 118102, Sept. 2009. Number: 11.

[10] L. Zheng, T. Hedrick, and R. Mittal, "A comparative study of the hovering efficiency of flapping and revolving wings," *Bioinspiration & Biomimetics*, vol. 8, p. 036001, May 2013. Number: 3.

[11] C. P. Ellington, C. van den Berg, A. P. Willmott, and A. L. R. Thomas, "Leading-edge vortices in insect flight," *Nature*, vol. 384, pp. 626–630, Dec. 1996. Number: 6610.

[12] A. P. Willmott and C. P. Ellington, "The mechanics of flight in the hawkmoth Manduca sexta. I. Kinematics of hovering and forward flight.," *The Journal of Experimental Biology*, vol. 200, p. 2705, Nov. 1997. Number: 21.

[13] A. P. Willmott, C. P. Ellington, and A. L. R. Thomas, "Flow visualization and unsteady aerodynamics in the flight of the hawkmoth, *Manduca sexta*," *Philosophical Transactions of the Royal Society of London. Series B: Biological Sciences*, vol. 352, pp. 303–316, Mar. 1997.

[14] M. H. Dickinson, "Wing Rotation and the Aerodynamic Basis of Insect Flight," *Science*, vol. 284, pp. 1954–1960, June 1999. Number: 5422.

[15] J. R. Usherwood and C. P. Ellington, "The aerodynamics of revolving wings I. Model hawkmoth wings," *Journal of Experimental Biology*, vol. 205, p. 1547, June 2002. Number: 11.

[16] S. Krishna, M. A. Green, and K. Mulleners, "Flowfield and Force Evolution for a Symmetric Hovering Flat-Plate Wing," *AIAA Journal*, vol. 56, pp. 1360–1371, Apr. 2018. Number: 4.

[17] Z. J. Wang, "Vortex shedding and frequency selection in flapping flight," *Journal of Fluid Mechanics*, vol. 410, pp. 323–341, May 2000.

[18] L. A. Miller and C. S. Peskin, "A computational fluid dynamics of 'clap and fling' in the smallest insects," *Journal of Experimental Biology*, vol. 208, pp. 195–212, Jan. 2005.

[19] S. Shammai, "Spy in the sky," *Nature*, vol. 445, pp. 808–809, Feb. 2007.

[20] M. Elbanhawi, A. Mohamed, R. Clothier, J. Palmer, M. Simic, and S. Watkins, "Enabling technologies for autonomous MAV operations," *Progress in Aerospace Sciences*, vol. 91, pp. 27–52, May 2017.

[21] D. Floreano and R. J. Wood, "Science, technology and the future of small autonomous drones," *Nature*, vol. 521, pp. 460–466, May 2015. Number: 7553.

[22] J. E. Bluman, J. A. Pohly, M. K. Sridhar, C.-k. Kang, D. B. Landrum, F. Fahimi, and H. Aono, "Achieving bioinspired flapping wing hovering flight solutions on Mars via wing scaling," *Bioinspiration & Biomimetics*, vol. 13, p. 046010, June 2018.

[23] J. Balaram, M. Aung, and M. P. Golombek, "The Ingenuity Helicopter on the Perseverance Rover," *Space Science Reviews*, vol. 217, p. 56, June 2021.

[24] C. P. Ellington and M. J. Lighthill, "The aerodynamics of hovering insect flight. VI. Lift and power requirements," *Philosophical Transactions of the Royal Society of London. B, Biological Sciences*, vol. 305, pp. 145–181, Feb. 1984. Publisher: Royal Society.

[25] D. Warrick and K. P. Dial, "Kinematic, aerodynamic and anatomical mechanisms in the slow, maneuvering flight of pigeons," *Journal of Experimental Biology*, vol. 201, pp. 655–672, Mar. 1998.

[26] S. P. Sane, "The aerodynamics of insect flight," *Journal of Experimental Biology*, vol. 206, pp. 4191–4208, Dec. 2003. Number: 23.

[27] W. Shyy, H. Aono, S. Chimakurthi, P. Trizila, C.-K. Kang, C. Cesnik, and H. Liu, "Recent progress in flapping wing aerodynamics and aeroelasticity," *Progress in Aerospace Sciences*, vol. 46, pp. 284–327, Oct. 2010. Number: 7.

[28] A. Beenakkers, D. Van der Horst, and W. Van Marrewijk, "Insect flight muscle metabolism," *Insect Biochemistry*, vol. 14, pp. 243–260, Jan. 1984.

[29] J. H. Marden, "Variability in the Size, Composition, and Function of Insect Flight Muscles," *Annual Review of Physiology*, vol. 62, pp. 157–178, Mar. 2000.

[30] L. Ristroph, G. Ristroph, S. Morozova, A. J. Bergou, S. Chang, J. Guckenheimer, Z. J. Wang, and I. Cohen, "Active and passive stabilization of body pitch in insect flight," *Journal of The Royal Society Interface*, vol. 10, p. 20130237, Aug. 2013.

[31] M. Sun, "Insect flight dynamics: Stability and control," *Reviews of Modern Physics*, vol. 86, pp. 615–646, May 2014.

[32] D. Floreano, J.-C. Zufferey, M. V. Srinivasan, and C. Ellington, eds., *Flying Insects and Robots*. Berlin, Heidelberg: Springer Berlin Heidelberg, 2010.

[33] S. Sponberg, T. L. Daniel, and A. L. Fairhall, "Dual Dimensionality Reduction Reveals Independent Encoding of Motor Features in a Muscle Synergy for Insect Flight Control," *PLOS Computational Biology*, vol. 11, p. e1004168, Apr. 2015.

[34] S. Sponberg, J. P. Dyhr, R. W. Hall, and T. L. Daniel, "Luminance-dependent visual processing enables moth flight in low light," *Science*, vol. 348, pp. 1245–1248, June 2015. Publisher: American Association for the Advancement of Science.

[35] J. M. V. Rayner, "Form and Function in Avian Flight," in *Current Ornithology* (R. F. Johnston, ed.), pp. 1–66, Boston, MA: Springer US, 1988.

[36] M. H. Dickinson, F. O. Lehmann, and K. G. Gotz, "The active control of wing rotation by Drosophila," *Journal of Experimental Biology*, vol. 182, pp. 173–189, Sept. 1993.

[37] D. K. Riskin, D. J. Willis, J. Iriarte-Díaz, T. L. Hedrick, M. Kostandov, J. Chen, D. H. Laidlaw, K. S. Breuer, and S. M. Swartz, "Quantifying the complexity of bat wing kinematics," *Journal of Theoretical Biology*, vol. 254, pp. 604–615, Oct. 2008.

[38] C. Le Roy, R. Cornette, V. Llaurens, and V. Debat, "Effects of natural wing damage on flight performance in *Morpho* butterflies: what can it tell us about wing shape evolution?," *Journal of Experimental Biology*, p. jeb.204057, Jan. 2019.

[39] H. Rajabi, J.-H. Dirks, and S. N. Gorb, "Insect wing damage: causes, consequences and compensatory mechanisms," *Journal of Experimental Biology*, vol. 223, p. jeb215194, May 2020.

[40] C. Roh and M. Gharib, "Honeybees use their wings for water surface locomotion," *Proceedings of the National Academy of Sciences*, vol. 116, pp. 24446–24451, Dec. 2019.

[41] S. Krishna, A. Gehrke, and K. Mulleners, "To tread or not to tread: comparison between water treading and conventional flapping wing kinematics," *Bioinspiration & Biomimetics*, vol. 17, p. 066018, Nov. 2022.

[42] S. A. Combes and T. L. Daniel, "Flexural stiffness in insect wings I. Scaling and the influence of wing venation," *Journal of Experimental Biology*, vol. 206, pp. 2979–2987, Sept. 2003.

[43] J. A. Cheney, J. C. Rehm, S. M. Swartz, and K. S. Breuer, "Bats actively modulate membrane compliance to control camber and reduce drag," *Journal of Experimental Biology*, p. 6, 2022.

[44] R. Dudley, "Biomechanics of Flight in Neotropical Butterflies: Aerodynamics and Mechanical Power Requirements," *Journal of Experimental Biology*, vol. 159, pp. 335–357, Sept. 1991.

[45] Y.-H. J. Fei and J.-T. Yang, "Importance of body rotation during the flight of a butterfly," *Physical Review E*, vol. 93, p. 033124, Mar. 2016.

[46] M. Keennon, K. Klingebiel, and H. Won, "Development of the Nano Hummingbird: A Tailless Flapping Wing Micro Air Vehicle," in *50th AIAA Aerospace Sciences Meeting including the New Horizons Forum and Aerospace Exposition*, Aerospace Sciences Meetings, American Institute of Aeronautics and Astronautics, Jan. 2012.

[47] H. V. Phan, T. Kang, and H. C. Park, "Design and stable flight of a 21 g insect-like tailless flapping wing micro air vehicle with angular rates feedback control," *Bioinspiration & Biomimetics*, vol. 12, p. 036006, Apr. 2017. Number: 3.

[48] M. Karásek, F. T. Muijres, C. De Wagter, B. D. W. Remes, and G. C. H. E. de Croon, "A tailless aerial robotic flapper reveals that flies use torque coupling in rapid banked turns," *Science*, vol. 361, pp. 1089–1094, Sept. 2018. Number: 6407.

[49] N. T. Jafferis, E. F. Helbling, M. Karpelson, and R. J. Wood, "Untethered flight of an insect-sized flapping-wing microscale aerial vehicle," *Nature*, vol. 570, pp. 491–495, June 2019. Number: 7762.

[50] Z. Tu, F. Fei, and X. Deng, "Untethered Flight of an At-Scale Dual-motor Hummingbird Robot with Bio-inspired Decoupled Wings," *IEEE Robotics and Automation Letters*, pp. 1–1, 2020.

[51] T. Ozaki, N. Ohta, T. Jimbo, and K. Hamaguchi, "A wireless radiofrequency-powered insect-scale flapping-wing aerial vehicle," *Nature Electronics*, vol. 4, pp. 845–852, Nov. 2021.

[52] N. Haider, A. Shahzad, M. N. Mumtaz Qadri, and S. I. Ali Shah, "Recent progress in flapping wings for micro aerial vehicle applications," *Proceedings of the Institution of Mechanical Engineers, Part C: Journal of Mechanical Engineering Science*, vol. 235, pp. 245–264, Jan. 2021.

[53] C. Busch, A. Gehrke, and K. Mulleners, "On the parametrisation of motion kinematics for experimental aerodynamic optimisation," *Experiments in Fluids*, vol. 63, p. 10, Jan. 2022. Number: 1.

[54] W. Shyy, M. Berg, and D. Ljungqvist, "Flapping and flexible wings for biological and micro air vehicles," *Progress in Aerospace Sciences*, vol. 35, pp. 455–505, July 1999. Number: 5.

[55] W. Shyy, ed., *Aerodynamics of low Reynolds number flyers*. No. 22 in Cambridge aerospace series, Cambridge ; New York: Cambridge University Press, 2008. OCLC: ocn124075023.

[56] S. A. Ansari, N. Phillips, G. Stabler, P. C. Wilkins, R. Żbikowski, and K. Knowles, "Experimental investigation of some aspects of insect-like flapping flight aerodynamics for application to micro air vehicles," in *Animal locomotion*, pp. 215–236, Springer, 2010.

[57] Y. Bayiz, M. Ghanaatpishe, H. Fathy, and B. Cheng, "Hovering efficiency comparison of rotary and flapping flight for rigid rectangular wings via dimensionless multi-objective optimization," *Bioinspiration & Biomimetics*, vol. 13, p. 046002, May 2018. Number: 4.

[58] E. W. Hawkes and D. Lentink, "Fruit fly scale robots can hover longer with flapping wings than with spinning wings," *Journal of The Royal Society Interface*, vol. 13, p. 20160730, Oct. 2016. Number: 123.

[59] S. Mandre, K. S. Breuer, and M. J. Miller, "Optimizing the periodic motion of a foil at high-Reynolds number," in *9th International Symposium on Adaptive Motion of Animals and Machines (AMAM 2019)*, 2019. Issue: CONF.

[60] I. H. Tuncer and M. Kaya, "Optimization of Flapping Airfoils For Maximum Thrust and Propulsive Efficiency," *AIAA Journal*, vol. 43, pp. 2329–2336, Nov. 2005. Number: 11.

[61] G. J. Berman and Z. J. Wang, "Energy-minimizing kinematics in hovering insect flight," *Journal of Fluid Mechanics*, vol. 582, pp. 153–168, July 2007.

[62] H. Liu and H. Aono, "Size effects on insect hovering aerodynamics: an integrated computational study," *Bioinspiration & Biomimetics*, vol. 4, p. 015002, Mar. 2009. Number: 1.

[63] N. Martin and M. Gharib, "Experimental trajectory optimization of a flapping fin propulsor using an evolutionary strategy," *Bioinspiration & Biomimetics*, vol. 14, p. 016010, Nov. 2018. Number: 1.

[64] S. S. Bhat, J. Zhao, J. Sheridan, K. Hourigan, and M. C. Thompson, "Effects of flapping-motion profiles on insect-wing aerodynamics," *Journal of Fluid Mechanics*, vol. 884, Feb. 2020.

[65] R. Hamming, *Numerical methods for scientists and engineers*. Courier Corporation, 2012.

[66] A. Chipperfield, P. J. Fleming, H. Pohlheim, and C. M. Fonseca, "The MATLAB Genetic Algorithm Toolbox," in *IEE Colloquium on Applied Control Techniques Using MATLAB*, vol. 1995, pp. 10–10, IEE, 1995.

[67] C. Audet, J. Bigeon, D. Cartier, S. Le Digabel, and L. Salomon, "Performance indicators in multiobjective optimization," *European Journal of Operational Research*, vol. 292, pp. 397–422, July 2021.

[68] D. A. Van Veldhuizen, *Multiobjective evolutionary algorithms: classifications, analyses, and new innovations*. Air Force Institute of Technology, 1999.

[69] J. Zhang and M. Small, "Complex Network from Pseudoperiodic Time Series: Topology versus Dynamics," *Physical Review Letters*, vol. 96, p. 238701, June 2006.

[70] S. Tandon and R. I. Sujith, "Condensation in the phase space and network topology during transition from chaos to order in turbulent thermoacoustic systems," *Chaos: An Interdisciplinary Journal of Nonlinear Science*, vol. 31, p. 043126, Apr. 2021.

[71] A. Gehrke and K. Mulleners, "Phenomenology and scaling of optimal flapping wing kinematics," *Bioinspiration & Biomimetics*, vol. 16, p. 026016, Mar. 2021. Number: 2.

[72] S. P. Sane and M. H. Dickinson, "The control of flight force by a flapping wing: lift and drag production," *Journal of Experimental Biology*, vol. 204, p. 2607, Aug. 2001. Number: 15.

[73] F.-O. Lehmann, S. P. Sane, and M. H. Dickinson, "The aerodynamic effects of wing-wing interaction in flapping insect wings," *Journal of Experimental Biology*, vol. 208, pp. 3075–3092, Aug. 2005. Number: 16.

[74] D. D. Chin and D. Lentink, "Flapping wing aerodynamics: from insects to vertebrates," *The Journal of Experimental Biology*, vol. 219, pp. 920–932, Apr. 2016. Number: 7.

[75] D. Lentink and M. H. Dickinson, "Rotational accelerations stabilize leading edge vortices on revolving fly wings," *Journal of Experimental Biology*, vol. 212, pp. 2705–2719, Aug. 2009. Number: 16.

[76] C. P. Ellington, "The Aerodynamics of Hovering Insect Flight. IV. Aeorodynamic Mechanisms," *Philosophical Transactions of the Royal Society B: Biological Sciences*, vol. 305, pp. 79–113, Feb. 1984. Number: 1122.

[77] M. H. Dickinson and K. G. Gotz, "Unsteady aerodynamic performance of model wings at low Reynolds numbers," *The Journal of Experimental Biology*, vol. 174, p. 45, Jan. 1993. Number: 1.

[78] M. Sun, "High-lift generation and power requirements of insect flight," *Fluid Dynamics Research*, vol. 37, pp. 21–39, July 2005. Number: 1-2.

[79] D. B. Mayo and J. G. Leishman, "Comparison of the Hovering Efficiency of Rotating Wing and Flapping Wing Micro Air Vehicles," *Journal of the American Helicopter Society*, vol. 55, pp. 25001–250015, Apr. 2010. Number: 2.

[80] S. N. Fry, R. Sayaman, and M. H. Dickinson, "The aerodynamics of hovering flight in Drosophila," *Journal of Experimental Biology*, vol. 208, pp. 2303–2318, June 2005. Number: 12.

[81] R. J. Bomphrey, T. Nakata, N. Phillips, and S. M. Walker, "Smart wing rotation and trailing-edge vortices enable high frequency mosquito flight," *Nature*, vol. 544, pp. 92–95, Mar. 2017. Number: 7648.

[82] N. Phillips and K. Knowles, "Effect of flapping kinematics on the mean lift of an insect-like flapping wing," *Proceedings of the Institution of Mechanical Engineers, Part G: Journal of Aerospace Engineering*, vol. 225, pp. 723–736, July 2011. Number: 7.

[83] H. E. Taha, M. R. Hajj, and A. H. Nayfeh, "Wing Kinematics Optimization for Hovering Micro Air Vehicles Using Calculus of Variation," *Journal of Aircraft*, vol. 50, pp. 610–614, Mar. 2013. Number: 2.

[84] Y. J. Lee and K. B. Lua, "Optimization of Simple and Complex Pitching Motions for Flapping Wings in Hover," *AIAA Journal*, vol. 56, pp. 2466–2470, June 2018. Number: 6.

[85] M. Milano and M. Gharib, "Uncovering the physics of flapping flat plates with artificial evolution," *Journal of Fluid Mechanics*, vol. 534, pp. 403–409, June 2005.

[86] A. Gehrke, G. Guyon-Crozier, and K. Mulleners, "Genetic Algorithm Based Optimization of Wing Rotation in Hover," *Fluids*, vol. 3, p. 59, Aug. 2018. Number: 3.

[87] C. P. Ellington, "The aerodynamics of hovering insect flight. III. Kinematics," *Philosophical Transactions of the Royal Society of London. B, Biological Sciences*, vol. 305, pp. 41–78, Feb. 1984. Number: 1122.

[88] K. Sum Wu, J. Nowak, and K. S. Breuer, "Scaling of the performance of insect-inspired passive-pitching flapping wings," *Journal of The Royal Society Interface*, vol. 16, p. 20190609, Dec. 2019. Number: 161.

[89] T. Jardin, A. Farcy, and L. David, "Three-dimensional effects in hovering flapping flight," *Journal of Fluid Mechanics*, vol. 702, pp. 102–125, July 2012.

[90] Y. Nan, M. Karásek, M. E. Lalami, and A. Preumont, "Experimental optimization of wing shape for a hummingbird-like flapping wing micro air vehicle," *Bioinspiration & Biomimetics*, vol. 12, p. 026010, Mar. 2017. Number: 2.

[91] S. A. Ansari, K. Knowles, and R. Zbikowski, "Insectlike Flapping Wings in the Hover Part II: Effect of Wing Geometry," *Journal of Aircraft*, vol. 45, pp. 1976–1990, Nov. 2008. Number: 6.

[92] F. Manar, A. Medina, and A. R. Jones, "Tip vortex structure and aerodynamic loading on rotating wings in confined spaces," *Experiments in Fluids*, vol. 55, Sept. 2014. Number: 9.

[93] Z. J. Wang, "Aerodynamic efficiency of flapping flight: analysis of a two-stroke model," *Journal of Experimental Biology*, vol. 211, pp. 234–238, Jan. 2008. Number: 2.

[94] T. Jardin, L. David, and A. Farcy, "Characterization of vortical structures and loads based on time-resolved PIV for asymmetric hovering flapping flight," *Experiments in Fluids*, vol. 46, pp. 847–857, May 2009.

[95] H. Park and H. Choi, "Kinematic control of aerodynamic forces on an inclined flapping wing with asymmetric strokes," *Bioinspiration & Biomimetics*, vol. 7, p. 016008, Mar. 2012. Number: 1.

[96] D. Ishihara, T. Horie, and T. Niho, "An experimental and three-dimensional computational study on the aerodynamic contribution to the passive pitching motion of flapping wings in hovering flies," *Bioinspiration & Biomimetics*, vol. 9, p. 046009, Nov. 2014. Number: 4.

[97] H. V. Phan and H. C. Park, "Wing inertia as a cause of aerodynamically uneconomical flight with high angles of attack in hovering insects," *The Journal of Experimental Biology*, vol. 221, p. jeb187369, Oct. 2018. Number: 19.

[98] L. Graftieaux, M. Michard, and N. Grosjean, "Combining PIV, POD and vortex identification algorithms for the study of unsteady turbulent swirling flows," *Measurement Science and Technology*, vol. 12, pp. 1422–1429, Sept. 2001. Number: 9.

[99] S. Krishna, M. A. Green, and K. Mulleners, "Effect of pitch on the flow behavior around a hovering wing," *Experiments in Fluids*, vol. 60, p. 86, May 2019. Number: 5.

[100] Y. Huang and M. A. Green, "Detection and tracking of vortex phenomena using Lagrangian coherent structures," *Experiments in Fluids*, vol. 56, p. 147, July 2015.

[101] M. Rockwood, Y. Huang, and M. Green, "Tracking coherent structures in massively-separated and turbulent flows," *Physical Review Fluids*, vol. 3, p. 014702, Jan. 2018.

[102] D. E. Rival, J. Kriegseis, P. Schaub, A. Widmann, and C. Tropea, "Characteristic length scales for vortex detachment on plunging profiles with varying leading-edge geometry," *Experiments in Fluids*, vol. 55, p. 1660, Jan. 2014. Number: 1.

[103] J. Kriegseis, M. Kinzel, and D. E. Rival, "On the persistence of memory: do initial conditions impact vortex formation?," *Journal of Fluid Mechanics*, vol. 736, pp. 91–106, Dec. 2013.

[104] F. Manar, P. Mancini, D. Mayo, and A. R. Jones, "Comparison of Rotating and Translating Wings: Force Production and Vortex Characteristics," *AIAA Journal*, vol. 54, pp. 519–530, Feb. 2016. Number: 2.

[105] P. Sattari, D. E. Rival, R. J. Martinuzzi, and C. Tropea, "Growth and separation of a start-up vortex from a two-dimensional shear layer," *Physics of Fluids*, vol. 24, p. 107102, Oct. 2012. Number: 10.

[106] K. Onoue and K. S. Breuer, "A scaling for vortex formation on swept and unswept pitching wings," *Journal of Fluid Mechanics*, vol. 832, pp. 697–720, Dec. 2017.

[107] J. O. Dabiri, "Optimal Vortex Formation as a Unifying Principle in Biological Propulsion," *Annual Review of Fluid Mechanics*, vol. 41, pp. 17–33, Jan. 2009. Number: 1.

[108] M. Gharib, E. Rambod, and K. Shariff, "A universal time scale for vortex ring formation," *Journal of Fluid Mechanics*, vol. 360, pp. 121–140, Apr. 1998.

[109] A. Gehrke, J. Richeux, E. Uksul, and K. Mulleners, "Aeroelastic characterisation of a bio-inspired flapping membrane wing," *Bioinspiration & Biomimetics*, vol. 17, p. 065004, Nov. 2022.

[110] R. J. Wootton, "Functional Morphology of Insect Wings," *Annual Review of Entomology*, vol. 37, pp. 113–140, Jan. 1992. Number: 1.

[111] S. M. Swartz, M. S. Groves, H. D. Kim, and W. R. Walsh, "Mechanical properties of bat wing membrane skin," *Journal of Zoology*, vol. 239, pp. 357–378, June 1996.

[112] E. D. Tytell and G. V. Lauder, "The hydrodynamics of eel swimming," *Journal of Experimental Biology*, vol. 207, pp. 1825–1841, May 2004.

[113] F. Fish and G. Lauder, "Passive and Active Flow Control by Swimming Fishes and Mammals," *Annual Review of Fluid Mechanics*, vol. 38, pp. 193–224, Jan. 2006.

[114] J. Young, S. M. Walker, R. J. Bomphrey, G. K. Taylor, and A. L. R. Thomas, "Details of Insect Wing Design and Deformation Enhance Aerodynamic Function and Flight Efficiency," *Science*, vol. 325, pp. 1549–1552, Sept. 2009. Number: 5947.

[115] D. B. Boerma, K. S. Breuer, T. L. Treskatis, and S. M. Swartz, "Wings as inertial appendages: how bats recover from aerial stumbles," *Journal of Experimental Biology*, p. jeb.204255, Jan. 2019.

[116] S. M. Swartz, M. B. Bennett, and D. R. Carrier, "Wing bone stresses in free flying bats and the evolution of skeletal design for flight," *Nature*, vol. 359, pp. 726–729, Oct. 1992.

[117] J. Rayner, "Bounding and undulating flight in birds," *Journal of Theoretical Biology*, vol. 117, pp. 47–77, Nov. 1985.

[118] D. Lentink, U. K. Müller, E. J. Stamhuis, R. de Kat, W. van Gestel, L. L. M. Veldhuis, P. Henningsson, A. Hedenström, J. J. Videler, and J. L. van Leeuwen, "How swifts control their glide performance with morphing wings," *Nature*, vol. 446, pp. 1082–1085, Apr. 2007.

[119] J. W. Jaworski and N. Peake, "Aeroacoustics of Silent Owl Flight," *Annual Review of Fluid Mechanics*, vol. 52, pp. 395–420, Jan. 2020.

[120] F. T. Muijres, P. Henningsson, M. Stuiver, and A. Hedenström, "Aerodynamic flight performance in flap-gliding birds and bats," *Journal of Theoretical Biology*, vol. 306, pp. 120–128, Aug. 2012.

[121] P. Henningsson, A. Hedenström, and R. J. Bomphrey, "Efficiency of Lift Production in Flapping and Gliding Flight of Swifts," *PLoS ONE*, vol. 9, p. e90170, Feb. 2014.

[122] A. M. Mountcastle and S. A. Combes, "Biomechanical strategies for mitigating collision damage in insect wings: structural design versus embedded elastic materials," *Journal of Experimental Biology*, p. jeb.092916, Jan. 2013.

[123] J. Sun and B. Bhushan, "Structure and mechanical properties of beetle wings: a review," *RSC Advances*, vol. 2, no. 33, p. 12606, 2012.

[124] X. Tian, J. Iriarte-Diaz, K. Middleton, R. Galvao, E. Israeli, A. Roemer, A. Sullivan, A. Song, S. Swartz, and K. Breuer, "Direct measurements of the kinematics and dynamics of bat flight," *Bioinspiration & Biomimetics*, vol. 1, pp. S10–S18, Dec. 2006.

[125] J. W. Bahlman, S. M. Swartz, and K. S. Breuer, "Design and characterization of a multi-articulated robotic bat wing," *Bioinspir. Biomim.*, p. 18, 2013.

[126] F. T. Muijres, L. Christoffer Johansson, Y. Winter, and A. Hedenström, "Leading edge vortices in lesser long-nosed bats occurring at slow but not fast flight speeds," *Bioinspiration & Biomimetics*, vol. 9, p. 025006, May 2014.

[127] A. Song, X. Tian, E. Israeli, R. Galvao, K. Bishop, S. Swartz, and K. Breuer, "Aeromechanics of Membrane Wings with Implications for Animal Flight," *AIAA Journal*, vol. 46, pp. 2096–2106, Aug. 2008. Number: 8.

[128] J. W. Jaworski and R. E. Gordnier, "High-order simulations of low Reynolds number membrane airfoils under prescribed motion," *Journal of Fluids and Structures*, vol. 31, pp. 49–66, May 2012.

[129] M. Abdulrahim, H. Garcia, and R. Lind, "Flight Characteristics of Shaping the Membrane Wing of a Micro Air Vehicle," *Journal of Aircraft*, vol. 42, pp. 131–137, Jan. 2005. Number: 1.

[130] D. J. Pines and F. Bohorquez, "Challenges Facing Future Micro-Air-Vehicle Development," *Journal of Aircraft*, vol. 43, pp. 290–305, Mar. 2006.

[131] B. Stanford, P. Ifju, R. Albertani, and W. Shyy, "Fixed membrane wings for micro air vehicles: Experimental characterization, numerical modeling, and tailoring," *Progress in Aerospace Sciences*, vol. 44, pp. 258–294, May 2008. Number: 4.

[132] R. Bleischwitz, R. de Kat, and B. Ganapathisubramani, "Aspect-Ratio Effects on Aeromechanics of Membrane Wings at Moderate Reynolds Numbers," *AIAA Journal*, vol. 53, pp. 780–788, Mar. 2015.

[133] A. Ramezani, S.-J. Chung, and S. Hutchinson, "A biomimetic robotic platform to study flight specializations of bats," *Science Robotics*, vol. 2, p. eaal2505, Feb. 2017. Number: 3.

[134] B. Thwaites and G. F. J. Temple, "The aerodynamic theory of sails. I. Two-dimensional sails," *Proceedings of the Royal Society of London. Series A. Mathematical and Physical Sciences*, vol. 261, pp. 402–422, May 1961. Number: 1306.

[135] J. N. Nielsen, "Theory of Flexible Aerodynamic Surfaces," *Journal of Applied Mechanics*, vol. 30, pp. 435–442, Sept. 1963. Number: 3.

[136] M. V. Cook and M. Spottiswoode, "Modelling the flight dynamics of the hang glider," *THE AERONAUTICAL JOURNAL*, p. 20, 2005.

[137] P. Fleming and S. Probert, "Design and performance of a small shrouded cretan windwheel," *Applied Energy*, vol. 10, pp. 121–139, Feb. 1982.

[138] B. G. Newman, "Aerodynamic theory for membranes and sails," *Progress in Aerospace Sciences*, vol. 24, pp. 1–27, Jan. 1987. Number: 1.

[139] R. Smith and W. Shyy, "Computational model of flexible membrane wings in steady laminar flow," *AIAA Journal*, vol. 33, pp. 1769–1777, Oct. 1995. Number: 10.

[140] R. Smith and W. Shyy, "Computation of aerodynamic coefficients for a flexible membrane airfoil in turbulent flow: A comparison with classical theory," *Physics of Fluids*, vol. 8, pp. 3346–3353, Dec. 1996. Number: 12.

[141] R. M. Waldman and K. S. Breuer, "Camber and aerodynamic performance of compliant membrane wings," *Journal of Fluids and Structures*, vol. 68, pp. 390–402, Jan. 2017.

[142] G. Alon Tzezana and K. S. Breuer, "Thrust, drag and wake structure in flapping compliant membrane wings," *Journal of Fluid Mechanics*, vol. 862, pp. 871–888, Mar. 2019.

[143] H. Hu, M. Tamai, and J. T. Murphy, "Flexible-Membrane Airfoils at Low Reynolds Numbers," *Journal of Aircraft*, vol. 45, pp. 1767–1778, Sept. 2008.

[144] G. Koekkoek, F. T. Muijres, L. C. Johansson, M. Stuiver, B. W. van Oudheusden, and A. Hedenström, "Stroke plane angle controls leading edge vortex in a bat-inspired flapper," *Comptes Rendus Mécanique*, vol. 340, pp. 95–106, Jan. 2012.

[145] P. Rojratsirikul, Z. Wang, and I. Gursul, "Unsteady fluid–structure interactions of membrane airfoils at low Reynolds numbers," *Experiments in Fluids*, vol. 46, pp. 859–872, May 2009. Number: 5.

[146] P. Rojratsirikul, M. Genc, Z. Wang, and I. Gursul, "Flow-induced vibrations of low aspect ratio rectangular membrane wings," *Journal of Fluids and Structures*, vol. 27, pp. 1296–1309, Nov. 2011. Number: 8.

[147] R. E. Gordnier, "High fidelity computational simulation of a membrane wing airfoil," *Journal of Fluids and Structures*, p. 21, 2009.

[148] P. Rojratsirikul, Z. Wang, and I. Gursul, "Effect of pre-strain and excess length on unsteady fluid–structure interactions of membrane airfoils," *Journal of Fluids and Structures*, vol. 26, pp. 359–376, Apr. 2010. Number: 3.

[149] R. E. Gordnier and P. J. Attar, "Impact of flexibility on the aerodynamics of an aspect ratio two membrane wing," *Journal of Fluids and Structures*, vol. 45, pp. 138–152, Feb. 2014.

[150] X. He and J.-J. Wang, "Fluid–structure interaction of a flexible membrane wing at a fixed angle of attack," *Physics of Fluids*, vol. 32, p. 127102, Dec. 2020. Number: 12.

[151] J. M. Birch, "Force production and flow structure of the leading edge vortex on flapping wings at high and low Reynolds numbers," *Journal of Experimental Biology*, vol. 207, pp. 1063–1072, Mar. 2004. Number: 7.

[152] W. Shyy and H. Liu, "Flapping Wings and Aerodynamic Lift: The Role of Leading-Edge Vortices," *AIAA Journal*, vol. 45, pp. 2817–2819, Dec. 2007. Number: 12.

[153] L. Tregidgo, Z. Wang, and I. Gursul, "Unsteady fluid–structure interactions of a pitching membrane wing," *Aerospace Science and Technology*, vol. 28, pp. 79–90, July 2013. Number: 1.

[154] P. Gopalakrishnan and D. K. Tafti, "Effect of Wing Flexibility on Lift and Thrust Production in Flapping Flight," *AIAA Journal*, vol. 48, pp. 865–877, May 2010. Number: 5.

[155] J. W. Jaworski and R. E. Gordnier, "Thrust augmentation of flapping airfoils in low Reynolds number flow using a flexible membrane," *Journal of Fluids and Structures*, vol. 52, pp. 199–209, Jan. 2015.

[156] S. Sekhar, P. Windes, X. Fan, and D. K. Tafti, "Canonical description of wing kinematics and dynamics for a straight flying insectivorous bat (Hipposideros pratti)," *PLOS ONE*, vol. 14, p. e0218672, June 2019.

[157] H. Hu, A. G. Kumar, G. Abate, and R. Albertani, "An experimental investigation on the aerodynamic performances of flexible membrane wings in flapping flight," *Aerospace Science and Technology*, vol. 14, pp. 575–586, Dec. 2010.

[158] V. Mathai, G. A. Tzezana, A. Das, and K. S. Breuer, "Fluid–structure interactions of energy-harvesting membrane hydrofoils," *Journal of Fluid Mechanics*, vol. 942, p. R4, July 2022.

[159] R. J. Bomphrey and R. Godoy-Diana, "Insect and insect-inspired aerodynamics: unsteadiness, structural mechanics and flight control," *Current Opinion in Insect Science*, vol. 30, pp. 26–32, Dec. 2018.

[160] P. Grandgeorge, C. Baek, H. Singh, P. Johanns, T. G. Sano, A. Flynn, J. H. Maddocks, and P. M. Reis, "Mechanics of two filaments in tight orthogonal contact," *Proceedings of the National Academy of Sciences*, vol. 118, p. e2021684118, Apr. 2021.

[161] A. Gehrke, J. Richeux, and K. Mulleners, "Video: Don't be rigid, be BILLY," in *74th Annual Meeting of the APS Division of Fluid Dynamics - Gallery of Fluid Motion*, (Phoenix, AZ), American Physical Society, Nov. 2021.

[162] B. J. Knörlein, D. B. Baier, S. M. Gatesy, J. D. Laurence-Chasen, and E. L. Brainerd, "Validation of XMALab software for marker-based XROMM," *Journal of Experimental Biology*, p. jeb.145383, Jan. 2016.

[163] E. M. Mikhail, J. S. Bethel, and J. C. McGlone, *Introduction to modern photogrammetry*, vol. 19. John Wiley & Sons, 2001.

[164] J. Fu, X. Liu, W. Shyy, and H. Qiu, "Effects of flexibility and aspect ratio on the aerodynamic performance of flapping wings," *Bioinspiration & Biomimetics*, vol. 13, p. 036001, Mar. 2018. Number: 3.

[165] O. M. Curet, A. Carrere, R. Waldman, and K. S. Breuer, "Aerodynamic Characterization of a Wing Membrane with Variable Compliance," *AIAA Journal*, vol. 52, pp. 1749–1756, Aug. 2014. Number: 8.

[166] J. R. Bohnker and K. S. Breuer, "Control of Separated Flow Using Actuated Compliant Membrane Wings," *AIAA Journal*, vol. 57, pp. 3801–3811, Sept. 2019.

[167] J. D. Eldredge, J. Toomey, and A. Medina, "On the roles of chord-wise flexibility in a flapping wing with hovering kinematics," *Journal of Fluid Mechanics*, vol. 659, pp. 94–115, Sept. 2010.

[168] J. Li, Y. Wang, M. Graham, and X. Zhao, "Vortex moment map for unsteady incompressible viscous flows," *Journal of Fluid Mechanics*, vol. 891, p. A13, May 2020.

[169] X. Fan, S. Swartz, and K. Breuer, "Power requirements for bat-inspired flapping flight with heavy, highly articulated and cambered wings," *Journal of The Royal Society Interface*, vol. 19, p. 20220315, Sept. 2022.

[170] D. B. Nicholson, A. J. Ross, and P. J. Mayhew, "Fossil evidence for key innovations in the evolution of insect diversity," *Proceedings of the Royal Society B: Biological Sciences*, vol. 281, p. 20141823, Oct. 2014.

[171] S. K. Jones, Y. J. J. Yun, T. L. Hedrick, B. E. Griffith, and L. A. Miller, "Bristles reduce the force required to 'fling' wings apart in the smallest insects," *Journal of Experimental Biology*, vol. 219, pp. 3759–3772, Dec. 2016.

[172] W. Shyy, C.-k. Kang, P. Chirarattananon, S. Ravi, and H. Liu, "Aerodynamics, sensing and control of insect-scale flapping-wing flight," *Proceedings of the Royal Society A: Mathematical, Physical and Engineering Sciences*, vol. 472, p. 20150712, Feb. 2016. Number: 2186.

[173] R. Dudley, *The biomechanics of insect flight: form, function, evolution*. Princeton University Press, 2002.

[174] W. Shyy, H. Aono, C.-k. Kang, and H. Liu, *An introduction to flapping wing aerodynamics*. Cambridge aerospace series, Cambridge ; New York: Cambridge University Press, 2013.

[175] C. Le Roy, V. Debat, and V. Llaurens, "Adaptive evolution of butterfly wing shape: from morphology to behaviour," *Biological Reviews*, p. brv.12500, Feb. 2019.

[176] B. R. Aiello, M. Tan, U. Bin Sikandar, A. J. Alvey, B. Bhinderwala, K. C. Kimball, J. R. Barber, C. A. Hamilton, A. Y. Kawahara, and S. Sponberg, "Adaptive shifts underlie the divergence in wing morphology in bombycoid moths," *Proceedings of the Royal Society B: Biological Sciences*, vol. 288, p. 20210677, Aug. 2021. Publisher: Royal Society.

[177] B. R. Aiello, U. B. Sikandar, H. Minoguchi, B. Bhinderwala, C. A. Hamilton, A. Y. Kawahara, and S. Sponberg, "The evolution of two distinct strategies of moth flight," *Journal of The Royal Society Interface*, vol. 18, no. 185, p. 20210632, 2021. Publisher: Royal Society.

[178] C. Vourtsis, W. Stewart, and D. Floreano, "Robotic *Elytra:* Insect-Inspired Protective Wings for Resilient and Multi-Modal Drones," *IEEE Robotics and Automation Letters*, vol. 7, pp. 223–230, Jan. 2022.

[179] D. L. Altshuler, W. B. Dickson, J. T. Vance, S. P. Roberts, and M. H. Dickinson, "Short-amplitude high-frequency wing strokes determine the aerodynamics of honeybee flight," *Proceedings of the National Academy of Sciences*, vol. 102, pp. 18213–18218, Dec. 2005.

[180] C. P. Ellington, "Non-Steady-State Aerodynamics of the Flight of Encarsia Formosa," in *Swimming and Flying in Nature* (T. Y.-T. Wu, C. J. Brokaw, and C. Brennen, eds.), pp. 783–796, Boston, MA: Springer US, 1975.

[181] A. M. Kuethe, "On the mechanics of flight of small insects," in *Swimming and flying in nature*, pp. 803–813, Springer, 1975.

[182] M. P. Ford, V. T. Kasoju, M. G. Gaddam, and A. Santhanakrishnan, "Aerodynamic effects of varying solid surface area of bristled wings performing clap and fling," *Bioinspiration & Biomimetics*, vol. 14, p. 046003, May 2019.

[183] M. Matthews, *Plant-pollinator aerodynamics*. PhD thesis, Georgia Tech, 2022.

[184] C. Somps and M. Luttges, "Dragonfly Flight: Novel Uses of Unsteady Separated Flows," *Science*, vol. 228, pp. 1326–1329, June 1985. Publisher: American Association for the Advancement of Science.

[185] G. Rüppell, "Kinematic Analysis of Symmetrical Flight Manoeuvres of Odonata," *Journal of Experimental Biology*, vol. 144, pp. 13–42, July 1989.

[186] M. Guasch, M. Matthews, A. Gehrke, and K. Mulleners, "Wing flexibility impacts LEV bursting location on hawkmoth wings," in *Bulletin of the American Physical Society*, vol. 66, APS, 2021.

[187] M. Matthews, M. Guasch, A. Gehrke, K. Mulleners, and S. Sponberg, "On the influence of wing aging on the quasi-steady aerodynamics of hawk moth wings," *(In preparation)*, 2022.

[188] A. Medina and A. R. Jones, "Leading-edge vortex burst on a low-aspect-ratio rotating flat plate," *Physical Review Fluids*, vol. 1, Aug. 2016. Number: 4.

[189] A. R. Jones, A. Medina, H. Spooner, and K. Mulleners, "Characterizing a burst leading-edge vortex on a rotating flat plate wing," *Experiments in Fluids*, vol. 57, Apr. 2016. Number: 4.

[190] C. J. Wojcik and J. H. J. Buchholz, "Vorticity transport in the leading-edge vortex on a rotating blade," *Journal of Fluid Mechanics*, vol. 743, pp. 249–261, Mar. 2014.

[191] J. M. Akkala and J. H. J. Buchholz, "Vorticity transport mechanisms governing the development of leading-edge vortices," *Journal of Fluid Mechanics*, vol. 829, pp. 512–537, Oct. 2017.

[192] J. Burns and R. Ydenberg, "The effects of wing loading and gender on the escape flights of least sandpipers (Calidris minutilla) and western sandpipers (Calidris mauri)," *Behavioral Ecology and Sociobiology*, vol. 52, pp. 128–136, July 2002.

ALEXANDER GEHRKE

EPFL STI IGM UNFOLD, (Bâtiment MED) 0 2326, Station 9, CH-1015 Lausanne
Email: **alexander.gehrke@epfl.ch** ⋄ Phone: **+41 21 693 98 27**

EDUCATION

École Polytechnique Fédérale de Lausanne (EPFL), January 2023
Lausanne, Switzerland
Doctor of Philosophy, Mechanical Engineering
Thesis: The effects of kinematics, flexibility, and planform on the vortex formation and aerodynamic performance of flapping wing flight
Advisor: Karen Mulleners

University of Kassel, Kassel, Germany October 2018
Master of Science, Mechanical Engineering
Thesis: Optimizing the kinematics of a pitching panel in forward motion with a genetic algorithm
Advisors: Karen Mulleners, Markus Rütten & Olaf Wünsch

University of Kassel, Kassel, Germany June 2017
Bachelor of Science, Mechanical Engineering Thesis: Calculation of integral surfaces from unsteady three-dimensional vector fields and their fluid mechanical interpretation
Advisors: Markus Rütten & Olaf Wünsch

HONORS, AWARDS & ACHIEVEMENTS

Best Poster Prize (3rd place) at the international symposium on Adaptive Motion of Animals and Machines (AMAM 2021) 2021
PROMOS scholar ship for studies abroad (DAAD, University of Kassel) 2018
SHOSTA scholar ship for academic travels (DAAD, University of Kassel) 2017

ACADEMIC & PROFESSIONAL EXPERIENCE

EPFL, Lausanne, Switzerland September 2018 - January 2023
Graduate Research and Teaching Assistant, Advisor: Karen Mulleners
Investigation of optimal aerodynamic performance of bio-inspired propulsors in terms of their kinematics, flexibility and planform. Combined experimental studies and data-driven methods.

German Aerospace Center (DLR), Göttingen, Germany June - November 2014
Research Assistant, Advisor: Markus Rütten
Applied studies at the Department of High Speed Configurations (AS-HGK): Numerical simulations and analysis of fluid mechanics systems.

TEACHING EXPERIENCE

EPFL, Lausanne, Switzerland Fall 2018/2020/2021
Designed and tutored exercise session for ME-445: Aerodynamics, Master level (MSc) course. Preparation of exercise session and graded project work following the course's lecture.

EPFL, Lausanne, Switzerland Fall 2018/2019
Supervision and grading of group project work for CS-433: Master level (MSc) course. Mentoring computer science students in the application of machine learning techniques on experimental data collected in our laboratory, including preparation of experiments, analyzing data and writing of a scientific report.

EPFL, Lausanne, Switzerland Spring 2020/2021
Tutored mechanical engineering measurement techniques for ME-301: Bachelor level (BSc) course. Teaching of particle image velocimetry as part of the measurement techniques seminar, including preparation of experiments, analyzing data and writing of a scientific report.

PUBLICATIONS & CONFERENCE PROCEEDINGS

Journal publications

1. Krishna, S., **Gehrke, A.** and Mulleners, K., To tread or not to tread: comparison between water treading and conventional flapping wing kinematics. Bioinspiration & Biomimetics (2022).
2. **Gehrke, A.**, Richeux, J., Uksul, E. and Mulleners, K. Aeroelastic characterisation of a bio-inspired flapping membrane wing. Bioinspiration & Biomimetics (2022).
3. Busch, C., **Gehrke, A.** and Mulleners, K. On the parametrisation of motion kinematics for experimental aerodynamic optimisation. Exp Fluids 63, 10 (2022).
4. **Gehrke, A.** and Mulleners, K. Phenomenology and scaling of optimal flapping wing kinematics. Bioinspiration & Biomimetics 16, 026016 (2021).
5. **Gehrke, A.**, Guyon-Crozier, G. and Mulleners, K. Genetic Algorithm Based Optimization of Wing Rotation in Hover. Fluids 3, 59 (2018).

Journal publications - In preparation

1. **Gehrke, A.** and Mulleners, K., Vortex dynamics and aerodynamic performance of highly deformable flapping wings. (To be submitted, 2022)
2. Matthews M., Guasch, M., **Gehrke, A.**, Mulleners, K. and Sponberg S., On the Influence of Wing Aging on the Quasi-Steady Aerodynamics of Hawk Moth Wings. (To be submitted, 2022)
3. **Gehrke, A.**, Matthews M., Guasch, M., Sponberg S. and Mulleners, K., Leading Edge Vortex Evolution and Force Production of Hawk Moth Wings. (To be submitted, 2023)

Conference proceedings

1. **Gehrke, A.**, Richeux, J. and Mulleners, K. Video: Don't be rigid, be BILLY. in 74th Annual Meeting of the APS Division of Fluid Dynamics - Gallery of Fluid Motion (American Physical Society, 2021).
2. **Gehrke, A.** and Mulleners, K. Role of adaptive camber on optimal flapping wing performance. in The international symposium on Adaptive Motion of Animals and Machines (AMAM 2021).
3. **Gehrke, A.** and Mulleners, K. Adaptive pitching motion kinematics for tuning flapping wing aerodynamic performance. The international symposium on Adaptive Motion of Animals and Machines (AMAM 2019).
4. **Gehrke, A.**, Wuensch, O. and Ruetten, M. Integral Surface Analysis of Vortical Lobed Nozzle Flows. in 55th AIAA Aerospace Sciences Meeting (American Institute of Aeronautics and Astronautics, 2017).

PRESENTATIONS

Colloquium Presentations

1. Gehrke, A., Aerodynamic performance of a bio-inspired membrane wing. Direct In-person Colloquium on Vortex Dominated Flows (DisCoVor), Villars-sur-Ollon, VD, Switzerland, May 2022.
2. Gehrke, A., Phenomenology and scaling of optimal flapping wing kinematics. Remote Colloquium on Vortex Dominated Flows (ReCoVor), Online, December 2020.

Conference Presentations

1. **Gehrke, A.** and Mulleners, K., Vortex dynamics and aerodynamic performance of highly deformable flapping wings. Proceedings of the 75th Annual Meeting of the American Physical Society, Division of Fluid Dynamics, Indianapolis, IN, USA, November 2022.
2. **Gehrke, A.**, Richeux J. and Mulleners, K., A bio-inspired membrane wing for passive aerodynamic control. Proceedings of the 74th Annual Meeting of the American Physical Society, Division of Fluid Dynamics, Phoenix, AZ, USA, November 2021.
3. Baskaran, M., Zuliani F., **Gehrke, A.**, Paik J. and Mulleners, K., Optimisation of a bio-inspired jet propulsor. Proceedings of the 74th Annual Meeting of the American Physical Society, Division of Fluid Dynamics, Phoenix, AZ, USA, November 2021.
4. Guasch, M., Matthews M., **Gehrke, A.**, Mulleners, K. and Sponberg S., Wing Flexabilty impacts LEV Bursting location on hawkmoth wings. Proceedings of the 74th Annual Meeting of the American Physical Society, Division of Fluid Dynamics, Phoenix, AZ, USA, November 2021.

5. **Gehrke, A.** and Mulleners, K., Optimization and scaling of aerodynamic performance for a flapping wing in hover. Proceedings of the 73rd Annual Meeting of the American Physical Society, Division of Fluid Dynamics, Chicago, IL, USA, November 2020.
6. **Gehrke, A.**, De Guyon-Crozier, G. and Mulleners, K., Genetic algorithm based optimisation of wing rotation in hover. Proceedings of the 71st Annual Meeting of the American Physical Society, Division of Fluid Dynamics, Atlanta, GA, USA, November 2018.
7. **Gehrke, A.**, Wuensch, O. and Ruetten, M. Integral Surface Analysis of Vortical Lobed Nozzle Flows. in *55th AIAA Aerospace Sciences Meeting* (American Institute of Aeronautics and Astronautics, 2017).

MENTORING AND ACADEMIC SERVICE

Peer Review

Referee for Physical Review Journals by *the American Physical Society*; 2022

Memberships

American Physical Society

Student thesis supervision

Henri Durliat (EPFL) Spring 2021
Clustering analysis of the induced aerodynamic loadings of vortices generated by flapping wings

Sameer Delaporte (EPFL) Fall 2020
Aerodynamic performances of flexible flapping wings

Daniil Morzhakov (EPFL) Fall 2020
Design and construction of a bi-stable flapping wing

Christoph Alexander Busch (EPFL) Spring 2020
Fourier-Series-Based kinematic function for Flapping Wing Optimization

Ce document a été imprimé au Centre d’impression EPFL,
imprimerie climatiquement neutre, certifiée myClimate.